Gold Mineralization in the Missanabie-Renabie District of the Wawa Subprovince (Missanabie, Ontario, Canada)

By

Jordan Alexander McDivitt

A thesis submitted in partial fulfillment
of the requirements for the degree of
Master of Science (MSc) in Geology

The Faculty of Graduate Studies
Laurentian University Sudbury,
Ontario, Canada

THESIS DEFENCE COMMITTEE/COMITÉ DE SOUTENANCE DE THÈSE

Laurentian Université/Université Laurentienne
School of Graduate Studies/École des études supérieures

Title of Thesis Titre de la thèse	Gold Mineralization in the Missanabie-Renabie District of the Wawa Subprovince (Missanabie, Ontario, Canada)
Name of Candidate Nom du candidat	McDivitt, Jordan Alexander
Degree Diplôme	Master of Science
Department/Program Département/Programme	Geology
Date of Defence Date de la soutenance	July 15th, 2016

APPROVED/APPROUVÉ

Thesis Examiners/Examinateurs de thèse:

Dr. Bruno Lafrance
(Co-supervisor/Co-directrice de thèse)

Dr. Daniel J. Kontak
(Co-supervisor/Co-directeur de thèse)

Lise Robichaud
(Committee member/Membre du comité)

Dr. Richard Goldfarb
(External Examiner/Examinateur externe)

Approved for the School of Graduate Studies
Approuvé pour l'École des études supérieures
Dr. David Lesbarrères
M. David Lesbarrères
Director, School of Graduate Studies
Directeur, École des études supérieures

ACCESSIBILITY CLAUSE AND PERMISSION TO USE

Abstract

The geological processes responsible for the formation of hydrothermal gold deposits are often equivocal. For example, gold-bearing, shear zone-hosted laminated quartz veins in the Missanabie-Renabie gold district (Archean Wawa subprovince, Ontario, Canada) have been interpreted as both intrusion-related and metamorphic-hydrothermal in origin.

The veins were mined at the past-producing Renabie mine, which yielded ~1.1 Moz of gold during production from 1941-1991. Whereas the intrusion-related interpretation links the veins to magmatic-hydrothermal fluids released during the crystallization and solidification of their hosting tonalitic pluton, the metamorphic interpretation suggests the veins were deposited from hydrothermal fluids produced during greenschist-facies metamorphism. This study integrates detailed structural field mapping with a number of geochemical techniques to unravel the evolution of the historically controversial ore zones. Results suggest that: (1) the laminated veins and their alteration envelopes pre-date regional deformation, and spatially localized later shear zones, which subsequently focused hydrothermal activity resulting in the formation multistage, composite ore zones; (2) the laminated veins formed during an early, intrusion-related gold event, and the later, co-spatial hydrothermal events are orogenic in nature, and thus more likely to be the products of metamorphic fluids; and (3) discriminating intrusion-related from orogenic events requires constraints provided by geological field mapping. Whereas pressure-temperature information from fluid inclusions and U-Pb geochronology facilitate discrimination, the geochemical signatures of the different hydrothermal events are largely overlapping and do not aid in classification.

Keywords: hydrothermal gold, economic geology, structural geology, geochemistry, Archean geology, Renabie gold mine, Superior craton, Wawa subprovince, shear zone-hosted gold mineralization

Co-Authorship Statement

Chapter 2 is written as a journal manuscript co-authored by J.A McDivitt, B. Lafrance, D.J. Kontak, and L. Robichaud. Chapter 3 is written as a second journal manuscript co-authored by J.A. McDivitt, D.J. Kontak, B. Lafrance, and M. Fayek. Field mapping, sample collection, sample preparation, and the characterization of samples using petrographic and scanning electron microscopes was completed by J.A. McDivitt. Although the two manuscripts benefited from revisions and suggestions by co-authors, J.A. McDivitt is responsible for all interpretations presented in the manuscripts and thesis.

Acknowledgments

I would like to express the utmost gratitude to my supervisors, Drs. Bruno Lafrance and Daniel Kontak, and also to my field supervisor, Lise Robichaud, for their guidance, expertise, and patience throughout the study. The project received generous funding from numerous institutions whose support made the study possible: I would like to convey sincere thanks to the Ontario Geological Survey, the Goodman School of Mines, the Society of Economic Geologists, and the Natural Sciences and Engineering Research Council of Canada. This thesis is supported through the Ontario Geological Survey-Laurentian University Mapping School Agreement.

TABLE OF CONTENTS

Thesis Defense Committee …… ii

Abstract ……..… iii

Co-Authorship Statement …….. iv

Acknowledgments ……..……..…….. v

Table of Contents ……..…….……..... vi

List of Tables ……..…….……...…..... x

List of Figures ……...…..…….……..... xii

List of Appendices ……..……. xv

Chapter 1 – Introduction …….……. 16

1.1 Introduction ……..…. 16

1.2 Structure of Thesis ……..…….. 18

Chapter 2 – Vein Inheritance and Multistage, Shear Zone-Hosted Gold Mineralization: An Example from the Missanabie-Renabie Gold District (Archean Wawa Subprovince, Canada) ……..…… 22

2.1 Introduction ……..… 23

2.2 Geological Setting of the Missanabie-Renabie Gold District ..…….. 25

2.3 The Renabie Area ..……. 26

2.3.1 Production History, Description of Ore Zones, and Gold-Bearing Samples ...……..……..… 26

2.3.2 Description of Structures ..…….……..… 28

2.3.2.1 Pileggi No. 1 and Baltic D ..……. 28

2.3.2.2 The Renabie Trend (C-zone, Nudulama, and Nudulama East) …… 30

2.3.2.3 The Boundary Outcrop …… 33

2.4 Discussion …… 34

2.4.1 Relative Timing of Vein Emplacement, Regional Deformation, and Gold Mineralization …… 34

2.4.2 Early and Late Controls on the Formation and Geometry of the Mineralized Zones …… 35

2.4.3 Comparison To Orogenic Gold Deposits …… 37

2.5 Conclusion …… 38

Chapter 3 – A Discriminatory-Geochemical Approach to Multistage Veining, Alteration, and Mineralization in the Missanabie-Renabie Gold District (Archean Wawa Subprovince, Canada) …… 70

3.1 Introduction …… 72

3.2 Geological Setting, Gold Mineralization, Deformation History, and Vein Types …… 75

3.3 Analytical Methods …… 77

3.3.1 Petrography, Mineral Identification, and Mineral Chemistry …… 77

3.3.2 Lithogeochemistry and Mass Balance …… 77

3.3.3 U-Pb Titanite Geochronology …… 78

3.3.4 LA-ICP-MS Pyrite Mapping …… 78

3.3.5 Fluid Inclusion Petrography and Microthermometry …… 79

3.3.6 Evaporite Mound Analysis …… 79

3.3.7 Oxygen Isotopes ..…….…… 80

3.3.8 Hydrogen Isotopes ..…….……..…… 81

3.3.9 Sulfur Isotopes ..……..…...…… 81

3.4 Veins: Textures, Mineralogy, and Defining Features ……..…… 82

3.4.1 Laminated Quartz Veins …… 82

3.4.2 Hematite-Associated Alteration Veins ……....…… 82

3.4.3 NW-Striking Quartz Tension Gashes ……..……..…… 83

3.4.4 Massive Pyrite Veins ……...……..…… 83

3.5 Hydrothermal Alteration Zones and Prograde Metamorphic Minerals: Setting, Mineralogy, and Key Relationships .…… 84

3.5.1 Saussuritization …… 84

3.5.2 Phyllic Alteration (Quartz-Sericite-Pyrite) ……...… 84

3.5.3 Prograde Metamorphic Assemblage and Epidote Chemistry …..…..… 85

3.5.4 Retrograde Type 1 Alteration: Chlorite-Titanite-Albite-Hematite ...… 86

3.5.5 Retrograde Type 2 Alteration: K-Feldspar-Hematite .....…… 86

3.6 Lithogeochemistry and Mass Balance ……..…… 87

3.7 LA-ICP-MS U-Pb Geochronology ……...…… 87

3.8 Whole Rock Au-Trace Element Associations ……...… 88

3.9 LA-ICP-MS Pyrite Mapping …… 89

3.10 Fluid Inclusions ……..…… 90

3.10.1 Petrography ..……...…… 90

3.10.2 Microthermometry and PT conditions ……...…..… 91

3.10.3 Evaporite Mound Analysis ..……..…….…… 92

3.11 Stable Isotopes …….....…… 93

3.11.1 Oxygen Isotopes ..……...…… 93

3.11.2 Hydrogen Isotopes ……...…… 94

3.11.3 Sulfur Isotopes ……..… 94

3.12 Discussion and Interpretation of Results ……...……...…… 94

3.12.1 Hydrothermal Evolution of the District ……..……. 94

3.12.2 A Discriminatory-Geochemical Approach to the Mineralization and Alteration Events

……..……..…… 100

3.12.3 Origin of Depleted $\delta^{18}O$ Vein Quartz Values: Insights from δD

…….....……..…… 107

3.12.4 Genetic and Discriminatory Implications for Gold Systems; Fluid Sources in Orogenic Deposits ……..…….....…… 110

3.12.5 Significance of Results for Mineral Exploration ……...… 113

3.13 Conclusion ……...……..… 114

List of Tables

Table 2.1 Deformation events, structural features, and vein types present at different outcrops 45

Table 2.2 Relative timing relationships between deformation events, veins, and gold events 45

Table 3.1 LA-ICP-MS U-Pb titanite geochronology: equipment information, machine operating conditions, standard information, and data reduction procedures 130

Table 3.2 LA-ICP-MS pyrite element mapping: equipment information, machine operating conditions, standard information, and data reduction procedures 131

Table 3.3 Summary of the mineralogy, textural characteristics, associated alteration, and defining features of the different vein types 132

Table 3.4 An integrated paragenesis, which builds upon that presented in Table 2.1 133

Table 3.5 Summary of the mineralogy, key features, spatial distributions, and main chemical changes of the different alteration types 134

Table 3.6 Whole-rock major and trace element analyses for representative samples of different alteration types 135

Table 3.7 Compositional data and isotopic ratios for the 41 titanite spot analyses used in age determination 137

Table 3.8 Correlation coefficients and comparative parameters ($X_{Au=1}$, $X_{Au=100}$, and ΔX_{Au}) derived from $\log_{10}$ trace element concentrations reported from whole rock analyses of mineralized samples 139

Table 3.9 Correlation coefficients and comparative parameters ($X_{Au=1}$, $X_{Au=100}$, and ΔX_{Au}) derived from log_{10} trace element data reported by LA-ICP-MS trace element mapping of gold-bearing pyrites ……...……...…… 140

Table 3.10 Summary of microthermometric measurements, salinity, and CO_2 density of fluid inclusion assemblages in Qtz_1 ……...…… 141

Table 3.11 Summary of microthermometric measurements and salinity of fluid inclusion assemblages in Qtz_2 ……..…….…… 142

Table 3.12 δD (‰) values from fluid inclusion waters in Qtz_2 …….…… 142

Table 3.13 Sulfur isotope ($\delta^{34}S$ and $\delta^{33}S$) and calculated $\Delta^{33}S$ values for pyrites …… 143

Table 3.14 Summary of the geochemical characteristics of the different hydrothermal events …….…… 144

List of Figures

Figure 2.1 Location of the Renabie gold deposit and simplified geology map of the Wawa Subprovince ……...……..…… 46

Figure 2.2 Location and simplified geology of the Missanabie-Renabie gold district (A) and the Renabie mine area (B) ……..…...…… 47

Figure 2.3 Grade-contour plan map of the 3540 ft level of the Renabie underground mine ……..…… 48

Figure 2.4 East-west longitudinal section of the Renabie trend ……...…… 49

Figure 2.5 Outcrop photographs and thin-section photomicrographs of Au mineralized zones and different vein types …….....…… 50

Figure 2.6 Detailed geological map of Nudulama East ……...…… 52

Figure 2.7 Logarithmic-scale scatter diagram of Au (ppm) versus Au/Ag for various vein and alteration types …… 54

Figure 2.8 Detailed geological map of Pileggi No.1 ……...…… 55

Figure 2.9 Outcrop photographs of laminated quartz veins and their relationships to structural features ….……...…… 57

Figure 2.10 Stereographic plot (A) and 3D schematic diagram (B) of the Baltic D outcrop ……...… 59

Figure 2.11 Stereographic plots of L2, and poles to S1 and S2 in the Renabie mine area (A), and L2 within and outside of shear zones along the Renabie trend (B) ……..……. 60

Figure 2.12 Detailed geological maps of C-zone and Nudulama …….……...…… 61

Figure 2.13 Nudulama East. F3 folds defined by folded S2, laminated quartz veins, and felsic dikes ……..……...…… 63

Figure 2.14 Outcrop photographs and thin-section photomicrographs of: shear sense indicators in D3 shear zones; hematite-associated alteration veins and massive pyrite veins ..……..... 64

Figure 2.15 Structural relationships at the Boundary outcrop …… 66

Figure 2.16 A mine-scale deformation model, with key overprinting relationships represented by schematic 3D diagrams ……..…… 67

Figure 3.1 Location of the Renabie gold deposit and simplified geology map of the western Wawa-Abitibi Subprovince ……...……...…… 145

Figure 3.2 Location and simplified geology of the Missanabie-Renabie gold district (A), and the Renabie mine area (B) ……..…… 146

Figure 3.3 Outcrop photographs and thin-section photomicrographs of the different vein types and alteration types (1) ……..…… 147

Figure 3.4 Detailed alteration map of the Nudulama East outcrop ……...…… 150

Figure 3.5 Thin-section photomicrographs and SEM-BSE images of the different alteration types (2) and prograde metamorphic minerals ……..…… 152

Figure 3.6 Epidote chemistry plots resulting from SEM-EDS analysis of different epidote types ……..…… 155

Figure 3.7 Mass balance of alteration types ……...…… 156

Figure 3.8 U-Pb titanite geochronology ……..…… 158

Figure 3.9 Bivariate scatter plots of log_{10} data reported by whole rock analyses of mineralized samples ……...…… 159

Figure 3.10 Results of LA-ICP-MS trace element mapping of Py_1 ……...…… 161

Figure 3.11 Results of LA-ICP-MS trace element mapping of Py_2 ……..…… 163

Figure 3.12 Correlation- and regression-based comparison diagrams displaying different populations of mineralized samples from the Au_1 and Au_2 events ……..…..…… 165

Figure 3.13 Thin-section photomicrographs of different fluid inclusion types; SEM-BSE images of decrepitate mounds in Qtz_2; Sketch of secondary fluid inclusion assemblages in Qtz_1 from sample BD-30 …… 166

Figure 3.14 Calculated isochores and interpreted pressure-temperature conditions of laminated quartz vein (A) and breccia quartz vein (B) formation …… 168

Figure 3.15 Graphical summaries of microthermometric measurements from fluid inclusion assemblages containing type 5 inclusions in sample NUE-11; calculated fluid inclusion salinity ternary diagrams …… 169

Figure 3.16 Histograms and cathodoluminesence image displaying results of SIMS $\delta^{18}O$ analyses from vein quartz …… 170

Figure 3.17 Pressure-temperature evolution model for the Missanabie-Renabie gold district …… 171

Figure 3.18 Schematic summary diagram of mineralized zones along the Renabie trend …… 172

Figure 3.19 **(**A) Temperature (X) versus $\delta^{18}O_{qtz}$ (Y) and isopleths of corresponding $\delta^{18}O_{H2O}$ values. (B) Evaluation of a fluid-mixing model to explain the range in $\delta^{18}O_{qtz}$ values. (C) Evaluation of a Rayleigh fractionation-based model to explain the range in $\delta^{18}O_{qtz}$ values …… 173

List of Appendices

Appendix 2.1 Results of precious metal assays from different vein types and alteration assemblages …….……..…… 68

Appendix 3.1 Metal concentrations (ppm) from the mineralized samples plotted in Figure 3.9 ..…… 176

Appendix 3.2 Results of SIMS $\delta^{18}O$ analysis of vein quartz …….……...…… 179

Chapter 1

1.1 Introduction

The processes responsible for gold mineralization in metamorphic terranes are often controversial. This is well-exemplified by studies that have resulted in conflicting genetic interpretations of individual deposits (e.g., the Hemlo deposit; Lin, 2001), and also by the numerous models that invoke different mechanisms to explain the formation of gold-rich hydrothermal fluids (e.g., metamorphic models (Phillips and Groves, 1983) versus magmatic models (Spooner, 1993)). Unlike epithermal gold deposits, which form at shallow crustal levels (<~1 km; Cooke and Simmons, 2000), and have exposed analogs that can be studied (e.g., the Taupo Volcanic Zone; Simmons *et al*., 2016), gold deposits in metamorphic terranes typically form at greater crustal depths (i.e., 2-20 km; Goldfarb *et al*., 2005), and are thus unable to be examined in a direct sense.

Geochemical studies of deposits are completed with the intent of constraining the origin of hydrothermal fluids and the constituents of mineralized zones, but it is well-recognized that geochemical data is typically equivocal (McCuaig and Kerrich, 1998; Goldfarb *et al*., 2005; Goldfarb and Groves, 2015), or not representative of the mineralizing event. Stable isotope (O, H, S) data from deposits emphasizes these points, with calculated $\delta^{18}O$ values for mineralizing fluids commonly plotting in the overlap range between magmatic and metamorphic waters (McCuaig and Kerrich, 1998), depleted δD values in fluid inclusion waters reflecting the presence of late-stage, secondary fluid inclusions (Kyser and Kerrich, 1990), and $\delta^{34}S$ values in sulfides that are strongly influenced by fluid-chemical parameters such as oxidation state (e.g., Evans *et al*., 2006), and thus modified from those characteristic of their source.

Uncertainty in the structural timing of mineralization further complicates genetic interpretations (Robert and Poulsen, 2001). Orogenic gold deposits (Groves *et al*., 1998), which

are considered to reflect primarily metamorphic processes (Goldfarb *et al*., 2005), typically comprise structures that formed late during the tectonic evolution of gold districts, and alteration assemblages which overprint metamorphic minerals in adjacent wallrocks (e.g., the Sigma deposit; Robert and Brown, 1986); conversely, deposits with anomalous metal associations (Groves *et al*., 2003), which are often considered to be overprinted porphyry-epithermal and volcanogenic massive sulfide (VMS) deposits (i.e., deposits of a magmatic affinity), commonly pre-date deformation and metamorphism. Although the timing of mineralization relative to the geologic evolution of terranes differs between the two deposits types, both can exist in a shear zone-hosted structural setting; thus, deposits that formed prior to regional deformation and were later deformed along major structures may coexist with, and appear similar to deposits that formed along the deforming structures.

The complex geological histories of gold-endowed metamorphic terranes, and presence of multiple gold mineralization events (e.g., the Timmins-Porcupine camp; Bateman *et al*., 2008), necessitates that geochemical studies are focused on samples constrained within detailed, holistic, field-based parageneses, which integrate igneous, metamorphic, hydrothermal, and tectonic events. The equivocal nature of geochemical data, and often ambiguous timing of mineralization relative to its host structure, emphasizes that isolated geochemical studies completed on mineralized samples that are not well-constrained, are unlikely to yield insightful results.

The main goals of this thesis are to characterize the mineralogy, geochemistry, and structural setting of past-producing ore zones in the Missanabie-Renabie gold district (Archean Wawa subprovince, Ontario, Canada), and to provide new insights into the geological processes responsible for their formation. This is done by the application of numerous geochemical techniques to samples constrained within an integrated, field-based paragenesis that defines the deformation history of the district. The employed geochemical techniques include those which are commonly used in deposit studies (e.g., lithogeochemistry and mass balance, $\delta^{34}S$ analysis of

pyrite), and also those which are not commonplace (e.g., SIMS $\delta^{18}O$ analysis of quartz, fluid inclusion decrepitate mound analysis), and thought to be more useful in defining a link to either magmatic or metamorphic fluid sources (e.g., $\Delta^{33}S$ analysis of sulfides; Xue *et al*., 2013).

1.2 Structure of Thesis

This thesis consists of a general introduction (Chapter 1) that provides background information and the thesis objectives. The introduction is followed by two manuscripts (Chapter 2 and Chapter 3), formatted for the journal of Economic Geology. Chapter 2 presents the results of a field-based structural study, which provides constraints on the deformation history of the district, the kinematics of the main structures hosting mineralization, and on the relative timing of veining, alteration, and mineralization events. Chapter 3 presents the results of a discriminatory-geochemical approach to the different hydrothermal phases, which tests the viability of using geochemistry to fingerprint and discriminate between different hydrothermal events in gold districts. Chapter 3 also discusses the implications the results of this study have for mineral exploration and outstanding issues in gold deposit models. Preliminary are presented in McDivitt *et al*., 2015, and an additional release, which includes whole rock and metal assay geochemical data and field photographs, comprises Ontario Geological Survey, Miscellaneous Release—Data 339 (McDivitt, 2016).

References

Bateman, R., Ayer, J. A., and Dubé, B., 2008. The Timmins-Porcupine Gold Camp, Ontario: Anatomy of an Archean greenstone belt and Ontogeny of Gold Mineralization: Economic Geology, v. 103, p. 1285–1308

Cooke, D.R., and Simmons, S.F., 2000, Characteristics and Genesis of Epithermal Gold Deposits: Reviews in Economic Geology, v. 13, p. 221–244.

Evans, K.A., Phillips, G.N., and Powell, R., 2006. Rock-Buffering of Aurifeous Fluids in Altered Rocks Associated with the Golden Mile-Style Mineralization, Kalgoorlie Gold Field, Western Australia: Economic Geology, v. 101, p. 805-817

Goldfarb, R.J., and Groves, D.I., 2015, Orogenic gold: Common or evolving fluid and metal sources through time: Lithos, v.233, p. 2-26

Goldfarb, R.J., Baker, T., Dubé, B., Groves, D.I., Hart, C.J.R., Gosselin, P., 2005, Distribution, Character, and Genesis of Gold Deposits in Metamorphic Terranes: Economic Geology 100th Anniversary, p. 407–450.

Groves, D.I., Goldfarb, R.J., Gebre-Mariam, M., Hagemann, S.G., and Robert, F., 1998, Orogenic gold deposits: A proposed classification in the context of their crustal distribution and relationship to other gold deposit types: Ore Geology Reviews, v. 13, p. 7–27.

Groves, D.I., Goldfarb, R.J., Robert, F., and Hart, C.J.R., 2003, Gold deposits in metamorphic belts: Overview of current understanding, outstanding problems, future research, and exploration significance: Economic Geology, v. 98, p. 1–29.

Kyser, T.K., Kerrich, R., 1990, Geochemistry of fluids in tectonically active crustal regions: Nesbitt, B.E. (Ed.), Fluids in Tectonically Active Regimes of the Continental Crust. Min. Assoc. Can. Short Course 19, p. 133-230.

Lin, S., 2001, Stratigraphic and Structural Setting of the Hemlo Gold Deposit, Ontario, Canada: Economic Geology, V. 96, p. 477-507.

McCuaig, T.C., and Kerrich, R., 1998, P-T-t-deformation-fluid characteristics of lode gold deposits: Evidence from alteration systematics: Ore Geology Reviews, v. 12, p. 381–454.

McDivitt, J.A., Lafrance, B., Kontak, D.J., and Robichaud, L., 2015, Characterization of Gold Mineralization in the Missanabie-Renabie District of the Wawa gold camp: Summary of Field Work and Other Activities, Open File Report 6313, p. 6-1 to 6-8.

McDivitt, J.A., 2016, Gold Mineralization in the Missanabie-Renabie District of the Wawa Subprovince: Geochemical Data and Photographs: Ontario Geological Survey, Miscellaneous Release—Data 339.

Phillips, G.N., and Groves, D.I., 1983, The Nature of Archaean gold-bearing fluids and deduced from gold deposits of Western Australis: Journal of the Geological Society of Australia, v. 30, p. 25-39.

Robert, F., and Brown, A.C., Archean Gold-Bearing Quartz Veins at the Sigma Mine, Abitibi Greenstone Belt, Quebec: Part II. Vein Paragenesis and Hydrothermal Alteration: Economic Geology, v. 81, p. 593-616.

Robert, F., and Poulsen, K.H., 2001, Vein formation and deformation in greenstone gold deposits: Reviews in Economic Geology, v. 14, p. 111–155.

Simmons, S.F., Brown, K.L., and Tutolo, B.M., 2016, Hydrothermal Transport of Ag, Au, Cu, Pb, Te, Zn, and Other Metals and Metalloids in New Zealand Geothermal Systems: Spatial Patterns, Fluid-Mineral Equilibria, and Implications for Epithermal Mineralization: Economic Geology, v. 111, p. 589-618.

Spooner, E.T.C., 1993, Magmatic sulfide/volatile interaction as a mechanism for producing chalcophile element enriched, Archean Au-quartz, epithermal Au-Ag and Au skarn hydrothermal ore fluids: Ore Geology Reviews, v. 7, p. 359–379.

Xue, Y., Campbell, I., Ireland, T, R., Holden, P., and Armstrong, R., 2013, No mass-independent sulfur isotope fractionation in auriferous fluids supports a magmatic origin for Archean gold deposits: Geology, v. 41, p. 791-794.

Chapter 2 - *Vein Inheritance and Multistage, Shear Zone-Hosted Gold Mineralization: An Example from the Missanabie-Renabie Gold District (Archean Wawa Subprovince, Canada)*

Jordan A. McDivitt[1,+,x], Bruno Lafrance[1], Daniel J. Kontak [1], and Lise Robichaud[2]

[1]*Mineral Exploration Research Centre, Department of Earth Sciences, Laurentian University, Ramsey Lake Road, Sudbury, On, P3E 2C6, Canada.*

[2]*Earth Resources and Geoscience Mapping Section, Ontario Geological Survey, Sudbury, Ontario, P3E 6B5*

[+] *jmcdivitt@laurentian.ca*

[x] *Current Address: Department of Earth Sciences, Laurentian University, 935 Ramsey Lake Road, Sudbury, Ontario, Canada P3E 2C6*

Abstract

The Missanabie-Renabie gold district is characterized by gold-bearing quartz veins within late, E-trending shear zones. The latter cut across ca. 2.72 Ga tonalite of the Missinaibi Lake batholith in the Wawa subprovince of the Archean Superior craton, Ontario, Canada. The veins were the focus of gold production at the Renabie mine, which over 50 years from 1941 to 1991 produced ~1.1 million ounces of gold at a grade of ~6.6 g/t. Because the veins are hosted by shear zones, they were interpreted as fault-fill veins that formed during the upward migration of magmatic or metamorphic hydrothermal fluids along actively deforming shear zones. The veins, which are laminated and very fine-grained with a saccharoidal texture, are characteristically similar to fault-fill veins associated with orogenic gold deposits; however, they differ by the relative chronology of the veins and shear zones. The veins are overprinted by several generations of structures. They were first locally folded by recumbent to inclined, isoclinal F_1 folds with an axial planar S_1 cleavage. They were then overprinted by NW- to NNW-striking F_2 folds with a steeply-

dipping, axial planar S_2 cleavage, and a W-plunging L_2 mineral stretching lineation. S_2 and L_2 are penetrative fabrics that formed during regional deformation of the tonalite and surrounding metavolcanic rocks. Subsequent NE-SW shortening induced shearing along the weak, altered wall rocks surrounding the veins. The S2 cleavage was deflected in anticlockwise fashion and, along with some of the veins, folded and transposed parallel to the axial planes of F3 folds into the orientation of the E-striking shear zones. The W-plunging L_2 lineation underwent a similar anticlockwise rotation and was rotated by ~35° along the shear zones. Along with localized sinistral-reverse shearing, this D3 event resulted in the formation of a strong S3 foliation within the alteration envelopes of the veins. Synchronously with shearing hydrothermal fluids entered the shear zones and resulted in the formation of quartz ± epidote ± chlorite ± K-feldspar ± hematite veins and local hydrothermal breccias surrounded by hematite-bearing alteration zones. The attitude of the ore zones is controlled by the strike and dip of the shear zones, and by the plunge of the rotated, older, regional L_2 lineation. A late dextral reactivation of the shear zones, as indicated by the presence of Z-shaped drag folds (F4), quartz-filled tension gashes, and dextral shear bands, had minimal effect on the geometry of the ore zones. Syn- to post-D4, NW-striking, gold-bearing pyrite veins were emplaced last along the shear zones, and represent a late-stage gold-mineralization event. The Renabie veins are excellent examples of early veins surrounded by weak altered wall rocks that acted as planar anisotropies and localized the development of shear zones and the migration of later hydrothermal fluids. Thus, the veins did not form along actively deforming shear zones as previously proposed; they formed prior to regional deformation and spatially localized the younger shear zones in which they are hosted.

2.1 Introduction

Orogenic gold deposits are typically associated with shear zones. The latter act as conduits for the migration of hydrothermal fluids because they are more permeable than their surrounding rocks (Cox et. al., 2001). With increases in fluid pressure, stress, and strain rate, they can undergo

brittle reactivation, resulting in a higher fluid flux as fluids migrate upward along the fault (Sibson et al., 1988). Greenschist grade deposits typically comprise fault-fill veins and breccias (Groves, 1993), which formed during multiple cycles of brittle reactivation and sealing of the faults or shear zones. This contrasts with deeper crustal, amphibolite grade deposits in which gold is often present as disseminations (Groves, 1993) due to diffuse flow of gold-bearing hydrothermal fluids through transient connected networks of grain-scale dilational sites induced by shearing (Cox et. al., 2001). In both cases mineralization and hydrothermal alteration are coeval with shear zone deformation, and occur late during the tectonic evolution of gold districts.

The Missanabie-Renabie gold district is located in the Wawa subprovince of the Archean Superior province, Canada (Fig. 2.1). It comprises numerous occurrences of auriferous, laminated quartz veins hosted by shear zones, which cut across tonalite of the Missinaibi Lake batholith (Percival, 1981). Aplite and pegmatite dikes are spatially associated with the veins and shear zones, and because of their geochemistry have been considered petrogenetically linked to the tonalite host rocks. This led to the suggestion that the laminated veins themselves are magmatic-hydrothermal in origin (Jemielita et al., 1986). Conversely, the presence of H_2O-CO_2 fluid inclusions within the veins has been interpreted to reflect their derivation from a metamorphic fluid (Studemeister and Kilias, 1987). Subsequently, Callan and Spooner (1998) suggested that the laminated veins formed by repeated hydraulic fracturing and sealing of the shear zones by overpressured hydrothermal fluids derived from a deep crustal source, to which the Kapuskasing structural zone (Percival, 1988; Percival and West, 1994) represents an analogue. Thus, the origin of the veins is contentious, and they have been interpreted as both intrusion-related and orogenic, although the latter term had not been yet introduced by Groves et al. (1998) at the time of these studies.

This paper is one of two companion papers on the origin of these veins, and discusses the formation of the veins in the context of the structural evolution of the district. The second paper

presents a mineralogical and geochemical study of the veins and associated hydrothermal alteration. We suggest that the veins were emplaced before regional deformation of their host rocks, and that they acted as strong planar anisotropies that localized subsequent shearing, hydrothermal alteration, and mineralization. Therefore, although the veins are spatially associated with shear zones, they predate the formation of these shear zones. This contrasts with previous interpretations of vein emplacement, wherein they have been considered to have formed synchronously with shear zone deformation.

2.2 Geologic Setting of the Missanabie-Renabie Gold District

The Missanabie-Renabie gold district (Fig. 2.2A) comprises numerous quartz vein occurrences distributed across the northeastern portion of the Michipicoten greenstone belt, and the western margin of the adjacent Wawa gneiss domain. Three main cycles of bimodal volcanism (~2.90 Ga, ~2.75 Ga, and ~2.70 Ga cycles) are defined within the greenstone belt (Sage, 1986; Turek *et al*., 1982, 1984; Sage and Heather, 1991; Turek *et al*., 1992; Heather and Arias, 1992), and the volcanic rocks are metamorphosed, to greenschist facies and amphibolite facies in the center and margins of the belt, respectively (Ayres, 1978; Studemeister, 1983; Heather and Buck, 1988). Plutons intruded the northeast portion of the belt, in the vicinity of the Missanabie-Renabie gold district, during a late magmatic episode, and vary in age from ~2.68-2.66 Ga; the plutons are predominantly granitoids (i.e., tonalities, granodiorites, and granites), but show significant variability in their compositions (Turek *et al*., 1990; Turek *et al*., 1992; Corfu and Sage, 1992; Turek *et al*., 1996). The timing of deformation across the belt is poorly constrained, but significant deformation likely occurred from ~2.68-2.66 Ga, synchronous with late-stage plutonism (Corfu and Sage, 1992; Turek *et al*., 1996).

The Michipicoten greenstone belt is bound to the east and south by the Wawa gneiss domain. The latter consists of felsic gneisses and granitoid plutons surrounding slivers of supracrustal rocks (Moser, 1989; Moser, 1993). The deformed plutonic and supracrustal rocks vary

in age from ~2.9 Ga to ~2.66 Ga, and thus largely overlap in age with the volcanic and plutonic rocks of the Michipicoten greenstone belt (Moser, 1993; Moser, 1994). Metamorphic grade is typically amphibolite facies, and deformation is bracketed between ~2.67 and ~2.64 Ga (Moser, 1994). The Wawa gneiss domain terminates to the east against the Kapuskasing structural zone, which represents a Neoarchean to Paleoproterozoic intracratonic uplift zone exposing deep crustal, amphibolite- to granulite-grade metamorphic rocks (Percival and West, 1994).

The Missanabie-Renabie gold district straddles the contact between volcanic rocks of the Michipicoten greenstone belt and plutonic rocks of the Missinaibi Lake batholith, a component of the Wawa gneiss domain. The volcanic rocks consist of massive to pillowed mafic flows and intermediate to felsic volcaniclastic rocks, dated (U-Pb zircon) at 2740±8 Ma (Turek et al., 1996), 2728.6±1.1 Ma (Kamo, 2015; Robichaud et al., 2015), and 2723±5 Ma (Kamo, 2014; Robichaud et al., 2015). They are intruded by gabbroic and fine-grained felsic dikes, which increase in abundance towards the contact of the volcanic rocks with a 2720.8±1.4 Ma (U-Pb zircon; Kamo, 2015; Robichaud et al., 2015) biotite-bearing tonalitic component of the Missinaibi Lake batholith. The batholith-greenstone belt contact, volcanic units, and dikes strike N to NW and dip 50˚ to 80˚W, parallel to a strong penetrative regional foliation. Late N- to NNW-trending Matachewan mafic dikes cut across the regional foliation and the mineralized zones.

2.3 The Renabie Area

2.3.1 Production History, Description of Ore Zones, and Gold-Bearing Samples

The only past-producing gold zones in the Missanabie-Renabie gold district are in the Renabie mine area (Fig. 2.2B). Gold was produced from the Renabie underground mine and from the C-zone, Nudulama, and Braminco open pits. Mining occurred over a 50 year period, from 1941-1991, and produced ~1.1 Moz of Au at a grade of ~6.6 g/t (Turek et al., 1996; Callan and Spooner, 1998). The production zones from the Renabie mine to Nudulama define an ESE trend, herein named the Renabie trend, which strikes close to perpendicular to the regional foliation.

Assay-defined ore shoots have E to ESE trends (Fig. 2.3) and a moderate westerly plunge (~50˚) (Fig. 2.4). The Braminco zone, which is located ~1.1 km south of the Renabie trend, differs in orientation: the zone strikes NW and dips steeply (~70˚) to the W, parallel to the regional foliation. Although the Braminco zone is roughly perpendicular to the Renabie trend, ore shoots plunge ~55˚ to the west, similar to those along the Renabie trend (Callan and Spooner, 1998).

Mineralization along the Renabie trend is exposed from west to east at the C-Zone, Nudulama, and Nudulam East. The mineralized zones are characterized by laminated quartz veins (Fig. 2.5A), varying in width from ~1-4 m, hosted by steeply-dipping, ESE-striking shear zones, which are only slightly wider than the veins (~2-10 m) (Fig. 2.5B, C). The shear zones are defined by strongly foliated quartz-sericite-pyrite schist. The veins consist of very fine-grained quartz layers with saccharoidal textures separated by sericitic laminae; the alternating domains are of mm- to cm-scale widths and define a laminated texture. Both the laminated veins and schist are mineralized. The veins typically contain 2-5% pyrite with minor chalcopyrite, molybdenite, galena, sphalerite, and rare specks of visible gold (Fig. 2.5D). The schist contains as much pyrite, but other sulfide minerals are rare to absent. In both the veins and schist pyrite occurs as fine-grained, subhedral to euhedral grains with hematite replacement rims.

In addition to the laminated veins, late quartz ± chlorite ± epidote ± K-feldspar veins are associated with the mineralized zones at Nudulama and Nudulama East. Hematite is present either in the alteration halo of the veins, or as an infill mineral within the veins. These veins are hereafter termed hematite-associated alteration veins. At Nudulama East (Fig. 2.6), where a large number of hematite-associated alteration veins are present, biotite within the host tonalite is pervasively chloritized, and the rock displays a distinct reddish hue due to the presence of hematite. Pyrite within this hematite alteration zone is replaced by hematite along its margins (Fig. 2.5E). A spectacular quartz-chlorite breccia body is associated with the hematite alteration zone and cuts across the mineralized shear zone (quartz-sericite-pyrite schist) and the laminated quartz veins. The

breccia contains clasts of laminated quartz veins and strongly foliated and hematite-altered tonalite enclosed within a matrix of quartz (Fig. 2.5F), which locally defines vugs infilled by chlorite. Although underground workings are no longer accessible, hematite-altered tonalite is described in association with gold mineralization at the Renabie underground mine (Callan and Spooner, 1998). Hematite alteration is also present within the Missinaibi Lake batholith at its contact with the Michipicoten greenstone belt (Chapter 3).

Massive pyrite veins, varying in thickness from ~1-5 cm, cut across the hematite-associated alteration veins (Fig. 2.5G) at Nuduluma East. Pyrite within the cm-thick veins occurs as medium to coarse, anhedral grains, with serrated grain boundaries. It differs from pyrite associated with the laminated veins and schist by its lack of hematite replacement rims and its anhedral grain shape (Fig. 2.5H).

Precious metal assay data subdivided by vein type and alteration assemblage is displayed in Appendix 2.1 and on Figure 2.7. The laminated quartz veins, schist, and massive pyrite veins all yielded significant gold values, consistently greater than 0.1 ppm, but the hematite-bearing alteration zones are unmineralized. Bulk channel sampling of the breccia zone at Nudulama East returned a weighted average of 32 ppb Au over 7.01 m (Tremblay, 2004, unpublished assessment report on the Nudulama East property).

2.3.2 Description of Structures (Table 2.1)

2.3.2.1 Pileggi No. 1 and Baltic D

Mineralized zones at Pileggi No. 1 and Baltic D (Fig. 2.2B) occur in structural settings that differ from those along the Renabie trend: at Pileggi No. 1 (Fig. 2.8) the mineralized zone is parallel to the regional foliation as opposed to at a high angle; at Baltic D mineralized veins are shallow in their dip, and define open folds to which the regional foliation is axial planar. Pileggi No. 1 further differs from the other mineralized zones as it is hosted by volcanic rocks of the Michipicoten greenstone belt rather than by tonalitic rocks of the Missinaibi Lake batholith. It

consists of laminated quartz veins and quartz tension gashes in strongly foliated, mafic to intermediate volcanic rocks. Deformed feldspar- and amphibole-phyric porphyry dikes, and late, undeformed Matachewan mafic dikes are intrusive to the volcanic rocks. The laminated quartz veins are overprinted by isoclinal folds (F1) associated with a differentiated axial planar cleavage (S1) defined by microlayers of plagioclase alternating with microlayers of epidote, amphibole, and opaque black minerals. The F1 folds and S1 cleavage formed during an early D1 deformation event, which predated the development of the regional foliation (S2) during D2. The S2 foliation is axial planar to an upright, shallowly-plunging fold (F2) (Fig. 2.9A), that occupies half the width of the outcrop. The fold overprints the S1 cleavage and the F1 folded laminated veins. Smaller parasitic folds in the hinge and limbs of the larger fold vary in plunge from sub-horizontal to moderately WNW- (up to 50˚) and ESE-plunging (up to 40˚). Elongate aggregates of quartz, carbonate, and pyrite are present in the hinges of the parasitic folds and plunge ~40˚ to the ESE. S2 has a steep dip and strike of ~100˚; it is expressed as a crenulation cleavage in the hinges of F2 folds, and as a slaty transposition cleavage along the limbs of the folds, where it is defined by microlayers of amphibole and opaque minerals alternating with recrystallized, epidote-altered plagioclase.

Z-shaped drag folds and sub-vertical quartz tension gashes overprint S2. The Z-shaped drag folds are steeply-plunging and ENE-striking. Excellent examples are preserved adjacent to stacked porphyry dike boudins. Because the boudinage of the dike indicates extension and the stacking of the boudins indicates subsequent shortening, this suggests that the dike was first stretched and boudinaged and then the boudins were thrusted above one another during dextral shear. Further evidence of dextral shear is suggested by the presence of quartz tension gashes cutting across F2-folded laminated quartz veins (Fig. 2.9B). The tension gashes are NW-striking and oriented clockwise to the S2 cleavage. They are either sigmoidal with Z-shaped asymmetry or straight: the sigmoidal tension gashes were emplaced early during dextral shear and were subsequently Z-

folded, whereas other tension gashes were emplaced late during the same event and remained straight. The Z-shaped drag folds and tension gashes suggest that the S2 cleavage was locally reactivated as a dextral shear fabric. This deformation is attributed to a D4 event because older structures related to a D3 deformation event are present along the Renabie trend.

Similar structural relationships are observed at the Baltic D outcrop (Fig. 2.10). The outcrop is located ~3 km southeast of the Renabie trend within tonalite of the Missinaibi Lake batholith. Observable are laminated quartz veins surrounded by sericite-pyrite-altered wallrocks that are isoclinally folded by near recumbent F1 folds (Fig. 2.9C), and refolded by upright, NW-striking F2 folds. The F1 folds have an axial planar, continuous S1 cleavage, defined by discontinuous microdomains of recrystallized quartz (~1-5 mm in length) surrounded by fine-grained sericite and minor epidote and biotite. The F2 folds have an axial planar S2 cleavage striking ~325˚ and dipping ~75˚ to the W. S2 is a continuous cleavage defined by thin (~0.5-1 mm), anastomosing microdomains of biotite alternating with thicker (~2 mm) microdomains of epidote-altered plagioclase and recrystallized quartz. F2 folds plunge ~35˚ to the NW subparallel to an L2 mineral stretching lineation defined by recrystallized, linear aggregates of quartz and plagioclase surrounded by biotite.

2.3.2.2 The Renabie Trend (C-zone, Nudulama, and Nudulama East)

The ESE-striking Renabie trend is exposed on several stripped outcrops and small open pits east of the contact between the Michipicoten greenstone belt and Missinaibi Lake batholith. South and north of the Renabie trend, the regional S2 foliation dips moderately to steeply W and strikes NNW to N (~330-360˚), roughly perpendicular to the Renabie trend (Fig. 2.11A). An older S1 foliation that has a similar strike to the S2 foliation and a more shallowly westerly dip is locally preserved. A regional stretching lineation (L2) lies along S2 foliation planes; it has a plunge of ~50° towards the WNW (~295˚). A few isolated, massive to laminated, saccharoidal quartz veins, similar to those along the Renabie trend, are present south and north of the trend. Locally, these

veins occur as sheeted sets. The veins are steeply dipping and in some instances, where they are associated with pronounced sericitic alteration envelopes, S2 is sinistrally deflected at the margins of the veins (Fig. 2.9D).

Laminated quartz veins and pegmatitic to aplitic felsic dikes become more abundant with increasing proximity to the mineralized shear zones along the Renabie trend (Fig. 2.12). Marginal to the shear zones the veins and dikes are overprinted by F2 folds with an S2 cleavage, which gradually changes in orientation from ~310˚outside of the shear zone to ~295˚inside the shear zone at Nudulama, and from ~330˚to ~280˚at the C-zone (Fig. 2.9E). The L2 lineation undergoes a similar change in orientation, and is more pronounced within the shear zones. It has an average regional trend of ~295˚and a plunge of ~50˚. Its plunge remains roughly the same within the shear zones, but its trend gradually changes to ~260˚within the shear zones (Fig. 2.11B). At Nudulama East, where the S2 foliation is oriented roughly perpendicular to the trend of the shear zones, the foliation and F2 folds are overprinted and transposed by F3 folds into parallelism with the orientation of the shear zones (Fig. 2.13). The folds have an axial planar S3 foliation, which becomes the main foliation within the shear zones. S3 is axial planar to rootless, isoclinal hook folds, and it wraps around less deformed lithons of tonalite with preserved S2 and L2 fabrics. S3 is defined by anastomosing, fine-grained sericite foliation planes, surrounding recrystallized quartz microdomains. S-C fabric relationships, shear bands (Fig. 2.14A, B), and the anticlockwise deflection of S2 and L2 along the Renabie trend, collectively indicate sinistral-reverse movement along the shear zones.

Mutual overprinting relationships are observed between hematite-associated veins and D3 structures. The veins are preferentially NE-striking and steeply-dipping (Fig. 2.6B). They cut across the S3 foliation (Fig. 2.14C), but are also deformed parallel to the foliation (Fig. 2.14D), and are overprinted by F3 folds with an axial planar S3 foliation (Fig. 2.14E). These mutual overprinting relationships between the veins and D3 structures suggest that the veins are syn-D3.

At Nudulama East infill mineralogy the veins consists of quartz, chlorite, and epidote, with hematite present in their altered wall rocks. They are spatially associated with a spectacular hydrothermal breccia, which is exposed over an area of ~50 m^2. The breccia contains fragments of laminated quartz veins and hematite-altered, S3-foliated tonalite, surrounded by a quartz ± chlorite matrix. Quartz ± chlorite veins occur as apophyses linked to the breccia; these cut across the S3 foliation and are folded by Z-shaped folds (Fig. 2.14F). Other similar Z-shaped folds overprint S3 in shear zones (Fig. 2.14G). The folds strike ENE and plunge moderately (~60°) to the W. These folds, together with the presence of steeply dipping dextral shear bands, suggest that the D3 shear zones were dextrally reactivated during a later D4 event.

Gold-bearing, massive pyrite veins cut across the laminated quartz veins, S3, and the hematite-associated alteration veins. The pyrite veins are mostly found at Nudulama East, where they generally strike ~330 ˚and dip steeply to moderately to the S (~70-35˚) (Fig. 2.6C, Fig. 2.14H). The veins are generally straight and presumably undeformed, except for one vein that gradually changes in orientation and may be openly folded. Although the veins postdate the formation of D3 structures, overprinting relationships between these veins and D4 structures are not observed on outcrop. As their NW to NNW orientation is consistent with the emplacement of the veins along tensile fractures during D4, the veins may have been emplaced during D4; conversely, they may represent post-D4 structures.

Late, north-trending, brittle faults (D5) cut across the Renabie trend. The faults have an apparent sinistral offset. One of these faults, the Shaft Fault (Fig. 2.2B), offsets the contact between the Michipicoten greenstone belt and the Missinaibi Lake batholith. It is interpreted as an oblique-slip fault, with a sinistral strike-slip component and a west-side-up, dip-slip component (Callan and Spooner, 1998).

2.3.2.3 The Boundary outcrop

The Boundary outcrop (Fig. 2.2B) is located in the Michipicoten greenstone belt, within ~200 m of the Missinaibi Lake batholith. It is described here because it shows how the regional NNW-striking S2 foliation was reactivated during the formation of E-striking shear zones along the Renabie trend. The Boundary outcrop consists of gabbro transected by fine-grained felsic dikes, and rusty sulfide-bearing felsic volcanic rocks and minor mafic volcanic rocks. S2 is well developed in both the gabbro and felsic dikes, and it strikes ~340˚, subparallel to lithologic contacts. In the felsic units it is locally oriented clockwise to lithologic trend and overprinted by S-shaped folds, which have a NNE-striking axial planar cleavage similar in orientation to S2. The orientation of these structural features and overprinting relationships suggest that S2 formed early during sinistral shearing parallel to N-trending lithological contacts, and it was then S-folded with the development of a new cleavage later during the same deformation event.

A few meters to the north on the same outcrop (Fig. 2.15), a small mafic dike truncates the limbs and axial planar cleavage of a NNW-trending fold, which is exposed over ~5 m. The fold overprints an early cleavage and isoclinally folded quartz veins with saccharoidal textures. The fold and overprinted cleavage are interpreted as F2 and S1, respectively, based on orientation and overprinting relationships. A mafic dike, which truncates the F2 fold, is overprinted by a Z-shaped fold on the west limb of the F2 fold (Fig. 2.15). This fold, as well as other Z-shaped folds defined by folded S2, suggest that the NNW-trending limb of the F2 fold underwent dextral shear after the emplacement of the late mafic dike. Thus, as described in the last paragraph, the formation of the penetrative, NNW-trending, regional S2 cleavage involved a sinistral component of shear, and it was dextrally reactively, presumably during D3 when the Renabie trend shear zones formed.

2.4 Discussion

2.4.1 Relative Timing of Vein Emplacement, Regional Deformation, and Gold Mineralization

The chronology of the veins, alteration assemblages, structural events, and gold mineralization events are summarized in Figure 2.16 and Table 2.2. Several lines of evidence suggest that the laminated quartz veins were emplaced early during the deformation history of the district. At Pileggi No. 1 and Baltic D the veins are isoclinally folded by F1 folds, and overprinted by F2 folds and the regional S2 cleavage (Fig. 2.9A, C). Along the Renabie trend, the veins are further overprinted by F3 folds and modified by shearing (Fig. 2.13). The emplacement of the laminated quartz veins corresponds to the first and main gold mineralization event in the district, and it predates regional deformation and the formation of the shear zones. This interpretation differs from that of Callan and Spooner (1988, 1998), who suggested that the veins and hydrothermal alteration were coeval with the development of the shear zones (i.e., syn-D3).

During the D3 event, shear deformation became localized in the weak, sericitic alteration envelopes surrounding the veins. This transformed the altered tonalitic wall rocks of the veins into the quartz-sericite-pyrite schist that characterizes the sinistral-reverse shear zones along the Renabie trend. D3 shearing was accompanied by the migration of hydrothermal fluids along the shear zones. Pyrite from the first mineralization event was altered to hematite, and hematite-associated alteration veins were emplaced across S3 (Fig. 2.14C), but were also deformed parallel to S3 (Fig. 2.14D), suggesting that the hematite alteration and veins were coeval with shear zone deformation. The D3 event ended with the formation of the hydrothermal breccias, which cut across the shear zone foliation (S3) and contain hematized fragments of the sheared tonalite (Fig. 2.5F).

During the D4 event, the main foliations at Pileggi No. 1 (i.e., S2) and along the Renabie trend shear zones (i.e., S3) were reactivated as dextral shear fabrics, as suggested by the presence of overprinting, NW-striking quartz tension gashes (Fig. 2.9B), dextral shear bands, and Z-shaped

drag folds (Fig. 2.14G). The massive, gold-bearing pyrite veins, which lack the hematite-replacement rims observed on early pyrite (Fig. 2.5H), were emplaced during a second gold mineralization event, which postdates the formation of the D3 shear zones and hematite alteration. Their preferred NW orientation (Fig. 2.6C) is consistent with their formation during D4, although the veins may have been emplaced during a later brittle event unrelated to D4. In summary, gold was deposited during two mineralization events in the Renabie mine area: an early pre-D1 mineralization event, represented by the gold-rich laminated quartz veins, and a syn- to post-D4 mineralization event, represented by the massive, gold-bearing pyrite veins.

The deformation history of the Missanabie-Renabie gold district is similar to that of major Archean gold camps in the Superior craton (Robert and Poulsen, 2001). D1 is a localized event, and as such possibly corresponds with the early thrusting event reported in other gold camps. D2 corresponds to the regional folding and foliation-forming deformation event associated with the main ductile movement along major transcrustal faults or deformation zones (Robert and Poulsen, 2001). Finally, D3 and D4 are consistent with sinistral followed by dextral transcurrent reactivation of the E-trending transcrustal faults or deformation zones, as reported in the Hemlo camp (Lin, 2001), the Timmins camp (Bateman et al. 2008; Bleeker 2012), and the Geraldton camp (Tòth et al. 2015).

2.4.2 Early and Late Controls on the Formation and Geometry of Mineralized Zones

The geometry of the mineralized zones is determined by the strain imposed on the laminated veins during the D1 to D3 events. For example, at Baltic D (Fig. 2.10), the geometry of the mineralized zones is controlled by the superposition of open, NNW-trending F2 folds on recumbent, isoclinal F1 folds defined by the gold-bearing laminated veins. Along the Renabie trend, the L2 stretching lineation controls the plunge of the ore zones. Thinner laminated veins are tightly folded by F3 folds and transposed parallel to the trend of the shear zones (Fig. 2.13). Thicker veins do not appear to be folded by these folds, suggesting that they were initially oriented

either parallel or at an acute angle to the trend of the shear zones and, if the latter, they were rotated into parallelism with the shear zones during D3. The L2 stretching lineation underwent a similar rotation, thus the geometry of the ore zones resulted from the superposition of both D2 and D3 strain.

Although the Renabie trend comprises several ore zones defining a linear trend, a single shear zone cannot be traced continuously from one ore zone to another (Callan and Spooner, 1988), nor is a connecting structure observed between the Renabie trend, Braminco, and Baltic D. The strike lengths of the Renabie shear zones are limited by that of the mechanically weak alteration envelope surrounding the veins. This suggests that the ore zones along the Renabie trend formed as a series of stepping en echelon structures (Callan and Spooner, 1988). These early structures were likely brittle in nature, as no ductile fabric older than the overprinting S1 cleavage is observed in the vicinity of the veins or regionally across the Renabie area. Pegmatitic and aplitic felsic dikes are more abundant next to the ore zones, suggesting that they exploited the same brittle conduits as the gold-rich, laminated quartz veins prior to regional ductile deformation.

The Braminco zone has been mined out and is no longer exposed. It is described by Callan and Spooner (1988, 1998) and Heather (1989) as a sinistral-reverse shear zone hosting deformed laminated quartz veins, similar to those along the Renabie trend. Although the shear sense along the Braminco zone is similar to that of the D3 shear zones along the Renabie trend, the Braminco zone is oriented NW and is parallel to S2, whereas the Renabie shear zones are oriented ENE and are oblique to S2. Thus, if the shear zone hosting the Braminco zone were to have formed during the same deformation event as the Renabie shear zones (D3), the strike-slip component of movement along the Braminco shear zone should be dextral, because the Renabie and Braminco shear zones are in conjugate orientations to one another. As the movement along the Braminco shear zone is described as sinistral-reverse (Callan and Spooner, 1988, 1998; Heather, 1989), this suggests that the sinistral-reverse shear zone at the Braminco zone likely formed during the D2

event, as sinistral movement is observed parallel to the NW-striking S2 foliation at the Boundary outcrop. This sinistral movement is followed by a dextral reactivation during D3, when the sinistral-reverse D3 shear zones along the Renabie trend formed. As suggested for the Renabie trend, the shear zone likely overprints the laminated quartz veins, which were emplaced along early brittle structures.

2.4.3 Comparison to Orogenic Gold Deposits

Ore zones along the Renabie trend are similar in many ways to ore zones in orogenic gold deposits. These similarities include: (1) the presence of gold-bearing, laminated veins and breccia veins within steeply-dipping, brittle-ductile shear zones; (2) oblique-reverse shear movement; (3) lenticular ore body geometries with a well-defined ore plunge; (4) late transcurrent reactivation of the shear zones; and (5) greenschist to amphibolite metamorphic grade (Hodgson, 1989; Poulsen and Robert, 1989; Robert et al., 1994; Robert and Poulsen, 2001). The principal contrast is that the ore zones in the Renabie area formed early during the tectonic evolution of the district, before the development of the shear zones in which they occur, whereas orogenic gold deposits form coevally with shear zones, which typically form late during the tectonic history of the gold districts.

The role of lithological competency contrast in localizing shear zones and hydrothermal activity has been discussed by Dubé et al. (1989), Hodgson (1989), and Robert and Poulsen (2001). The D3 Renabie shear zones, which nucleated and propagated within the weak alteration envelopes surrounding strong quartz veins, provide an excellent example of this. Because the resulting shape of the ore bodies and the spatial relationships between structures and mineralization are similar to those of orogenic gold deposits, pre-tectonic veins hosted by later shear zones can easily be mistaken for orogenic deposits. Differentiating between the two is even more difficult when textures and structures that formed during the emplacement of the veins are overprinted and partially obliterated during subsequent deformation events. This is the case for the Renabie ore

zones, which were thought to have formed late along deforming shear zones in a manner similar to orogenic gold deposits (Callan and Spooner, 1988, 1998).

2.5 Conclusion

The emplacement of auriferous, laminated quartz veins in tonalite and volcanic rocks of the Missanabie-Renabie gold district predated regional ductile deformation (D1-D4). The veins were deposited in early, brittle structures, which also acted as conduits for the emplacement of felsic pegmatites and aplites. During regional deformation, the veins and their weak quartz-sericite-pyrite alteration halos were stretched parallel to the regional stretching lineation, and then acted as planar structural anisotropies, which controlled the formation of the sinistral-reverse shear zones along the Renabie trend. These shear zones subsequently focused syn-deformational hydrothermal fluids, which resulted in the formation of shear zone-hosted quartz breccias and distinct hematite-bearing alteration zones. Massive pyrite veins cut across these features and represent a late-stage gold event. The early timing of laminated vein emplacement provides an example of how the inheritance of veins and their alteration envelopes from an early brittle deformation event can later localized the formation of ductile shear zones and focus hydrothermal activity. The ore zones will show features similar to those commonly encountered in orogenic gold deposits, and will also display a high degree of geometric variability as their geometry and shape will be the result of the total finite strain imposed on the ore zones during multiple overprinting deformation events.

References

Ayres, L.D., 1978, Metamorphism in the Superior Province of Northwestern Ontario and its relationship to crustal development: Metamorphism in the Canadian Shield, p. 25-36, Geological Survey of Canada Paper 78-10.

Bateman, R., Ayer, J. A., and Dubé, B., 2008. The Timmins-Porcupine Gold Camp, Ontario: Anatomy of an Archean greenstone belt and Ontogeny of Gold Mineralization: Economic Geology, v. 103, p. 1285–1308.

Bleeker, W., 2012. Targeted Geoscience Initiative 4. Lode gold deposits in ancient deformed and metamorphosed terranes: the role of extension in the formation of Timiskaming Basins and large gold deposits, Abitibi Greenstone Belt - a discussion: Summary of Field Work and Other Activities 2012; Ontario Geological Survey, Open File Report 6280, 2012; p. 47.1-47.12

Bennett, G., 1972, Precambrian geology of Stover and Brackin townships: Ontario Geological Survey, Preliminary Map P.2380, scale 1:31 680.

Bruce, E.L., and Horwood, H.C., 1942, Rennie–Leeson area, District of Sudbury, Ontario: Ontario Geological Survey, Annual Report Map 51G, scale 1:31 680.

Callan, N.J., and Spooner, E.T.C., 1988, Archean Au quartz vein mineralization hosted in a tonalite-trondhjemite terrane, Renabie Mine area, Wawa, north Ontario, Canada: The Geology of Gold Deposits, The Perspective in 1988, Society of Economic Geologists, Economic Geology Monograph 6, p. 9-18.

Callan, N.J., and Spooner, E.T.C., 1998, Repetitive hydraulic fracturing and shear zone inflation in an Archean granitoid-hosted, ribbon banded, Au-quartz vein system, Renabie area, Ontario, Canada: Ore Geology Reviews, v. 12, p. 237-266.

Corfu, F. and Sage, R.P., 1992, U-Pb age constraints for deposition of clastic metasedimentary rocks and late-tectonic plutonism, Michipicoten Belt, Superior Province: Canadian Journal of Earth Sciences, v. 29, p. 1640—1651.

Cox, S.F., Knackstedt, M.A., and Braun, J., 2001, Principles of structural control on permeability and fluid flow in hydrothermal systems, in Richards, J.P., and Tosdal, R.M., eds., Structural Controls on Ore Genesis: Reviews in Economic Geology, v. 14, p. 1–24.

Dubé, B., Poulsen, K.H., and Guha, J., 1989, The effects of layer anisotropy on auriferous shear zones: The Norbeau mine, Quebec: Economic Geology, v. 84, p. 871–878.

Ferguson, S.A., 1968, Renabie Mines, Nudulama Mines and adjoining properties, surface geology, parts of Renabie, Leeson and Brackin townships, District of Sudbury: Ontario Department of Mines, Preliminary Geological Map p. 492.

Groves, D.I., 1993, The crustal continuum model for late-Archean lode-gold deposits of the Yilgarn Blobk, Western Australia: Mineralium Deposita, v. 28, p. 366-374.

Groves, D.I., Goldfarb, R. J., Gebre-Mariam, M., Hagemann, S. G. & Robert, F., 1998, Orogenic gold deposits: a proposed classification in the context of their crustal distribution and relationship to other gold deposit types: Ore Geology Reviews v. 13, p.7–27.

Heather, K.B., and Buck, S., 1988, The Geological and Structural Setting of Gold Mineralization in the Missanabie-Renabie District of the Michipicoten Greenstone Belt, Wawa, Ontario: Summary of Field Work and Other Activities 1988, Ontario Geological Survey, Miscellaneous Paper 141, p. 257-270.

Heather, K.B., 1989, Project unit 89-15. The geological and structural setting of gold mineralization in the Renabie portion of the Missanabie–Renabie gold district, Wawa Gold Camp, Wawa: Ontario Geological Survey Miscellaneous Paper 146, p. 99–107.

Heather, K.B., and Arias, Z., 1992, Geological and structural setting of gold mineralization in the Goudreau–Lochalsh area, Wawa gold camp: Ontario Geological Survey, Open File Report 5832, 159 p.

Hodgson, C.J., 1989, The structure of shear-related, vein-type gold deposits: A review: Ore Geology Reviews, v. 4, p. 231–273.

Jemiellta, R.A., Callan, N.J., and Spooner, E.T.C., 1988, Petrogenesis of Archean Trondhjemite-Tonalite-Granodiorite (TTG) Intrusions and Their Relationships to Gold Mineralization, Renabie and Magino Areas, Wawa: Ontario Geological Survey, Miscellaneous Paper 140, p.78-93. Journal of Earth Sciences, v.21, p. 457-464.

Kamo, S.L., 2014, Report on U-Pb CA-ID-TIMS geochronology on volcanic and plutonic rocks, Superior and Grenville provinces, Ontario: internal report for the Ontario Geological Survey, Jack Satterly Geochronology Laboratory, University of Toronto, Toronto, Ontario, 27 p.

Kamo, S.L., 2015, Report on U-Pb CA-ID-TIMS geochronology on volcanic and plutonic rocks, Superior and Grenville provinces, Ontario: internal report for the Ontario Geological Survey, Jack Satterly Geochronology Laboratory, University of Toronto, Toronto, Ontario, 48 p.

Lin, S., 2001, Stratigraphic and Structural Setting of the Hemlo Gold Deposit, Ontario, Canada: Economic Geology, V. 96, p. 477-507.

McDivitt, J.A., Lafrance, B., Kontak, D.J., and Robichaud, L., 2015, Characterization of Gold Mineralization in the Missanabie-Renabie District of the Wawa gold camp: Summary of Field Work and Other Activities, Open File Report 6313, p. 6-1 to 6-8.

Moser, D., 1989, Mid-crustal structures of the Wawa gneiss terrane near Chapleau, Ontario: Current Research, Part C. Geological Survey of Canada, Paper 88-lC, p. 93 -99.

Moser, D.E., 1993, A Geological, Structural and Geochronological Study of the Central Wawa Gneiss Domain: Implications for the Development of Different Crustal Levels of the Archean Abitibi-Wawa Orogen of the Southern Superior Province, Canadian Shield: Ph.D. thesis, Queen's University, Kingston, Ontario.

Moser, D.E., 1994, The geology and structure of the mid-crustal Wawa gneiss domain: a key to understanding tectonic variation with depth and time in the late Archean Abitibi-Wawa orogen: Canadian Journal of Earth Sciences v. 31 p. 1064-1080.

Percival, J.A., 1981, Stratigraphic, structural, and metamorphic relations between the Wawa and Abitibi Subprovinces and the Kapuskasing Structural Zone near Chapleau, Ontario: Current Research, Part A, Geological Survey of Canada, Paper 81-1A, p. 83–90.

Percival, J.A., 1988, Deep geology out in the open: Nature, v. 335, p. 671.

Percival, J.A., and West, G.F., 1994, The Kapuskasing uplift: a geological and geophysical synthesis: Canadian Journal of Earth Sciences v. 31 p. 1256-1286.

Poulsen, K.H., and Robert, F., 1989, Shear zones and gold: Practical examples from the southern Canadian Shield, in Bursnall, J.T., ed., Mineralization and shear zones: Geological Association of Canada, Short Course Notes 6, p. 239–266.

Riley, R.A., 1971, Precambrian geology of Glascow, Meath and Rennie townships: Ontario Geological Survey, Preliminary Map p. 2210, scale 1:31 680.

Robert, F., Poulsen, K.H., and Dubé, B., 1994, Structural analysis of lode gold deposits in deformed terranes: Geological Survey of Canada, Open File Report 2850, 140 p.

Robert, F., and Poulsen, K.H., 2001, Vein formation and deformation in greenstone gold deposits: Reviews in Economic Geology, v. 14, p. 111–155.

Robichaud, L., McDivitt, J.A., and Trevisan, B.E., 2015, Geology and Mineral Potential of Rennie and Leeson Townships, Michipicoten Greenstone Belt: Summary of Field Work and Other Activities 2015, Ontario Geological Survey, Open File Report 6313, p.5-1 to 5-11.

Sage, R.P., 1986, Stratigraphic correlation in the Wawa area; in Volcanology and Mineral Deposits, Ontario Geological Survey, Miscellaneous Paper 129, p.62-68.

Sage, R.P., and Heather, K.B., 1991, The structure, stratigraphy and mineral deposits of the Wawa area: Geological Association of Canada–Mineralogical Association of Canada–Society of Economic Geologists, Joint Annual Meeting, Toronto 1991, Field Trip A6, 118p.

Sibson, R.H., Robert, F., and Poulsen, K.H., 1988, High-angle reverse faults, fluid-pressure cycling, and mesothermal gold-quartz deposits: Geology, v. 16, p. 551–555.

Stott, G.M., Corkery, M.T., Percival, J.A.., Simard, M., and J. Goutier, J., 2010, A revised terrane subdivision of the Superior Province: Summary of Field Work and Other Activities 2010, Ontario Geological Survey, Open File Report 6260, p. 20-1 to 20-10.

Studemeister, P.A., 1983. The greenschist facies of an Archean assemblage near Wawa, Ontario: Canadian Journal of Earth Sciences, v. 20, p. 1409-1420.

Studemeister, P.A., and Kilias, S., 1987, Alteration Pattern and Fluid Inclusions of Gold-Bearing Quartz Veins in Archean Trondhjemite near Wawa, Ontario, Canada: Economic Geology, v. 82, p. 429-439.

Tóth, Z., Lafrance, B., Dubé, B., McNicoll, V.J., Mercier-Langevin, P., and Creaser, R.A., 2015. Banded iron formation-hosted gold miner- alization in the Geraldton area, northwestern Ontario: Structural setting, mineralogical characteristics, and geochronology, In: Targeted Geoscience Initiative 4: Contributions to the Understanding of Precambrian Lode Gold Deposits and Implications for Exploration, (ed.) B. Dubé and P. Mercier-Langevin; Geological Survey of Canada, Open File 7852, p. 85–97.

Turek, A., Smith, P.E. and Van Schmus, W.R. 1982. Rb-Sr and U-Pb ages of volcanism and granite emplacement in the Michipicoten Belt—Wawa, Ontario: Canadian Journal of Earth Sciences, v. 19, p. 1608-1626.

Turek, A., Smith, P.E. and Van Schmus, W.R. 1984. U-Pb zircon ages and the evolution of the Michipicoten plutonic-volcanic terrane of the Superior Province, Ontario: Canadian Journal of Earth Sciences, v. 21, p. 457-464.

Turek, A., Sage, R.P., and Van Schmus, W.R., 1990, Advances in geochronology of the Michipicoten greenstone belt: Proceedings and Abstract, Institute on Lake Superior Geology, v. 36, p. 110-111.

Turek, A., Sage, R. P., and Van Schmus, W. R., 1992, Advances in the U-Pb zircon geochronology of the Michipicoten greenstone belt, Superior Province, Ontario: Canadian Journal of Earth Sciences, v. 29, p. 1154- 1165.

Turek, A., Heather, K.B., Sage, R.P. and Van Schmus, W.R. 1996, U/Pb zircon ages for the Missanabie–Renabie area and their relation to the rest of the Michipicoten greenstone belt, Superior Province, Ontario, Canada: Precambrian Research, v. 76, p. 191-211.

Williams, H.R., Stott, G.M., Heather, K.B., Muir, T.L., Sage, R.P., 1991, Wawa Subprovince. In: Thurston, P.C., Williams, H.R., Sutcliffe, R.H., Stott, G.M. (Eds.): Geology of Ontario, Special vol. 4 (1), Ministry of Northern Development and Mines, Ontario Geological Survey, Sudbury, Ontario, p. 485–538

Tables

Table 2.1 Deformation events, structural features, and vein types at mineralized zones assessed during the study.

Deformation Event	Pileggi No. 1	Baltic D	C-zone	Nudulama	Nudulama East	Boundary
D1	isoclinal F1 folds, S1 cleavage	isoclinal F1 folds, S1 cleavage	-	-	-	tight to isoclinal F1 folds, S1 cleavage
D2	tight to isoclinal F2 folds, S2 cleavage	open F2 folds, S2 cleavage, L2 lineation	open to tight F2 folds, S2 cleavage, L2 lineation	open to tight F2 folds , S2 cleavage, L2 lineation	open to tight F2 folds, S2 cleavage, L2 lineation	open to isoclinal F2 folds, S2 cleavage, L2 lineation
D3	-	-	S3 cleavage, tight to isoclinal F3 folds, E-trending, sinistral-reverse shear zones	S3 cleavage, tight to isoclinal F3 folds, E-trending, sinistral-reverse shear zones	S3 cleavage, tight to isoclinal F3 folds, E-trending, sinistral-reverse shear zones	S3 cleavage, F3 drag folds with Z asymmetry
D4	F4 drag folds with Z asymmetry	-	dextral shear bands	F4 drag folds with Z asymmetry	F4 drag folds with Z asymmetry	-
Vein Types	laminated quartz, NW-striking quartz tension gashes	laminated quartz	laminated quartz, NW-striking quartz tension gashes, massive pyrite	laminated quartz, hematite-associated alteration, massive pyrite	laminated quartz, hematite-associated alteration, NW-striking quartz tension gashes, massive pyrite	saccharoidal-textured quartz (non-laminated)

Table 2.2 Chronology of deformation events, veins, and gold mineralization events.

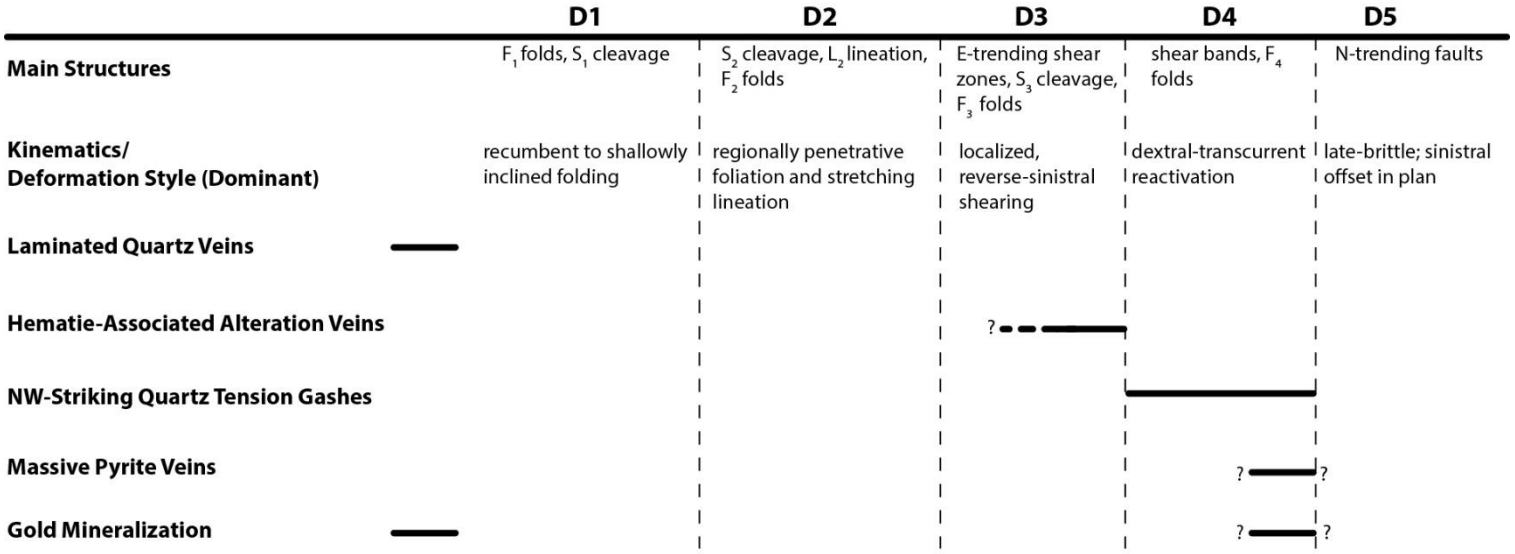

Figures

Figure 2.1 Simplified regional geology map of the Wawa subprovince showing the location of the Missanabie-Renabie gold district (modified after Williams et al., 1991; Stott et al., 2010). Inset displays the location of the main figure relative to the Superior craton.

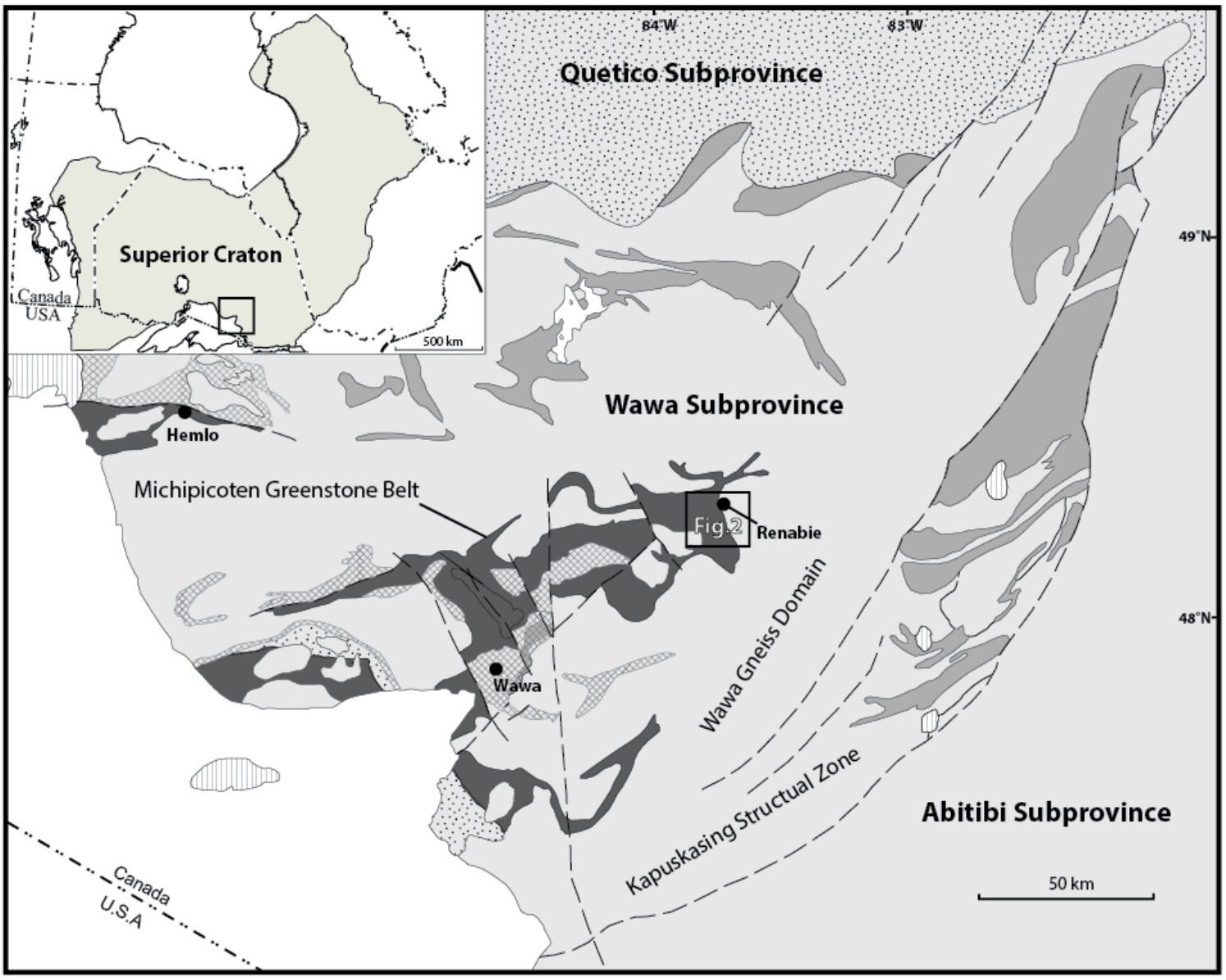

Figure 2.2 (A) Location and simplified geology map of the Missanabie-Renabie gold district (modified after Bruce and Horwood, 1942; Riley, 1971; Bennett, 1972). Location of gold occurrences is from the Ontario Mineral Deposit Inventory hosted on the web site of the Ontario Geological Survey. (B) Geology map of the Renabie mine area (modified after McDivitt et al., 2015; Ferguson, 1968). Coordinates in NAD83 UTM zone 17N.

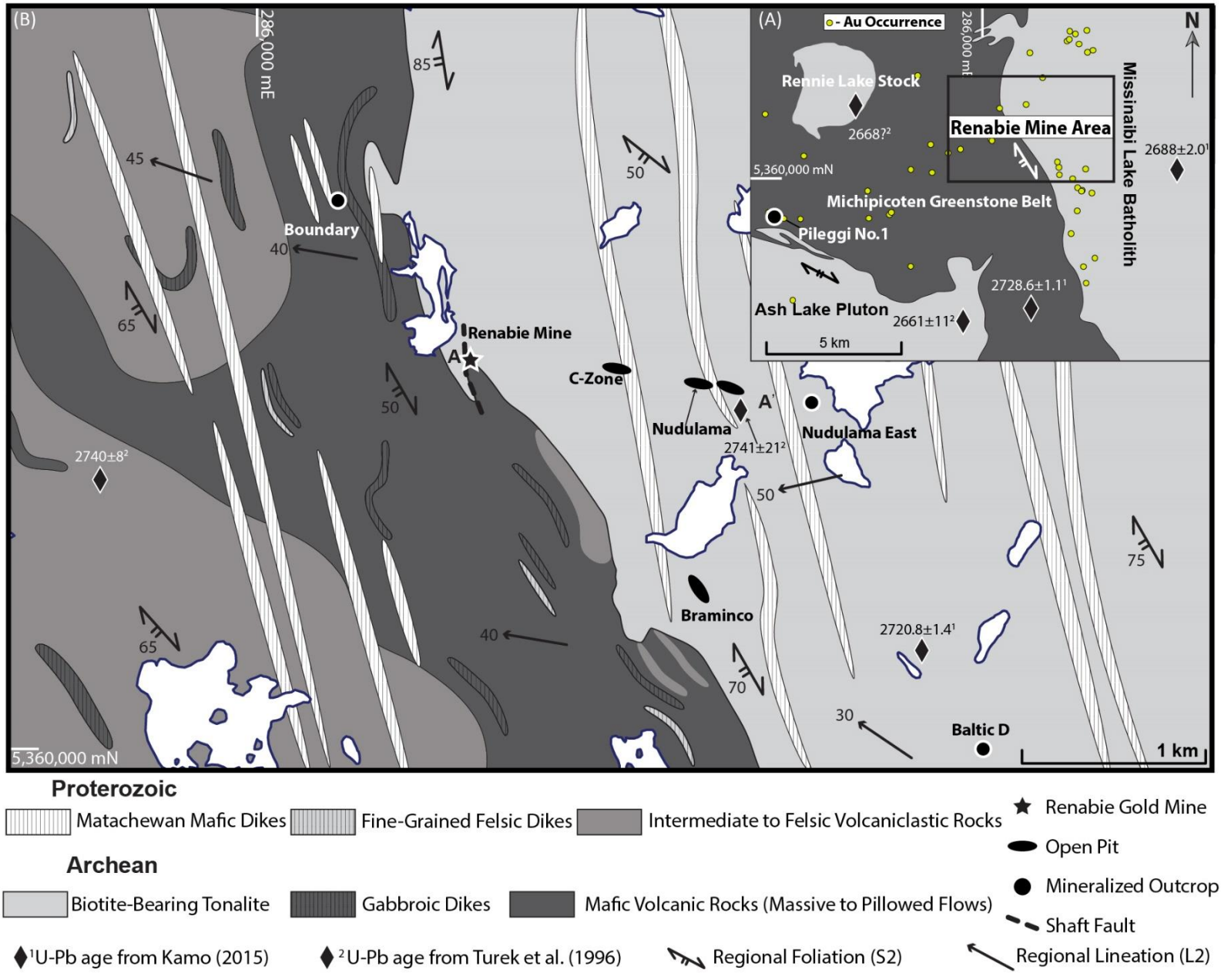

Figure 2.3 Grade-contour plan map of the 3540 ft level of the Renabie underground mine (modified after Barclay, 1990; unpublished grade-contour map from the Mines and Minerals Division Sault Ste. Marie District Office). Mine grid in feet. Location of map is shown in Figure 2.4.

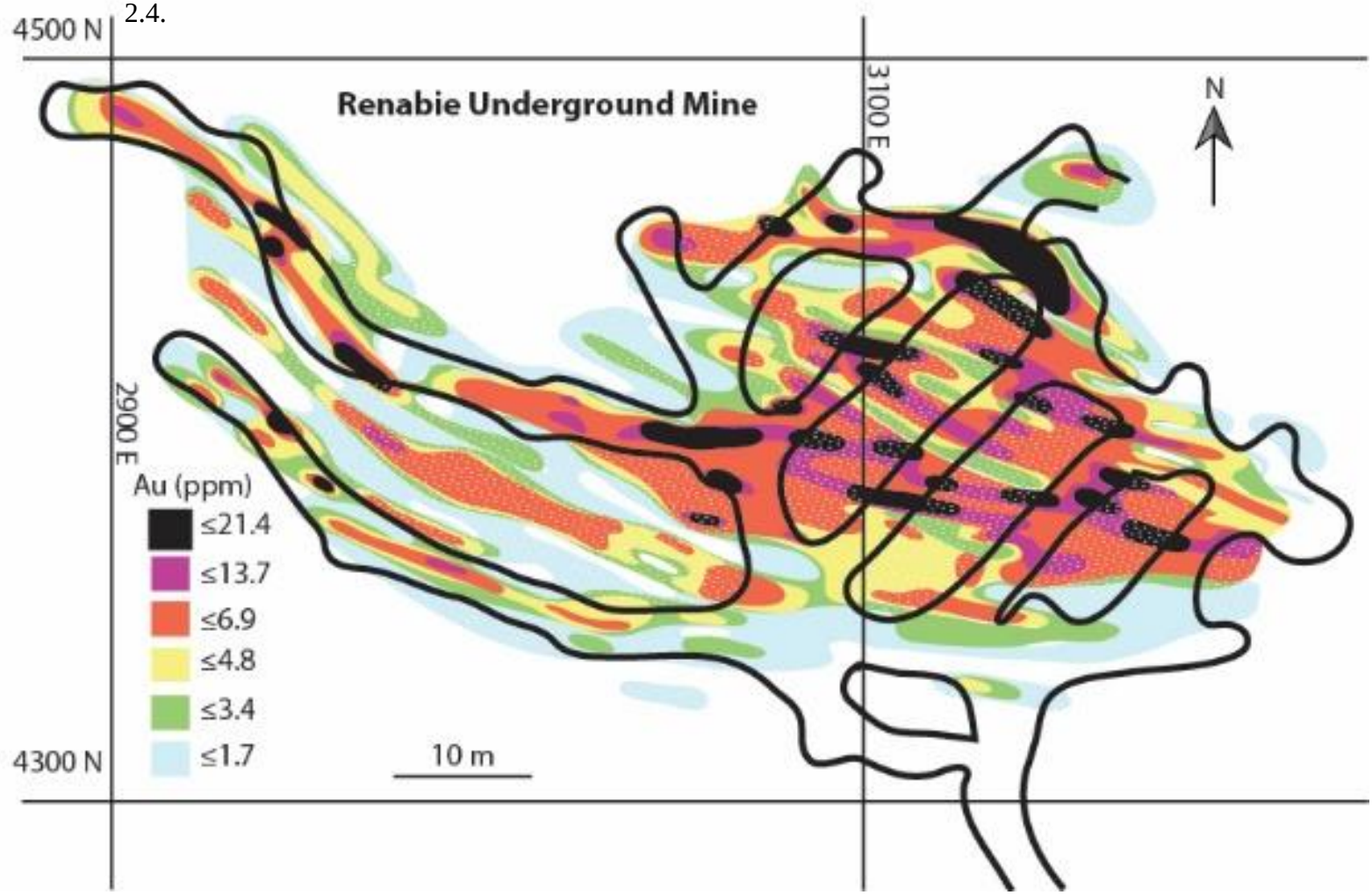

Figure 2.4 East-west longitudinal section of the Renabie trend (modified after Renabie Gold Mines Ltd. (1986), unpublished longitudinal section at the Mines and Minerals Division Sault Ste. Marie District Office). The plunge of the ore shoots is roughly parallel to that of the regional L2 lineation. Location of section A-A' is displayed in Figure 2.2B.

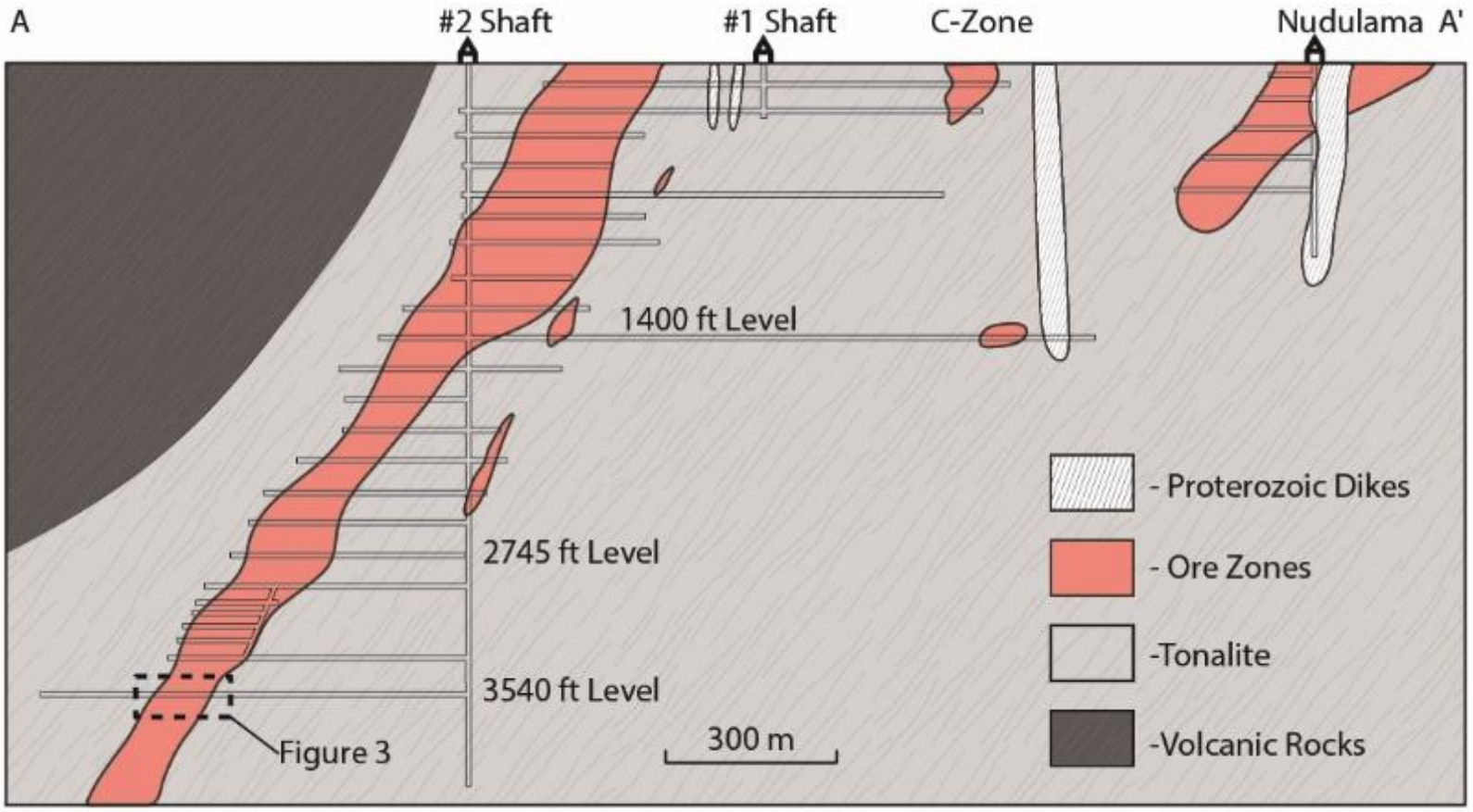

Figure 2.5 (A) Laminated quartz vein at Nudulama East. Pencil for scale. (B) Mineralized zone at Nudulama; a laminated quartz vein (LQV) surrounded by quartz-sericite-pyrite schist (QSP). Compass for scale. (C) East-facing, vertical wall at the Nudulama open pit (~10 m wide), displaying the same mineralized zone as in Fig. 2.5B. (D) Reflected-light photomicrograph of gold (Au) and molybdenite (Mlb) within a laminated quartz vein at the C-zone. (E) Combined reflected and plane-polarized light photomicrograph of pitted, rectangular pyrite with hematite replacement rims. The pyrite is adjacent to the hematite-associated alteration vein shown in Fig. 2.5G. (F) Hydrothermal breccia with fragments of foliated, hematite-altered tonalite surrounded by a quartz matrix at Nudulama East. Scale card for scale. (G) Gold-bearing, massive pyrite vein cutting across a hematite-associated alteration vein at Nudulama East. Pencil for scale. (H) Reflected-light photomicrograph of anhedral, serrated pyrite lacking hematite-replacement rims taken where the massive pyrite vein in Fig. 2.5G cuts across the hematite-associated alteration vein. Compass and pencil (7 cm and 1 cm wide, respectively) indicate north; scale card divisions are 1 cm.

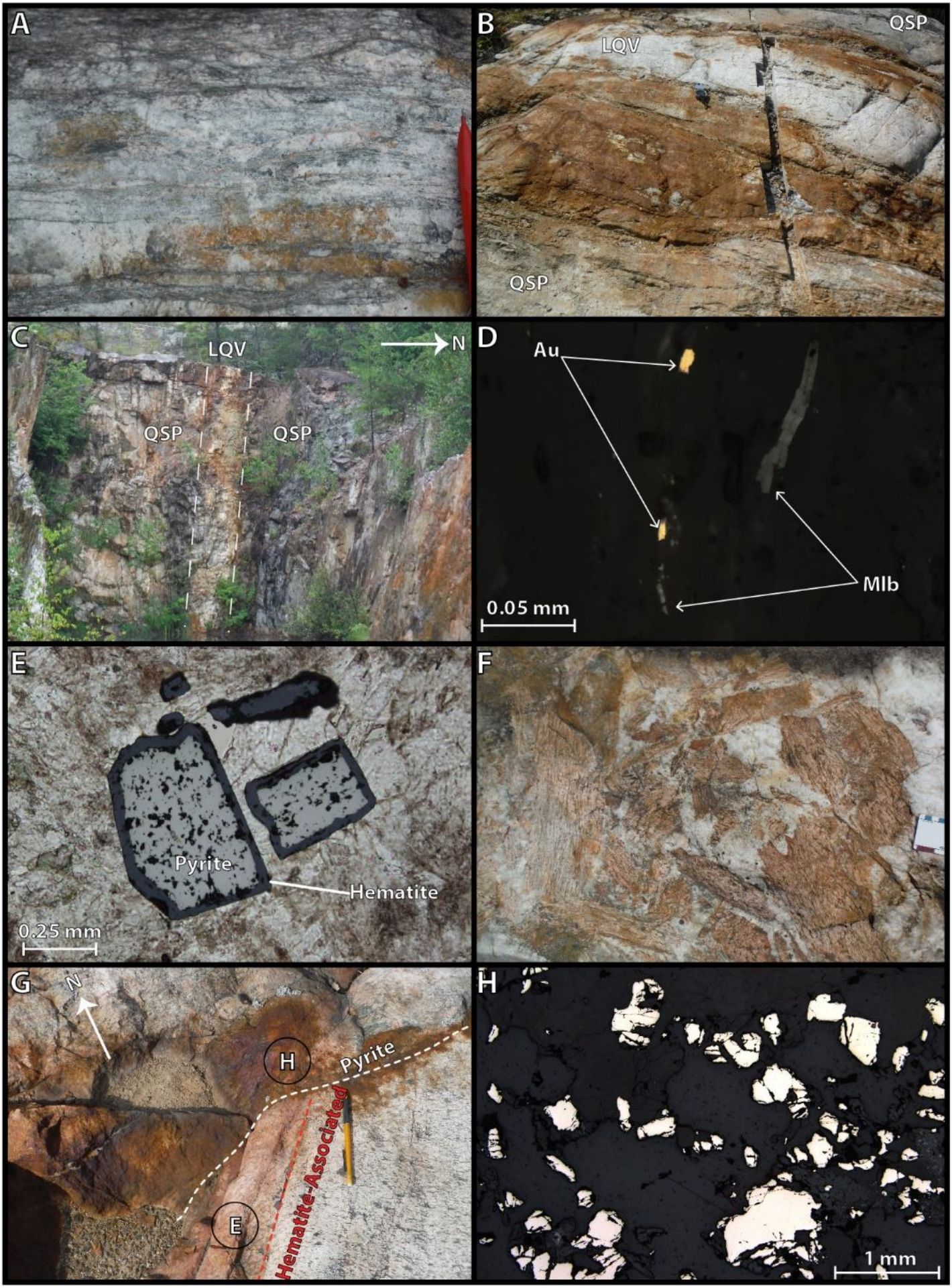
A
B
LQV
QSP
QSP
C
LQV
N
QSP
QSP
D
Au
Mlb
0.05 mm
E
Pyrite
Hematite
0.25 mm
F
G
N
H
Pyrite
Hematite-Associated
E
H
1 mm

Figure 2.6 (A) Detailed geological map of Nudulama East. Lower-hemisphere, equal-area stereographic plots of the L2 stretching lineation and poles to the S2 and S3 foliations. Coordinates in NAD83 UTM zone 17N. (B) Lower-hemisphere, equal-area stereographic plot of poles to hematite-associated alteration veins from Nudulama and Nudulama East. (C) Lower-hemisphere, equal-area stereographic plot of poles to massive pyrite veins from Nudulama and Nudulama East. N = number of measurements.

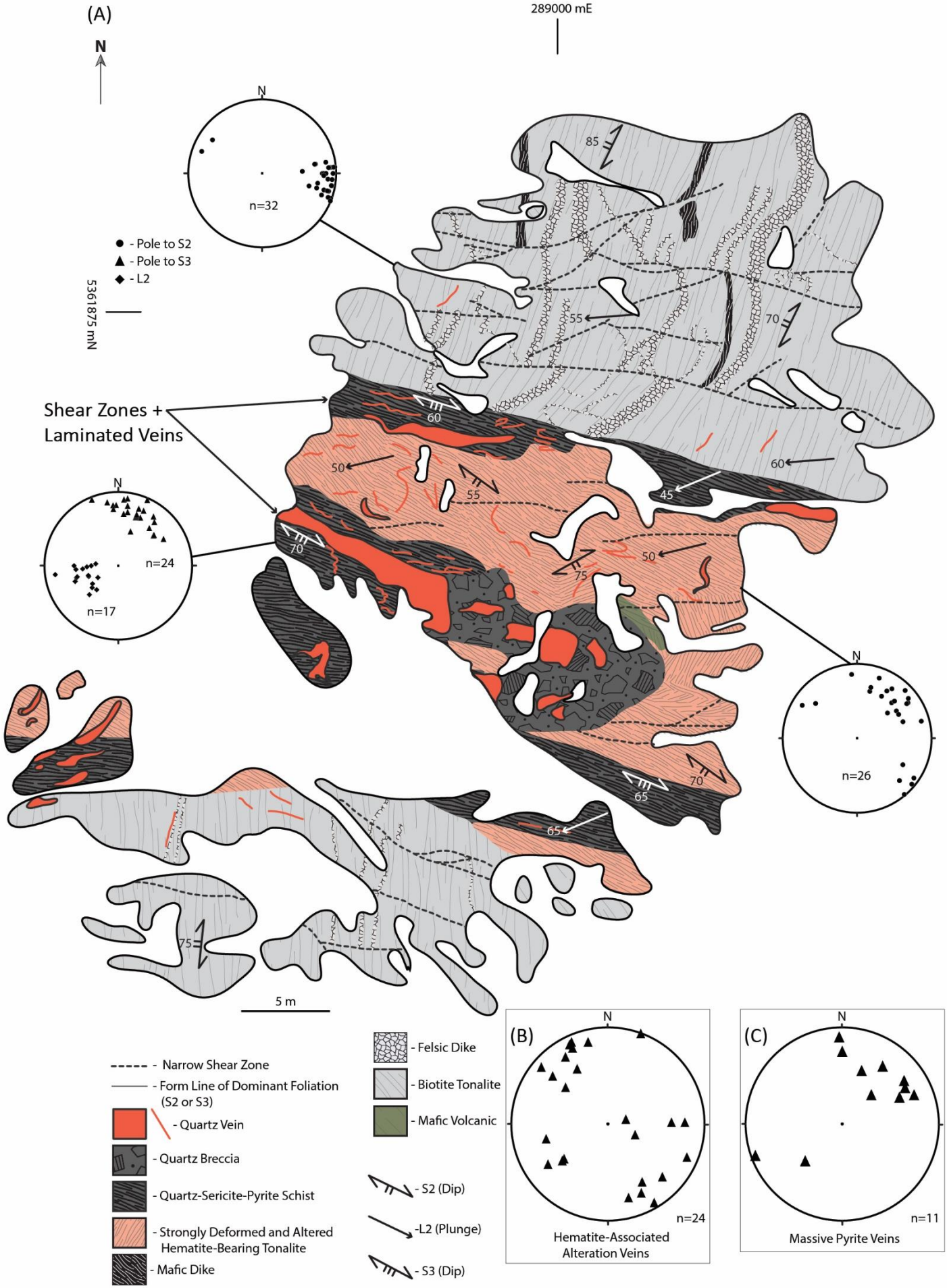
(A)
N
289000 mE
5361875 mN
N
n=32
● - Pole to S2
▲ - Pole to S3
◆ - L2
Shear Zones +
Laminated Veins
N
n=24
n=17
N
n=26
85
55
70
60
50
55
60
45
70
50
75
70
65
65
75
5 m
- Narrow Shear Zone
- Form Line of Dominant Foliation (S2 or S3)
- Quartz Vein
- Quartz Breccia
- Quartz-Sericite-Pyrite Schist
- Strongly Deformed and Altered Hematite-Bearing Tonalite
- Mafic Dike
- Felsic Dike
- Biotite Tonalite
- Mafic Volcanic
- S2 (Dip)
-L2 (Plunge)
- S3 (Dip)
(B)
N
n=24
Hematite-Associated Alteration Veins
(C)
N
n=11
Massive Pyrite Veins

Figure 2.7 Logarithmic-scale scatter diagram of Au (ppm) versus Au/Ag for various veins and alteration types.

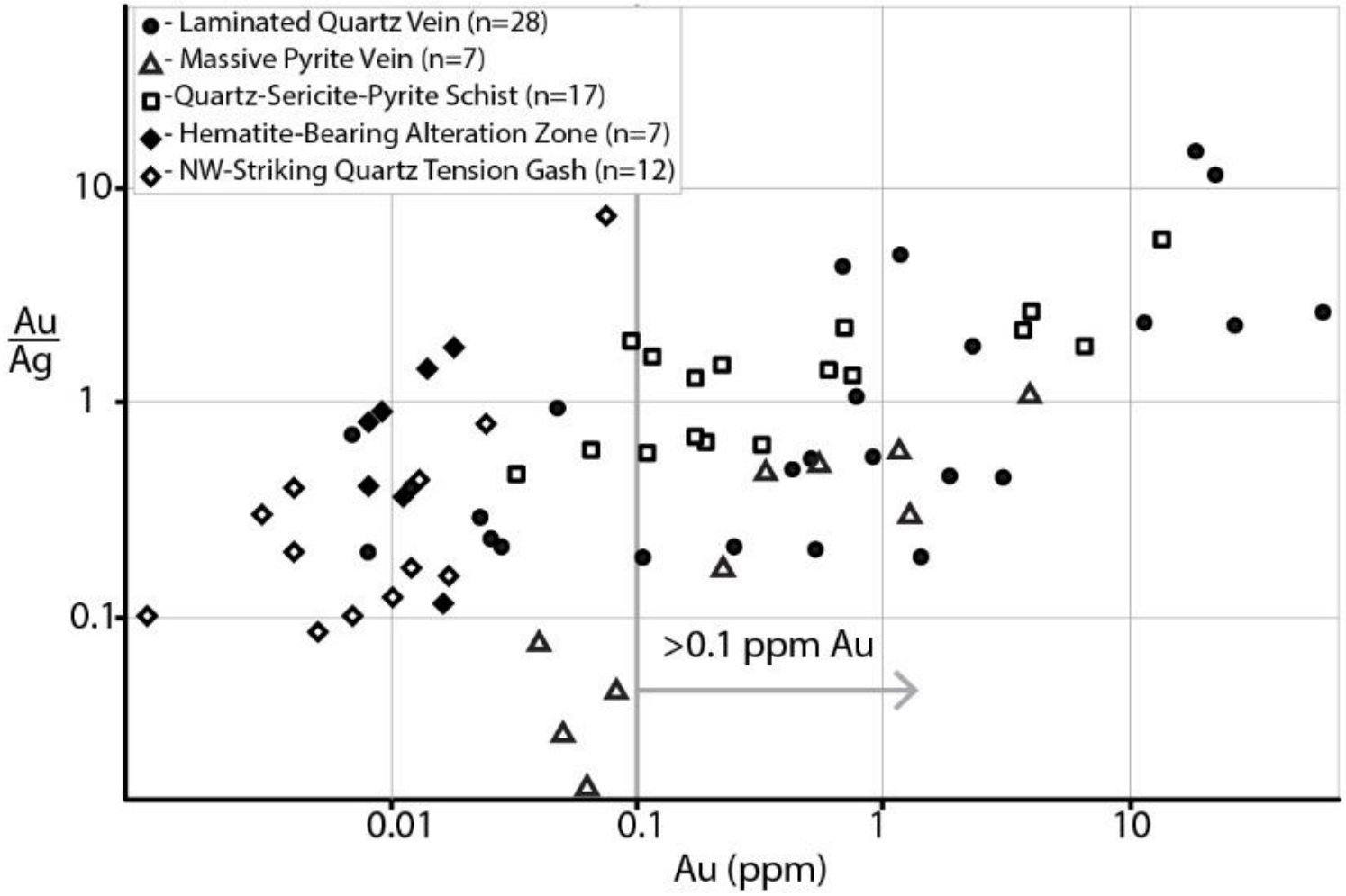

Figure 2.8 Detailed geological maps of Pileggi No. 1 north (A) and south (B) exposures. Coordinates in NAD83 UTM zone 17N. (C) Lower-hemisphere, equal-area stereographic plot of F2 fold axis and poles to S1 cleavage, S2 cleavage, and quartz tension gashes. N = number of measurements. Inset map showing the relative location of the two exposures.

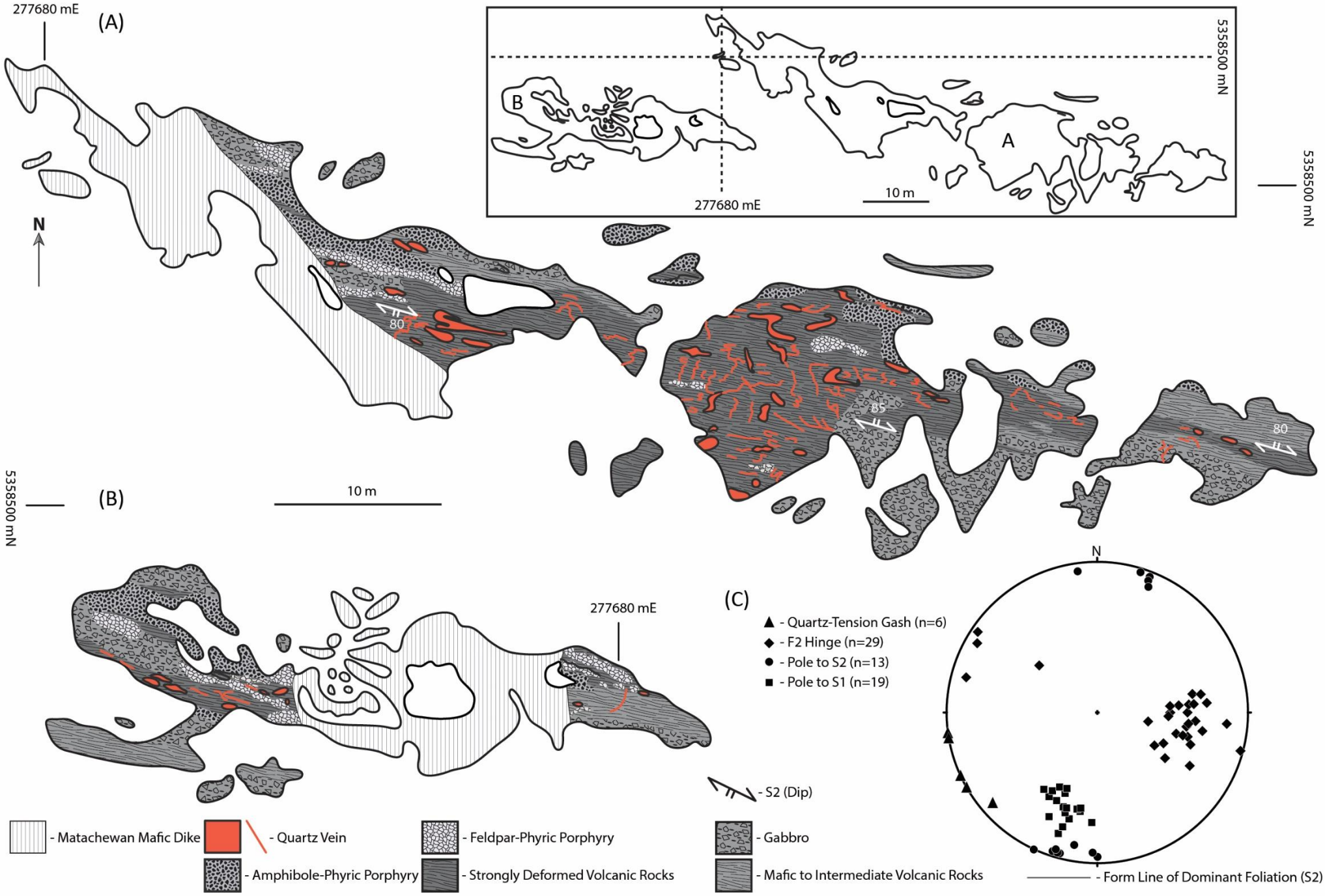
277680 mE
(A)
5358500 mN
B
A
10 m
277680 mE
5358500 mN
N
80
85
80
5358500 mN
(B)
10 m
277680 mE
(C)
▲ - Quartz-Tension Gash (n=6)
◆ - F2 Hinge (n=29)
● - Pole to S2 (n=13)
■ - Pole to S1 (n=19)
N
- S2 (Dip)
- Matachewan Mafic Dike
- Quartz Vein
- Feldpar-Phyric Porphyry
- Gabbro
- Amphibole-Phyric Porphyry
- Strongly Deformed Volcanic Rocks
- Mafic to Intermediate Volcanic Rocks
- Form Line of Dominant Foliation (S2)

Figure 2.9 (A) Laminated quartz vein overprinted by isoclinal F1 fold and tight F2 folds at Pileggi No. 1. The S1 and S2 cleavages are axial planar to F1 and F2 folds, respectively. (B) Northwest-striking quartz tension gash at Pileggi No. 1 cutting across the S2 foliation and strongly folded, laminated quartz veins transposed parallel to S2. (C) Recumbent F1 folds defined by laminated quartz veins at Baltic-D outcrop; the S1 cleavage is axial planar to F1 folds. (D) Sinistral shear of the S2 cleavage along the margin of NW-trending, laminated quartz veins south of the Renabie trend. (E) Anticlockwise deflection of the S2 cleavage (white broken line) along an E-trending D3 shear zone, 5 meters north of the mineralized zone at the C-zone. E-trending felsic dikes and shear zone outlined by blue and black broken lines, respectively. Compass and pencil (7 cm and 1 cm wide, respectively) point to north; scale card divisions are 1 cm.


A
N
S1
S2
F1
B
N
S2
1 cm
C
S1
F1
D
S2
N
E
N
S2
Felsic Dikes

Figure 2.10 Baltic-D (A) Lower-hemisphere, equal-area stereographic plot of the L2 stretching lineation, F2 fold axes, and poles to S1 and S2 foliations. N = number of measurements. (B) A schematic 3D diagram showing the laminated quartz veins (LQV) in grey overprinted by F1 and F2 folds.

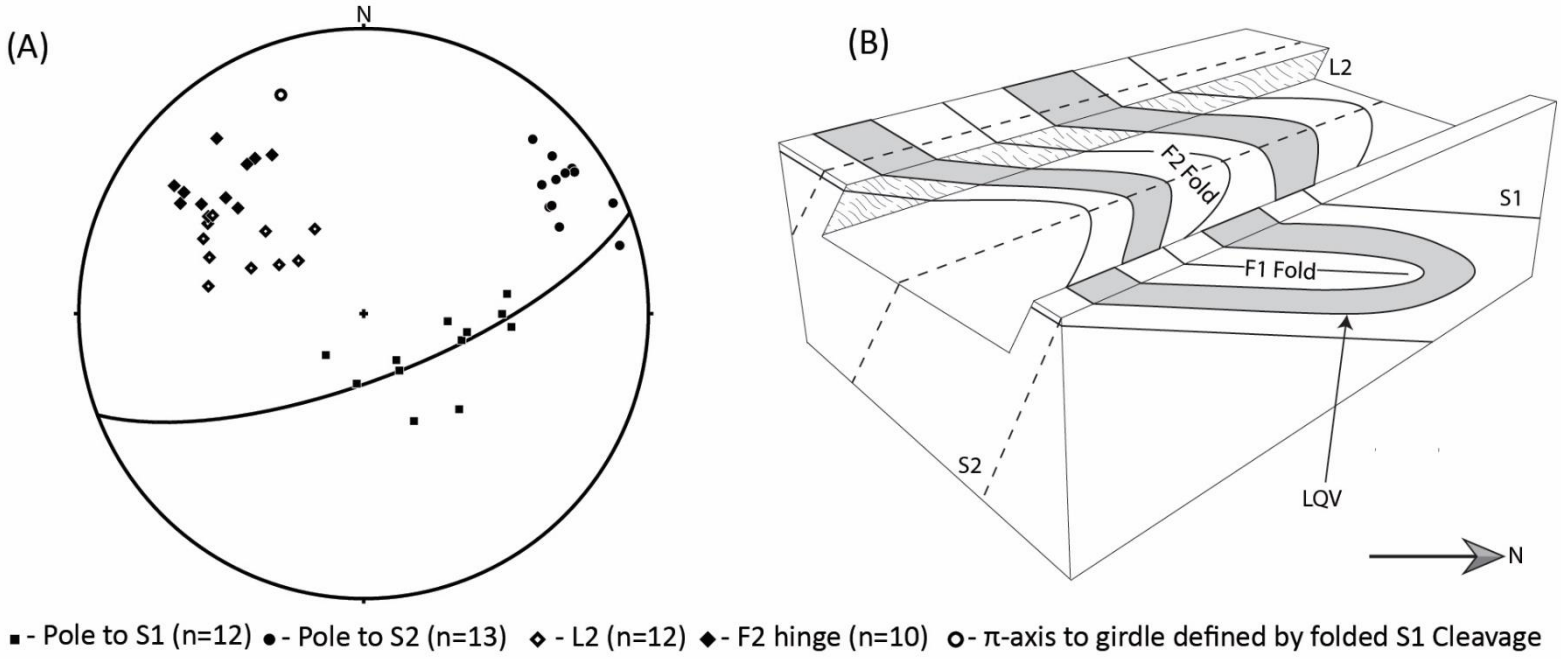

Figure 2.11 (A) Lower-hemisphere, equal-area stereographic plot of the L2 stretching lineation and poles to S1 and S2 in the Renabie mine area. (B) Lower-hemisphere, equal-area stereographic plot of the L2 stretching lineation north and south of the Renabie shear zones (open diamond) and along the shear zones (solid diamond). N = number of measurements.

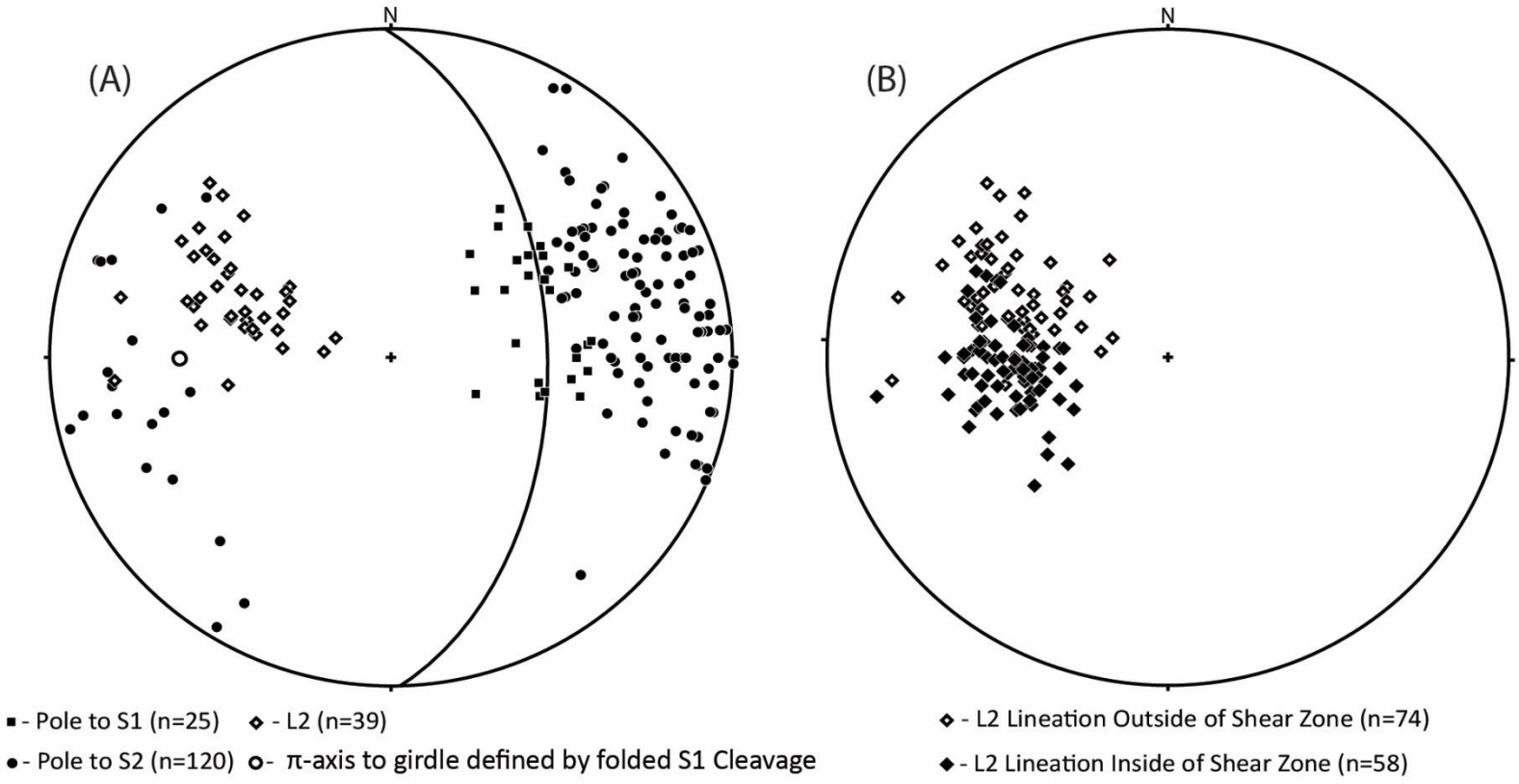

Figure 2.12 Detailed geological maps of (A) the C-zone and (B) Nudulama. Lower-hemisphere, equal-area stereographic plots of the L2 stretching lineation and poles to S2 and S3. N = number of measurements. Coordinates in NAD83 UTM zone 17N.

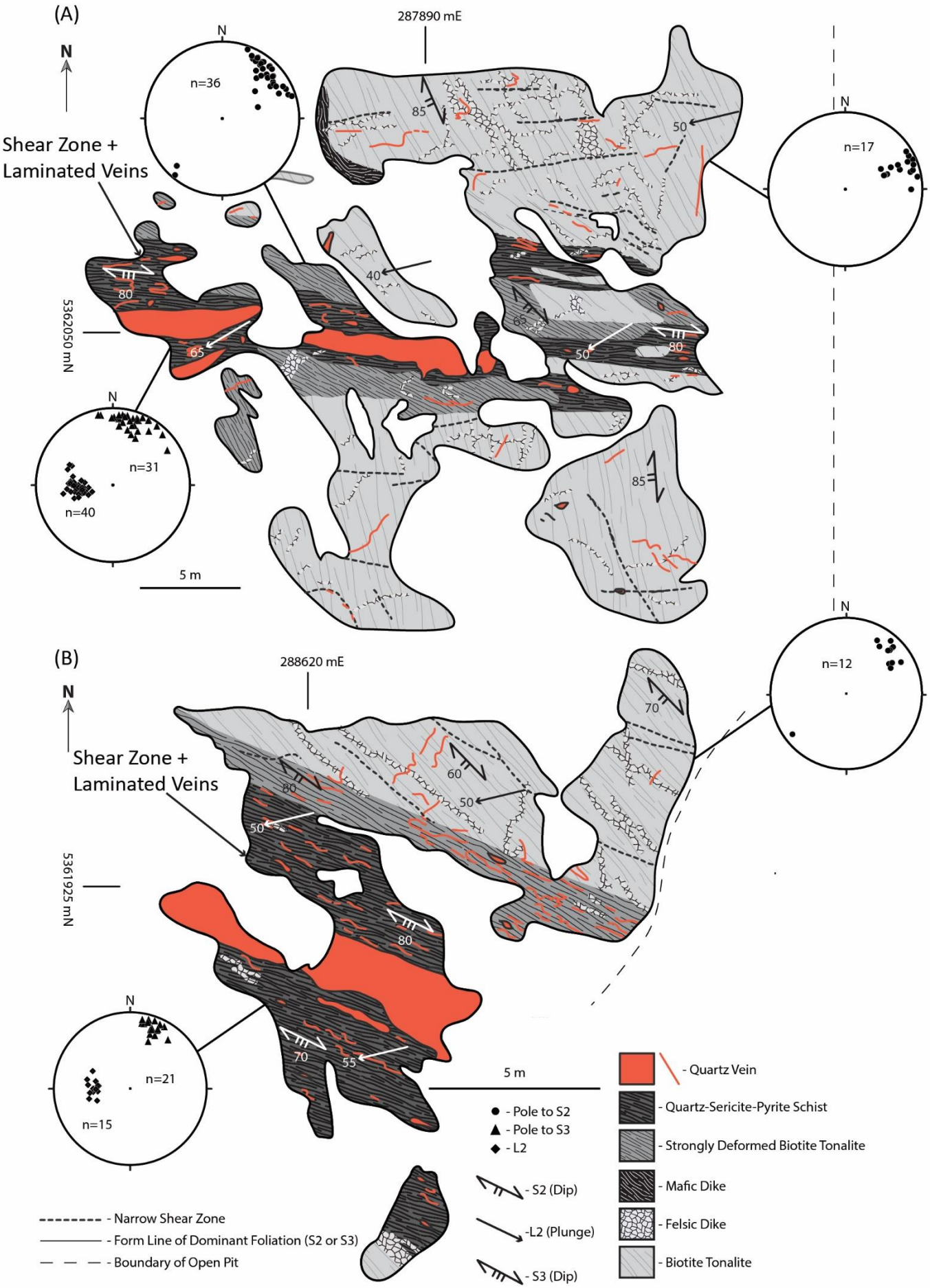
(A)
N
287890 mE
Shear Zone +
Laminated Veins
n=36
n=17
n=31
n=40
5362050 mN
5 m
(B)
288620 mE
n=12
Shear Zone +
Laminated Veins
5361925 mN
n=21
n=15
5 m
- Pole to S2
- Pole to S3
- L2
- S2 (Dip)
-L2 (Plunge)
- S3 (Dip)
- Quartz Vein
- Quartz-Sericite-Pyrite Schist
- Strongly Deformed Biotite Tonalite
- Mafic Dike
- Felsic Dike
- Biotite Tonalite
- Narrow Shear Zone
- Form Line of Dominant Foliation (S2 or S3)
- Boundary of Open Pit

Figure 2.13 Nudulama East. F3 folds defined by folded S2, laminated quartz veins, and felsic dikes (solid blue lines) on the southern margin of the southern shear zone in Figure 2.6. Close-up of F2-F3 fold interference pattern displayed in the right inset; close-up of the F3-folded S2 cleavage displayed in the left inset.

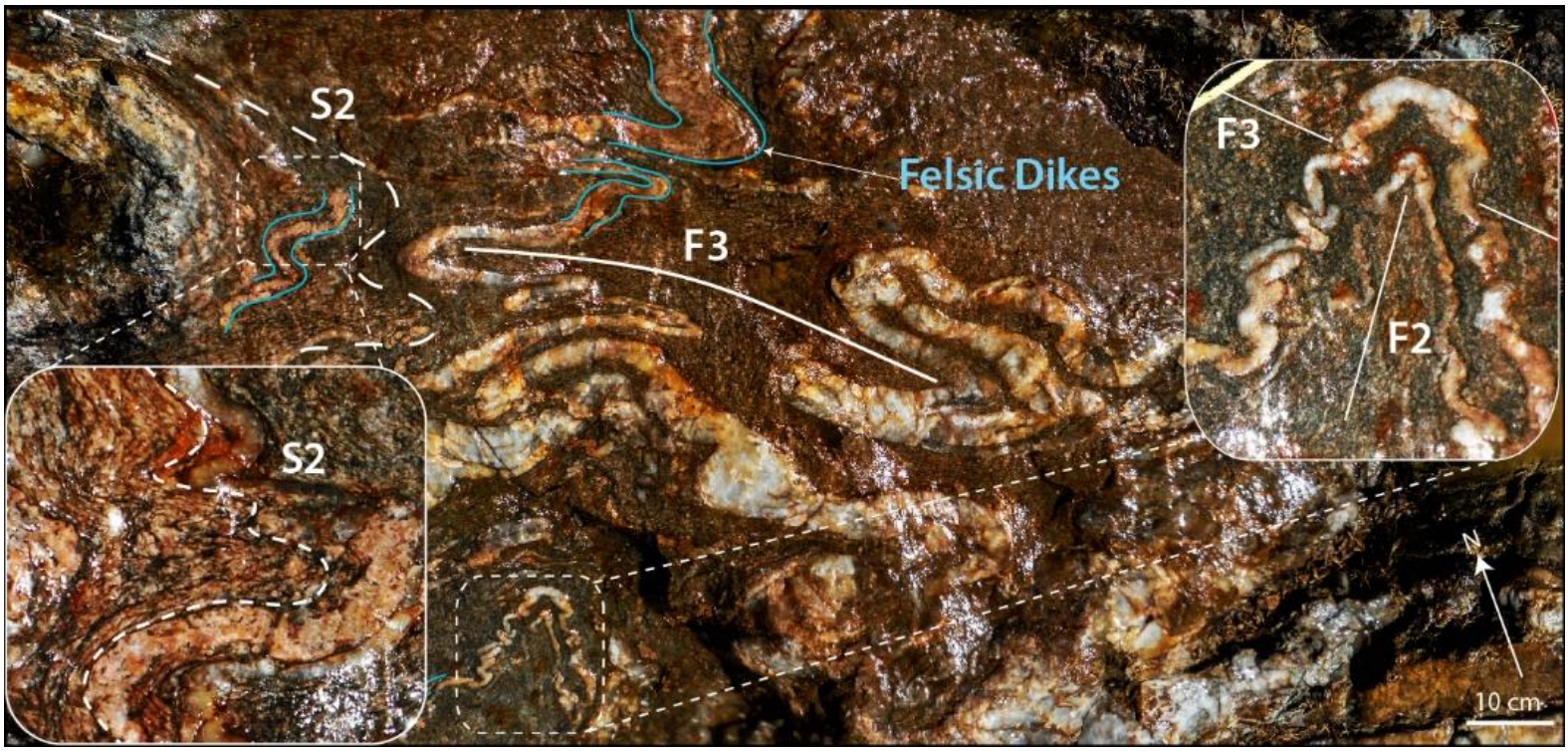

Figure 2.14 (A) Nudulama East. Sinistral shear band in the northern D3 shear zone visible in horizontal section. The shear band offsets S3 within strongly deformed, hematite- and chlorite-altered tonalite. (B) Nudulama. Cross-polarized light photomicrograph of a reverse shear band in the quartz-sericite-pyrite D3 shear zone. Photomicrograph is vertical, facing 280˚, and indicates a south-side-up sense of movement. (C) Nudulama. An epidote-filled, hematite-associated alteration vein cutting across the Z-folded S3 foliation in the shear zone. Pencil for scale. (D) Nudulama. Epidote, K-feldspar, and hematite-filled, hematite-associated alteration veins deformed into parallelism with the S3 foliation in the shear zone. The green broken line denotes the trend of the deformed veins. Compass for scale. (E) Nudulama East. Folded, quartz- and chlorite-filled, hematite-associated alteration vein with an axial planar S3 cleavage. (F) Nudulama East. Quartz vein linked to the hydrothermal breccia overprinted by a Z-shaped F4 fold. Compass for scale. (G) Nudulama. Z-shaped F4 fold defined by the folded S3 foliation and quartz vein material in the shear zone. Pencil for scale. (H) Nudulama East. Massive, NW-striking pyrite vein. Compass for scale. Compass and pencil (7 cm and 1 cm wide, respectively) indicate north.

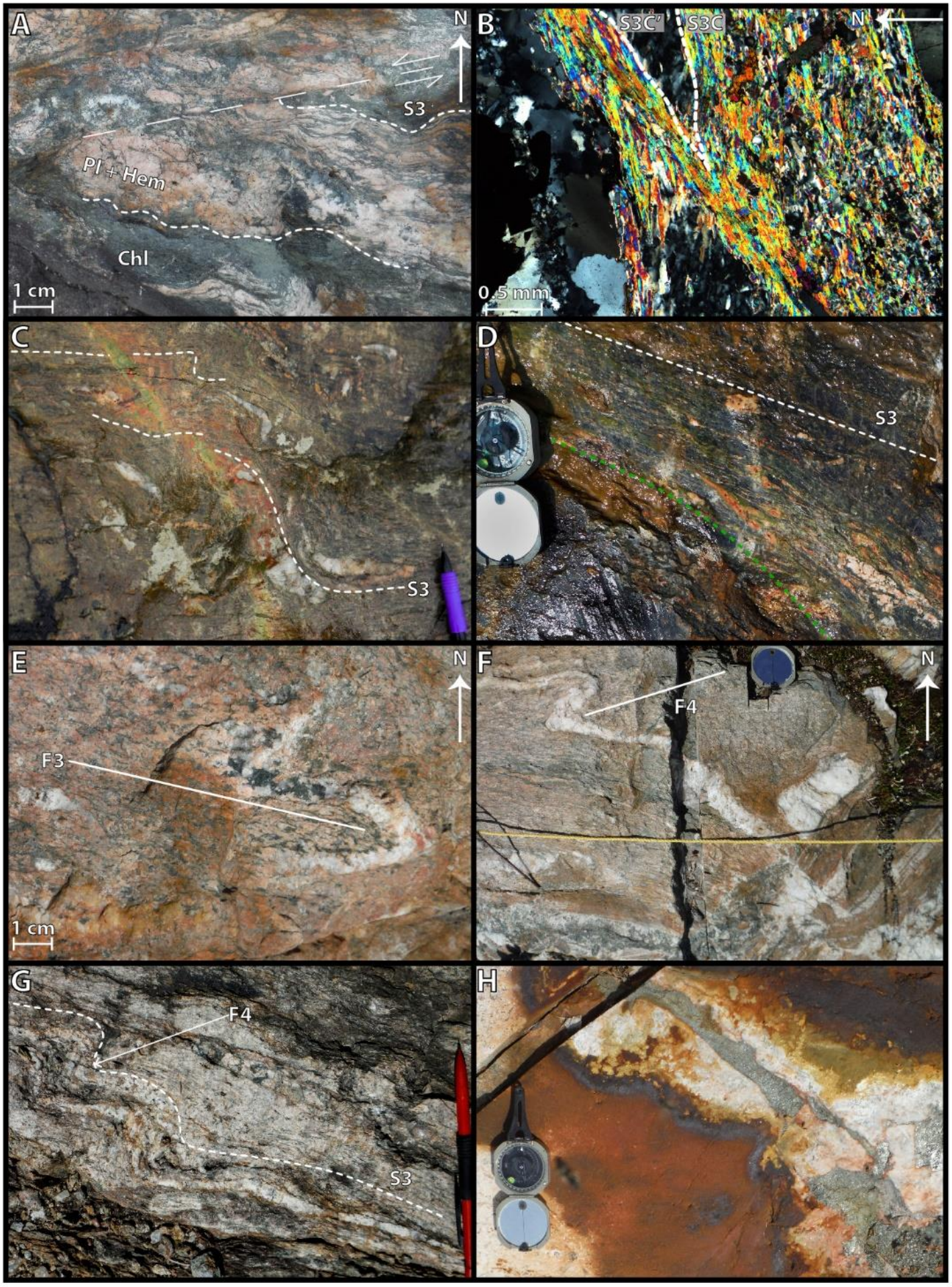
A
N
S3
Pl + Hem
Chl
1 cm
B
S3C'
S3C
N
0.5 mm
C
S3
D
S3
E
N
F3
1 cm
F
N
F4
G
F4
S3
H

Figure 2.15 Boundary Outcrop. East-southeast trending mafic dike (outlined in red) cuts across S2 and an F2 fold (outlined in blue) defined by strongly S1-foliated and quartz-veined gabbro. The dike is overprinted by a Z-shaped F3 fold along the west (right) limb of the F2 fold. Close-ups to the left of the S1 cleavage and a boudinaged quartz vein and to the right of the F3 Z-folded mafic dike. See text for further description. Compass (7 cm wide) used for scale in photographs indicates north.

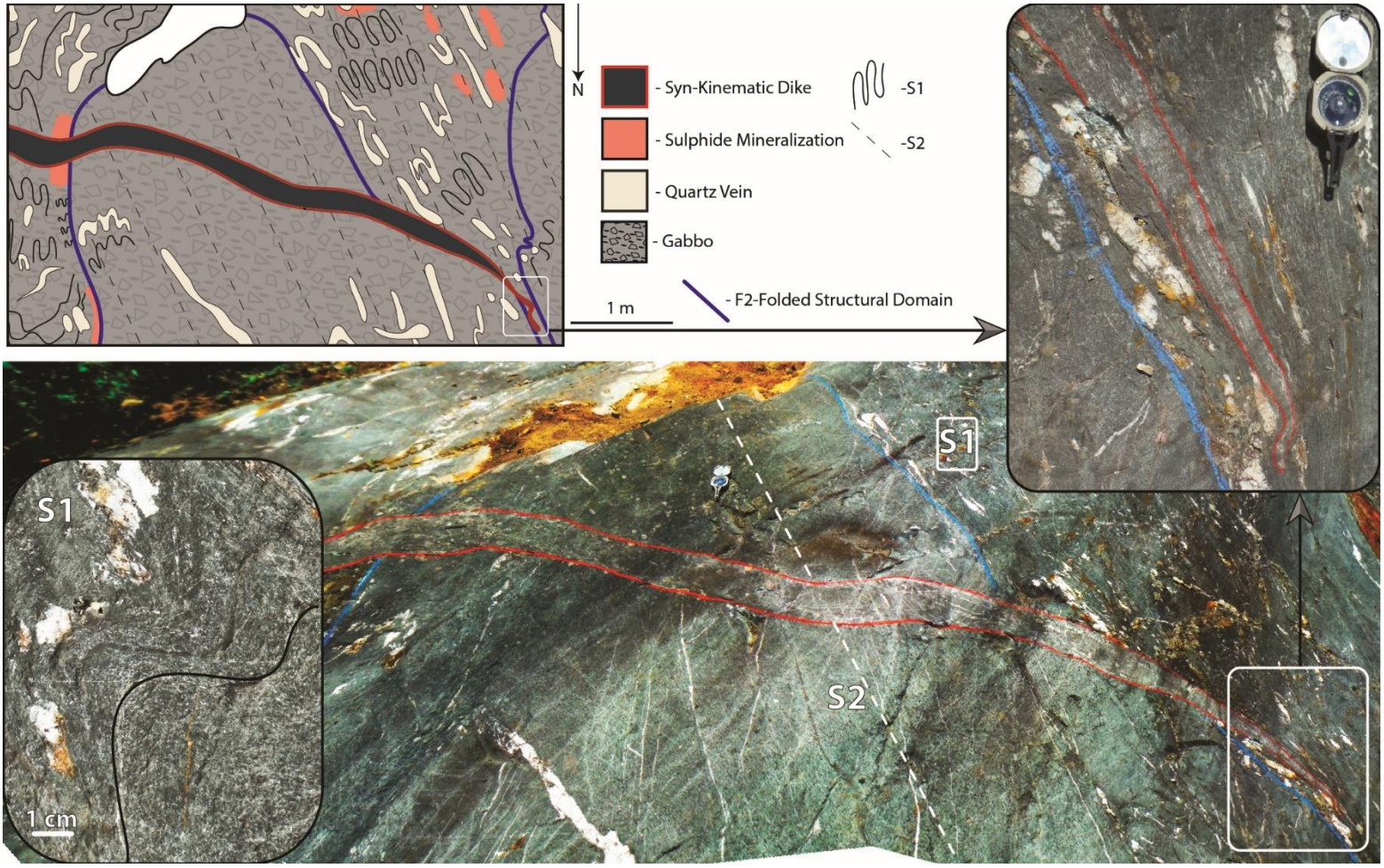

Figure 2.16 Deformation model for the Renabie mine area, with key overprinting relationships represented by schematic 3D diagrams.

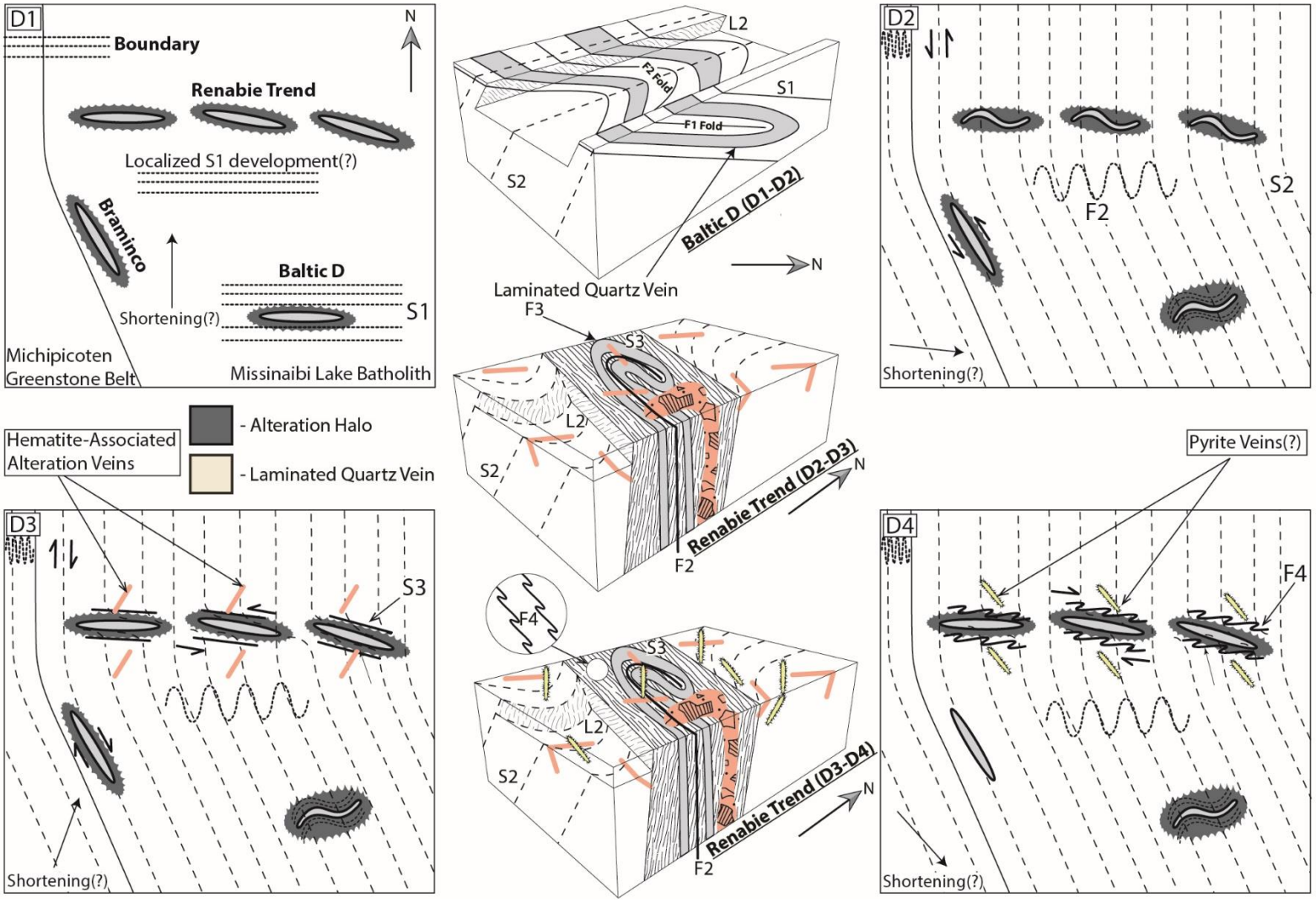

Appendices

Appendix 2.1 Results of precious metal assay. Samples were analyzed using IML-100 (agua regia digestion and ICP-MS analysis) at Geoscience Laboratories (Sudbury, Ontario).

Sample	Outcrop	Population	Type	Au (ppm)	Ag (ppm)
BD-12	Baltic D	Laminated Quartz Vein	Vein	3.066	6.88
BD-17	Baltic D	Laminated Quartz Vein	Vein	1.41	7.47
BD-13	Baltic D	Laminated Quartz Vein	Vein	0.526	2.54
BD-16	Baltic D	Laminated Quartz Vein	Vein	0.247	1.17
NUE-29b	Baltic D	Laminated Quartz Vein	Vein	0.028	0.13
BD-15	Baltic D	Laminated Quartz Vein	Vein	0.007	0.01
C-9	C-zone	Laminated Quartz Vein	Vein	61.027	23.48
C-8	C-zone	Laminated Quartz Vein	Vein	27.05	11.83
C-11	C-zone	Laminated Quartz Vein	Vein	11.604	4.95
C-6	C-zone	Laminated Quartz Vein	Vein	2.328	1.26
C-19	C-zone	Quartz-Sericite-Pyrite Schist	Wallrock	6.697	3.76
C-13	C-zone	Quartz-Sericite-Pyrite Schist	Wallrock	4.003	1.5
P-9.5	Nudulama	Laminated Quartz Vein	Vein	1.902	4.3
P-10.5	Nudulama	Laminated Quartz Vein	Vein	0.509	0.96
P-10	Nudulama	Laminated Quartz Vein	Vein	0.012	0.03
P-18	Nudulama	Quartz-Sericite-Pyrite Schist	Wallrock	0.739	0.56
P-8	Nudulama	Quartz-Sericite-Pyrite Schist	Wallrock	0.222	0.15
P-9	Nudulama	Quartz-Sericite-Pyrite Schist	Wallrock	0.189	0.29
P-11	Nudulama	Quartz-Sericite-Pyrite Schist	Wallrock	0.174	0.25
P-4	Nudulama	Quartz-Sericite-Pyrite Schist	Wallrock	0.032	0.07
P-13	Nudulama	Massive Pyrite Vein	Vein	0.329	0.71
Nu-12-04 #13	Nudulama (Drill Core)	Laminated Quartz Vein	Vein	18.564	1.26
Nu-12-05 #18	Nudulama (Drill Core)	Laminated Quartz Vein	Vein	1.174	0.24
Nu-12-05 #28	Nudulama (Drill Core)	Laminated Quartz Vein	Vein	0.915	1.68
Nu-12-05 #30	Nudulama (Drill Core)	Laminated Quartz Vein	Vein	0.777	0.73
Nu-12-05 #29	Nudulama (Drill Core)	Laminated Quartz Vein	Vein	0.422	0.87
Nu-12-05 #18	Nudulama (Drill Core)	Quartz-Sericite-Pyrite Schist	Wallrock	13.249	2.37
Nu-12-04 #13	Nudulama (Drill Core)	Quartz-Sericite-Pyrite Schist	Wallrock	3.782	1.71
Nu-12-04 #13	Nudulama (Drill Core)	Quartz-Sericite-Pyrite Schist	Wallrock	0.704	0.32
Nu-12-05 #27	Nudulama (Drill Core)	Quartz-Sericite-Pyrite Schist	Wallrock	0.6	0.43
Nu-12-05 #28	Nudulama (Drill Core)	Quartz-Sericite-Pyrite Schist	Wallrock	0.32	0.51
Nu-12-04 #14	Nudulama (Drill Core)	Quartz-Sericite-Pyrite Schist	Wallrock	0.169	0.13
Nu-12-05 #18	Nudulama (Drill Core)	Quartz-Sericite-Pyrite Schist	Wallrock	0.115	0.07
Nu-12-05 #19	Nudulama (Drill Core)	Quartz-Sericite-Pyrite Schist	Wallrock	0.096	0.05
Nu-12-05 #25	Nudulama (Drill Core)	Quartz-Sericite-Pyrite Schist	Wallrock	0.064	0.11
Nu-12-05 #33	Nudulama (Drill Core)	Hematite-Bearing Alteration	Wallrock	0.018	0.01
Nu-12-04 #18	Nudulama (Drill Core)	Hematite-Bearing Alteration	Wallrock	0.014	0.01

Nu-12-04 #19	Nudulama (Drill Core)	Hematite-Bearing Alteration	Wallrock	0.011	0.03
Nu-12-05 #35	Nudulama (Drill Core)	Hematite-Bearing Alteration	Wallrock	0.008	0.01
NUE-27	Nudulama East	Laminated Quartz Vein	Vein	0.105	0.55
NUE-14	Nudulama East	Laminated Quartz Vein	Vein	0.025	0.11
NUE-17	Nudulama East	Laminated Quartz Vein	Vein	0.008	0.04
NUE-24	Nudulama East	Laminated Quartz Vein	Vein	0.007	0.07
NUE-25	Nudulama East	Laminated Quartz Vein	Vein	0.004	0.01
NUE-13	Nudulama East	Quartz-Sericite-Pyrite Schist	Wallrock	0.113	0.2
NUE-8	Nudulama East	Hematite-Bearing Alteration	Wallrock	0.016	0.14
NUE-29a	Nudulama East	Hematite-Bearing Alteration	Wallrock	0.009	0.01
NUE-32	Nudulama East	Hematite-Bearing Alteration	Wallrock	0.008	0.02
NUE-23b	Nudulama East	NW-Striking Quartz Tension Gash	Wallrock	0.004	0.02
NUE-23a	Nudulama East	NW-Striking Quartz Tension Gash	Vein	0.004	0.01
NUE-10	Nudulama East	Massive Pyrite Vein	Vein	3.993	3.75
NUE-1	Nudulama East	Massive Pyrite Vein	Vein	1.271	4.34
NUE-31	Nudulama East	Massive Pyrite Vein	Vein	1.182	2
NUE-6	Nudulama East	Massive Pyrite Vein	Vein	0.544	1.06
NUE-26	Nudulama East	Massive Pyrite Vein	Vein	0.225	1.33
NUE-22	Nudulama East	Massive Pyrite Vein	Vein	0.081	1.82
NUE-21	Nudulama East	Massive Pyrite Vein	Vein	0.062	3.91
NUE-20	Nudulama East	Massive Pyrite Vein	Vein	0.05	1.8
NUE-25	Nudulama East	Massive Pyrite Vein	Vein	0.04	0.53
PL-9b	Pileggi No.1	Laminated Quartz Vein	Vein	22.832	1.98
PL-9a	Pileggi No.1	Laminated Quartz Vein	Vein	18.858	1.3
PL-13	Pileggi No.1	Laminated Quartz Vein	Vein	0.684	0.16
PL-5	Pileggi No.1	Laminated Quartz Vein	Vein	0.047	0.05
PL-6	Pileggi No.1	Laminated Quartz Vein	Vein	0.023	0.08
PL-7c	Pileggi No.1	NW-Striking Quartz Tension Gash	Vein	<0.002	0.01
PL-9b	Pileggi No.1	NW-Striking Quartz Tension Gash	Vein	0.074	0.01
PL-9a	Pileggi No.1	NW-Striking Quartz Tension Gash	Vein	0.024	0.03
PL-22a	Pileggi No.1	NW-Striking Quartz Tension Gash	Vein	0.017	0.11
PL-12a	Pileggi No.1	NW-Striking Quartz Tension Gash	Vein	0.013	0.03
PL-22b	Pileggi No.1	NW-Striking Quartz Tension Gash	Wallrock	0.012	0.07
PL-12b	Pileggi No.1	NW-Striking Quartz Tension Gash	Wallrock	0.01	0.08
PL-7b	Pileggi No.1	NW-Striking Quartz Tension Gash	Wallrock	0.007	0.07
PL-7d	Pileggi No.1	NW-Striking Quartz Tension Gash	Wallrock	0.005	0.06
PL-7a	Pileggi No.1	NW-Striking Quartz Tension Gash	Vein	0.003	0.01

Chapter 3 – *A Discriminatory-Geochemical Approach to Multistage Veining, Alteration, and Mineralization in the Missanabie-Renabie Gold District (Archean Wawa Subprovince, Canada)*

Jordan A. McDivitt[1,+,x], Daniel J. Kontak[1], Bruno Lafrance [1], and Mostafa Fayek[2]

[1]*Mineral Exploration Research Centre, Department of Earth Sciences, Laurentian University, Ramsey Lake Road, Sudbury, On, P3E 2C6, Canada.*

[2]*Department of Geological Sciences, University of Manitoba, Winnipeg, Manitoba, R3T 2N2*

[+] *jmcdivitt@laurentian.ca*

[x] *Current Address: Department of Earth Sciences, Laurentian University, 935 Ramsey Lake Road, Sudbury, Ontario, Canada P3E 2C6*

Abstract

Archean gold districts display a level of geological complexity unparalleled by younger analogues. Defining a link between gold deposits and the processes that resulted in their formation is the main objective of research, but the link between process and ore formation is often confounded by multiple mineralization events, the effects of polyphase deformation and metamorphism, and equivocal geochemical data.

We herein provide insight into the viability of using geochemistry to discriminate between different hydrothermal events in gold districts, and into the significance that the geochemical signatures of hydrothermal events have for genetic implications. A number of geochemical techniques—including lithogeochemistry and mass balance, LA-ICP-MS element mapping of pyrite, SEM-EDS analysis of fluid inclusion solutes, and stable isotope (D, O, S) analysis—were applied to hydrothermal phases constrained within a field-based paragenesis from a structural study in the Missanabie-Renabie gold district (Archean Wawa subprovince, Ontario, Canada). The hydrothermal phases are categorized into three main events: (1) early (i.e., pre-regional

deformation), auriferous, laminated quartz veins and phyllic alteration zones (the Au_1 event); (2) ca. 2.55 Ga, post-peak-metamorphic retrograde alteration zones and quartz ± epidote ± chlorite ± K-feldspar ± hematite veins (the Retrograde event); and (3) auriferous pyrite veins that overprint the ca. 2.55 Ga retrograde alteration zones (the Au_2 event). Whereas the Au_1 event displays characteristics similar to intrusion-related gold deposits, the Retrograde and Au_2 events are orogenic in nature; therefore, a meaningful geochemical comparison between intrusion-related and orogenic mineralization is possible.

Results display: (1) chemical constituents of the "causative fluids" responsible for the Au_1 and Retrograde events (an H_2O-CO_2-Au-Ag-Cu-Bi-Pb-Te-W-Mo-Zn-S-LILE-bearing fluid versus an H_2O-Na-S-bearing fluid, respectively) differed; (2) $\delta^{18}O$ values in different generations of vein quartz show large ranges, significant overlap, and depleted values relative to other Archean lode gold deposits; (3) slightly depleted $\delta^{34}S$ and $\delta^{33}S$ values, and near-zero $\Delta^{33}S$ values in pyrites of both the Au_1 and Au_2 events; and (4) similar gold-trace element associations in both the Au_1 and Au_2 events (Ag-Bi-Te±Pb±U±W), but geochemical discrimination using these associations is possible via a comparative approach to correlation coefficients, and correlation- and regression-based parameters.

The significance of these results in the context of geochemical discrimination and genetic models for gold deposits include: (1) non-discriminatory stable isotopes (O and S), along with the similar gold-trace element associations in both the Au_1 and Au_2 events, suggests that the geochemical similarities between intrusion-related and orogenic gold deposits do not necessitate a genetic link between the two deposit types; (2) geochemical differences between the events (i.e., "causative fluid" constituents, correlation- and regression-based parameters) are equally as ambiguous as overlapping data in constraining the nature of mineralization; this is best exemplified by H_2O-CO_2 inclusions in intrusion-related (Au_1) as opposed to orogenic (Retrograde) veins; (3) the backbone for discrimination is geological field mapping, herein supported by P-T constraints

provided by fluid inclusions and U-Pb titanite geochronology; (4) apparent displays of closed-system behavior recorded in quartz veins indicates that $\delta^{18}O$ values from quartz ± carbonate ± alkali feldspar veins may not provide temperature corrected values representative of a fluids source; (5) near-zero $\Delta^{33}S$ values are equivocal in defining an intrusion-related origin, as near-zero $\Delta^{33}S$ values occur within pyrite veins of the Au_2 event, which were emplaced subsequent to magmatism in the district; and (6) the "young" age of the Retrograde event relative to local magmatism and metamorphic events in the Wawa subprovince, coupled with the retrograding nature of the alteration, gives credibility to late-gold models that invoke a deep-crustal fluid source in orogenic gold deposits.

3.1 Introduction

Gold deposits in metamorphic terranes are generally classified into three categories (Groves *et al*., 2003): (1) deposits with anomalous metal associations (e.g., Boddington, Bosquet, Hemlo); (2) orogenic; and (3) intrusion-related. Of these deposit types, those with anomalous metal associations are arguably the most distinct in their character, which often includes high concentrations of base metal-bearing sulfides, strongly deformed and transposed veins and orebodies, and the overprinting of alteration zones by metamorphic mineral assemblages. As these latter deposits are commonly overprinted by regional deformation and metamorphism, they are often considered to represent porphyry-epithermal or VMS styles of mineralization.

Orogenic deposits (Groves *et al*., 1998; Goldfarb *et al*., 2005) and those associated with reduced granitic intrusions (intrusion-related gold (IRG) deposits; Thompson *et al*., 1999; Thompson and Newberry 2000) share a number of characteristics which makes differentiating them challenging. Similarities between the two deposit types include: (1) elemental associations (Au-As-Bi-W-Sb-Te); (2) reduced sulfide assemblages (pyrite-arsenopyrite-pyrhhotite) with an overall low sulfide content (~3-5%); (3) low-salinity, H_2O-CO_2 fluid inclusions; (4) mineralization that is post-peak host rock metamorphism; (5) veins that formed in mesozonal to epizonal

environments; and (6) an association (although not necessarily genetic) with felsic intrusions (Goldfarb *et al*., 2005). In the cases of IRG mineralization, there is good evidence to suggest a genetic connection between intrusions and gold mineralization, such as the association of veins with magmatic-hydrothermal features (e.g., pegmatites, aplites, miarolitic cavities) (Hart, 2007), and in rare cases, overlapping ages for magmatic and hydrothermal events (e.g., Fort Knox; Selby *et al*., 2002). In other examples, however, this genetic connection is not well defined, and for a number of deposits their genesis is controversial (Goldfarb *et al*., 2005; Goldfarb and Groves, 2015). Although most well-defined IRG deposits are restricted to Phanerozoic terranes (e.g., Tintina gold province, Hart, 2007; Tasman fold belt, Walshe *et al*., 1995), similar alteration characteristics and metal associations are noted for syenite-associated Au deposits of the Archean Abitibi greenstone belt (Robert, 2001), wherein orogenic Au deposits are also prevalent.

The noted geochemical similarities between IRG and orogenic deposits have led to questions regarding their genetic affinities (Goldfarb and Groves, 2015): for example, if a Bi-W-As association in IRG deposits indicates a magmatic origin (cf., Thompson *et al*., 1999), does the same association in orogenic deposits implicate a link to magmatism? As the genesis of orogenic gold deposits is controversial, in both a historic (e.g., Phillips and Groves, 1983; Spooner, 1993) and contemporary (e.g., Goldfarb *et al*., 2005; Phillips and Powell, 2009; Goldfarb and Groves, 2015) context, the geochemical similarities they share with IRG deposits, and their significance in a genetic context is an important outstanding issue.

Geochemical data from orogenic gold deposits is often, if not always, equivocal in a genetic sense (Goldfarb and Groves, 2015). This is exemplified by the fact that the calculated $\delta^{18}O_{H2O}$ values of 6-11‰ for a number of Archean and Proterozoic deposits (McCuaig and Kerrich, 1998) overlap the inferred $\delta^{18}O_{H2O}$ for both magmatic and metamorphic fluids (Taylor, 1974; Sheppard, 1977). Attempts to geochemically fingerprint different mineralization events are also complicated where multiple mineralizing episodes are present, as is the case for the Timmins-Porcupine camp

(Bateman *et al*., 2008). This highlights that extreme care is required in distinguishing samples paragenetically prior to geochemical analysis. These issues are emphasized in greater detail in review papers on gold deposits in metamorphic terranes (e.g., Hagemann and Cassidy, 2000; Groves *et al*., 2003; Goldfarb *et al*., 2005; Goldfarb and Groves, 2015). Thus, in order to further genetic models and the understanding of these systems, studies must integrate detailed-field mapping with the application geochemical and geochronological techniques. In addition, in these studies one must utilize methods that provide improved spatial and temporal resolution (e.g., SIMS isotopic analysis, U-Pb TIMS dating) along with techniques that are novel or less conventional (e.g., multiple S-isotope analysis, in situ analysis of fluid inclusions).

In order to further the understanding of gold systems in the manner just discussed, herein presented are the results of a geochemical study on gold mineralization and associated vein and alteration phases in the Archean Missanabie-Renabie gold district of the Superior craton. Of particular importance is that integrated with this work is a complementary field-based study, which provides a paragenesis defining the deformation history of the area. Whereas the details of the structural study are presented elsewhere (Chapter 2), here a variety of geochemical techniques are used to geochemically fingerprint the different hydrothermal events. The more routine methods employed include petrography, SEM-EDS imaging and analysis, and fluid inclusion microthermometry; with these are integrated the lesser used methods of secondary ion mass spectrometry (SIMS) for $\delta^{18}O$ of vein quartz, $\Delta^{33}S$ analysis of pyrite, LA-ICP-MS elemental mapping of Au-bearing pyrite, *in situ* U-Pb dating, and decrepitate mound analysis of fluid inclusions. The data represent, therefore, one of the most comprehensive studies yet reported for a hydrothermal gold setting. These data were used to address two primary objectives: (1) provide pressure-temperature-time (P-T-t) constraints on the hydrothermal evolution of the district; and (2) fingerprint the geochemical and isotopic signatures of different hydrothermal events in the area in

order to assess the viability of using geochemical techniques to discriminate between different styles of mineralization.

3.2 Geological Setting, Gold Mineralization, Deformation History, and Vein Types

The Missanabie-Renabie gold district is located in the Wawa subprovince of the Archean Superior craton ~200 km west of the prolific Timmins gold camp (Abitibi subprovince; Fig. 3.1). The district (Fig. 3.2A) is defined by a series of gold-bearing quartz vein occurrences dispersed across the northeast portion of the Michipicoten greenstone belt and the adjacent Missinaibi Lake batholith (Pervical, 1981), which is a plutonic component of the Wawa gneiss domain (Moser, 1994). The Michipicoten greenstone belt consists of mafic- to felsic-metavolcanic rocks that comprise 3 main bimodal volcanic cycles (~2.90 Ga, ~2.75 Ga, and ~2.70 Ga; Sage, 1986; Turek *et al*., 1982, 1984; Sage and Heather, 1991; Turek *et al*., 1992; Heather and Arias, 1992). Intermediate- to felsic-volcaniclastic rocks near the Renabie mine area (Fig. 3.2B) have been dated at 2740±8 Ma (Turek *et al*., 1996), 2728.6±1.1 Ma (Kamo, 2015; Robichaud *et al*., 2015), and 2723±5 Ma (Kamo, 2014; Robichaud *et al*., 2015). East of these volcaniclastic units, massive- to pillowed-mafic flows occur on the margin of the Michipicoten greenstone belt at its contact with a 2720.8±1.4 Ma (Kamo, 2015; Robichaud *et al*., 2015) biotite-bearing tonalitic component of the Missinaibi Lake batholith. A series of late-stage, compositionally-variable (predominantly granitoids with some gabbros and syenites) plutons were emplaced from ~2.68-2.66 Ga (Turek *et al*., 1990; Turek *et al*., 1992; Corfu and Sage, 1992; Turek *et al*., 1996).

Historic production in the Renabie mine area consisted of ~1.1 Moz Au from ore containing ~6.6 g/t Au sourced from the Renabie underground mine in addition to the C-zone, Nudulama, and Braminco open pits (Turek *et al*., 1996; Callan and Spooner, 1998). This gold was extracted from shear zone-hosted laminated quartz veins within the Missinaibi Lake batholith. Previous studies suggested contrasting genetic models for the formation of these mineralized veins,

with both magmatic (Jemielita *et al*., 1988) and metamorphic (Studemeister and Kilias, 1987) origins proposed.

Hematite-bearing zones of alteration are present throughout large parts of the Missinaibi Lake batholith: these are easily recognized due to their intense reddish coloration and the presence of chlorite. This alteration is preferentially located at the contact between the Missinaibi Lake batholith and adjacent Michipicoten greenstone belt, and in proximity to shear zones along the Renabie trend. Where present at the contact, the hematite-bearing alteration spatially overlaps with what has been interpreted as the older (i.e., ca. 2728 Ma) trondhjemitic component of the Missinaibi Lake batholith; this interpretation is based on the batholiths distinct mineralogy, geochemistry, and fabric at the contact zone (Callan and Spooner, 1987, 1998; Jemielita *et al*., 1988). As part of this study, hematite-bearing alteration zones were also encountered within the Ash Lake pluton (Fig. 3.2A), which is a biotite-bearing tonalite member of the ca. 2.68-2.66 Ga plutonic suite.

As discussed in Chapter 2, four deformation events are defined in the district. The earliest event is represented by recumbent to inclined, isoclinal folds and an associated S1 cleavage (D1), the second by regionally-penetrative S2 and L2 fabrics (D2), the third by E-trending, sinistral-reverse shear zones and related fabrics and folds (i.e., S3, F3) (D3), with D4 consisting of a late dextral-strike slip reactivation of the E-trending D3 shear zones. A principal conclusion of the structural study is that the auriferous laminated quartz veins and related phyllic alteration halos, from which the majority of gold was produced, were emplaced prior to D1. This conclusion contrasts to earlier interpretations of vein emplacement suggesting the veins formed as fault-fill type veins during sinistral-reverse shearing (i.e., a syn-D3 timing of emplacement; Callan and Spooner 1988, 1998). Relevant constraints provided by our structural study include: (1) the laminated veins and their phyllic alteration halos reflect an early (i.e., pre-D1) phase of gold mineralization in the district (Au_1); (2) hematite-bearing alteration zones, associated veins, and

shear zone-hosted quartz breccias formed at various times during the D3 event; (3) NW-striking quartz tension gashes formed synchronously with D4 dextral-transcurrent movement in E-trending shear zones; and (4) massive, gold-bearing pyrite veins were emplaced in proximity to D3 shear zones as either a brittle phase of D4 or as a later unrelated event. These latter veins represent a late-stage gold event (Au_2).

3.3 Analytical Methods

3.3.1 Petrography, Mineral Identification, and Mineral Chemistry

Polished thin sections were studied in reflected and transmitted light using an Olympus BX-51 microscope. Selected samples were then analyzed in both back scattered electron (BSE) and secondary electron (SEI) modes on a JEOL 6400 scanning electron microscope (SEM) at the Central Analytical Facility of Laurentian University. Semi-quantitative mineral chemistry was collected using Oxford Sight energy dispersive X-ray spectrometer (EDS) coupled to the SEM. Data was collected using an accelerating voltage of 20 kV, a 1.005nA beam current, and a working distance of 15 mm. Acquisition time was varied from 5-30s depending on whether data were for mineral identification or part of a chemical comparison.

3.3.2 Lithogeochemistry and Mass Balance

Representative samples of the different alteration types were chosen to quantitatively assess elemental gains and losses associated with alteration. Weathered surfaces and vein material were cut from samples and the remainder submitted to the Geoscience Laboratories of the Ontario Geological Survey, Sudbury, Ontario, where they were pulverized using an agate mill to minimize potential contamination of immobile phases (e.g., Al).

Major element oxides, in addition to loss on ignition (LOI), were determined using the XRF-M01 technique on fused disks using a borate flux. Total carbon (as CO_2) and total sulfur (as S) were determined by combustion in an oxygen-rich environment with measurements done by infrared absorption (IRC-100). Ferrous iron was determined by potentiometric titration with a

standardized permanganate solution subsequent to sample dissolution in a non-oxidizing acid mix (FEO-ION). Trace element abundances were determined using the IMC-100 technique, in which analysis is done on solutions prepared in closed-vessels with a multi-acid digestion. Metal concentrations (e.g., Au, Ag, Bi, Co, Cu, Ni, Pb) were determined by IML-100, wherein samples are subjected to an open-vessel, agua regia digestion prior to analysis. Further details of analyses, and information on method codes is provided in McDivitt (2016).

Mass balance calculations utilized the Grant (1986) isocon method with the relative changes calculated as percentages and displayed on histograms (e.g., Hutson, 1993). In this way the relative percentage change in the concentration of an element during alteration is modelled as a function of the original concentration of the element in the precursor and the slope of the isocon. For the purpose of mass balance, elements present in concentrations below that of analytical detection were reported at values of one half the detection limit.

3.3.3 U-Pb Titanite Geochronology

In situ laser ablation-inductively coupled plasma-mass spectrometry (LA-ICP-MS) was used to obtain U-Pb ages forvtitanite from the retrograde type 1 alteration at Nudulama East (Sample NUE-28C), of which the setting is described in more detail below (Section 5.3). Prior to analysis the grains, which are ~20-100 μm in diameter and locally cored by rutile, were imaged in BSE mode on the SEM. The analyses were completed at the Geochemical Fingerprinting Lab of Laurentian University with the operating conditions, data collection, and data reduction parameters given in Table 3.1.

3.3.4 LA-ICP-MS Pyrite Mapping

Select grains of pyrite from Au-bearing samples were analyzed using LA-ICP-MS in traverse mode to generate elemental distribution maps, and also to assess the trace element associations of the different gold events (i.e., Au_1 and Au_2). Elements analyzed included Ag, As, Au, Bi, Cd, Co, Fe, In, Mo, Ni, Pb, Sb, Sc, Te, U, W, and Zn. This was completed at the

Geochemical Fingerprinting Lab of Laurentian University. The operating conditions and details of data collection and reduction are presented in Table 3.2. As well as being used to generate elemental distribution maps, the results of the LA-ICP-MS traverse analyses were converted into time-slice domains allowing the data to be displayed as individual points in a series of trivariate scatter plots.

3.3.5 Fluid Inclusion Petrography and Microthermometry

Petrographic study (at 20ºC) of doubly-polished thin sections (100 µm) was done on quartz vein material following procedures in Goldstein (2003), and using the fluid inclusion assemblage (FIA) approach of Goldstein and Reynolds (1994). Where FIAs are coincident with growth zones a primary origin is assigned, FIAs on planes cutting growth features are categorized as secondary, and isolated FIAs are considered indeterminate.

Microthermometry was completed at Laurentian University using a Linkham THMSG600 heating-freezing stage attached to an Olympus BX-51 microscope with a Q-Imaging digital capture system. Calibration of the heating-freezing stage was done with synthetic standards using the triple point of CO_2 (T_m=-56.6˚C), melting temperature of pure H_2O (0˚C), and the critical point of H_2O (374.1˚C).

3.3.6 Evaporate Mound Analysis

Evaporate mound analysis (Haynes *et al*., 1988; Kontak, 2004) was completed to complement the fluid inclusion salinity calculations and identify cations (e.g., K, Fe, Mg) in solution. In order to induce decrepitation and mound formation, chips were heated at a rate of 50˚C per minute to 400˚C and were then held at 400˚C for ~2 minutes. Chips were then carbon coated and analyzed using SEM-EDS analysis as described above. Mounds were subjected to a raster-type analysis as opposed to spot analysis to compensate for the effects of elemental zonation, a consequence of fractionation during decrepitation (Haynes *et al*. 1988; Kontak, 2004). The results were normalized to 100% subsequent to removal of the influence of the quartz substrate.

3.3.7 Oxygen Isotopes

Samples of vein quartz selected for $\delta^{18}O_{qtz}$ analysis were crushed into mm-size fragments and hand sorted using tweezers and a binocular microscope to avoid impurities (i.e., muscovite, chlorite, feldspars etc.). These grains were mounted in epoxy pucks, ground, and polished with 6 µm, 3 µm, and 1 µm grit polishing powder. Quartz grains were then imaged in reflected and transmitted light and spot locations selected for Secondary Ion Mass Spectrometry (SIMS) O-isotope analysis based on "cleanliness" of appearance (i.e., areas that lacked fractures, mineral inclusions etc.). In addition, a polished thin section of the quartz from the breccia zone at Nudulama East (NUE-30) (see Chapter 2) was subjected to cathodoluminesence (CL) imaging, and based on this a single crystal cut perpendicular to its c axis was selected for a detailed SIMS O-isotope traverse.

Prepared samples were sent to the SIMS Laboratory at the University of Manitoba, where they were cleaned with ethanol, polished with a 1 µm diamond cleaning compound, and immersed in an ultrasonic cleaner. The cleaned samples were sputter-coated with a thin layer of gold to produce a conductive surface. SIMS O-isotope analysis was completed using the using the CAMECA 7f ion microprobe, which used a 3 nA cesium (Cs^+) primary beam, accelerated to +10 kV, and focused to a 20 µm spot size using a 100 µm aperture. An offset voltage of 300 volts was used to eliminate molecular ion interferences. Ions were detected with a Balzers SEV 1217 electron multiplier coupled with an ion-counting system using a dead time of 52 ns. Both ^{18}O and ^{16}O were detected by switching the magnetic field. The data is presented using δ-notation relative to Vienna Standard Mean Ocean Water in units of per mil (‰). Internal standards were used for the purpose of calibration and analyzed at multiple times during the analysis of the quartz grains; the spot reproducibility on the standards ranged from 0.4-0.5‰.

3.3.8 Hydrogen Isotopes

Vein quartz samples were sent to the Facility for Isotope Research at Queen's University for δD analysis of fluid inclusion waters. Samples were weighed into silver capsules, degassed at 100˚C for 1 hour, and then loaded into a zero-blank auto sampler. Values of δD were measured using a Thermo-Finnigan thermo-combustion elemental analyzer coupled to a Thermo-Finnigan Delta^{plus} XP Continuous-Flow Isotope-Ratio Mass Spectrometer. The values are reported relative to Vienna Standard Mean Ocean Water with a precision of 3‰.

3.3.9 Sulfur Isotopes

Powdered pyrite separates were prepared using a Dremel^{TM} drill and sent to the Stable Isotopes for Innovative Research Laboratory at the University of Manitoba. Samples, ranging from ~0.2-0.8 mg, were analyzed by a Costech^{TM} 4010 Elemental Analyzer coupled to a Thermo Finnigan^{TM} Delta V Plus isotope-ratio mass-spectrometer via an open-split interface. Each sample was analyzed three times non-consecutively as a test of reproducibility. Isotopic ratios are reported as $\delta^{34}S$ and $\delta^{33}S$ relative to international standards of the Vienna Cañon Diablo Troilite. The international standards *(*IAEA-S1, IAEA-S2, and IAEA-S3) were analyzed at the beginning, middle, and end of each run. The internal sulfide standards were treated as unknowns for quality control measures. Least-squares linear regression of the known and measured standard values was used to produce a calibration line. The precision of $\delta^{34}S$ and $\delta^{33}S$, based on the replicate analysis of internal standards, is ≤0.2‰ and ~0.3‰, respectively.

3.4 Veins: Textures, Mineralogy, and Defining Features

This section expands on the different vein types introduced in our complementary structural study (Chapter 2) by characterizing both their textures and infill mineralogy, as it is the latter and vein-related alteration that are the subject of this analytical study. A summary table of the features described in this section is presented in Table 3.3.

3.4.1 Laminated Quartz Veins

Quartz (Qtz_1) is the dominant constituent of the laminated veins (~80-90%; Fig. 3.3A). Grains range from equidimensional to irregular and have amoeboid morphologies, with lobate- to cuspate-grain boundaries (Fig. 3.3B). Primary growth features are absent, undulatory extinction is common, and a bimodal distribution of grain size is present (~1-2 mm versus ~0.1-0.2 mm), with the coarser grains generally having an amoeboid shape whereas the finer grains are more equant with well-defined triple junction boundaries. Sericite and carbonate are the second most abundant phases (≤10% each) and are preferentially associated with zones of the finer-grained quartz. Accessory phases (≤10% combined total; Fig. 3.3C) include: (1) fragments of both twinned and epidote-altered plagioclase incorporated from the tonalite wall rock; (2) allanite that is commonly overgrown by LREE-free epidote; (3) a sulfide assemblage; and (4) native gold along with electrum and Au±Ag±Bi±Te±Pb alloys. The sulfide assemblage (≤5%) consists of pyrite>chalcopyrite~molybdenite>galena>sphalerite, with the pyrite often partly hematite-replaced (Py_1). The domains of the finer-grained quartz and sericite define a laminated texture with cm- to mm-scale spacing. Molybdenite, often intergrown with gold (Fig. 2.5D in Chapter 2), is present within the sericite domains, along with allanite, epidote, and titanite.

3.4.2 Hematite-Associated Alteration Veins

Hematite-associated alteration veins are defined by hematite-bearing alteration assemblages in the wall rock marginal to quartz ± epidote ± chlorite ± K-feldspar ± hematite veins (Fig. 3.3D). Both chlorite-titanite-albite-hematite and K-feldspar-hematite alteration assemblages are present,

with the former more common as a distal expression of alteration whereas the latter is proximal. Vein fill consists of quartz, chlorite, epidote, K-feldspar, and earthy-red hematite. Although the vein infill mineralogy is generally limited to this assemblage, the modal proportions can vary with hematite and K-feldspar the least abundant (typically <20%) whereas quartz (Qtz_2), chlorite, and epidote are most common (up to 100%). Infill minerals are commonly euhedral and locally define comb-like textures (Fig. 3.3E), with quartz and epidote generally medium- to coarse-grained whereas chlorite is commonly fine-grained. The veins are both discrete, with mm- to cm-scale widths, and present as shear zone-hosted hydrothermal breccias, as exemplified by common infill mineralogy and indicated timing of emplacement for both types at the Nudulama East outcrop (Chapter 2).

3.4.3 NW-striking Quartz Tension Gashes

Quartz tension gashes (Fig. 3.3F) are present as NW-striking veins dominated by quartz (Qtz_3; ~90-95%), with lesser, brown, granular iron oxides; fine-grained pyrite is present in trace amounts (<1%). Wall rock fragments (chlorite, amphibole, epidote-altered plagioclase) are present in the veins. Quartz grains are typically acicular in thin section (~1-5 mm), display undulatory extinction, and have irregular- to jagged-grain boundaries. Microfracturing is abundant in some of the quartz (Fig. 3.3G) and is most dense in zones of cataclasite. Locally zones of silicification are present marginal to the veins.

3.4.4 Massive Pyrite Veins

Infill mineralogy of the pyrite veins (Fig. 3.3H, I) is limited to medium-grained, anhedral pyrite (Py_2), which commonly displays jagged- to serrated-grain boundaries (Fig. 3.3J). These veins lack visible alteration halos, but pyrite is commonly present as disseminations in the wall rock marginal to the veins.

3.5 Hydrothermal Alteration Zones and Prograde Metamorphic Minerals: Setting, Mineralogy, and Key Relationships

Hydrothermal alteration types and prograde metamorphic minerals are integrated paragenetically in Table 3.4 and summarized in Table 3.5. Whereas some types of alteration are developed on a regional scale (e.g., saussuritization), other types are only locally developed (e.g., phyllic alteration). The Nudulama East outcrop (Fig. 3.2B, Fig. 3.4) is the only area of continuous exposure encountered where all alteration types and prograde metamorphic minerals are well-developed.

3.5.1 Saussuritization

Saussuritization, visible as beige aggregates within plagioclase in hand sample, is present in the tonalite phase of the Missinaibi Lake batholith, which consists of biotite (~10-15%; ~12 wt.% Fe, Fe/(Fe+Mg) = ~0.4), quartz (~30%), and variably saussuritized plagioclase (~50-60%) (Fig. 3.3K). The saussuritized plagioclase occurs as fine-grained, acicular, Fe-poor (≤~2 wt.% Fe) epidote (Ep_1) intergrown with optically continuous plagioclase (An_{20}) (Fig. 3.3L). The Ep_1 is consistently overgrown and/or variably replaced by a more Fe-rich epidote (Fig. 3.5A). Relict, twinned primary plagioclase typically accounts for ≤10% of the total plagioclase. Based on petrographic examination of numerous samples from the Missinaibi Lake batholith, this alteration is noted to be widespread and shows no spatial association with the mineralized zones.

3.5.2 Phyllic Alteration (Quartz-Sericite-Pyrite)

Phyllic alteration zones, which surround the laminated quartz veins, are dominated by quartz (~30%), sericite (~65%), and pyrite (~2-5%) and contain fragments of saussuritized plagioclase which are locally altered to sericite (Fig. 3.5B). Accessory minerals include carbonate, titanite, pyrite, and allanite (Ep_2; ~1-2%) (Fig. 3.5C); the latter is commonly overgrown by a later, LREE-free epidote (Ep_3) (Fig. 3.5 D). Pyrite within these zones is fine- to medium-grained, euhedral to subhedral, and commonly altered to hematite (i.e., Py_1). The mineralogical similarities

between the phyllic alteration zones and laminated quartz veins supports our earlier interpretation (Chapter 2) that these features are broadly contemporaneous, and formed from focused fluid activity within the same structures.

3.5.3 Prograde Metamorphic Assemblage and Epidote Chemistry

The prograde metamorphic mineral assemblage within the Missinaibi Lake batholith is present as overgrowths of biotite by poikiloblastic hornblende, epidote (Ep_3) (Fig. 3.5E), Fe-Ti oxides, and in rare instances garnet. In such cases, however, biotite still remains the dominant phyllosilicate even where the prograde metamorphic assemblage is well developed. The assemblage typically accounts for a small proportion (<3%) of total mineralogy. Both saussuritized plagioclase and rarely chalcopyrite are present as inclusions in minerals of the prograde assemblage (Fig. 3.5F).

The best relative time constraints between the prograde metamorphic minerals and deformation events comes from the Boundary outcrop, where poikiloblastic hornblende both defines and overgrows S1 in metagabbro (Fig. 3.5G), and also accounts for ~40-50% of the mineralogy in a late- to post-D2, pre-D3 mafic dike (see Fig. 2.15 in Chapter 2). These relationships indicate that pokiloblastic hornblende growth, and thus prograde metamorphism, occurred during D1 and either outlasted or continued until the latter stages of D2.

The chemistry of the different epidote phases (i.e., Ep_1, Ep_2, Ep_3) illustrates they are distinct in terms of both Ca-Al-Fe (Fig. 3.6A) and Fe versus ΣLREEs (Fig. 3.6B). Importantly, when the overgrowth rims on Ep_1 (Ep_3-Ep_1) and Ep_2 (Ep_3-Ep_2) are compared to Ep_3, where it overgrows biotite in association with hornblende (Ep_3-Bt), it is seen that they all plot as a coherent group. This latter observation clearly indicates these various epidote overgrowths all represent the same generation of epidote and formed as part of the prograde metamorphic mineral assemblage.

3.5.4 Retrograde Type 1 Alteration: Chlorite-Titanite-Albite-Hematite

This alteration is defined by the retrogression of biotite (~12 wt.% Fe) to chlorite (~16 wt.% Fe) and titanite, and the conversion of saussuritized plagioclase to an assemblage of fine-grained sericite, hematite, and albite inter-grown with residual An_{20} plagioclase (Fig. 3.5H, I, J). Accessory phases in the alteration zones include Fe-Ti oxides and apatite, which occur in association with chlorite and low concentrations of hematite-rimmed pyrite (<~1%). Brown, granular sulphates and Fe oxides form preferentially along micro-fractures as an alteration of Ep_3. Hornblende is retrograded, along with biotite, to chlorite—thus, the term "retrograde alteration" is utilized.

These alteration zones are readily identified during mapping due to the presence of hematite and chlorite. At the Nudulama East outcrop, the retrograde alteration is well-developed in a central area bounded by ESE-trending domains of laminated quartz veins surrounded by phyllic alteration zones (i.e., D3 shear zones; Fig. 3.4). The retrograde alteration is also present, but to a lesser degree, at the Nudulama outcrop, and absent from both the C-zone and Baltic D outcrops (see Fig. 3.2B for locations). As previously discussed, these hematite-bearing retrograde alteration zones are present on a regional scale and are not restricted to zones of gold mineralization.

3.5.5 Retrograde Type 2 Alteration: K-Feldspar-Hematite

These zones are typically narrow, with widths of ~10 cm, and are easily identified in the field based on their dark red hue, due to an increased abundance of hematite compared to the retrograde type 1 alteration. Mineralogically, these zones are dominated by fine- to medium-grained, generally prismatic and euhedral K-feldspar (50-70%), which defines a net-like texture with abundant porosity (Fig. 3.5K, L). The remaining inter-crystal space is commonly lined by a mineralogy similar to that of the hematite-associated alteration veins (i.e., quartz, chlorite, epidote, etc.), pyrite with hematite-altered rims, and brown, granular sulphates and Fe oxides. Whereas the

retrograde type 1 alteration is not texturally destructive, the retrograde type 2 alteration is and resulted in the dissolution of pre-existing fabrics and minerals.

3.6 Lithogeochemistry and Mass Balance

The results of lithogeochemistry and mass balance are presented in Table 3.6 and Figure 3.7, respectively, with a summation of the main chemical changes in the alteration zones given in Table 3.5. No overall mass change is indicated in the phyllic alteration zone, as shown by an isocon slope of ~1. Both Ca and Na are strongly depleted, whereas large ion lithophile elements (i.e., K, Ba, Rb; LILEs), CO_2, and S are enriched along with Au, Ag, Mo, Cu, W, Te, Pb and W. Although total Fe (shown as Fe_2O_3t) shows only a slight increase, ferric Fe (as Fe_2O_3) is significantly increased during the alteration and ferrous Fe (as FeO) is decreased.

For retrograde alteration type 1, it also reflects constant mass, but in this case, except for gains in S, LOI, Na, W, and Bi, most elements show variable losses, including the LILEs and the REEs. The retrograde alteration type 2 reflects mass loss, as indicated by the positive slope of the isocon (1.33), which is constrained by Zr, Ti and the HREEs. This mass loss is accompanied by depletion of Na, Si, Fe, Mn, Mg, Al, Ca, ferrous Fe and the metals Zn, Mo, Pb. In contrast there is significant enrichment in K, Ba, Rb, ferric Fe and S along with the metals Au, Ag, Te, and W.

3.7 LA–ICP-MS U-Pb Titanite Geochronology

Titanite in retrograde alteration (type 1) at Nudulama East was dated by *in situ* LA ICP-MS using grains first characterized by SEM-EDS imaging and analysis (Fig. 3.8A, B). The data show significant discordance when plotted, in part due to the variable incorporation of common Pb (Fig. 3.8C). In order to generate the most robust age from the data set, the following criteria were applied to the analyses: (1) those falling along the lead-loss trend were discarded; (2) isolated points with exceptionally large 2σ errors were discarded; and (3) analyses discordant to the tie line between $^{207}Pb/^{206}Pb = 1.07$, the inferred common-Pb value (Stacey and Kramers, 1975) at the time of formation, and 2.6 Ga on the isochron were discarded. The rational for the latter is that titanite is

susceptible to incorporating Pb during its crystallization (Frost *et al*., 2001; Storey *et al*., 2006), and since the retrograde alteration occurs within the Ash Lake pluton (a member of the ca. 2.68-2.66 Ga plutonic suite), a common Pb value of 1.07 is a reasonable estimate. The residual points (n = 41, Table 3.7) define an age using a common Pb anchor ($^{207}Pb/^{206}Pb = 1.07$) in isoplot (Ludwig, 2003) of 2549 ± 24 Ma (MSWD = 2.4) (Fig. 3.8D).

3.8 Whole Rock Au-Trace Element Associations

Gold-bearing samples discussed in Chapter 2 were subjected to a Pearson product-moment correlation-based assessment of Au-trace element associations using $\log_{10}$ values reported by whole rock metal assays (Appendix 3.1). For elemental concentrations below detection, a value of one half of the detection limit was used for substituted. Well-defined correlations are defined between Au and Ag, Bi, Pb, and Te in the laminated vein and phyllic alteration (Au_1) samples, whereas correlations between Au and Ag, Bi and Te are also defined for the pyrite vein (Au_2) samples, but these are of lower magnitude and no Au-Pb correlation exists. Linear regression lines normalized to sample populations were calculated using the power function in Microsoft Excel™ and projected to values of Au=0 ppm and Au=100 ppm on scatter diagrams of Au (X-axis) versus selected trace elements (Y-axis) that correlate with Au (i.e., Ag, Bi, Te, Pb; Fig. 3.9).

Additional parameters introduced for comparison are $\Delta C_{x\text{-}Au}$, $\sum\Delta C$, $X_{Au=1}$, $X_{Au=100}$, and $\Delta X_{Au.}$ For these values, $\Delta C_{x\text{-}Au}$ is the difference in the absolute correlation value between an element (x) and Au from two selected sample populations; $\sum\Delta C$ is the sum of all $\Delta C_{x\text{-}Au}$ values within a sample population that have been calculated relative to another sample population; $X_{Au=1}$ is the value of element X (in ppm) when [Au]=1 ppm, as determined by regression analysis; $X_{Au=100}$ is the value of element X (in ppm) when [Au]=100 ppm, as determined by regression analysis; ΔX_{Au} is equal to $((X_{Au=100)} - X_{Au=0})/ X_{Au=0})*100$. The comparative parameters, along with correlation coefficients, are presented in Table 3.8.

3.9 LA-ICP-MS Pyrite Mapping

Elemental maps of Py_1, which contains inclusions of Au_1 alloys (sample C-5 from a laminated vein at the C-zone), and Py_2 (sample NUE-31), where it overprints a retrograde alteration zone (Fig. 3.3H), are shown, along with corresponding trivariate scatter plots of time-series data, in Figures 3.10 and 3.11, respectively. The elemental maps of Py_1 illustrate that the Au_1-bearing inclusions are enriched in Ag, Bi, Te, and Pb. These relationships are also visible on the trivariate plots, and represented by strong, positive linear relationships between Au and Ag, Bi, and Te; Pb, however, displays a weak, positive linear relationship with Au. Although U and W are enriched in some areas of the pyrite grain, they do not show an association with Au on either the element maps or the trivariate plots. Where elemental values are exceptionally high (e.g., >1000 ppm), they are likely representative of the Au-Ag-Bi-Te-Pb-bearing inclusions; lower values may reflect the presence of metals in the pyrites structure (i.e., invisible Au)

The elemental maps of Py_2 illustrate that Au is enriched in the core of the grain along with Ag, Bi, Te, Pb, U and W. The trivate plots also document Au-Ag and Au-Bi-Te-Pb associations in the form of strong and moderate-to-weak, positive linear relationships, respectively. Uranium and W, however, do not display linear relationships with gold in the trivariate diagrams.

LA-ICP-MS data was subjected to correlation- and regression-based analysis in the same manner previously discussed for the whole rock trace element data, with exclusion of data at lower limits of detection. The comparative parameters $\Delta C_{x\text{-}Au}$, $\sum \Delta C$, $X_{Au=1}$, $X_{Au=100}$, and ΔX_{Au} were also calculated, as described above, and are presented in Table 3.9. Graphical comparisons of whole rock trace element data to LA-ICP-MS trace element data are shown in Figure 3.12. The Au-trace element associations defined by correlations in $\log_{10}$ data reported by whole rock analysis of Au_1-bearing samples (Au_1-Ag-Bi-Pb-Te) are of similar magnitudes (with the exception of Pb) to those defined by $\log_{10}$ LA-ICP-MS data from trace element mapping of Py_1 (Fig. 3.12A). Similarly, the Au_2-Ag-Bi-Te correlations defined by $\log_{10}$ data reported by the whole rock analysis of Py_2 veins

are reproduced to similar magnitudes in the log_{10} LA-ICP-MS data (Fig. 3.12A), although, the Au_2-Ag and Au_2-Te correlations show significant increases and decreases, respectively.

3.10 Fluid Inclusions

3.10.1 Petrography

Five types of fluid inclusions are present in Qtz_1: (1) H_2O-CO_2 inclusions with the CO_2 phase present as either two phases (liquid (L) and vapour (V)), or one phase (L) and occupying ~30 vol.% of the inclusion (Fig. 3.13A); (2) H_2O-CO_2 inclusions, where CO_2 consists of either L and V, or L, and occupies ~70-80 vol.% of the inclusion (Fig. 3.13 B); (3) H_2O-CO_2 inclusions, where CO_2 consists of either L and V, or L, and occupies ~5-10 vol.% of the inclusion (Fig. 3.13B); (4) CO_2-only inclusions of either two (L-V) or one phase (L) (Fig. 3.13B); and (5) two phase (L-V) H_2O with ~10-20 vol.% V.

The abundance of fluid inclusions in Qtz_1 is typically low, inclusions range from ~<10-20 µm in size, and are generally equidimensional, or near equidimensional with oval shapes. No primary inclusions occur within Qtz_1, and inclusion types 1, 4, and 5 are present as discrete secondary and indeterminate FIAs. Inclusion types 2 and 3 are present as isolated secondary and indeterminate FIAs, or co-existing in secondary FIAs (Figs. 3.13B, G). Based on these relationships, inclusion types 2, 3, and 4 are considered to be the products of fluid unmixing, with type 1 inclusions representing the parental fluid. It is possible that type 2 inclusions reflect the heterogeneous entrapment of type 4 inclusions with a co-existing, H_2O-dominated fluid represented by type 3 inclusions (e.g., Diamond, 1990). The fluid inclusions types identified are in general agreement with those previously documented in auriferous quartz veins from the Renabie mine and Braminco zone by Studemeiser and Kilias (1987). These authors considered our type 1 (H_2O-CO_2), type 4 (CO_2), and type 5 (H_2O) inclusions to be of primary origin. In the context of the classification scheme used herein, however, these inclusions would be considered of indeterminate origin.

In sections of Qtz_2 the abundance of fluid inclusions is high and type 5 inclusions dominate as primary, secondary, and indeterminate types (Fig. 3.13C, D). No carbonic inclusions are noted. The shapes of inclusions are more varied than in Qtz_1, with prolate- to negative-crystal shaped inclusions common, and they also tend to be larger (~< 50 μm). In some instances, these H_2O inclusions are either L or V dominated (i.e., up to ~90-100 vol.%) as a result of necking. As type 5 inclusions are present within primary FIAs in Qtz_2, it is likely that their presence in Qtz_1 reflects the interaction of Qtz_1 with a later fluid.

3.10.2 Microthermometry and PT conditions

Sample BD-30, from the Baltic D outcrop, contained the best preserved and most abundant FIAs for inclusion types 1-4, and was therefore the main focus of the microthermometry in Qtz_1. For Qtz_2, sample NUE-11 (from the breccia zone at Nudulama East) contained abundant type 5 inclusions and was studied in detail.

For FIAs containing CO_2-bearing inclusions (types 1, 2, 3, and 4), melting and homogenization temperatures of CO_2 (T_mCO_2 and T_hCO_2, respectively) were recorded. The small volume of CO_2 in type 3 inclusions precluded the collection of accurate T_mCO_2 and T_hCO_2 data. Where T_hCO_2 was recorded in inclusion types 1, 2, and 4 it occurred to the liquid phase. Clathrate melting (T_mClath), which was used for salinity calculations, was recorded for type 1 inclusions, and generally occurred prior to T_hCO_2, although, in a few instances it occurred subsequently. Ice melting occurred at temperatures higher than 21.2˚C, an indication that Na is the dominant cation in solution (Bodnar, 2003a). Based on microthermometric measurements, calculations for the density of CO_2, the density of the total inclusion, and salinity (in wt.% equiv. NaCl) were made using programs Q2, DENSITY (Bakker, 1997), and BULK and ISOC (Bakker, 2003). The results of all measurements and calculations are summarized in Table 3.10, and calculated isochores are shown in Figure 3.14A.

Type 1 inclusions contain 0.13-0.17 X_{CO2}, and vary in salinity from 3.7-8.0 wt.% eq. NaCl. If the fluid is considered to have been trapped at ~300˚C where isochores for type 1, 2, and 4 inclusions converge with solvus for an appropriate bulk composition in the H_2O-CO_2-NaCl system (6 wt.% NaCl, 10 mol% CO_2; Schmidt and Bodnar, 2000), as expected for a system undergoing fluid unmixing, then the variable densities documented in type 1 isochores suggest pressure fluctuation of ~2 kbars (Fig. 3.14A).

Microthermometric data for primary, secondary, and indeterminate FIAs of type 5 inclusions in sample NUE-11 is presented in Table 3.11 and Figure 3.15A-B. The data consist of homogenization temperature (T_h; all to the liquid phase), ice melting temperature (T_mIce), and the melting temperature of hydrohalite (T_mHH). The first observed melting of inclusions following their freezing was consistently observed to occur between ~-55º to -50˚C, an indication of the presence of $CaCl_2$ in the fluid (Bodnar, 2003a). Thus, the values of T_mHH and T_m ice (Fig. 3.15B) were used to determine values of wt.% equiv. NaCl + $CaCl_2$ using equations provided in Steele-MacInnis *et al*. (2012). The results are given in Table 3.11 and shown graphically in Figure 3.15C. In the latter diagram it can be seen that the data for individual FIAs define a trend of increasing salinity, from ~7 to 24 wt.%, as the wt.% $CaCl_2$ increases. The T_h values for type 5 inclusions within assessed FIAs range from a minimum of 89˚C to a maximum of 164˚C, with most in the range of 100-150 ˚C; individual FIAs show a narrower range in T_h (Table 3.11, Fig. 3.15A).

3.10.3 Evaporite Mound Analysis

The results of evaporate mound analysis from type 5 inclusions within sample NUE-11 (Fig. 3.13E, F) are summarized in a Na-Ca-K ternary plot in Figure 3.15D. The most abundant cations are Ca and Na, followed by K, with Fe also detected in a number of mounds (to ~0.5 wt.%). These results are consistent with the fluid compositions inferred from the microthermometric data, which documents a mixed Na-Ca-bearing fluid with both Na- and Ca-

dominant endmembers and intermediate compositions. The scarcity and small size of inclusions in Qtz_1 precluded mound analysis of inclusions types 1-4.

3.11 Stable Isotopes

3.11.1 Oxygen Isotopes

The results of SIMS $\delta^{18}O$ analysis of 40 grains of Qtz_1 (selected from 11 different laminated quartz veins at the C-zone, Nudulama, Nudulama East, and Pileggi No.1 outcrops), 11 grains of Qtz_2 (from various samples of the breccia zone at Nudulama East), and 12 grains of Qtz_3 (from a number of quartz tension gashes at the Pileggi No.1 outcrop) are summarized in Figure 3.16 and Appendix 3.2.

The $\delta^{18}O$ values in Qtz_1 range from 3.9 to 13.4‰, with the results approximating a standard-normal data distribution (Fig. 3.16A). In contrast, the $\delta^{18}O$ values from Qtz_2 define a negatively-skewed distribution, with a larger number of lower (i.e., <6‰) values, with minimum and maximum values of 1.2‰ and 9.7‰, respectively (Fig. 3.16B). The $\delta^{18}O$ values in Qtz_3 are similar to those of Qtz_1, but are more tightly clustered, with a range from 5.8 to 10.9‰ (Fig. 3.16C). The $\delta^{18}O$ values from the SIMS transect of the single Qtz_2 crystal (sample NUE-30) yielded a range of 5.4 to 12.6‰ (Fig. 3.16D). The transect analysis was focused on a portion of the crystal cut perpendicular to its c-axis, where growth zones defined by primary FIAs of type 5 inclusions are present (Fig. 3.16E). The $\delta^{18}O$ values are plotted on a CL image of the transect area in Figure 3.16F. In general, the data show a trend of lower values in the core and heavier values towards the rim. There is, however, no apparent correlation between the CL response and the $\delta^{18}O$ values.

3.11.2 Hydrogen Isotopes

Results of δD analysis for fluid inclusion waters (from type 5 inclusions) extracted from two samples of the breccia vein at Nudulama East (NUE-10a, NUE-10b) are given in Table 3.12. Both analyses returned values of -37‰ which agrees with petrographic study that there is a single fluid type (i.e., type 5 L_{H2O}-V inclusion) present in Qtz_2.

3.11.3 Sulfur Isotopes

Results of multiple S-isotope analysis for Py_1 and Py_2 are presented in Table 3.13. Both generations of pyrite returned similarly depleted $\delta^{34}S$ values (Py_1 $\delta^{34}S_{Avg.}$ = -5.5‰ ± 0.2‰; 1σ; n=3; Py_2 $\delta^{34}S_{Avg.}$ = -3.5‰ ± 0.3‰; 1σ; n=12) and $\delta^{33}S$ values (Py_1 $\delta^{33}S_{Avg.}$ = -3.2‰ ± 0.2‰; 1σ; n=3; Py_2 $\delta^{33}S_{Avg.}$ = -2.1‰ ± 0.3‰; 1σ; n=12), which are consistent with the values reported by Callan (1988) for pyrite from the Renabie underground mine ($\delta^{34}S_{Avg.}$ = -5.7‰ ± 0.9‰; 1σ; n=8). Calculated $\Delta^{33}S$ values for both Py_1 ($\Delta^{33}S_{Avg}$ = -0.4± 0.1; 1σ; n=3) and Py_2 ($\Delta^{33}S_{Avg}$ = -0.3± 0.2; 1σ; n=12) are near zero.

3.12 Discussion and Interpretation of Results

3.12.1 Hydrothermal Evolution of the District

Evidence for a Pre-Deformation, Pre-Metamorphic, Intrusion-Related Au Event: the Au_1 Event

Controversy regarding the hydrothermal fluid source in orogenic gold deposits is largely due to the timing of mineralization relative to the geologic evolution of districts: chronological overlap occurs between inferred ages for mineralization, host-rock metamorphism, and syn-metamorphic intrusions (e.g., Timmins-Val d'Or gold belt; Robert, 2005). Therefore, it is generally unclear as to whether fluids are magmatic or metamorphic in origin. The problem is further confounded by spatial relationships between orogenic deposits and intrusions, which have been interpreted to be either genetically (e.g., Cameron and Hattori, 1987) or structurally (e.g., Witt, 1992) significant.

The pre-regional deformation timing of the laminated quartz veins and their phyllic alteration halos (the "Au_1 event") precludes the involvement of a regional metamorphic fluid. The Au_1 event is overprinted by syn-prograde-metamorphic deformation (i.e., D1 and D2 of Chapter 2), as shown by relationships at the Boundary outcrop (Fig. 3.5G), and is thus a pre-regional-metamorphic event. Supporting mineralogical evidence occurs as overgrowths of Ep_2 (a component of the phyllic alteration zones) and chalcopyrite (a common sulphide within the laminated veins) by Ep_3 (a component of the prograde metamorphic mineral assemblage) (Fig. 3.5D, F).

Features of the Au_1, as described in more detail in Chapter 2, are similar to some of those noted in IRG deposits (cf., Hart, 2007). These similarities include: (1) the steeply dipping and locally sheeted nature of the quartz veins, which are preferentially intrusion-hosted and typically contain a low sulphide content (i.e., ≤5%); (2) a spatial association between the mineralized veins and pegmatite and aplite dikes; and (3) the presence of phyllic (quartz-sericite-pyrite) alteration zones (e.g., Sillitoe, 2010). Thus, due to the pre-deformation, pre-metamorphic timing of the Au_1 event and its similarities to aspects of IRG deposits, the Au_1 event is interpreted to be intrusion-related. It is also noted that the gold deposits with anomalous metal associations, which are commonly overprinted by regional deformation and metamorphism, are typically considered to be of magmatic affinity (i.e., porphyry-epithermal and VMS deposits; Groves *et al.,* 2003)

Although H_2O-CO_2 and CO_2 fluid inclusions within the laminated veins are considered to be of secondary and indeterminate origins, the presence of carbonate and CO_2 enrichment in the phyllic alteration zones defined by mass balance (Fig. 3.7) indicates the inclusions are reliable indicators of the P-T conditions of vein formation. The P-T conditions are constrained by petrographic observations indicating the coexistence of inclusion type 2 and 3 within individual FIAs (Fig. 3.13B, G). This observation suggests unmixing (i.e., immiscibility) of a parental H_2O-CO_2 fluid (type 1 inclusions) occurred to generate H_2O and CO_2 dominant endmembers, and that the solvus in the fluid system provides a constraint in P-T space (Fig. 3.14A).

Isochores for type 1 inclusions (Fig. 3.14A) are variable even within individual FIAs. This observation might be considered to result from necking (Bodnar, 2003b), however, the variability in density is instead attributed to changes in the density of the carbonic phase, since the relative proportions of H_2O and CO_2 are relatively constant within an FIA (e.g., Sterner and Bodnar, 1991), an example of this shown in Figure 3.13G. This indicates that the density variability is the result of transient pressure changes (i.e., changing from $P_{lithostatic}$ to $P_{hydrostatic}$), at which time the fluid density was modified, as opposed to subsolvus, post-entrapment necking, which would have modified the H_2O:CO_2 of the inclusions. The isochores record a pressure range of ~2 kbar if entrapment is assumed to have occurred at ~300º to 400 ˚C. If the intersection of the solvus is considered as a P-T constraint, then all inclusion assemblages are explained if the 2 kbar pressure change occurred between ~200º and 400˚C. Thus, the best estimate for vein formation is over ~1-3 kbar and ~200º-400˚ C. The range in P can be explained by pressure cycling from lithostatic to hydrostatic conditions via fluid overpressuring and hydraulic fracturing. The laminated texture of the veins is analogous to crack-seal textures (Ramsay, 1980), which is generally attributed to fluid overpressuring (e.g., Cox *et al*., 2001). In summary, the laminated veins formed from a parental H_2O-CO_2 fluid at ~3 kbar (~9 km crustal depth) and ~300-400˚C that underwent intermittent unmixing during transient changes in P from lithostatic to hydrostatic conditions. The estimated crustal depth of ~9 km is deeper than that at which most magmatic hydrothermal systems, such as porphyry deposits form (~1-6 km; Seedorf *et al*., 2005), but deeper systems have been noted (e.g., Butte porphyry Cu; Rusk *et al*., 2008). In addition, the depth of formation is similar to that of some IRG deposits (~5-7 km; Hart, 2007), and overlaps with the indicated depth of emplacement for granitic to granodioritic plutons in the Abitibi greenstone belt (~6-12 km; Ayer *et al*., 2010).

If it is assumed that the parental fluid is magmatic in origin, and existed at ~3 kbar and ~300-400˚C, it must have cooled subsequent to its exsolution from a wet tonalite (Fig. 3.17), which represents the dominant intrusive type in the district. Isochores from type 1 inclusions do not

intersect the wet tonalite solidus until a minimum pressure of ~6 kbar (~18 km crustal depth), hence cooling of the fluid from ~700-400 ˚C subsequent to its exsolution at a lower pressure is the more likely scenario for fluid evolution.

Fragments of saussuritized plagioclase within the laminated quartz veins, the presence of phyllic alteration overprinting these clasts (Fig. 3.5B), and the regional presence of saussuritization together suggest saussuritization predates the Au_1 event. Overgrowths of Ep_1 by Ep_3 (Fig. 3.5A) also suggest that saussuritization is an early hydrothermal event that occurred prior to regional metamorphism. Thus, this alteration is likely the product of the ingress of an early, higher temperature, orthomagmatic or deuteric fluid that is related to the same hydrothermal event responsible for the Au_1 event. It is not clear if this early hydrothermal activity is associated with the emplacement of the Missinaibi Lake batholith or, alternatively, related to younger intrusions, such as those of the ca. 2.68-2.66 Ga suite.

Retrograde Alterations and Late-Stage Au Mineralization: Products of Orogenic-Type Hydrothermal Activity?

Many features of the Retrograde event (hematite-associated alteration veins and the retrograde alteration types) are similar to those reported in orogenic gold deposits (cf., Hagemann and Cassidy, 2000; Robert and Poulsen, 2001; Goldfarb *et al*, 2005). Similarities include: (1) the localization of veins and alteration within brittle-ductile structures (e.g., Renabie trend shear zones); (2) a late-syn-tectonic timing (i.e., syn-D3); (3) a post-peak-metamorphic timing (Fig. 3.5H, K); and (4) the presence of albitization (Fig. 3.5J).

The age of titanite in the retrograde type 1 alteration zone (2549 ± 24 Ma) is significantly younger than the youngest Archean intrusion in the district, the 2611 ± 11 Ma Ruby Lake stock (Turek *et al*., 1996). The age is also older than the dominant Proterozoic intrusions in the area (2454 ± 2 Ma Matachewan dikes; Halls and Palmer, 1990). Furthermore, the age is younger than metamorphic events in the Wawa gneiss domain (~2.67-2.64 Ga, Corfu, 1987; ~2.69 Ga, Sullivan

and Leclair, 1992), but it does have an upper error limit slightly younger (~7 Ma) than lower limit of the Floranna interval of Moser (1994) (2637 – 2580 Ma), which represents a period of ductile deformation in the Kapuskasing structural zone. The young age also overlaps younger ages recorded for hydrothermal minerals (i.e., biotite, sericite, titanite, and rutile) in Au deposits and major structures (e.g., the Larder Lake-Cadillac fault) in the southern Superior province (Kerrich and Cassidy, 1994). These younger ages are interpreted to reflect resetting due to later thermal disturbances related to uplift of the Kapuskasing structural zone and emplacement of Proterozoic dikes (Kerrich and Cassidy, 1994). In consideration of the potential for resetting of titanite, it is noted that this phase is considered robust to complete Pb loss up to 750˚C and has been reported to provide pre-metamorphic dates despite its subjection to later, ultrahigh-pressure, subduction-type metamorphism (Spencer *et al*., 2013). Also relevant is that the titanite analyzed in this study showed no evidence of hydrothermal disturbance as would be evident in SEM images (Fig. 3.8B). In consideration of the evidence, the age of 2549 ± 24 Ma is interpreted as the time of titanite crystallization.

The retrograding nature of the alteration, and its late timing relative to local magmatism and metamorphic events in the Wawa gneiss domain, indicates the fluids were not generated from local magmatism or metamorphism. The transition from the Michipicoten greenstone belt across the Wawa gneiss domain into the Kapuskasing structural zone is considered to represent an oblique-crustal cross section, with the Kapuskasing structural zone representing the deep-crustal equivalent of the Michipicoten greenstone belt (Percival and Card, 1985; Moser, 1994). Age constraints on deformation and metamorphism in the Wawa subprovince document a general younging trend from the greenstone belts, through the Wawa gneiss domain, and into the Kapuskasing structural zone (Corfu, 1987; Moser, 1994) displaying, therefore, the characteristic "deep-later" style of metamorphism that is common in gold districts (Goldfarb *et al*., 2005). The characteristics and timing of the Retrograde event are compatible with a situation wherein

hydrothermal fluids were sourced from a distal, prograding, deep-crustal environment and channeled into a shallower crustal environment at lower P-T conditions (i.e., the Missanabie-Renabie gold district). Such a model has been previously suggested by Jemielita *et al*. (1990) to explain the young ages of hydrothermal minerals relative to magmatic and metamorphic events in the Abitibi subprovince (i.e., ~50 Ma age difference). Primary fluid inclusions (type 5) from the breccia vein at Nudulama East provide P-T constraints on the Retrograde event. Applying a minimum entrapment temperature of 300 ˚C to the representative iso-Th lines (Fig. 3.14B), which is based on the brittle-ductile nature of D3 shear zones during the event, infers either a range in pressures during fluid entrapment (i.e., ~3.5-5.5 kbar at 300˚C) or temperature fluctuations (i.e., ~300º-450˚C at 5 kbar), or a combination thereof. In either case these constraints imply the Retrograde event occurred at a higher P than the Au_1 event (Fig. 3.17). These P-T conditions are also consistent with the retrograding nature of alteration (i.e., chlorite after biotite and horneblende; Fig. 3.5H, I), and imply a causative fluid derived from a deeper crustal level.

The Py_2 veins reflect a hydrothermal event (the "Au_2 event") distinct from the Retrograde event, as exemplified by (see Chapter 2): (1) pyrite-hematite stability relationships; (2) a change in preferred vein orientation from the NE (hematite-associated veins) to NW (Py_2 veins); and (3) difference in timing relative to deformation events (syn-D3 for the Retrograde event versus syn- or post-D4 for Py_2 veins).

The presence of late-stage Au mineralization in discrete fractures has sometimes been attributed to the remobilization of an earlier gold event (e.g., Red Lake Mine; Dubé *et al*., 2004). In a comparative sense, the Py_2 veins differ from examples of remobilized gold. These difference include: (1) the absence of free gold or Au alloys (Au occurs as an invisible variety in Py_2) (cf., Perring and McNaughton, 1990; Mumin *et al*., 1994; Larocque *et al*., 1995; Dubé *et al*., 2004); (2) a lack of Au grade increase Py_2 veins relative to Au_1 bearing samples, which contain the highest Au concentrations (Fig. 3.9; cf., Dubé *et al*., 2004); (3) a lack of base metal-bearing sulfides

(which are likely to be remobilized along with Au) in Py_2 veins (cf. Perring and McNaughton, 1990; Larocque *et al*., 1995), particularly as chalcopyrite, molybdenite, galena, and sphalerite are present in the laminated veins; and (4) where remobilization has been suggested, it is often connected to peak thermal episodes related to either magmatism (Dubé *et al*., 2004) or metamorphism (Perring and McNaughton, 1990; Mumin *et al*., 1994), and in the case of metamorphic remobilization, Au mobility is thought to increase correspondingly with metamorphic grade (Mumin *et al*., 1994). The post-Retrograde event timing of the Au_2 event indicates that the Py_2 veins did not form during peak-thermal metamorphic conditions.

Considering the differences noted above, a case for Au_2 representing remobilization of Au_1 is not convincing. In concert, the S-isotope data suggests that the sulfur in Py_2 was not sourced from Py_1 during the Retrograde event. If this were the case it is likely that $\delta^{34}S$ and $\delta^{33}S$ values in Py_2 would be significantly depleted relative to Py_1 due to the oxidized (i.e., hematite-stable) nature of the Retrograde event, during which sulphates formed in alteration zones (e.g., Ohmoto and Rye, 1979). This also indicates any metals liberated from Py_1 during the Retrograde event were not subsequently deposited in the Py_2 veins. It is therefore suggested that Au_2 may be a new addition to the ore zones as opposed to remobilized Au_1, and is potentially an excellent example of a paragenetically late Au mineralization event, as is often the timing indicated for Au deposition in orogenic deposits (McCuaig and Kerrich, 1998; Goldfarb, 2005).

3.12.2 A Discriminatory-Geochemical Approach to the Mineralization and Alteration Events

Based on constraints provided in Chapter 2 and those presented herein, the Au_1 event is considered to be an IRG event that pre-dated regional metamorphism and deformation. In contrast, the Retrograde event is orogenic in nature due to its late-syn-deformational, post-peak-metamorphic timing and the young ages of alteration minerals (i.e., titanite) relative to local magmatism. An orogenic nature is also suggested by the high P of formation indicated by fluid inclusions, as 5 kbar of lithostatic pressure (~15 km crustal depth) is more consistent with an

orogenic as opposed to an intrusion-related event. Similarly, the quartz tension gashes (Qtz_3) and gold-bearing Py_2 veins likely reflect orogenic events due to their late, post-Retrograde-event timing. As depicted in Figure 3.18, although the various events occur at different times and reflect different ore forming processes, they overlap spatially and form composite ore zones. The presence of co-spatial intrusion-related and orogenic mineralization presents an opportunity that is ideal to assess the viability of using geochemistry to discriminate between the different styles of mineralization. The salient results of the methods in this approach are presented in Table 3.14, and discussed further in the following section.

Integration of Alteration Mineralogy, Lithogeochemistry, Mass Balance and Fluid Inclusion Chemistry

This section discusses the results of mass balance in the context of alteration mineralogy and fluid inclusion chemistry in order to constrain the chemical constituents of the fluids responsible ("causative fluids") for the Au_1 and Retrograde events. This approach aids in constraining mobile elements as having either a local (i.e., liberated during wall rock alteration) or foreign (i.e., added during fluid ingress) source.

Potassium, Ba, and Rb enrichment in the phyllic alteration zone is expressed mineralogically as sericite. Depletions in Ca and Na reflects the destruction of saussuritized plagioclase (epidote and An_{20} plagioclase) that occurred during sericite formation. In the retrograde type 1 alteration zone, saussuritized plagioclase is further altered to albite and residual An_{20} plagioclase, which is represented chemically by Ca depletion (destruction of epidote in the plagioclase) and an increase in Na (formation of albite). In contrast to the phyllic alteration zone, K, Ba, and Rb are depleted: this is likely due to loss of the LILEs during chloritization of biotite. The enrichment of K, Ba, and Rb in the retrograde type 2 alteration zone reflects the sequestration of the LILEs in K-feldspar. The Na and Ca depletion in this zone is due to the destruction of intergrown Ab and An_{20} plagioclase from the retrograde type 1 alteration assemblage.

Residual retrograde type 1 mineralogy in retrograde type 2 alteration zones, the spatial relationship of the two alteration types to one another (i.e., vein proximal and vein distal), and the mass loss within retrograde type 2 alteration zones indicated by mass balance and textural evidence (i.e., fabric dissolution and abundant pore space), suggests that the two alteration types occur as part of the same hydrothermal event, but differ due to fluid-rock ratio and relative timing. If retrograde alteration types 1 and 2 are interpreted as a continuous process, then the K, Ba, and Rb from lost from the type 1 alteration zone can be reconstituted into the type 2 alteration zone. Although the magnitudes of K, Ba, and Rb loss in type 1 alteration are lesser (~1 order of magnitude) than their gains in type 2 alteration, the latter zones are much smaller than the type 1 alteration zones that surround them, thus this explanation is plausible. Importantly, if these mass balance constraints are integrated, then for the elements thus far discussed (i.e., Ca, Na, LILEs) the fluid responsible for the Retrograde event only contained externally sourced Na.

Gains and losses of Ca, Na, and LILEs interpreted in the context of fluid inclusion chemistry, from microthermometry and SEM-EDS mound analysis, provides further insight: deviations from Na-rich to Ca-rich endmembers, with varying amounts of K (Fig. 3.15D), likely reflects variable amounts of fluid-rock interaction between a "primitive" H_2O-NaCl fluid (~5-10 wt. % NaCl) and a protolith consisting of saussuritized tonalite. Deviations to a Ca-rich endmember, with increases in K, can be explained by the liberation of Ca and K during the dissolution of epidote in saussuritized plagioclase and the chloritization of biotite.

The main Fe-bearing phase in the saussuritized tonalite protolith is biotite (~10-15 vol.%, ~12 wt.% Fe). If the volume percentage of pyrite within phyllic alteration zones (~2-5 %) is considered in the context of available Fe from biotite, ~2 vol.% pyrite can be explained by 15 vol.% biotite (if a density of 3.00 g/cc is assumed for biotite); thus, the results are in general agreement with a local source for Fe, but in order to explain higher concentrations of pyrite, external Fe may be necessary. The low relative changes of total Fe in the retrograde type 1 and 2

alteration zones suggests that Fe within Fe-bearing phases (i.e., chlorite, hematite) was locally sourced.

Changes in the redox state of Fe occur in all three alteration zones. In the phyllic alteration zone Fe2O3p increase may partially correspond to the liberation of Fe^{2+} from biotite during the formation of sericite, and its subsequent oxidation and sequestration in Fe^{3+} bearing (?) Ep_2, but Ep_2 accounts for a low proportion of the total mineralogy. The increase is most likely reflective of hematite-replacement rims on Py_1, which are presumably related to the later Retrograde event. A decrease of Fe_2O_3p in the retrograde type 1 alteration zone is largely counterintuitive due to the presence of hematite. This may be explained if the dominant Fe source during the alteration were Fe^{3+}-bearing (?) minerals of the saussuritized tonalite protolith (i.e., Ep_1) and prograde metamorphic assemblage (i.e., Ep_3 and horneblende), which provided the excess Fe necessary for the chloritization of biotite (~16 wt.% Fe in chlorite versus ~12 wt.% Fe in biotite). This explanation presents an issue in terms of the redox state of the altering fluid, which the presence of hematite shows was oxidized and thus unable to reduce liberated Fe to form chlorite. This is likely an indication that the retrograde type 1 alteration occurred in two stages: (1) an early reduced stage during which pyrite was able to form, and liberated Fe^{3+} was able to be reduced and sequestered in chlorite; and (2) a later oxidized stage during which hematite was stable. This would explain the presence of low concentrations of hematite-altered pyrite in the retrograde alteration zones. Considered in the context of the change in oxidation state of Fe in the retrograde type 2 alteration—a later progression of the retrograde type 1 alteration— Fe_2O_3p shows a relative increase of ~48% compared to the retrograde type 1 alteration, which is supportive of this interpretation. The presence of pyrite and the significant S increases defined by mass balance in both types of retrograde alteration zones indicates that S was added during the alteration.

A major difference between the phyllic and retrograde alteration zones is the addition of CO_2 and metals (Au, Ag, Cu, Bi, Pb, Te, W) in the former. The addition of these elements is

expressed by the presence of carbonate, sulfides, and alloys; these phases (with the exception of pyrite) are lacking from the retrograde alteration zones. The significant relative changes in metal concentrations within the retrograde alteration zones defined by mass balance likely lack significance as the absolute changes are typically <1 ppm, and locally approach the lower detection limits.

A summation of the geochemical characteristics of the fluids responsible for the Au_1 and Retrograde events follows: (1) the Au_1 event relates to an H_2O-CO_2 (X_{CO2}~0.15) fluid carrying metals (Au, Ag, Cu, Bi, Pb, Te, W, Mo, Zn), S, and LILE's (Ba, K, Rb); the salinity of fluid inclusions (3.7-8.0 wt.% eq. NaCl) may reflect Na depletion during dissolution of the saussuritized tonalite protolith; and (2) the Retrograde event occurred due to an early, reduced (i.e., pyrite stable), H_2O-Na-S-bearing fluid, which became enriched in Ca and K due to fluid-rock interaction, and subsequently became oxidized to the point where hematite was stabilized. Although mass balance suggests these two events show similarities in terms of mobile elements (i.e., S, Ca, Na, LILEs), marked differences are evident when the geochemical data is coupled with petrographic and field observations, and interpreted in the context of alteration mineralogy and fluid inclusion chemistry. Thus, in a discriminatory sense this integrated approach reveals that the chemical constituents of the "causative fluids" responsible for the Au_1 and Retrograde events differed significantly.

$\delta^{18}O$ Values in Vein Quartz

The $\delta^{18}O$ values for Qtz_1, Qtz_2, and, Qtz_3 do not define distinct populations but instead overlap (Fig. 3.19A). When compared to $\delta^{18}O$ data for vein quartz from other Archean lode Au deposits, they are consistently lower. It follows that if Qtz_2, for example, is considered to have formed in equilibrium with a fluid at ~300-400˚C, the calculated $\delta^{18}O_{H2O}$ of ~-5‰ to 5‰ is considerably lighter than the range of 6-11‰ for Archean and Proterozoic lode gold deposits (Fig. 3.19A; McCuaig and Kerrich, 1998). The calculated $\delta^{18}O_{H2O}$ values primarily overlap with the

fields of formational and metamorphic waters (Taylor, 1974), as opposed to metamorphic and magmatic waters (Taylor, 1974; Sheppard, 1977), where $\delta^{18}O_{H2O}$ values from lode Au deposits commonly lie. The isotopically light nature of $\delta^{18}O$ values in vein quartz, and the constraints provided by δD values, is further discussed in *Section 3.12.3*.

S-Isotope Values in Py_1 and Py_2

Mass-dependent fractionation of S isotopes in hydrothermal systems is strongly influenced by factors such as T, fO_2, and pH (e.g., Ohmoto and Rye, 1979; Seal, 2006); thus, the intensive properties of fluids can significantly modify the $\delta^{34}S$ and $\delta^{33}S$ values recorded in sulfides from those characteristic a source reservoir. The recognition of mass-independent fractionation (MIF) of S isotopes has provided a means to assess whether sulfur is isotopically characteristic of a primitive mantle sulfur ($\Delta^{33}S = \sim 0$ ‰) or indicative of sulfur exposed to an Archean surficial environment (Farquhar and Wing, 2003).The $\Delta^{33}S$ calculated for Py_1 and Py_2 are, in the context of all errors, indicative of sulfur that has not undergone MIF and consistent with primitive mantle sulfur. Therefore, the slightly depleted $\delta^{34}S$ and $\delta^{33}S$ values are attributed to slightly oxidizing conditions of the fluid, which may have approached the pyrite-magnetite redox buffer (Ohmoto and Rye, 1979). As the S isotopic data are comparable in both generations of pyrite, it is suggested that the S in each Au event was sourced from a primitive S-bearing reservoir.

Similar near-zero $\Delta^{33}S$ values obtained from pyrites in other Archean gold deposits have been used to preclude involvement of supracrustal units as a significant sulfur contributor and also to support a magmatic origin (Xue *et al*., 2013). The late timing of the Py_2 veins indicates that they are not of magmatic affinity, thus illustrating that near-zero $\Delta^{33}S$ values appear to be equivocal in defining a link to a magmatic source for mineralization, but this does not negate the remobilization of sulfur from earlier magmatic sulfides.

Elemental Associations of the Au Events: Evidence from Whole Rock Geochemistry and LA-ICP-MS Mapping

The trace element associations with Au, as defined spatially by LA-ICP-MS mapping, that are not present as correlations in $\log_{10}$ data (e.g., Au_2-U-W-Pb; Fig. 3.11) exemplify how correlation-defined and spatially-defined elemental associations may be decoupled. It is noted that the lack of correlation between Au_2, W, and U is in part confounded by these elements having concentrations close to their lower detection limits; however, the absence of correlation between Au_2 and Pb in both LA-ICP-MS (Fig. 3.11) and whole rock data (Fig. 3.9) emphasizes this point. Thus, care must be taken in how elemental associations are defined, that is, by spatial association or statistically. As elemental correlations are often used as evidence for such elements being simultaneously enriched or depleted as part of a common process (i.e., magmatic fractionation, Cox and Clifford, 1982; hydrothermal precipitation, Ispolatov *et al*., 2008), a lack of correlation may indicate a decoupling of the enriched elements. Thus, in a manner similar to the spatial Au_2-U-W-Pb association, the presence of chalcopyrite and molybenite in Au_1 veins but a lack of Au_1-Cu-Mo correlation (Fig. 3.9) may indicate disparity in the timing of precious and base metal deposition due to variable fluid chemistry.

A successful approach using correlation coefficients to discriminate samples from Au_1 and Au_2 is shown in Figure 3.12A. This suggests that linear relationships in $\log_{10}$ trace element data have the potential to geochemically fingerprint Au events, particularly as the data used to discriminate is sourced from different analytical techniques (i.e., whole rock and LA-ICP-MS analysis). This is also emphasized using the parameters $\Delta C_{x\text{-}Au}$ and $\sum\Delta C$ (correlation based) and $X_{Au=1}$, $X_{Au=100}$, and ΔX_{Au} (regression based). Calculated $\sum\Delta C$ between sample populations of the same Au event are smaller (i.e., <1) than when calculated for sample populations of different gold events (i.e., Au_1 versus Au_2) (Fig. 3.12A): this reflects the general consistency in correlation coefficients values in different sample populations of the same Au event (the magnitude of $\sum\Delta C$

values are obviously influenced by the number of correlation coefficients utilized in the calculation, and thus are not significance in an isolated context). When $X_{Au=1}$, $X_{Au=100}$, and ΔX_{Au} are considered as discriminatory parameters, it becomes evident that ΔX_{Au} is the more useful in separating the different sample populations (Au_1 versus Au_2 samples) (Fig. 3.12B). This indicates that regression-defined elemental concentrations at specific values of Au (e.g., $X_{Au=1}$, $X_{Au=100}$) may be less characteristic of an event than the relative change in elemental concentration between two regression defined points at specific values of Au (ΔX_{Au}).

Geochemical Discrimination: Summary Points

From the above discussion the following aspects of geochemical discrimination are noted: (1) lithogeochemistry and mass balance must be considered in the context of other critical information such as field relationships, alteration/protolith mineralogy, and fluid inclusion chemistry. Only afterward can this data be interpreted to provide a likely geochemical signature for a "causative fluid", which may differ from that indicated by isolated mass balance study, for example; (2) the results of O- and S-isotope analysis are shown to essentially be non-discriminatory. Furthermore, S isotopes display primitive S values characteristic of a mantle and/or magmatic source for both the intrusion-related and orogenic events; and (3) trace element associations defined by linear relationships with Au in $\log_{10}$ data can discriminate between different Au events.

3.12.3 Origin of Depleted $\delta^{18}O$ Vein Quartz Values: Insights from δD

Vein quartz with $\delta^{18}O$ values similar to those encountered in this study are known from porphyry settings, such as the Endako deposit (i.e., ~5.2 ‰) where, together with other O and D isotopic data, were used to infer a mixture of meteoric and magmatic fluids (Selby *et al*., 2000). Although models which invoke deeply circulating meteoric waters in the formation orogenic Au deposits have been proposed (e.g., Nesbitt *et al*., 1986; Nesbitt, 1990), they are largely based on the presence of depleted δD values in fluid inclusion extracts from the vein quartz, as opposed to

primary vein phases (e.g., muscovite), and therefore such results are viewed with caution (e.g., Goldfarb et al. 2015). Instead, such depleted δD values have been attributed to the presence of later secondary fluid inclusions that are not representative of the vein-forming fluid (Kyser and Kerrich, 1990). Also discussed by the latter are numerous mechanistic issues in transporting surficial fluids into the mesozonal, compressional environment where orogenic deposits form. Thus, surficial waters are typically not thought to be a significant contributor to the fluid budget of orogenic gold systems.

Samples of Qtz_2 from the breccia vein at Nudulama East were used to constrain the nature and origin of the depleted $\delta^{18}O$ quartz values for the following reasons: (1) this quartz returned the lowest $\delta^{18}O$ values (minimum value of 1.2‰); (2) P-T conditions constrained by fluid inclusions indicate quartz formation under significant lithostatic pressure (i.e., ~5 kbar or 15 km depth), which is typical of orogenic gold systems; and (3) type 5 fluid inclusions are present as primary FIAs, which indicates the δD values from inclusion extracts are representative of the vein forming fluid.

Assessment of a fluid-mixing model to explain the range of $\delta^{18}O$ values in Qtz_2 illustrates that the values could be explained by mixing a $\delta^{18}O$ = 10‰ fluid with a $\delta^{18}O$ = -15‰ fluid (a high-latitude meteoric water; Taylor, 1974) over a temperature range of 200°-500˚C (Fig. 3.19B). In this model, large proportions of the latter fluid would be required (~30-50% depending on temperature). Similarly, the range in $\delta^{18}O$ values obtained from the detailed SIMS traverse of Qtz_2 (5.9 to 12.5‰; Fig. 3.13G) can be accounted for by this same model over a temperature range from ~200° to 400˚C, with the lower core values representing precipitation from a higher temperature fluid and the higher rim values a cooler fluid. However, δD values of -37 ‰ (Table 3.12) preclude the involvement of a high-latitude meteoric fluid, which in the necessary proportions would produce δD values of ~ -55 to -70 ‰, as a $\delta^{18}O$ = -15‰ meteoric fluid would have corresponding

δD values of ~ -100 ‰ (Taylor, 1974). We conclude therefore that involvement of surficial fluids to explain the depleted $\delta^{18}O$ quartz values is not supported.

In consideration of other means by which the $\delta^{18}O$ values of a fluid may be modified, mineralogical changes during hydrothermal alteration (e.g., destruction of feldspars, chloritization of biotite) present a way by which this modification can occur, but the relative proportion of reactive O in an aqueous fluid (~89 g O per 100 g fluid), compared to a tonalite protolith (~36 g O per 100 g) requires that low fluid-rock ratios would be necessary to produce a significant shift. The formation of chlorite is unlikely to significantly modify $\delta^{18}O$ fluid values, as $\delta^{18}O$ fractionation between chlorite and H_2O from 300° to 400˚C is minimal (i.e., ~0 to -2‰; Wenner and Taylor, 1971). Further constraints are provided by whole rock and mineral $\delta^{18}O$ values reported by Li *et al*. (1990), wherein they document $\delta^{18}O$ values ranging from 6.4-9.5‰ from whole rock analyses of tonalitic and granodioritic lithologies in the Wawa gneiss domain, and values of ~9 to 11‰ for quartz, ~6 to 8‰ for feldspars, and ~2 to 5‰ for biotite in selected granitic samples. Based on these values, dissolution of protolith mineralogy would not be able to account for the required $\delta^{18}O$ fluid values necessary to explain the range in $\delta^{18}O$ values of Qtz_2.

Given the positive $\delta^{18}O$ fractionation between vein quartz and H_2O over the 200° to 500˚C temperature range (Taylor, 1979), there is the potential to significantly deplete the $\delta^{18}O$ value of vein forming fluid in the case of a closed system. This process, known as distillation or Rayleigh fractionation, provides a means by which excursions to low $\delta^{18}O$ fluid values and thereby also $\delta^{18}O$ quartz values may be explained (Kontak *et al*., 2016; Neyedley *et al*., 2016).

For example, for a fluid with an initial $\delta^{18}O = 10‰$ that precipitates quartz in a closed system the $\delta^{18}O$ values of Qtz_2 can be explained using a temperature range of 200° to 400˚C (Fig. 3.19C). Thus, the closed-system approach to vein formation provides an explanation by which the mixing of isotopically distinct fluids is unnecessary to explain the depleted $\delta^{18}O$ values in Qtz_2. Although the range in $\delta^{18}O$ values in each of the quartz population illustrates that temperature

and/or the isotopic composition of the precipitating fluids was variable during the different veining events (Fig. 3.19A), the range of ~7‰ recorded by the detailed SIMS traverse (Fig. 3.13G) illustrates that this $\delta^{18}O$ variability occurs at the scale of individual quartz crystals. Significantly different $\delta^{18}O$ values (e.g., 5.4 versus 9.4‰) within ~20 μm of one another, in quartz-growth zones that display a continuous CL response (i.e., not evidently different generations), indicate that temperature fluctuation was not the sole cause of the range in $\delta^{18}O$ values. The large ranges and high degree of variability in $\delta^{18}O$ values recorded down to the scale of an individual crystal are considered as further evidence indicating closed-system behavior during vein formation.

3.12.4 Genetic and Discriminatory Implications for Gold Systems; Fluid Sources in Orogenic Deposits

Although the Au_1 event shares similarities with orogenic and IRG deposits (e.g., laminated veins, H_2O-CO_2 fluid inclusions), its pre-deformation, pre-metamorphic timing is a feature atypical of both, and more characteristic of Au deposits with anomalous metal associations, which are often considered to be of magmatic affinity (Groves *et al*., 2003). This being said, however, there are no metal associations that would be considered unusual (e.g., Hg, Sb, Ba), and base metals are present in concentrations below those of economic interest (Appendix 3.1). Therefore, as distinguishing IRG and orogenic deposits is often further complicated by their similar timing of emplacement (i.e., post-peak-metamorphism, late-stage deformational), the Missanabie-Renabie district provides an example of intrusion-related and orogenic hydrothermal events that largely overlap in their geochemical characteristics, but are emplaced over a temporal lag (defined by metamorphism and deformation) that allows them to be clearly distinguished. Thus, the geochemical overlap between IRG and orogenic deposits clearly does not reflect a genetic link, or necessitate a magmatic contribution to orogenic deposits.

As has often been emphasized, it is generally difficult to use geochemical parameters to discriminate the main gold deposit types (e.g., Groves et al., 2003; Goldfarb et al., 2005; Goldfarb

and Groves, 2015). In fact, the IRG deposit model, as presented by Hart (2007) for example, is primarily based on field observations rather than geochemical data. In this context, the following points from the discriminatory-geochemical approach in the Missanabie-Renabie district are noted: (1) intrusion-related (i.e., Au_1 event) and orogenic (i.e., Retrograde and Au_2 events) hydrothermal events are only discriminated through the integration of field observations with petrographic studies, inferred P-T conditions, and geochronology; (2) defining geochemical distinction was done after sample affinity was determined and relied on an integrated approach to defining fluid chemistry, and Au-trace element associations in $\log_{10}$ trace element data; and (3) stable isotope data is non-discriminatory, with S-isotopes indicating involvement of primitive S in both Au events and $\delta^{18}O$ values in vein quartz showing large variability and significant overlap. The latter may be specific to veins containing minerals with high mineral-fluid fractionation factors, and in part may reflect the scale of the analysis used in this study (i.e., SIMS). As noted by Kontak et al. (2016), where a similar approach has been used in other studies, a large variation in $\delta^{18}O$ has been noted. The ranges in $\delta^{18}O$ values within vein populations herein documented (i.e., ~5-10‰) are similar to those reported in compilation studies, which show that $\delta^{18}O$ values can vary significantly within individual districts (e.g., Beaudoin, 2011). The results of this study show that this variation occurs at the scale of individual quartz crystals (Fig. 3.16D). Evidence for closed-system behavior during vein formation, such as high variability on the micro-scale and extremely depleted $\delta^{18}O$ values, indicates veins that have precipitated minerals with high mineral-fluid fractionation factors (quartz ± carbonate ± alkali feldspar) may not provide $\delta^{18}O$ values representative of fluid source. Similarly, these values may not be able to discriminate between different hydrothermal events, as it the case for this study.

Overall these results emphasize how the geochemical signatures of hydrothermal events are equivocal in defining a link to mineralization type (i.e., intrusion related and orogenic). This is shown by the overlapping stable isotope data, similar Au-trace element signatures, and also by the

main geochemical differences such a fluid chemistry, as these differences are equally as ambiguous as the overlapping data. This is best exemplified by the presence of H_2O-CO_2 inclusions in the intrusion-related Au_1 veins as opposed to the orogenic Retrograde event veins; this low salinity, H_2O-CO_2 fluid inclusion type has been considered a defining feature of orogenic gold deposits (e.g., Ridley and Diamond, 2000). In light of the inability of geochemistry to act as a discriminator, it becomes evident that constraints provided from detailed- to regional-scale geological field mapping act as the backbone for discrimination, and are here supported by P-T constraints from fluid inclusion studies and U-Pb titanite geochronology.

Insight into potential fluid sources for orogenic Au deposits is provided by the alteration characteristics and late timing of the Retrograde event: the main critique of the late-gold models, such as those presented by Jemilita *et al*. (1990), is that the young ages of mineralization indicated by hydrothermal minerals do not correspond to alteration assemblages that are disparate to the metamorphic facies of their host rocks (i.e., greenschist facies alteration assemblages are typical of greenschist facies host rocks etc.; Kerrich and Cassidy, 1994). The similarities in the metamorphic facies of alteration minerals and wall rock minerals is a feature explained in the continuum model (Groves et al., 1993), and whereas it is noted that deposits tend to form while on their retrograde P-T paths, the relationships between the metamorphic grade of host rocks, alteration and sulphide assemblages, and structural features are used as an indication that mineralization is broadly contemporaneous with the peak-metamorphic conditions of the host terrane (Groves et al., 1993; Goldfarb et al., 2005). The 2549 ± 24 Ma age of the titanite, compared to local magmatic and metamorphic events, coupled with the retrograding nature of the alteration, presents a situation wherein a plausible explanation is that the event reflects the focusing of deep crustal fluids at a time significantly younger than that at which host-rock metamorphism occurred (in a manner akin to that discussed by Jemilita *et al*., (1990)). Furthermore, the brittle-ductile deformation characteristics displayed by shear zones during the Retrograde event, and subsequent transition

from oblique slip to strike slip (Chapter 2), are characteristics common to shear zones in orogenic gold deposits (Robert and Poulsen, 2001), an indication that this type of late-stage fluid activity may not be limited to the Missanabie-Renabie gold district.

3.12.5 Significance of Results for Mineral Exploration

The pre-deformation timing of the Au_1 event has resulted in a situation where ductile structures preferentially localized around the early mineralized zones and focused subsequent hydrothermal events (Chapter 2). In this sense, the retrograde alterations are able to act as useful exploration vectors to mineralization, particularly due to their well-developed expression at the outcrop and hand-sample scale, as they may demarcate areas that contain mineralization related to the Au_1 event. Thus, it is exemplified that although later hydrothermal events may not be metal endowed, they may be preferentially localized in mineralized structures and able to be used as exploration vectors.

Although the distinct mineralogy and chemistry of the Missinaibi Lake batholith at its contact with the Michipicoten greenstone belt has been previously interpreted as a petrogenetically distinct “throndhjemite” phase (Callan and Spooner 1987, 1998; Jemielita *et al*., 1988), the mineralogical similarities it shares with the retrograde alteration zones (i.e., chlorite and hematite bearing) is an indication that it may reflect post-peak metamorphic fluid flow localized to the contact zone. This could also explain the higher documented Na content relative to tonalitic portions of the Missinaibi Lake batholith (i.e., Na is enriched metasomatically as opposed to petrologically) (Jemiellta *et al*., 1988). In this context, the contact zone remains a prospective target for future exploration efforts as it may have acted as a long-lived fluid corridor, particularly as the main Renabie ore body occurs in its vicinity.

3.13 Conclusion

A discriminatory-geochemical approach to intrusion-related (the Au_1 event) and orogenic (the Retrograde and Au_2 events) veining, alteration, and gold mineralization, constrained relative to the deformation history of the Missanabie-Renabie gold district, emphasizes the equivocal nature of geochemical data in defining a link to different types of mineralization. Stable isotope data ($\delta^{18}O$ values in vein quartz and $\delta^{34}S$, $\delta^{33}S$, $\Delta^{33}S$ values in pyrites) largely overlaps and is non-discriminatory. Gold-trace element associations (Ag-Bi-Te±Pb±W±U) in whole rock and LA-ICP-MS geochemical data are similar in mineralized samples of both the Au_1 and Au_2 events, but a comparative approach to correlation coefficients and correlation- and regression-based parameters reveals differences. An integrated approach to defining the chemistry of the "causative fluids" responsible for the Au_1 and Retrograde events illustrates that they differed significantly in their compositions (H_2O-CO_2-Au-Ag-Cu-Bi-Pb-Te-W-Mo-Zn-S-LILE-bearing versus H_2O-Na-S-bearing, respectively). The geochemical differences are as ambiguous as the overlapping data in defining a link to mineralization type. This is best emphasized by the presence of H_2O-CO_2 inclusions in intrusion-related as opposed to orogenic veins. Geological field mapping provides the backbone necessary for discrimination, and is here supported by P-T constraints from fluid inclusions and U-Pb titanite geochronology.

The majority of $\delta^{18}O$ values in vein quartz are depleted in comparison to other lode gold deposits. We interpret these depleted values to reflect closed-system behavior during vein formation as opposed to the incursion of meteoric waters. From a discriminatory standpoint this apparent display of close-system behavior is significant, as it suggests $\delta^{18}O$ values from minerals in quartz ± carbonate ± alkali feldspar veins may be unlikely to discriminate between different hydrothermal events and provide information relating to fluid source. Near-zero $\Delta^{33}S$ values in pyrites of both the Au_1 and Au_2 events illustrate that although sulfur isotopically characteristic of primitive mantle sulfur is used to form pyrite in each event, near-zero $\Delta^{33}S$ values appear to be

equivocal in constraining mineralization as intrusion-related, as the pyrite veins that comprise the Au_2 event post-date the ca. 2.55 Ga retrograde event, which formed subsequent to the cessation of magmatism in the district.

The "young" age of the retrograde event relative to local magmatism and metamorphism, coupled with its retrograding nature, indicates that the event, and the later Au_2 event, reflect the focusing of distally sourced fluids, potentially generated in a deep-crustal environment analogous to the Kapuskasing structural zone. The similarity in the age of the retrograde event to the young ages of hydrothermal minerals from gold deposits in the Abitibi subprovince gives credibility to late gold models, wherein gold mineralization significantly post-dates local magmatism and metamorphism.

Although the retrograde event did not result in economic mineralization, hematite-bearing alteration that formed during the event provides an exploration vector: the alteration is often localized in structures containing pre-existing gold mineralization. This emphasizes the commonly punctuated nature of fluid flow in structural conduits, and that metal-barren hydrothermal events may be useful in demarcating zones containing earlier metalliferous phases.

References

Aleinkoff, J.N., Wintsch, R.P., Tollo, R.P., Unruch, D.M., Fanning, C.M., and Schmitz, M.D., 2007, Ages and Origins of Rocks of the Killingworth Dome, South-Central Connecticut: Implications for the Tectonic Evolution of the Southern New England: Americal Journal of Science, v. 307, p.63-118.

Ayer, J.A, Goutier, J., Thurston, P.C, Dubé, B., and Kamber, B.S, 2010, Abitibi-Wawa Subprovince Tectonic and Metallogenic evolution, Yilgarn-Superior Workshop: Abstracts GSWA Record 2010-20 p.7-11.

Bakker, R.J., 1997, CLATHRATES: computer programs to calculate fluid inclusion: V–X. Properties using clathrate melting temperatures: Computational Geosciences, v. 23, p. 1–18.

Bakker, R.J., 2003, Package FLUIDS 1. Computer programs for analysis of fluid in- clusion data and modelling bulk fluid properties: Chemical Geology, v. 194, p. 3–23.

Bateman, R., Ayer, J. A., and Dubé, B., 2008. The Timmins-Porcupine Gold Camp, Ontario: Anatomy of an Archean greenstone belt and Ontogeny of Gold Mineralization: Economic Geology, v. 103, p. 1285–1308.

Beaudoin, G., and Pitre, D., 2005, Stable isotope geochemistry of the Archean Val-d'Or (Canada) orogenic gold vein field: Mineralium Deposita, v. 40, p. 59-75.

Beaudoin, G., 2011. The stable isotope geochemistry of orogenic gold deposits. In: Barra, F., Reich, M., Campos, E., Tornos, F. (Eds.), Proceedings of the Eleventh Biennial SGA Meeting. Antogfagasta, Chile, pp. 556–558.

Bennett, G., 1972, Precambrian geology of Stover and Brackin townships: Ontario Geological Survey, Preliminary Map P.2380, scale 1:31 680.

Bodnar, R.J., 2003a, Introduction to aqueous fluid systems, in I. Samson, A. Anderson, & D. Marshall, eds. Fluid Inclusions: Analysis and Interpretation, Mineralogical Association of Canada, Short Course 32, 81-99.

Bodnar, R.J., 2003b, Reequilibration of fluid inclusions, in I. Samson, A. Anderson, & D. Marshall, eds. Fluid Inclusions: Analysis and Interpretation, Mineralogical Association of Canada, Short Course 32, 213-230.

Bodnar, R.J., and Vityk, M.O., 1994, Interpretation of microthermometric data for H2O-NaCl fluid inclusions, in De Vivo, B., and Frezzotti, M.L., eds., Fluid Inclusions in Minerals: Methods and Applications, Short Course of the Working Group (IMA) Inclusions in Minerals, p. 117–130.

Bruce, E.L., and Horwood, H.C., 1942, Rennie–Leeson area, District of Sudbury, Ontario: Ontario Geological Survey, Annual Report Map 51G, scale 1:31 680.

Bucher, K., and Grapes, R., 2011, Petrogenesis of Metamorphic Rocks: Springer-Cerlag Berlin Heidelberg, 428p.

Callan, N.J., 1988, Syn-deformational shear zone-hosted Au- quartz vein mineralization in TTG host rocks, Renabie Mine area, north Ontario: structural analysis, microstructural characteristics and vein paragenesis: unpublished MSc thesis, University of Toronto, Toronto, 234p.

Callan, N.J., and Spooner, E.T.C., 1987, Gneissose trondhjemite/tonalite hosted Au-quartz vein mineralization, Renabie Mine area, Wawa: geological characteristics and shear zone control: Geoscience Research Grant Program, Summary of Research, 1986-1987, Ontario Geological Survey, Miscellaneous Paper 136, p.153-175.

Callan, N.J., and Spooner, E.T.C., 1988, Archean Au quartz vein mineralization hosted in a tonalite-trondhjemite terrane, Renabie Mine area, Wawa, north Ontario, Canada: The

Geology of Gold Deposits, The Perspective in 1988, Society of Economic Geologists, Economic Geology Monograph 6, p. 9-18.

Callan, N.J., and Spooner, E.T.C., 1998, Repetitive hydraulic fracturing and shear zone inflation in an Archean granitoid-hosted, ribbon banded, Au-quartz vein system, Renabie area, Ontario, Canada: Ore Geology Reviews, v. 12, p. 237-266.

Cameron, E.M., and Hattori, K., 1987, Archean gold mineralization and oxidized hydrothermal fluids: Economic Geology, v. 82, p. 1177-1191.

Chen, G-N., and Grapes, R., 2007, Granite genesis: in-situ melting and crustal evolution: Springer, Dordrecht, The Netherlands, 273 p.

Corfu, F. and Sage, R.P., 1992, U-Pb age constraints for deposition of clastic metasedimentary rocks and late-tectonic plutonism, Michipicoten Belt, Superior Province: Canadian Journal of Earth Sciences, v. 29, p. 1640—1651.

Corfu, F., 1987, Inverse age stratification in the Archean crust of the Superior Province: evidence for infra- and subcrustal accretion from high resolution U-Pb zircon and monazite ages: Precambrian Research, v. 36, p. 259 -275.

Cox, K.G., and Clifford, P., 1982, Correlation Coefficient Patterns and Their Interpretation in Three Basaltic Suites: Contributions to Mineralogy and Petrology, v. 79, p.268-278.

Cox, S.F., Knackstedt, M.A., and Braun, J., 2001, Principles of structural control on permeability and fluid flow in hydrothermal systems, in Richards, J.P., and Tosdal, R.M., eds., Structural Controls on Ore Genesis: Reviews in Economic Geology, v. 14, p. 1–24.

Diamond, L.W., 1990, Fluid Inclusion Evidence for P-V-T-X Evolution of Hydrothermal Solutions in Late-Alpine Gold-Quartz Veins at Brusson, Val D'Ayas, Northwest Italian Alps: American Journal of Science, v. 290, p. 912-958.

Dubé, B., and Gosselin, P., 2007, Greenstone-hosted quartz-carbonate vein deposits, in Goodfellow, W.D., ed., Mineral Deposits of Canada: A Synthesis of Major Deposit-Types,

District Metallogeny, the Evolution of Geological Provinces, and Exploration Methods: Geological Association of Canada, Mineral Deposits Division, Special Publication No. 5, p. 49-73.

Dubé, B., Williamson, K., McNicoll, V ., Malo, M., Skulski, T ., Twomey, T., and Sanborn-Barrie, M., 2004, Timing of gold mineralization in the Red Lake gold camp, northwestern Ontario, Canada: New constraints from U- Pb geochronology at the Goldcrop High-grade zone, Red Lake mine and at the Madsen mine: Economic Geology, v. 99, p. 1611–1641.

Farquhar, J., and Wing, B., 2003, Multiple sulfur isotopes and the evolution of the atmosphere: Earth and Planetary Science Letters, v. 213, p. 1-13.

Faure, G., and Mensing, T.M., 2005, Isotopes; principles and applications: John Wiley & Sons Inc, p. 897.

Ferguson, S.A., 1968, Renabie Mines, Nudulama Mines and adjoining properties, surface geology, parts of Renabie, Leeson and Brackin townships, District of Sudbury: Ontario Department of Mines, Preliminary Geological Map p. 492.

Frost, B.R., Chamberlain, K.R., and Schumacher, J.C., 2001, Sphere (titantie): phase relations and role as a geochronometer: Chemical Geology, v. 172, p. 131-148.

Goldfarb, R.J., and Groves, D.I., 2015, Orogenic gold: Common or evolving fluid and metal sources through time: Lithos, v.233, p. 2-26.

Goldfarb, R.J., Baker, T., Dubé, B., Groves, D.I., Hart, C.J.R., Gosselin, P., 2005, Distribution, Character, and Genesis of Gold Deposits in Metamorphic Terranes: Economic Geology 100th Anniversary, p. 407–450.

Goldstein, R.H., 2003, Petrographic analysis of fluid inclusions, in Samson, I., Anderson, A., and Alderton, D.H.M., eds., Fluid Inclusions: Interpretation and Analysis: Mineralogical Association of Canada, Short Course Series Volume 32, Vancouver, British Columbia, p. 9–53.

Goldstein, R.H., and Reynolds, T.J., 1994, Systematics of fluid inclusions in diagenetic minerals: SEPM Short Course, v. 31, p. 1–199.

Grant, J.A., 1986, The Isocon diagram-A simple solution to Gresen's equation for metasomatic alteration: Economic Geology, v. 81, p. 1976–1982.

Groves, D.I., 1993, The crustal continuum model for late-Archean lode-gold deposits of the Yilgarn Blobk, Western Australia: Mineralium Deposita, v. 28, p. 366-374.

Groves, D.I., and Foster, R.P., 1991, Archaean lode gold deposits, in Foster, R.P., ed., Gold metallogeny and exploration: London, Blackie, p. 63–103.

Groves, D.I., Goldfarb, R. J., Gebre-Mariam, M., Hagemann, S. G. & Robert, F., 1998, Orogenic gold deposits: a proposed classification in the context of their crustal distribution and relationship to other gold deposit types: Ore Geology Reviews v. 13, p.7–27.

Groves, D.I., Goldfarb, R.J., Robert, F., and Hart, C.J.R., 2003, Gold deposits in metamorphic belts: Overview of current understanding, outstanding problems, future research, and exploration significance: Economic Geology, v. 98, p. 1–29.

Hagemann S.G., and Cassidy, K.F., 2000, Archean orogenic lode gold deposits: Reviews in Economic Geology, v. 13, p. 9–68.

Halls, H.C., and Palmer, H.C., 1990, The tectonic relationship of two Early Proterozoic dyke swarms to the Kapuskasing structural zone: A paleomagetic and petrographic study: Canadian Journal of Earth Sciences, v. 27, p. 87-103.

Hart, C.J.R., 2007, Reduced intrusion-related gold systems, in Goodfellow, W.D., ed., Mineral deposits of Canada: A Synthesis of Major Deposit Types, District Metallogeny, the Evolution of Geological Provinces, and Exploration Methods: Geological Association of Canada, Mineral Deposits Division, Special Publication No. 5, p. 95-112.

Haynes, F.M., Sterner, S.M., and Bodnar, R.J., 1988, Synthetic fluid inclusions in natural quartz—IV. Chemical analysis of fluid inclusions by SEM/EDA: Evaluation of method: Geochimica et Cosmochimica Acta, v. 52, p. 969–977.

Heather, K.B., and Arias, Z., 1992, Geological and structural setting of gold mineralization in the Goudreau–Lochalsh area, Wawa gold camp: Ontario Geological Survey, Open File Report 5832, 159 p.

Huston, D.L., 1993, The effect of alteration and metamorphism on wall rocks to the Balcooma and Dry River South volcanic-hosted massive sulfide deposits, Queensland, Australia: Journal of Geochemical Exploration, v. 48, p. 277–307.

Ispolatov, V., Lafrance, B., Dubé, B, Creaser, R., Hamilton, M., 2008, Geologic and structural setting of gold mineralization in the Kirkland Lake-Larder Lake gold belt. Ontario: Economic Geology, v. 103, p. 1309–1340.

Jemiellta, R.A., Callan, N.J., and Spooner, E.T.C., 1988, Petrogenesis of Archean Trondhjemite-Tonalite-Granodiorite (TTG) Intrusions and Their Relationships to Gold Mineralization, Renabie and Magino Areas, Wawa: Ontario Geological Survey, Miscellaneous Paper 140, p.78-93.

Jemielita, R.A., Davis, D.W., and Krogh, T.E., 1990, U-Pb evidence for Abitibi gold mineralization postdating greenstone magmatism and metamorphism: Nature, v. 346, p. 831-834.

Kamo, S.L., 2014, Report on U-Pb CA-ID-TIMS geochronology on volcanic and plutonic rocks, Superior and Grenville provinces, Ontario: internal report for the Ontario Geological Survey, Jack Satterly Geochronology Laboratory, University of Toronto, Toronto, Ontario, 27 p.

Kamo, S.L., 2015, Report on U-Pb CA-ID-TIMS geochronology on volcanic and plutonic rocks, Superior and Grenville provinces, Ontario: internal report for the Ontario Geological

Survey, Jack Satterly Geochronology Laboratory, University of Toronto, Toronto, Ontario, 48 p.

Kennedy, K.A., Kamo, S.L., Nasdala, L., Timms, N.E., 2010, Grenvillle Skarn Titanite: Potential Reference Material for SIMS U-Th-Pb Analysis: The Canadian Mineralogist, v. 48, p. 1423-1443.

Kerrich, R., 1989, Geochernical evidence on the sources of fluids and solutes for shear zone hosted mesothermal Au deposits. In: Bursnall, J.T. (Ed.), Mineralization and Shear Zones. Geol. Assoc. Can. Short Course Notes 6, pp. 129-197.

Kerrich, R., and Cassidy, K.F., 1994, Temporal relationships of lode gold mineralization to accretion, magmatism, metamorphism and deformation— Archean to present: A review: Ore Geology Reviews, v. 9, p. 263–310.

Kontak, D.J., 2004, Analysis of evaporate mounds as a complement to fluid-inclusion thermometric data: case studies from granitic environments in Nova Scotia and Peru: The Canadian Mineralogist, v. 42, p. 1315–29.

Kontak, D.J., Hanley, J.B., and Fayek, M., 2016, A Rayleigh distillation model to explain large variations in oxygen isotope data for orogenic gold veins: Abstract, Geological Association of Canada-Mineralogical Association of Canada 2016.

Kyser, T.K., Kerrich, R., 1990, Geochemistry of fluids in tectonically active crustal regions: Nesbitt, B.E. (Ed.), Fluids in Tectonically Active Regimes of the Continental Crust. Min. Assoc. Can. Short Course 19, p. 133-230.

Larocque, C.L.A., Hodgson, C.J., Cabri, L.J., and Jackman, J.A., 1995, Ion-Microprobe Analysis of Pyrite, Chalcopyrite, and Pyrrhotite from the Mobrun VMS deposit in Northwestern Quebec: Evidence for Metamorphic Remobilization of Gold: The Canadian Mineralogist, v. 33, p. 373-388.

Li, H., Schwarez, H.P., and Shaw, D.M., 1991, Deep crustal oxygen isotope variations: the Wawa-Kapuskasing crustal transect, Ontario: Contributions to Mineralogy and Petrology, v. 107, p. 448-458.

Ludwig, K.R., 2003, User's manual for Isoplot 3.00 a geochronological toolkit for Excel: Berkeley, CA, Berkeley Geochronological Center Special Publication 4, 71 p.

Matsuhisa, Y., Goldsmith, J.R., and Clayton, R.N., 1979, Oxygen isotopic fractionation in the system quartz-albite-anothite-water: Geochimica et Cosmochimica Acta, v. 43, p. 1131–1140.

McCuaig, T.C., and Kerrich, R., 1998, P-T -t-deformation-fluid characteristics of lode gold deposits: Evidence from alteration systematics: Ore Geology Reviews, v. 12, p. 381–454.

McDivitt, J.A., Lafrance, B., Kontak, D.J., and Robichaud, L., 2015, Characterization of Gold Mineralization in the Missanabie-Renabie District of the Wawa gold camp: Summary of Field Work and Other Activities, Open File Report 6313, p. 6-1 to 6-8.

McDivitt, J.A., 2016, Gold Mineralization in the Missanabie-Renabie District of the Wawa Subprovince: Geochemical Data and Photographs: Ontario Geological Survey, Miscellaneous Release—Data 339.

Moser, D.E., 1994, The geology and structure of the mid-crustal Wawa gneiss domain: a key to understanding tectonic variation with depth and time in the late Archean Abitibi-Wawa orogen: Canadian Journal of Earth Sciences v. 31 p. 1064-1080.

Müller, W., Michael, S., Miller, P., and Sergey, B., 2009, Initial performance metrics of a new custom-designed ArF excimer LA-ICPMS system coupled to a two-volume laser-ablation cell: Journal of Analytical Atomic Spectrometry, v. 24, p. 209-214.

Mumin, A.H., Fleet, M.E., and Chryssoulis, S.L., 1994, Gold mineralization in As-rich mesothermal gold ores of the Bogosu-Prestea mining district of the Ashanti gold belt, Ghana—remobilization of "invisible" gold: Mineralium Deposita, v. 29, p. 445–460.

Nesbitt, B.E., 1990, Fluid flow and chemical evolution in the genesis of hydrothermal ore deposits. In: Nesbitt, B.E. (Ed.), Short Course in Fluids in Tectonically Active Regimes of the Continental Crust, vol. 18. Mineralogical Association of Canada, Montreal, QB, Canada, pp. 261 – 298.

Nesbitt, B.E., Murowchick, J.B., and Muehlenbachs, K., 1986, Dual origins of lode gold deposits in the Canadian Cordillera: Geology, v. 14, p. 506- 509.

Neyedley, K., Hanley, J., Fayek, M., and Kontak, D.J., 2016, Textural, fluid inclusion, and stable O isotope constraints on vein formation and gold precipitation, 007 deposit, Bissett, Manitoba, Canada: Economic Geology, In Press.

Oakes, C.S., Bodnar, R.J., and Simonson, J.M., 1990, The system NaCl-=CaCl2-H2O. I. The ice liquidus at 1 atm total pressure: Geochimica et Cos- mochimica Acta, v. 54, p. 603–610.

Ohmoto, H., and Rye, R.O., 1979, Isotopes of sulfur and carbon, in Barnes, H.L., ed., Geochemistry of hydrothermal ore deposits, 2nd ed.: New York, NY, John Wiley and Sone, p. 509-567.

Ontario Geological Survey 2011. 1:250 000 scale bedrock geology of Ontario: Ontario Geological Survey, Miscellaneous Release—Data 126–Revision 1.

Paton, C., Hellstrom, J., Paul, B.,Woodhead, J., and Hergt, J., 2011, Iolite: Freeware for the visualisation and processing of mass spectrometric data: Journal of Analytical Atomic Spectrometry, v. 26, p. 2508-2518.

Percival, J.A., 1981, Stratigraphic, structural, and metamorphic relations between the Wawa and Abitibi Subprovinces and the Kapuskasing Structural Zone near Chapleau, Ontario: Current Research, Part A, Geological Survey of Canada, Paper 81-1A, p. 83–90.

Percival, J.A., and Card, K.D., 1985, Structure and evolution of Archean crust in central Superior province, Canada. In: Ayres LD, Thurston PC, Card KD, Weber W (eds) Evolution of

Archean Supracrustal Sequences. Geological Association of Canada Special Paper 28, p. 179-192.

Perring, C.S., and McNaughton, N.J., 1990, Geological note: Proterozoic remobilization of ore metals within Archaean gold deposits: Lead isotope evidence from Norseman, Western Australia: Australian Journal of Earth Sciences, v. 37, p. 369-372.

Phillips, G.N., and Groves, D.I., 1983, The Nature of Archaean gold-bearing fluids and deduced from gold deposits of Western Australis: Journal of the Geological Society of Australia, v. 30, p. 25-39.

Phillips, G.N., and Powell, R., 2009, Formation of gold deposits: Review and evaluation of the continuum model: Earth-Science Reviews, v. 94, p. 1–21.

Ramsay, J.G., 1980, The crack-seal mechanism of rock deformation: Nature, v. 284, p. 135–139.

Riley, R.A., 1971, Precambrian geology of Glascow, Meath and Rennie townships: Ontario Geological Survey, Preliminary Map p. 2210, scale 1:31 680.

Robert, F., 2001, Syenite-associated disseminated gold deposits in the Abitibi greenstone belt, Canada: Mineralium Deposita, v. 36, p. 503–516.

Robert, F., and Poulsen, K.H., 2001, Vein formation and deformation in greenstone gold deposits: Reviews in Economic Geology, v. 14, p. 111–155.

Robert, F., Poulsen, K.H., Cassidy, K.F., and Hodgson, C.J., 2005, Gold metallogeny of the Yilgarn and Superior cratons: Economic Geology 100th Anniversary Volume, p. 1001–1033.

Robichaud, L., McDivitt, J.A., and Trevisan, B.E., 2015, Geology and Mineral Potential of Rennie and Leeson Townships, Michipicoten Greenstone Belt: Summary of Field Work and Other Activities 2015, Ontario Geological Survey, Open File Report 6313, p.5-1 to 5-11.

Roedder, E., and Bodnar, R.J., 1997, Fluid inclusion studies of hydrothermal ore deposits, in Barnes, H.L., ed., Geochemistry of hydrothermal ore deposits,3rd ed. .: New York, NY, John Wiley and Sone, p. 657-697.

Rusk, B.G., Reed, M.H., and Dilles, J.H., 2008, Fluid inclusion evidence for magmatic-hydrothermal fluid evolution in the porphyry copper-molybdenum deposit at Butte, Montana: Economic Geology, v. 103, p. 307−334.

Sage, R.P., 1986, Stratigraphic correlation in the Wawa area: Volcanology and Mineral Deposits, Ontario Geological Survey, Miscellaneous Paper 129, p.62-68.

Sage, R.P., and Heather, K.B., 1991, The structure, stratigraphy and mineral deposits of the Wawa area: Geological Association of Canada–Mineralogical Association of Canada–Society of Economic Geologists, Joint Annual Meeting, Toronto 1991, Field Trip A6, 118p.

Schmidt, C., and Bodnar, R.J., 2000, Synthetic fluid inclusions: XVI. PVTX properties in the system H2O-NaCl-CO2 at elevated temperatures, pressures and salinities: Geochim Cosmochim Acta v. 64, p. 3853–3869.

Schmitz, M.D., and Bowring, S.A., 2001, U-Pb zircon and titanite systematics of the Fish Canyon Tuff: An assessment of high-precision UPb geochronology and its application to young volcanic rocks: Geochimica et Cosmochimica Acta, v. 65, p. 2571–2587.

Seal, R.R., 2006, Sulfur Isotope Geochemistry of Sulfide Minerals, 2006, Reviews in Mineralogy and Geochemistry, v. 61, p. 633-677.

Seedorff, E., Dilles, J. H., Phoffett, Jr., J. M., Einaudi, M. T., Zurcher, L., Stavast, W. J. A., Johnson, D. A. and Barton, M. D., 2005, Porphyry deposits: Characteristics and origin of hypogene features: Economic Geology 100th Anniversary Volume, Society of Economic Geologists, p. 251 – 298.

Selby, D., Creaser , R.A., Hart, C.J.R., Rombach, C.S., Thompson, J.F .H., Smith, M.T., Bakke, A.A., and Goldfarb, R.J., 2002, Absolute timing of sulfide and gold mineralization—a

comparison of Re-Os molybdenite and Ar- Ar mica methods from the Tintina gold belt, Alaska: Geology , v. 30, p. 791–794.

Selby, D., Nesbitt, B.E., Muehlenbachs, K., and Prochaska, W., 2000, Hydrothermal alteration and fluid chemistry of the Endako porphyry molybdenum deposit, British Columbia: Economic Geology, v. 95, p. 183–202.

Sheppard, S.M.F., 1977, The Cornubian batholith; S.W. England: D/H and 18O/16O studies of kaolinite and other alteration minerals: Journal of the Geological Society, London, v. 133, p. 573-591.

Sillitoe, R. H., 2010, Porphyry copper systems: Economic Geology, v. 105, p.3– 41.

Spencer, K.J., Hacker, B.R., Kylander-Clark, A.R.C., Andersen, T.B., Cottle, J.M., Stearns, M.A., Poletti, J.E., Seward, G.G.E., 2013, Campaign-style titanite U-Pb dating by laser ablation ICP: Implications for crustal flow, phase transformations and titanite closure: Chemical Geology, v. 341, p. 84–101.

Spooner, E.T.C., 1993, Magmatic sulfide/volatile interaction as a mechanism for producing chalcophile element enriched, Archean Au-quartz, epithermal Au-Ag and Au skarn hydrothermal ore fluids: Ore Geology Reviews, v. 7, p. 359–379.

Stacey, J.S., and Kramers, J.D., 1975. Approximation of terrestrial lead isotope evolution by a two-stage model: Earth and Planetary Science Letters, v. 26, p. 207-221.

Steele-MacInnis, M., Lecumberri-Sanchez, P., and Bodnar, R.J., 2012, HokieFlincs_H2O-NaCl: A Microsoft Excel spreadsheet for interpreting microthermometric data from fluid inclusions based on the PVTX properties of H2O- NaCl: Computers and Geosciences v. 49, p. 334–337.

Sterner, S.M., and Bodnar, R.J., 1991, Synthetic Fluid Inclusions. X: Experimental Determination of P-V-T-X properties in the CO_2-H_2O system to 6 Kb and 700 ˚C: American Journal of Science, V. 291, p. 1-54.

Storey C.D., Jeffries T.E., and Smith M., 2006, Common Pb-corrected laser ablation ICP-MS U-Pb systematics and geochronology of titanite: Chemical Geology, v. 227, p. 37–52.

Studemeister, P.A., and Kilias, S., 1987, Alteration Pattern and Fluid Inclusions of Gold-Bearing Quartz Veins in Archean Trondhjemite near Wawa, Ontario, Canada: Economic Geology, v. 82, p. 429-439.

Sullivan, R.W., and Leclair, A.D., 1992, U-Pb zircon age of the mid-crustal tonalite gneiss in the central Kapuskasing Uplift, north- ern Ontario. In Radiogenic age and isotopic studies: Report 5. Geological Survey of Canada, Paper 91-2, p.7 1 - 78.

Taylor, H.P. Jr., 1974, The application of oxygen and hydrogen isotope studies to problems of hydrothermal alteration and ore deposition: Economic Geology, v. 69, p. 843-883.

Taylor, H.P. Jr., 1979, Oxygen and Hydrogen Isotope Relationships in Hydrothermal Mineral Deposits, in Barnes, H.L., ed., Geochemistry of hydrothermal ore deposits, 2nd ed.: New York, NY, John Wiley and Sone, p. 236-277.

Thompson, J.F.H., and Newberry, R.J., 2000, Gold deposits related to reduced granitic intrusions: Reviews in Economic Geology, v. 13, p. 377–400.

Thompson, J.F.H., Sillitoe, R.H., Baker, T., Lang, J.R., and Mortensen, J.K., 1999, Intrusion-related gold deposits associated with tungsten-tin provinces: Mineralium Deposita, v. 34, p. 323–334.

Turek, A., Smith, P.E. and Van Schmus, W.R. 1982. Rb-Sr and U-Pb ages of volcanism and granite emplacement in the Michipicoten Belt—Wawa, Ontario: Canadian Journal of Earth Sciences, v. 19, p. 1608-1626.

Turek, A., Smith, P.E. and Van Schmus, W.R. 1984. U-Pb zircon ages and the evolution of the Michipicoten plutonic-volcanic terrane of the Superior Province, Ontario: Canadian Journal of Earth Sciences, v. 21, p. 457-464.

Turek, A., Sage, R.P., and Van Schmus, W.R., 1990, Advances in geochronology of the Michipicoten greenstone belt: Proceedings and Abstract, Institute on Lake Superior Geology, v. 36, p. 110-111.

Turek, A., Sage, R. P., and Van Schmus, W. R., 1992, Advances in the U-Pb zircon geochronology of the Michipicoten greenstone belt, Superior Province, Ontario: Canadian Journal of Earth Sciences, v. 29, p. 1154- 1165.

Turek, A., Heather, K.B., Sage, R.P. and Van Schmus, W.R. 1996, U/Pb zircon ages for the Missanabie–Renabie area and their relation to the rest of the Michipicoten greenstone belt, Superior Province, Ontario, Canada: Precambrian Research, v. 76, p. 191-211.

Walshe, J.L., Heithersay, P.S., and Morrison, G.W., 1995, Toward an understanding of the metallogeny of the Tasman fold belt system: Economic Geology, v. 90, p. 1382–1401.

Wenner, D.B., and Taylor, H.P., 1971. Temperatures of serpentinization of ultramafic rocks based on 18O/16O fractionation between coexisting serpentinite and magnetite, Contributions to Mineralogy and Petrology, v. 32, p. 165-185.

Witt, W.K., 1992, Porphyry intrusions and albities in the Bardoc-Kalgoorlie area, Western Australia, and their role in Archean epigenetic gold mineralization: Canadian Journal of Earth Sciences, v. 29, p. 1609-1622.

Woodhead, J.D., Hellstrom, J., Hergt, J.M, Greig, A., and Maas, R., 2007, Isotopic and Elemental Imaging of Geological Materials by Laser Ablation Inductively Coupled Plasma-Mass Spectrometry: Journal of Geostandards and Geoanalytical Research, v. 31, p. 331-343.

Xue, Y., Campbell, I., Ireland, T, R., Holden, P., and Armstrong, R., 2013, No mass-independent sulfur isotope fractionation in auriferous fluids supports a magmatic origin for Archean gold deposits: Geology, v. 41, p. 791-794.

Tables

Table 3.1 List of the analytical procedures and equipment operating conditions used for LA-ICP-MS U-Pb titanite geochronology.

LA	
Model	Resonetics RESOlution M-50
Type	ArF excimer
Wavelength	193 nm
Pulse Duration	20 ns
Sample Cell	Laurin technic two-volume sample cell, ArF excimer laser; Müller *et al*., (2009)
Gas Flows:	
He (carrier gas)	0.65 L/min
Ar (neb gas)	0.83 L/min
N_2 (additional gas)	0.006 L/min
ICP-MS	
Model	Thermo X-series II Quadrupole ICP-MS
Plasma	Argon
Tuning Parameters	ThO^+/Th^+ <0.4 % and U/Th ~1% by ablating NIST612 with a 26 µm spot size and scanning parameters of 5 µm/s, 10 Hz, and 6 J/cm^2
Dwell Times (ms)	^{43}Ca*=5; ^{47}Ti*=5; ^{202}Hg=10; ^{204}Pb=10; ^{206}Pb=40; ^{207}Pb=50; ^{208}Pb=20; ^{232}Th=30; ^{238}U=40
Data Acquisition and Reduction	
Spot diameter	22 µm
Energy Density	6 J/cm^2
Rep Rate	6 Hz
Standards	OLT1 titanite (calibration; Kennedy *et al*., 2010); BLR (secondary; Aleinikoff *et al*., 2007) and FCT titanite (secondary; Schmitz and Bowring, 2001)
Accepted Ages	BLR = 1047.1±0.4 ma; FCT = 28.53±0.05 ma
Determined Ages (N=6)	BLR = 1033±18 ma; FCT = 29.6±1.2 ma
Data reduction	Completed using the procedure outlined in Petrus and Kamber, (2012)

Table 3.2 List of the analytical procedures and equipment operating conditions used for LA-ICP-MS pyrite trace element mapping.

LA	
Model	Resonetics RESOlution M-50
Type	ArF excimer
Wavelength	193 nm
Pulse Duration	20 ns
Sample Cell	Laurin technic two-volume sample cell, ArF excimer laser; Müller*et al*., (2009)
Gas Flows:	
He (carrier gas)	0.65 L/min
Ar (neb gas)	0.75 L/min
N_2 (additional gas)	0.006 L/min
ICP-MS	
Model	Thermo X-series II Quadrupole ICP-MS
Plasma	Argon
Tuning Parameters	ThO^+/Th^+ <0.5 % and U/Th ~1% by ablating NIST612 with a 26 µm spot size and scanning parameters of 5 µm/s, 10 Hz, and 6 J/cm^2
Data Acquisition and Reduction	
Spot diameter	C5 = 19 µm, NUE31 = 14 µm
Energy Density	6 J/cm^2
Scan Rate	C5 = 9 µm/s, NUE31 = 7 µm/s
Standards	NIST 610 (external), Fe (internal)
Data reduction	Iolite v.3 after Woodhead *et al*., (2007); Patron *et al*., (2011)

Table 3.3 Summary of the mineralogy, textural characteristics, associated alteration, and defining features of the different vein types.

Vein Type	Dominant Mineralogy[1]	Accessory phases (combined total of ~≤10 %)[1]	Textural Characteristics	Associated Alteration	Defining Features
Laminated Quartz	quartz (Qtz_1) (~80-90%), sericite (~5-10%), carbonate (~5-10%)	pyrite (Py_1), chalcopyrite, molybdenite, galena, sphalerite, allanite (Ep_2), Au-Ag-Te-Bi-Pb alloys, titanite, epidote-altered plagioclase (wall rock fragments)	intensely recrystallized quartz grains displaying undulatory extinction, lobate- to cuspate-grain boundaries in coarser grains, triple point boundaries in smaller grains; mm-scale planar domains of sericite define a laminated texture	quartz-sericite-pyrite (Py_1) (phyllic) alteration zones	laminated-saccharoidal texture; phyllic alteration halos; diverse sulfide assemblage; visible gold; contain Py_1 replaced by hematite
Hematite-Associated Alteration	quartz (Qtz_2), epidote, chlorite (variable proportions of each phase; one phase can dominate up to ~100%)	quartz, epidote, chlorite, K-feldspar, hematite	medium- to coarse-grained euhedral infill mineralogy; locally defined comb textures; moderate microfracture abundance preferentially expressed by epidote	chlorite-titanite-albite-hematite (vein distal); k-feldspar-hematite (vein proximal)	invariable association with hematite-bearing alteration assemblages; quartz-epidote-chlorite infill assemblage; medium- to coarse-grained, euhedral infill minerals
Massive Pyrite	pyrite (Py_2) (~100%)		medium-grained, anhedral-serrated pyrite		pyrite-only mineralogy; lack of alteration; anhedral-serrated pyrite morphology
NW-Striking Quartz Tension Gash	quartz (Qtz_3) (~80-90%)	chlorite and amphibole (wall rock fragments), pyrite, brown granular Fe oxides	quartz grains are typically recrystallized (sub-grain development and undulatory extinction); primary growth zones are locally visible, but generally not preserved; abundant microfracturing and the formation of local cataclasites	local, cm-scale wall rock silicification	NW orientation and late relative timing; domination of mineralogy by quartz; abundant microfractures and local cataclasite

[1]Dominant mineralogy and accessory phase categories refer to infill mineralogy, and include fragments of wallrock incorporated within veins.

Table 3.4 An integrated paragenesis for different vein, alteration, and mineral types that builds upon that presented in Chapter 2.

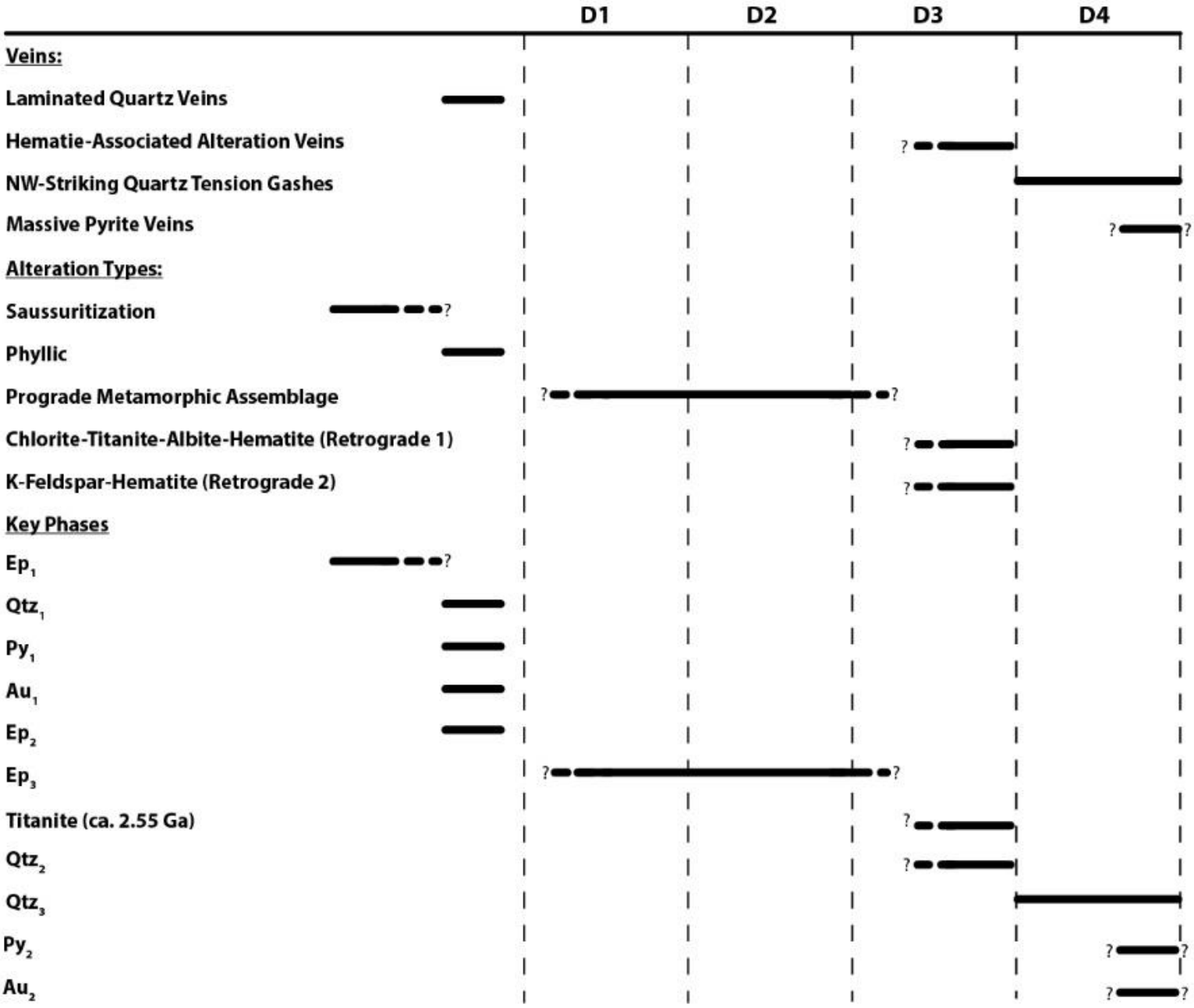

Table 3.5 Summary of the mineralogy, key features, spatial distributions, and main chemical changes defined by mass balance of the different alteration types.

Alteration Type	Defining Mineralogy	Accessory Phases	Key Features	Spatial Distribution	Major Elemental Gains (≥30%)[1]	Major Elemental Losses (≤30%)[1]
Saussuritization	Fe-poor epidote (Ep_1), An_{20} plagioclase	none identified	optically-continuous, grey plagioclase in thin section; fine-grained disseminations of acicular, Ep_1 intergrown with the optically continuous plagioclase	regional: wide-spread, non-mappable distribution	-	-
Phyllic	quartz, sericite, pyrite (Py_1)	carbonate, allanite (Ep_2), titanite, Fe-Ti oxides	present as alteration halos, ~2-10 m wide, surrounding laminated quartz veins	localized to laminated quartz veins	CO_2, S, K_2O, LOI, Fe_2O_3p, Ba, Rb, W, Ag, Au, Te, Bi, Pb, Cu	MnO, Na_2O, CaO
Prograde Metamorphic Assemblage	hornblende, epidote (Ep_3), Fe-Ti oxides	garnet	pokiloblastic minerals preferentially overgrowing biotite	regional: wide-spread, non-mappable distribution	-	-
Retrograde Type 1 (Vein Distal)	chlorite, titanite, albite, sericite, hematite	Fe-Ti oxides, apatite, brown granular Fe oxides and sulphates, hematite-replaced pyrite	alteration of biotite to chlorite-titanite-Fe-Ti-oxide assemblage; destruction of Ep_1 in plagioclase; inter-grown sericite, albite, and An_{20}; texturally preservative; faint hematite-red hue well defined in outcrop and hand sample	regional: structurally controlled, mappable distribution	S, LOI, Na_2O	P_2O_5, MnO, ∑HREE, ∑LREE, CaO, Ba, Cu
Retrograde Type 2 (Vein Proximal)	K-feldspar, hematite	quartz, epidote, chlorite, brown granular Fe oxides and sulphates, hematite-replaced pyrite	dissolution of pre-existing mineralogy and fabrics; porous K-feldspar infilled by hematite rosettes; dark hematite-red coloration well defined in outcrop and hand sample	regional: structurally controlled, mappable distribution	S, K_2O, Fe_2O_3P. Ba, Rb	~15% total mass loss; FeOp, SiO_2, Na_2O

[1]Metals (W, Ag, Au, Te, Bu, Pb, Cu, Mo, Zn) that have isocon-corrected percentage changes of ≥30 % or ≤30 %, but changes in absolute value of ~≤1 ppm are excluded from these columns.

Table 3.6 Whole-rock major and trace element analyses for representative samples of different alteration types. Values for the lower limit of detection are reported in brackets.

Sample:	C-16	C-13	NUE-29	NUE-8
Zone:	C-zone	C-zone	Nudulama East	Nudulama East
Alteration Type:	Saussuritization	Phyllic	Retrograde 1: Chlorite-Titanite-Albite-Hematite	Retrograde 2: K-Feldspar-Hematite
SiO_2 Wt. % (0.04)[1]:	67.87	67.87	67.73	61.32
TiO_2 Wt. % (0.01)[1]:	0.45	0.53	0.39	0.5
Al_2O_3 Wt. % (0.02)[1]:	15.01	15.3	15.5	16.42
Fe_2O_3t Wt. % (0.01)[1]:	4.47	5.26	4.08	5.12
Fe_2O_3p Wt. %[3]:	1.91	3.37	1.37	2.65
FeOp (0.06) Wt. %[2]:	2.3	1.7	2.44	2.22
MnO Wt. % (0.002)[1]:	0.078	0.054	0.052	0.048
MgO Wt. % (0.01)[1]:	1.89	1.98	2.09	2.12
CaO Wt. % (0.006)[1]:	4.228	1.094	1.719	1.862
Na_2O Wt. % (0.02)[1]:	4.06	1.50	5.56	0.09
K_2O Wt. % (0.01)[1]:	1.36	4.43	0.96	11.4
P_2O_5 Wt. % (0.002)[1]:	0.126	0.159	0.088	0.123
Cr_2O_3 Wt. % (0.002)[1]:	0.01	0.01	<0.002	<0.002
Total Wt. %	100.41	100.54	99.83	100.89
LOI Wt. % (0.05)[1]:	0.82	2.29	1.64	1.78
S Wt. % (0.003)[4]:	0.01	0.087	0.088	0.565
CO_2 Wt. % (0.023)[4]:	<0.023	0.196	<0.023	<0.023
Ag ppm (0.01)[5]:	0.06	1.5	0.01	0.14
As ppm (0.8)[5]:	<0.8	1	0.9	<0.8
Au ppm (0.002)[5]:	0.014	4.003	0.009	0.016
Bi ppm (0.01)[5]:	0.02	2.04	0.06	0.33
Cu ppm (0.7)[5]:	20.4	44.5	2	3
Mo ppm (0.03)[5]:	0.66	1.74	0.44	0.32
Pb ppm (0.2)[5]:	1.1	14.4	0.7	0.6
Sb ppm (0.06)[5]:	<0.06	<0.06	<0.06	<0.06

	C-16	C-13	NUE-29	NUE-8
	C-zone	C-zone	Nudulama East	Nudulama East
	Saussuritization	Phyllic	Retrograde 1: Chlorite-Titanite-Albite-Hematite	Retrograde 2: K-Feldspar-Hematite
Te ppm (0.01)[5]:	0.02	6.99	0.03	0.17
U ppm (0.01)[5]	0.37	0.34	0.22	0.37
Zn ppm (3)[5]:	60.57	67.77	44.5	48.78
Ba ppm (0.8)[6]:	366.7	617	134.4	1001.3
Rb ppm (0.11)[6]:	33.98	126.97	24.97	175.52
W ppm (0.05)[6]:	0.1	1.9	0.41	0.88
Zr ppm (6)[6]:	110	123	115	151
Ce ppm (0.12)[6]:	48.76	49.22	22.01	33.72
Dy ppm (0.009)[6]:	2.252	2.122	1.316	2.214
Er ppm (0.007)[6]:	1.197	1.214	0.746	0.892
Eu ppm (0.0031)[6]:	1.0003	0.939	0.5531	1.3622
Gd pppm (0.009)[6]:	2.916	2.638	1.522	3.551
Ho ppm (0.0025)[6]:	0.4244	0.4204	0.2546	0.3533
La ppm (0.1)[6]:	22.73	21.23	11.19	15.89
Lu ppm (0.002)[6]:	0.1674	0.1544	0.1004	0.1398
Nd ppm (0.06)[6]:	20.96	20.06	9.31	16.98
Pr ppm (0.014)[6]:	5.564	5.278	2.547	4.208
Sc ppm (1.1)[6]:	11	11.9	9	13.5
Sm ppm (0.026)[6]:	3.618	3.392	1.681	3.775
Tb ppm (0.0023)[6]:	0.3936	0.3697	0.2208	0.4575
Tm ppm (0.0019)[6]:	0.171	0.1717	0.1096	0.1238
Y ppm (0.05)[6]:	12.08	12.2	7.19	10.09
Yb ppm (0.009)[6]:	1.096	1.067	0.707	0.844
∑LREE ppm[7]:	116.55	114.66	57.81	92.99
∑HREE ppm[8]:	17.78	17.72	10.64	15.11

[1]Concentrations determined by XRF-M01. [2]Concentration determined by FEO-ION. [3]Concentration determined by a calculation based on the results of XRF-M01 and FEO-ION. [4]Concentrations determined by IRC-100. [5]Concentrations determined by IML-100. [6]Concentrations determined by IMC-100. [7]∑LREE=(Ce+Eu+Gd+La+Nd+Pr+Sc+Sm). [8]∑HREE=(Dy+Er+Ho+Lu+Tb+Tm+Y+Yb).

Table 3.7 Analytical data for the 41 titanite spot analyses used in U-Pb age determination.

	Compositional data				Isotopic ratios						
Spot	Pb [ppm]	U [ppm]	Th [ppm]	U/Th	$^{207}Pb/^{235}U$	2σ	$^{206}Pb/^{238}U$	2σ	ρ	$^{207}Pb/^{206}Pb$	2σ
NUE28C/16	25.36	223.09	63.51	3.51	13.2	0.6	0.519	0.019	0.744	0.185	0.006
NUE28C/23	2.52	13.85	0.03	464.13	18.2	1.9	0.514	0.034	0.213	0.257	0.030
NUE28C/35	11.39	62.47	0.13	491.54	19.1	1.2	0.561	0.017	0.815	0.247	0.010
NUE28C/36	1.40	26.76	0.05	577.43	13.7	0.6	0.490	0.013	0.288	0.202	0.008
NUE28C/37	2.11	27.48	0.03	836.66	14.9	0.6	0.518	0.013	0.431	0.209	0.007
NUE28C/38	2.73	46.15	0.04	1095.56	14.1	0.5	0.481	0.010	0.464	0.212	0.006
NUE28C/39	9.00	26.70	0.12	214.78	20.4	1.0	0.554	0.017	0.366	0.267	0.012
NUE28C/40	1.92	28.04	0.03	865.90	14.6	0.5	0.517	0.012	0.546	0.205	0.007
NUE28C/41	2.64	24.82	0.05	461.36	15.5	0.8	0.524	0.017	0.426	0.215	0.010
NUE28C/42	1.64	19.79	0.06	339.33	15.2	1.1	0.527	0.039	0.368	0.209	0.014
NUE28C/45	1.62	9.59	0.04	245.55	19.0	1.7	0.539	0.024	0.027	0.255	0.020
NUE28C/46	1.21	11.32	0.05	238.60	16.3	1.5	0.526	0.033	0.128	0.225	0.025
NUE28C/47	2.26	15.37	0.09	173.41	16.3	0.9	0.504	0.016	0.349	0.235	0.012
NUE28C/48	2.40	44.60	0.08	589.07	13.7	0.5	0.499	0.013	0.216	0.200	0.008
NUE28C/49	1.81	82.40	0.16	510.28	13.0	0.8	0.502	0.019	0.685	0.187	0.008
NUE28C/50	1.75	20.39	0.06	321.96	15.3	1.1	0.521	0.027	0.830	0.213	0.009
NUE28C/52	1.32	21.99	0.07	323.73	13.0	1.3	0.509	0.032	0.432	0.185	0.016
NUE28C/55	3.36	27.07	0.02	1131.91	15.2	1.9	0.516	0.030	0.599	0.213	0.024
NUE28C/56	3.56	57.00	0.15	385.12	14.2	0.5	0.507	0.011	0.552	0.203	0.005
NUE28C/57	9.23	65.93	0.19	355.40	15.0	1.2	0.491	0.018	0.612	0.222	0.014
NUE28C/58	6.42	47.93	0.15	319.90	16.3	1.0	0.522	0.020	0.388	0.226	0.012
NUE28C/59	2.20	40.31	0.11	370.85	13.9	0.7	0.514	0.019	0.420	0.196	0.009
NUE28C/60	2.55	45.31	0.07	607.60	14.1	0.8	0.509	0.017	0.651	0.201	0.009
NUE28C/61	2.41	87.83	0.18	480.22	12.7	0.2	0.489	0.007	0.384	0.189	0.003
NUE28C/62	2.49	94.56	0.10	948.46	13.0	0.4	0.511	0.014	0.820	0.184	0.005
NUE28C/63	3.97	65.71	0.23	279.94	14.4	0.8	0.512	0.016	0.577	0.204	0.009
NUE28C/64	2.89	86.54	0.07	1253.62	14.2	0.6	0.516	0.013	0.487	0.200	0.007
NUE28C/67	2.14	16.95	0.03	650.73	14.8	1.0	0.522	0.028	0.429	0.206	0.014
NUE28C/68	1.90	27.94	0.04	738.51	13.6	0.6	0.488	0.017	0.622	0.202	0.008
NUE28C/69	3.69	43.48	0.14	321.20	14.1	0.7	0.506	0.016	0.449	0.202	0.010
NUE28C/71	2.65	34.99	0.08	415.65	13.9	0.9	0.514	0.019	0.244	0.197	0.014
NUE28C/72	3.27	104.85	0.23	454.95	13.2	0.7	0.512	0.019	0.880	0.188	0.005
NUE28C/73	1.98	28.58	0.12	240.73	13.2	1.3	0.520	0.031	0.348	0.185	0.018
NUE28C/74	2.94	80.84	0.20	400.39	13.9	0.8	0.512	0.022	0.619	0.197	0.008
NUE28C/75	2.13	46.59	0.15	310.33	13.2	0.7	0.517	0.019	0.022	0.185	0.014
NUE28C/77	2.27	32.73	0.10	324.39	14.1	0.7	0.510	0.019	0.367	0.200	0.010
NUE28C/78	2.60	72.12	0.19	370.45	13.4	0.6	0.515	0.021	0.636	0.189	0.010
NUE28C/80	1.97	24.62	0.12	197.54	14.4	0.8	0.509	0.015	0.258	0.205	0.011

NUE28C/81	1.43	39.88	0.07	601.11	13.2	1.3	0.522	0.058	0.561	0.183	0.018
NUE28C/84	2.01	30.09	0.05	619.70	15.2	0.8	0.522	0.018	0.139	0.212	0.013
NUE28C/85	2.96	47.05	0.09	520.80	14.0	0.6	0.507	0.015	0.594	0.200	0.007

Table 3.8 Correlation coefficients and comparative parameters ($X_{Au=1}$, $X_{Au=100}$, and ΔX_{Au}) derived from $\log_{10}$ trace element concentrations from whole rock analysis (IML-100) of mineralized samples.

Laminated Quartz Veins	Correlation Coefficient	$X_{Au=1}$ (ppm)	$X_{Au=100}$ (ppm)	ΔX_{Au} (%)
Au	1			
Ag	0.87	$Ag_{Au=1}$ = 0.90	$Ag_{Au=100}$ = 16.38	ΔAg_{Au} = 1720
Bi	0.55	$Bi_{Au=1}$ = 0.74	$Bi_{Au=100}$ = 6.15	ΔBi_{Au} = 731
Pb	0.54	$Pb_{Au=1}$ =3.28	$Pb_{Au=100}$ = 13.67	ΔPb_{Au} = 317
Te	0.73	$Te_{Au=1}$ =1.80	$Te_{Au=100}$ = 22.66	ΔTe_{Au} = 1159
Phyllic Alteration[1]				
Au	1			
Ag	0.94	$Ag_{Au=1}$ = 0.61	$Ag_{Au=100}$ = 15.32	ΔAg_{Au} = 2411
ΔC_{Ag-Au}	0.07			
Bi	0.87	$Bi_{Au=1}$ = 0.55	$Bi_{Au=100}$ = 19.07	ΔBi_{Au} = 3367
ΔC_{Bi-Au}	0.32			
Pb	0.75	$Pb_{Au=1}$ = 3.28	$Pb_{Au=100}$ = 35.10	ΔPb_{Au} = 970
ΔC_{Pb-Au}	0.21			
Te	0.99	$Te_{Au=1}$ = 1.90	$Te_{Au=100}$ =181.45	ΔTe_{Au} = 9450
ΔC_{Te-Au}	0.26			
$\sum\Delta C$	0.86			
Massive Pyrite Veins[1]				
Au	1			
Ag	0.41	$Ag_{Au=1}$ = 2.18	$Ag_{Au=100}$ = 5.23	ΔAg_{Au} = 140
ΔC_{Ag-Au}	0.46			
Bi	0.24	$Bi_{Au=1}$ = 5.13	$Bi_{Au=100}$ = 12.89	ΔBi_{Au} = 151
ΔC_{Bi-Au}	0.31			
Pb	0.04	$Pb_{Au=1}$ = 3.17	$Pb_{Au=100}$ = 3.48	ΔPb_{Au} = 10
ΔC_{Pb-Au}	0.50			
Te	0.54	$Te_{Au=1}$ = 4.76	$Te_{Au=100}$ = 27.39	ΔTe_{Au} = 475
ΔC_{Te-Au}	0.19			
$\sum\Delta C$	1.46			

[1] ΔC_{x-Au} and $\sum\Delta C$ values for both phyllic alteration and pyrite vein samples are calculated relative to laminated quartz vein samples.

Table 3.9 Correlation coefficients and comparative parameters ($X_{Au=1}$, $X_{Au=100}$, and ΔX_{Au}) derived from $\log_{10}$ trace element data from LA-ICP-MS trace element analysis of gold-bearing Py_1 and Py_2.

Py_1[1]	Correlation Coefficient	$X_{Au=1}$ (ppm)	$X_{Au=100}$ (ppm)	ΔX_{Au} (%)
Au	1			
Ag	0.74	$Ag_{Au=1}$ = 1.64	$Ag_{Au=100}$ = 47.30	ΔAg_{Au} = 2784
ΔC_{Ag-Au}	0.13	*$Ag_{Au=1}$ = 0.74	*$Ag_{Au=100}$ = 30.92	*ΔAg_{Au} = 1064
Bi	0.74	$Bi_{Au=1}$ = 1.61	$Bi_{Au=100}$ = 24.37	ΔBi_{Au} = 940
ΔC_{Bi-Au}	0.19	*$Bi_{Au=1}$ = 0.87	*$Bi_{Au=100}$ = 18.22	*ΔBi_{Au} = 209
Pb	0.26	$Pb_{Au=1}$ = 3.66	$Pb_{Au=100}$ = 11.57	ΔPb_{Au} = 216
ΔC_{Pb-Au}	0.28	*$Pb_{Au=1}$ = 0.38	*$Pb_{Au=100}$ = 2.1	*ΔPb_{Au} = 101
Te	0.76	$Te_{Au=1}$ = 11.23	$Te_{Au=100}$ = 169.97	ΔTe_{Au} = 1414
ΔC_{Te-Au}	0.03	*$Te_{Au=1}$ = 9.43	*$Te_{Au=100}$ = 147.31	*ΔTe_{Au} = 255
$\Delta C_{\Sigma-Au}$	0.63			
Py_2[1]				
Au	1			
Ag	0.65	$Ag_{Au=1}$ = 1.59	$Ag_{Au=100}$ = 55.13	ΔAg_{Au} = 3367
ΔC_{Ag-Au}	0.24	*$Ag_{Au=1}$ = 0.59	*$Ag_{Au=100}$ = 49.9	*ΔAg_{Au} = 3227
Bi	0.22	$Bi_{Au=1}$ = 4.27	$Bi_{Au=100}$ = 18.64	ΔBi_{Au} = 337
ΔC_{Bi-Au}	0.02	*$Bi_{Au=1}$ = 0.86	*$Bi_{Au=100}$ = 5.75	*ΔBi_{Au} = 186
Pb	0.09	$Pb_{Au=1}$ = 9.35	$Pb_{Au=100}$ = 17.82	ΔPb_{Au} = 91
ΔC_{Pb-Au}	0.05	*$Pb_{Au=1}$ = 6.18	*$Pb_{Au=100}$ = 14.34	*ΔPb_{Au} = 81
Te	0.26	$Te_{Au=1}$ = 47.69	$Te_{Au=100}$ = 114.40	ΔTe_{Au} = 140
ΔC_{Te-Au}	0.28	*$Te_{Au=1}$ = 42.93	*$Te_{Au=100}$ = 87.01	*ΔTe_{Au} = 335
$\Delta C_{\Sigma-Au}$	0.59			

[1] ΔC_{x-Au} and $\Delta C_{\Sigma-Au}$ values calculated for Py_1 are relative to the laminated quartz vein population; ΔC_{x-Au} and $\Delta C_{\Sigma-Au}$ values calculated for Py_2 are relative to the massive pyrite vein population. * X_{Au} values are the differences between X_{Au} values calculated for the laminated quartz veins population and massive pyrite vein population, and X_{Au} values calculated for Py_1 and Py_2, respectively.

Table 3.10 Summary of microthermometric measurements, salinity, and density of fluid inclusion assemblages in Qtz_1 (sample BD-30).

Site	Inclusion Type	FIA Type[1]	T_m CO_2 (˚C)	T_m Clath (˚C)[2]	T_h CO_2 (l) (˚C)	Wt. % Equiv. NaCl	Density (CO_2)	XCO_2	No. Inclusions
1	4	S	-57.5		9.6 (2)		0.864		5
					16.8 (3)		0.805		
2	1	S	-57.6	5.9	3.8	7.1	0.904	0.17	4
					21.5	7.3	0.757	0.15	
					23.0 (2)	7.3	0.738	0.15	
3	4	I	-56.5		0.5		0.924		6
					3.0		0.909		
					3.5		0.906		
					5.7 (3)		0.891		
4	1	S	-57.2	5.5	24.4	8.0	0.719	0.14	3
					27.7(2)	8.0	0.662	0.13	
5	1	S	-56.7	7.9	9.1 (2)	3.7	0.868	0.16	4
					20.0	3.7	0.773	0.15	
					23.9	3.7	0.726	0.14	
6	1	S	-57.4	7.1	10.5	5.2	0.857	0.16	11
					12.4	5.2	0.843	0.16	
					13.3(2)	5.2	0.835	0.16	
					16.3(2)	5.2	0.810	0.15	
					16.8	5.2	0.805	0.15	
					18.9	5.2	0.785	0.15	
					21.7	5.2	0.754	0.15	
					23.9	5.2	0.726	0.14	
					24.2	5.2	0.722	0.14	
7	2	S	-57.4		0.1(2)		0.927	0.62	11
					0.6		0.924	0.61	
					3.0		0.909	0.62	
					8.3		0.873	0.61	
					10.2		0.860	0.60	
					10.7(2)		0.856	0.60	
					12.3		0.843	0.60	
					13.6		0.833	0.60	
					14.8		0.824	0.59	
7	1	S	-57.6	6.6	12.3	6.1	0.843	0.16	3
					13.6	6.1	0.833	0.16	
					14.1	6.1	0.829	0.16	
8	4	S	-57.2		6.7(3)		0.885		4
					8.8		0.870		
9	1	S	-57.7	7.2	13.3	5.0	0.836	0.17	8
					14.8	5.0	0.824	0.16	
					15.8	5.0	0.815	0.15	
					16.8	5.0	0.806	0.15	
					17.7	5.0	0.797	0.15	
					19.6	5.0	0.778	0.15	
					21.1	5.0	0.762	0.15	
					21.3	5.0	0.760	0.15	
10	1	S	-56.5	6.5	11.1	6.2	0.853	0.16	4
					26.2 (3)	6.2	0.691	0.14	
11	1	S	-57.7	5.5	7.3 (4)	8.0	0.880	0.16	8
					8.6 (1)	8.0	0.871	0.16	
					17.9 (2)	8.0	0.795	0.15	
					27.3 (1)	8.0	0.670	0.13	

[1]S = secondary, I = indeterminate. [2]Clath = clathrate.

Table 3.11 Summary of microthermometric measurements and salinity for fluid inclusion assemblages of type 5 inclusions in Qtz_2 (sample NUE-11).

Site	FIA Type[1]	T_m HH (˚C)[2]	T_m Ice (˚C)	Wt. % NaCl	Wt. % $CaCl_2$	T_h (Liquid;˚C)	No. Inclusions
1	I	-29	-25 to -22	7.9	15.2	104-124	11
2	S	-27.5	-18.5	8.4	11.9	114-130	12
3	P	-23	-5	6.3	1.9	135-142	6
4	S	-30 to -26	-13.5	6.6	10.4	135-145	6
5	I	-45	-13	1.3	15.2	145-148	15
6	S	-45	-18.5	1.6	18.4	133-164	10
7	I	-40	-21.5	2.4	19.1	140-153	6
8	S	-28	-18 to -15	7.4	11.7	120-125	7
9	P	-30 to -26.5	-20.5	8.1	13.4	98 -130	13
10	P	-51 to -48	-27 to -24	1.5	21.8	109-121	10
11	P	-42 to -39	-20	2.2	18.5	124-129	6
12	I	-33	-18 to -14	4.0	14.6	134-147	7
13	S	-43 to -40	-23 to -19	2.1	19.1	118-122	5
14	I	-26	-11.5	7.7	7.6	111-120	7
15	S	-42 to -38	-21	2.4	18.9	89-111	5
16	I	-48 to -45	-19	1.5	18.7	75-114	4
17	S	-25	-15 to -12	9.8	7.2	101-132	4
18	S	-34.5	-9	2.4	10.7	129-139	2
19	I	-23.5	-14	12.5	5.0	130-149	5
20	S	-46	-25	1.7	21.3	118-119	3
21	S	-36	-11	2.4	12.6	130	3

[1]P = primary, S = secondary, I = indeterminate. [2]HH = hydrohalite.

Table 3.12 δD (‰) values for type 5 fluid inclusion extracts in vein quartz (Qtz_2).

Sample ID	δD ‰ (SMOW)
NUE-10a	-37
NUE-10b	-37

Table 3.13 Sulfur isotope values ($\delta^{34}S$ and $\delta^{33}S$), and calculated $\Delta^{33}S$ values from samples of Py_1 and Py_2.

Analysis	Generation	$\delta^{34}S$ (‰, VCDT)	$\delta^{33}S$ (‰, VCDT)	$\Delta^{33}S^*$
NUE-1a	Py_2	-3.7	-2.0	-0.1
NUE-1b		-3.7	-2.3	-0.4
NUE-1c		-3.5	-2.1	-0.3
NUE-25a	Py_2	-3.7	-2.3	-0.4
NUE-25b		-2.9	-1.5	0.1
NUE-25c		-3.1	-2.0	-0.4
NUE-31a	Py_2	-3.8	-2.1	-0.2
NUE-31b		-3.8	-2.1	-0.1
NUE-31c		-3.8	-2.2	-0.2
NUE-10a	Py_2	-3.8	-2.5	-0.5
NUE-10b		-3.3	-2.2	-0.4
NUE-10c		-3.2	-1.8	-0.1
P-5a	Py_1	-5.3	-3.0	-0.3
P-5b	Py_1	-5.8	-3.5	-0.5
P-5c	Py_1	-5.4	-3.1	-0.3

*$\Delta^{33}S = \delta^{33}S\text{-}1000((1+ \delta^{34}S/1000)^{0.515}\text{-}1$; after Farquhar and Wing, (2003)

Table 3.14 Summary of the geochemical characteristics of the different hydrothermal events (Au_1, retrograde, and Au_2).

Hydrothermal Event	Mass Balance: Main Chemical Changes[1]	Whole Rock Trace Element Au Associations[2]	LA-ICP-MS Trace Element Au Associations[3]	Fluid Inclusion Chemistry[4]	Causative Fluid Constituents[5]	$\delta^{18}O$ Values in Vein Quartz (‰)	S-Isotope Values in Pyrite (‰)
Au_1 (intrusion-related)	Gains: CO_2, S, K_2O, LOI, Fe_2O_3p, Ba, Rb, W, Ag, Au, Te, Bi, Pb, Cu; Losses: MnO, Na_2O, CaO	Ag, Bi, Te, Pb	Ag, Bi, Te, Pb	H_2O-CO_2-NaCl (avg. X_{CO2}=0.15, 6 wt. % eq. NaCl)	H_2O, CO_2, S, Au, Ag, Cu, Bi, Pb, Te, W, Mo, Zn Ba, K, Rb	Qtz_1—3.9 to 13.4, $\bar{x}$ = 8.4	Py_1— $\delta^{34}S_{Avg.}$ = -5.5; $\delta^{33}S_{Avg.}$ = -3.2; $\Delta^{33}S_{Avg.}$ = -0.3
Retrograde (orogenic)	Retrograde 1— Gains: S, LOI, Na_2O; Losses: P_2O_5, MnO, ∑HREE, ∑LREE, CaO, Ba, Cu Retrograde 2— Gains: S, K_2O, Fe_2O_3P. Ba, Rb; Losses: ~15% total mass loss; FeOp, SiO_2, Na_2O	-	-	H_2O-NaCl-$CaCl_2$-KCl (avg. 18 wt. % total salts, Na/Na+Ca = 0.28)	H_2O, S, Na	Qtz_2—1.2 to 9.7, $\bar{x}$ = 6.7	-
Au_2 (orogenic)	-	Ag, Bi, Te	Ag, Bi, Te, Pb, W, U	-	-	Qtz_3—5.8 to 10.9, $\bar{x}$ = 8.0	Py2— $\delta^{34}S_{Avg.}$ = -3.5; $\delta^{33}S_{Avg.}$ = -2.1; $\Delta^{33}S_{Avg.}$ = -0.4

[1]Reflective of relative % changes ≥30 %. [2]Defined by correlation coefficients in log_{10} data from whole rock analysis. [3]Defined by LA-ICP-MS trace element maps of Py_1 and Py_2. [4]Bulk fluid properties as defined by microthermometry and SEM-EDS mound analysis.[5]Constrained by integrating lithogeochemistry and mass balance with fluid inclusions chemistry, alteration and vein mineralogy, and constraints provided by field-based and petrographic relationships.

Figures

Figure 3.1 Regional location and geological map for the Wawa-Abitibi Subprovince showing the location of the Renabie gold deposit and other producing mines. The geology is simplified from the Ontario Geological Survey (2011); Au deposit locations and tonnage data are from Dubé and Gosselin (2007).

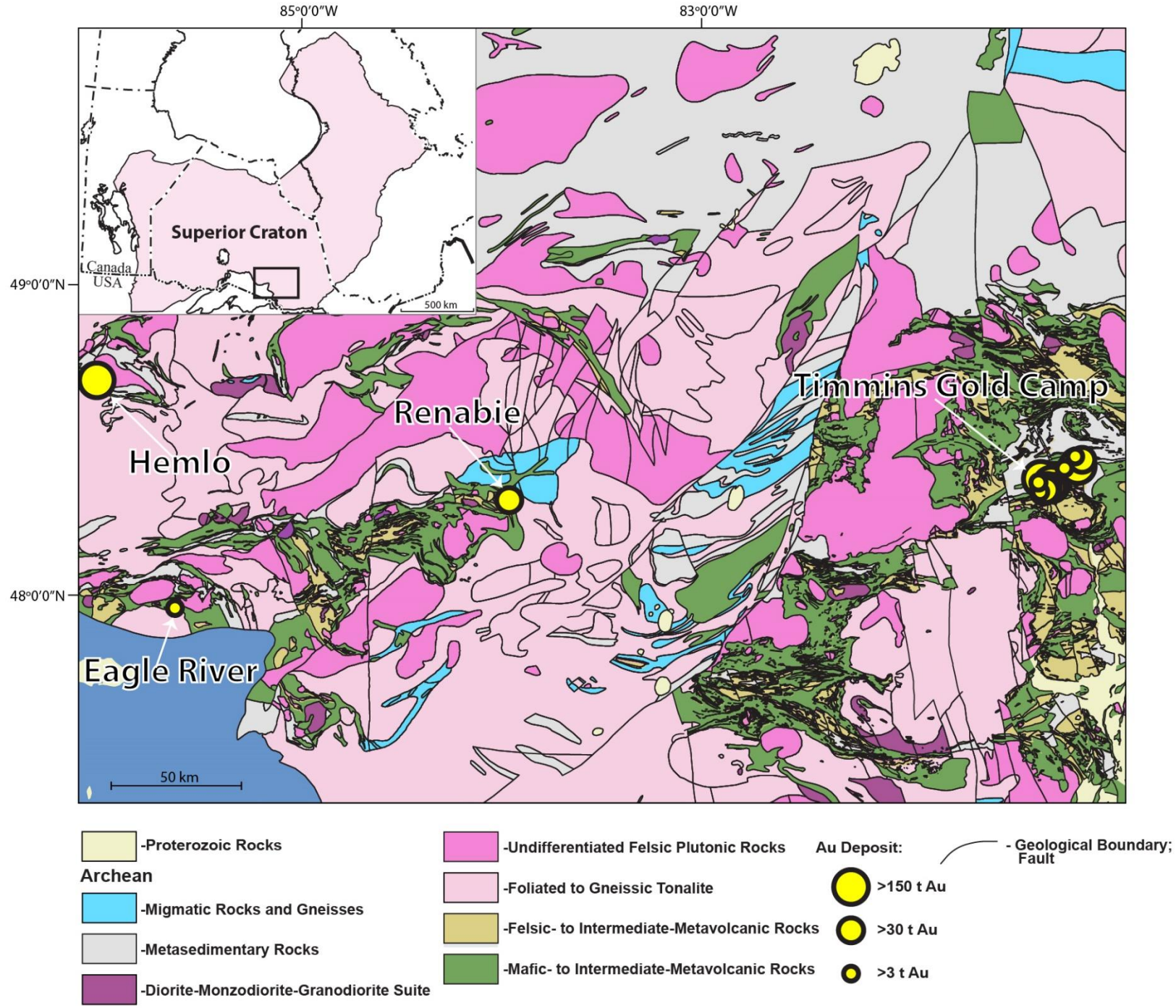

Figure 3.2 (A) Location and simplified geology map of the Missanabie-Renabie gold district (based on Bruce and Horwood, 1942; Riley, 1971; Bennett, 1972). Locations of the various Au occurrences are from Ontario Mineral Deposit Inventory. (B) Geology map of the Renabie mine area (after McDivitt *et al*., 2015; Ferguson, 1968). Coordinates in NAD83 UTM zone 17N.

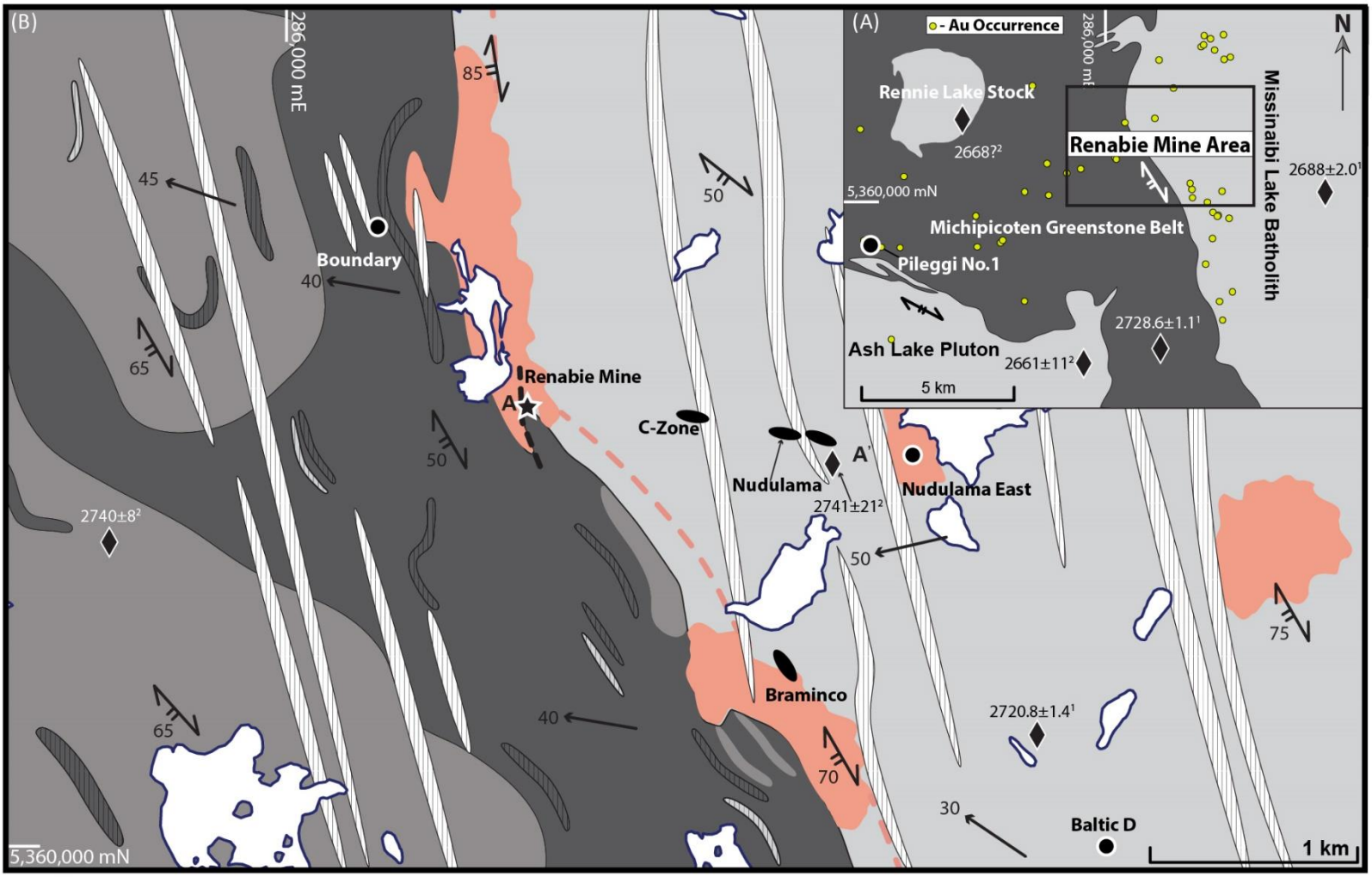

Figure 3.3 Outcrop and photomicrograph images of the different and alteration types. (A) Example of typical laminated quartz vein at the Nudulama East outcrop. Pencil for scale. (B) Textural features of the laminated quartz veins seen in thin section (cross polarized light (CPL)) showing: (1) bimodal grain size distribution of quartz; and (2) planar domains of sericite defining the laminated texture. (C) Photomicrograph (plane polarized light (PPL)) showing the accessory phases present in the laminated quartz veins: (1) Allanite (Ep_2) overgrown by a later, non-LREE bearing epidote (Ep_3); and (2) Pyrite with hematite replacement rims (Py_1). (D) Example of hematite-associated alteration at Nudulama East displaying both proximal (K-feldspar-hematite) and distal (chlorite-titanite-albite-hematite) types of alteration. Scale card for scale (E) Photomicrograph (PPL) of area in D (white box) showing the common infill mineralogy of the hematite-associated alteration veins which consist of quartz (Qtz_2) and epidote; note the euhedral nature of the infill minerals and their comb-like texture. (F) Example of a NW-striking quartz (Qtz_3) tension gash from the Pileggi No. 1 outcrop. Note the S2-transposed nature of the earlier quartz (Qtz_1), and sigmoidal shape of the upper tension gash, which is consistent with dextral movement. Pencil for scale (G) Photomicrograph (PPL) showing typical textural features of Qtz_3, which include high fracture density and local cataclasite. (H) Gold-bearing pyrite (Py_2) vein crosscutting a both proximal and distal hematite-bearing alteration. Photo was taken at the Nudulama East outcrop. Compass for scale (I) Gold-bearing pyrite (Py_2) vein at Nudulama East outcrop showing pyrite on a freshly exposed surface. (J) Photomicrograph (in combined transmitted (PPL) and reflected light) showing pyrite (Py_2) overgrowing the K-feldspar-hematite alteration, which contrasts with image in Chapter 2 showing earlier pyrite being altered to hematite. (K) Photomicrograph (PPL) of biotite-bearing tonalite typical of the Missinaibi Lake batholith. Note the abundant epidote disseminated in the plagioclase which is characteristic of saussuritization. (L) Close up photomicrograph (CPL) of area indicated in image K (black box)

showing saussuritized plagioclase. Compass and pencil are 7 cm and 1 cm wide, respectively; scale card divisions are 1 cm.

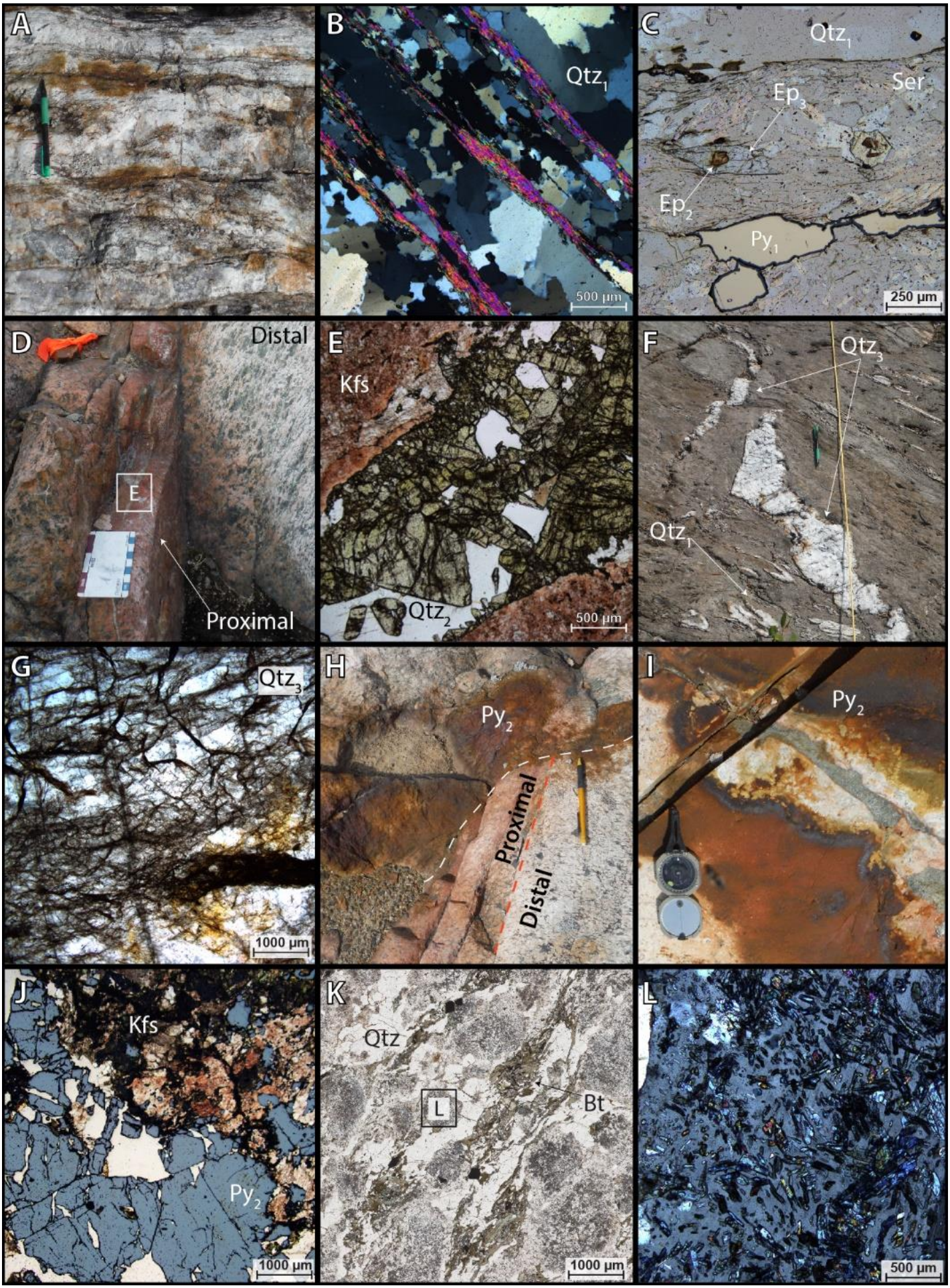
A
B
Qtz1
500 µm
C
Qtz1
Ser
Ep3
Ep2
Py1
250 µm
D
Distal
E
Proximal
E
Kfs
Qtz2
500 µm
F
Qtz3
Qtz1
G
Qtz3
1000 µm
H
Py2
Proximal
Distal
I
Py2
J
Kfs
Py2
1000 µm
K
Qtz
L
Bt
1000 µm
L
500 µm

Figure 3.4 An alteration map of the Nudulama East outcrop showing the following features: (1) saussuritization, which is widespread in the Missinaibi Lake batholith, marginal to the mineralized zones; (2) the phyllic alteration zones and contained veins, which correspond to D3 shear zones (Chapter 2); and (3) the retrograde alteration zones (in red), which represent post-peak-metamorphic hydrothermal activity, in this case preferentially localized proximal to the D3 shear zones. The inset sketches of epidote show Ep_1 and Ep_2, which formed during the saussuritization and phyllic alteration events, respectively, and Ep_3, which formed as part of the prograde metamorphic mineral assemblage, and overgrows both Ep_1 and Ep_2. However, Ep_3 is altered within the retrograde alterations zones, where biotite and horneblende are also retrograded to chlorite (see text for discussion). Coordinates shown are in NAD83 UTM zone 17N.

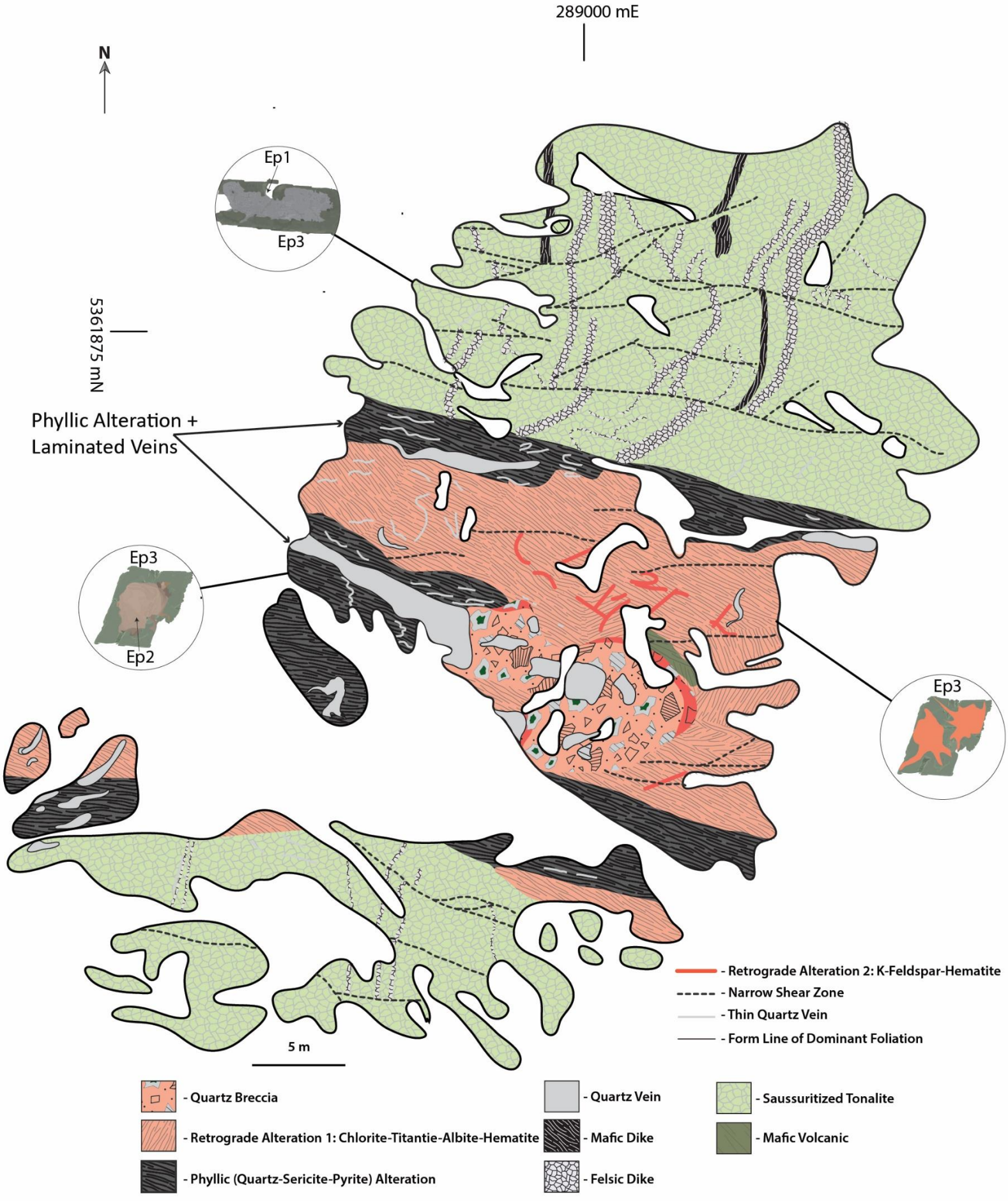
289000 mE
N
Ep1
Ep3
5361875 mN
Phyllic Alteration +
Laminated Veins
Ep3
Ep2
Ep3
- Retrograde Alteration 2: K-Feldspar-Hematite
- Narrow Shear Zone
- Thin Quartz Vein
- Form Line of Dominant Foliation
5 m
- Quartz Breccia
- Retrograde Alteration 1: Chlorite-Titantie-Albite-Hematite
- Phyllic (Quartz-Sericite-Pyrite) Alteration
- Quartz Vein
- Mafic Dike
- Felsic Dike
- Saussuritized Tonalite
- Mafic Volcanic

Figure 3.5 Representative images of alteration mineralogy and minerals of the prograde metamorphic assemblage. (A) An SEM back scattered electron (BSE) image of saussuritized plagioclase; An_{20} plagioclase and Fe-poor Ep_1 define the alteration assemblage. Note that Ep_3 is a later generation with higher Fe content (bright outer rim). (B) Photomicrograph (CPL) displaying clasts of saussuritized plagioclase within a phyllic alteration zone marginal to a laminated quartz vein. (C) Photomicrograph (combined transmitted (PPL) and reflected light) displaying mineralogy characteristic of the phyllic alteration zones: abundant sericite, pyrite that is often rectangular (Py_1), and dark colored allanite (Ep_2). (D) An SEM-BSE image from within a phyllic alteration zone displaying the allanite (Ep_2) overgrown by Ep_3 in a matrix of sericite. (E) Photomicrograph (PPL) of prograde metamorphic minerals: horneblende (Hbl) and epidote (Ep_3) overgrowing biotite (Bt). Note the poikiloblastic nature of the minerals. (F) Photomicrograph (PPL) of prograde-metamorphic Ep_3 overgrowing chalcopyrite (Ccp) and biotite (Bt) at the margin of the phyllic alteration zone at the Nudulama outcrop. (G) Photomicrograph (XPL) of pokiloblastic hornblende (Hbl) both defining and overgrowing the S1 foliation at the Boundary outcrop. (H) Photomicrograph (PPL) displaying the retrograding nature of the retrograde type 1 alteration: both biotite (Bt) and horneblende (Hbl) are altered to chlorite (Chl). Note that a reddish hue seen in plagioclase due to the presence of micro-inclusions of hematite. (I) Photomicrograph (PPL) displaying a more advanced development of the retrograde type 1 alteration compared to that seen in image H. Here biotite (Bt) is pervasively altered to chlorite (Chl) and titanite (Ttn), saussuritized plagioclase is altered to albite (Ab), hematite (Hem), and sericite (Ser), and Ep_3 is in textural disequilibrium with the retrograde type 1 alteration assemblage. (J) An SEM-BSE image of plagioclase in the retrograde type 1 alteration zone shown in I (black box). Note the intergrowth of albite (Ab; darkest), sericite (Ser), and residual An_{20} plagioclase (light grey). (K) Photomicrograph (PPL) displaying mineralogy of the retrograde type 2 alteration. Fine-grained, acicular K-feldspar (Kfs) defines a net-like texture with the inter-crystal space infilled by chlorite. The Ep_3 is altered to

earthy-brown Fe oxides and sulphates. (L) An SEM-BSE image of retrograde type 2 alteration showing K-feldspar (Kfs) hosting rosettes of hematite (Hem).

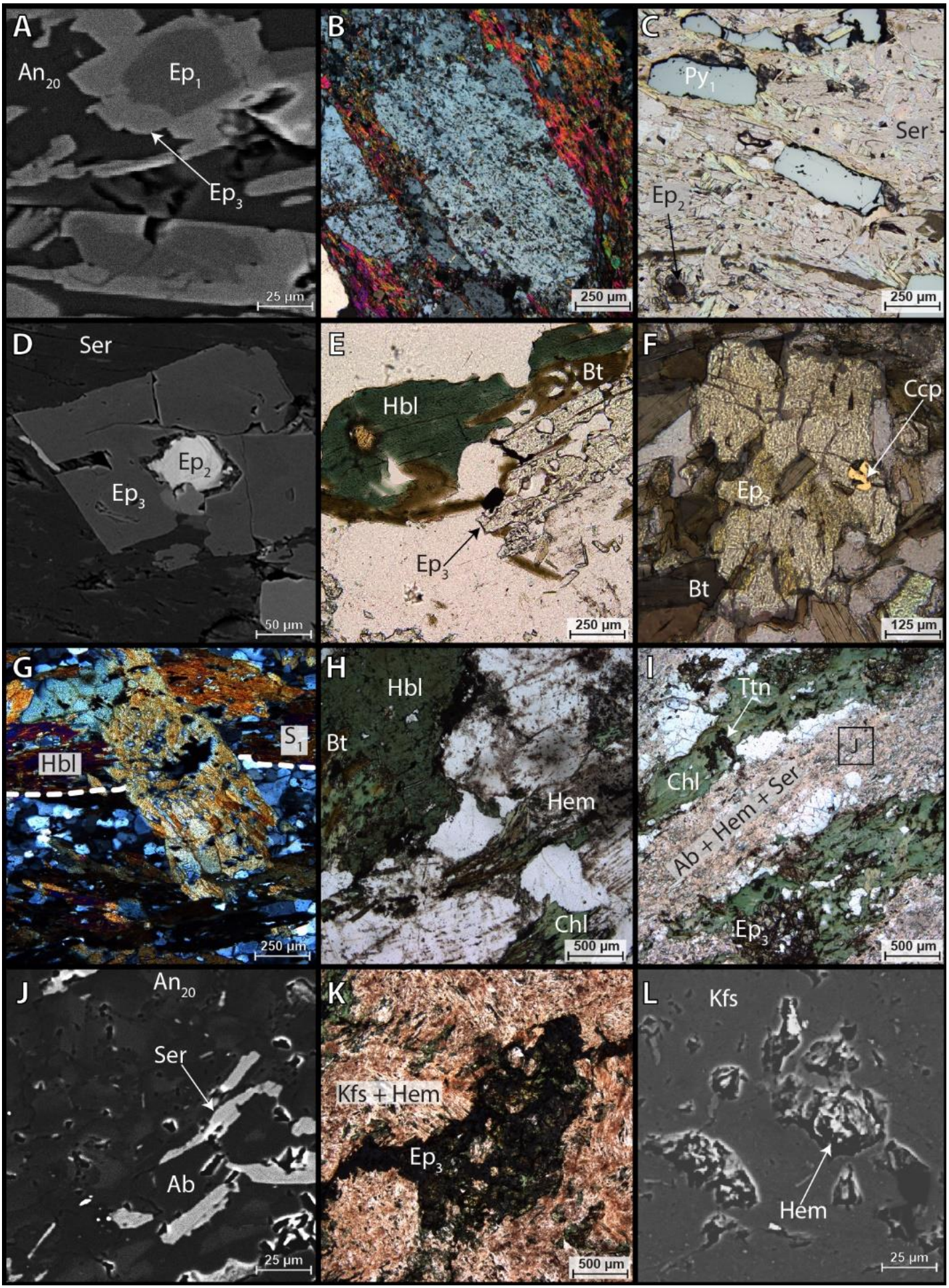
A
An20
Ep1
Ep3
25 µm
B
250 µm
C
Py1
Ser
Ep2
250 µm
D
Ser
Ep2
Ep3
50 µm
E
Bt
Hbl
Ep3
250 µm
F
Ccp
Ep2
Bt
125 µm
G
S1
Hbl
250 µm
H
Hbl
Bt
Hem
Chl
500 µm
I
Ttn
J
Chl
Ab + Hem + Ser
Ep3
500 µm
J
An20
Ser
Ab
25 µm
K
Kfs + Hem
Ep3
500 µm
L
Kfs
Hem
25 µm

Figure 3.6 Plots summarizing the chemistry for the three different types of epidote: (A) a Ca-Al-Fe ternary diagram with an inset to show the different chemistries for Ep_3 (see text for discussion); (B) a bivariate plot for wt. % ∑La, Ce, Nd (Y) versus wt.% Fe (X). Note that while Ep_1, Ep_2, and Ep_3 form distinct populations based on their chemistry, the overgrowths on Ep_1 (Ep_3-Ep_1) and Ep_2 (Ep_3-Ep_2) plot with Ep_3 where it overgrows biotite (Ep_3-Bt).

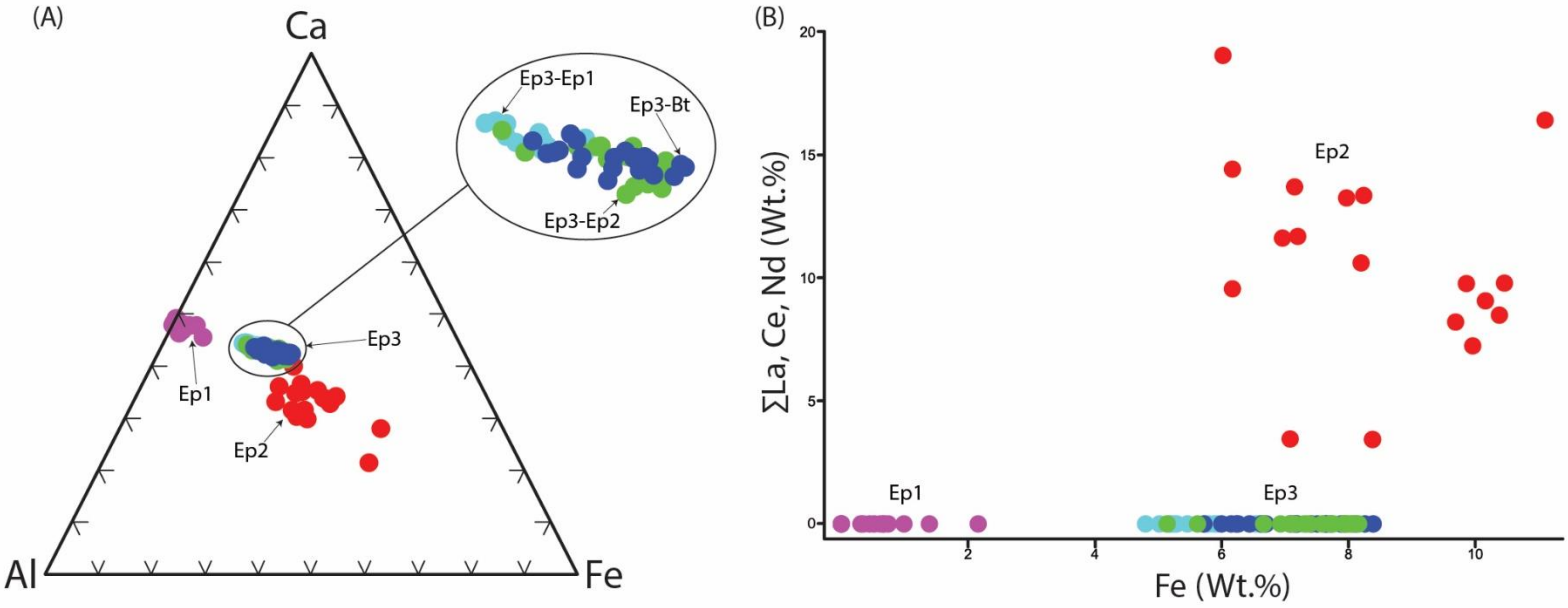

Figure 3.7 The results of mass balance calculations for three altered samples: phyllic (top), retrograde type 1 (middle), and retrograde type 2 (lower). The diagrams on the left are Grant (1986) type isocon plots displaying the least altered precursor (X-axis) versus altered (Y-axis) samples; those on the right show the relative % changes for individual elements in altered samples compared to their precursor. Both the relative % change and change in absolute concentration (above the bar and within the bars) are shown.

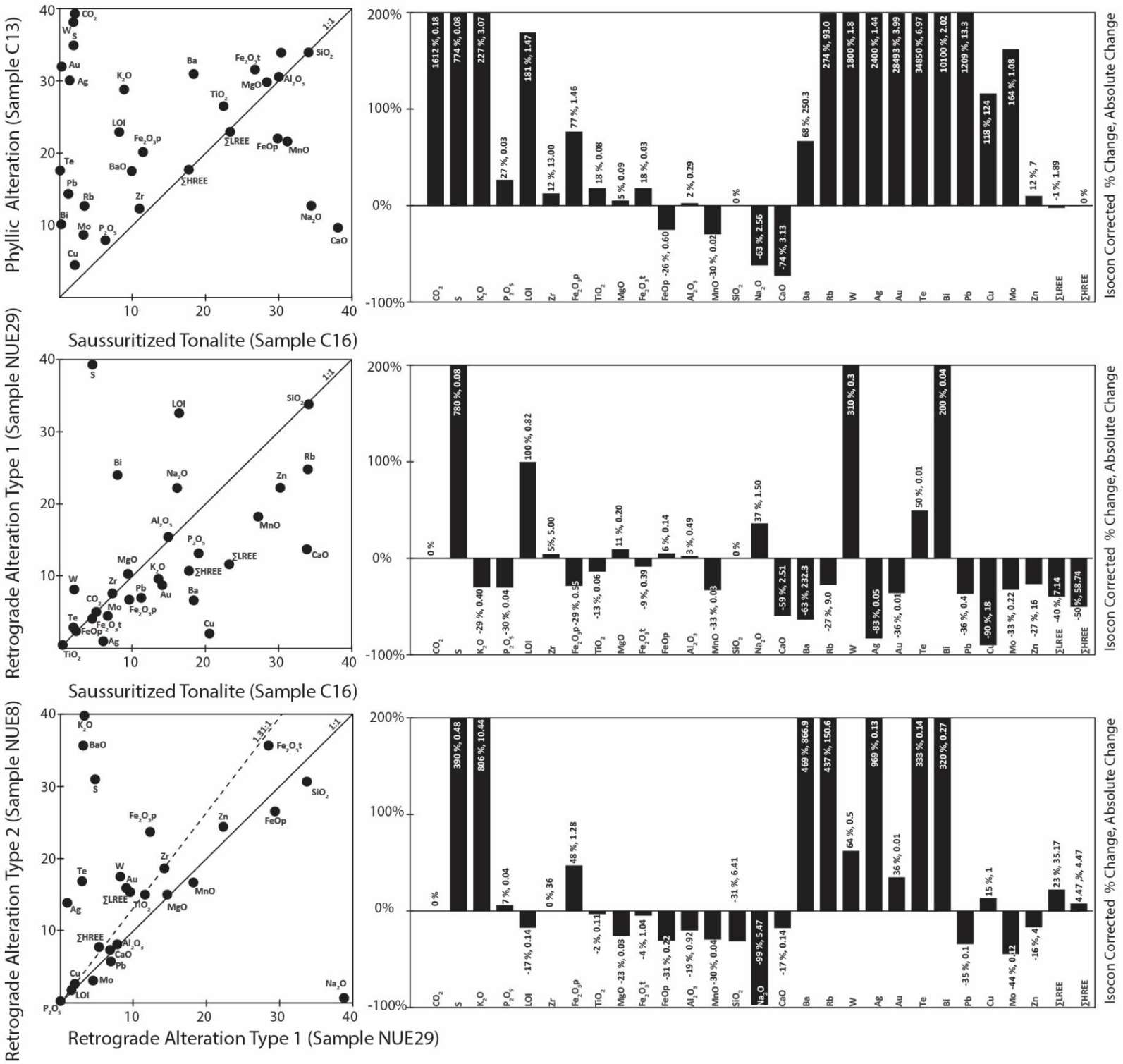
Phyllic Alteration (Sample C13)
Saussuritized Tonalite (Sample C16)
Isocon Corrected % Change, Absolute Change
Retrograde Alteration Type 1 (Sample NUE29)
Saussuritized Tonalite (Sample C16)
Isocon Corrected % Change, Absolute Change
Retrograde Alteration Type 2 (Sample NUE8)
Retrograde Alteration Type 1 (Sample NUE29)
Isocon Corrected % Change, Absolute Change
1:1
1:3:1:1

Figure 3.8 Petrographic images and the results of U-Pb geochronology for titanite in sample NUE-28C. (A) Photomicrograph (PPL) of sample NUE-28 from Nudulama East displaying titanite (Ttn) in association with chlorite (Chl) formed after biotite in a retrograde type 1 alteration zone. (B) An SEM-BSE image in grey scale and overlay of an X-ray map (Ti is red, Mg is green) of titanite grains intergrown with chlorite that were used for in situ LA-ICP-MS U-Pb dating. The light colored cores in some titanite are rutile. (C) A Tera-Wasserburg Concordia diagram summarizing all the analytical data (n=90) for titanite. (D) A Tera-Wasserburg Concordia for the titanite data (n=44) that remained after applying various filters, as discussed in the text. These data provide an age of 2549 ± 24 Ma.

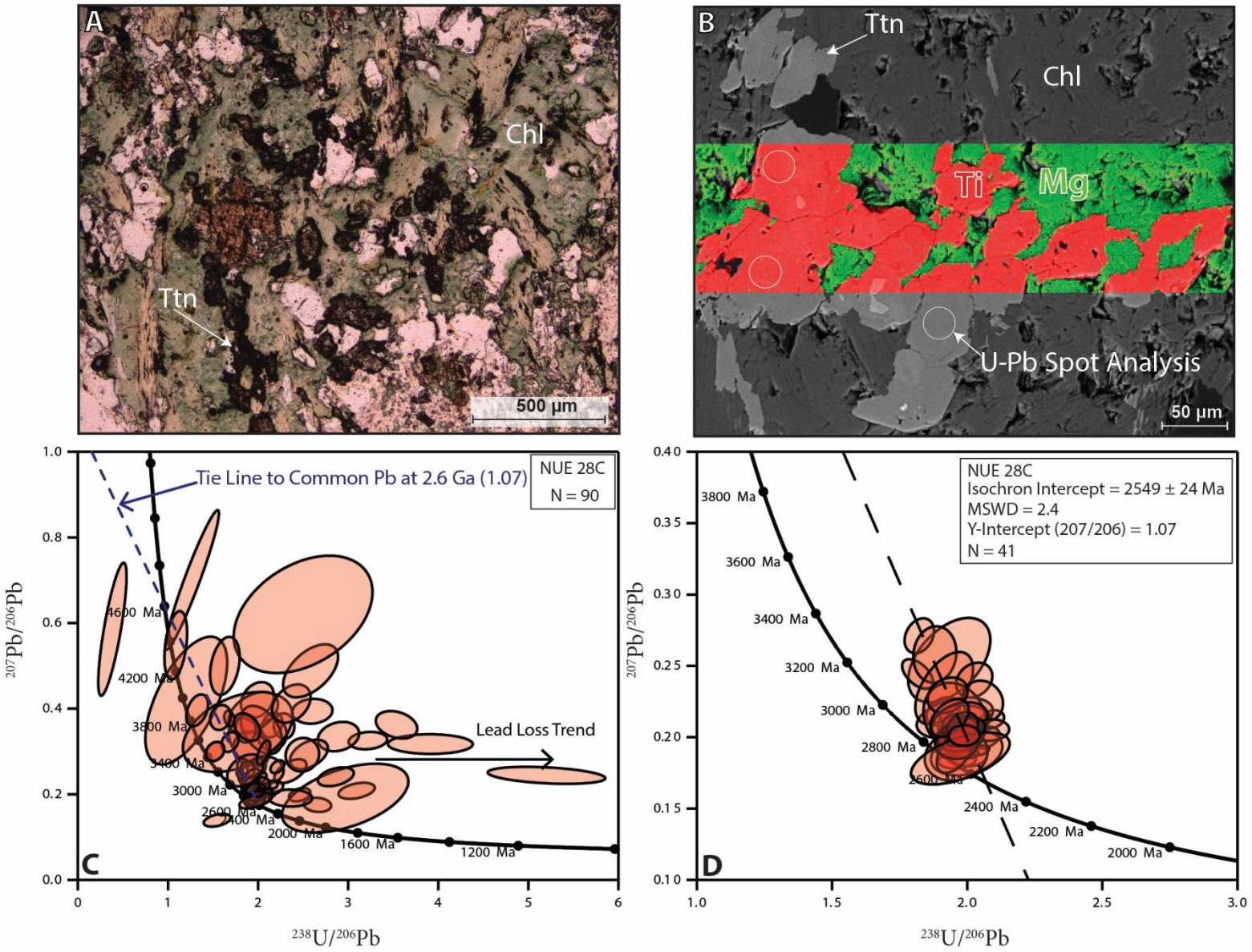

Figure 3.9 Bivariate scatter plots of $\log_{10}$ data from the whole rock analysis of mineralized samples. The elements displayed were selected based on their correlation with Au, the sulfide species within mineralized samples (e.g., chalcopyrite, molybdenite), and the results of LA-ICP-MS trace element mapping of Au-bearing pyrites. For elements that showed a significant correlation with Au in any sample population, a linear regression line and regression equation were determined for each sample population.

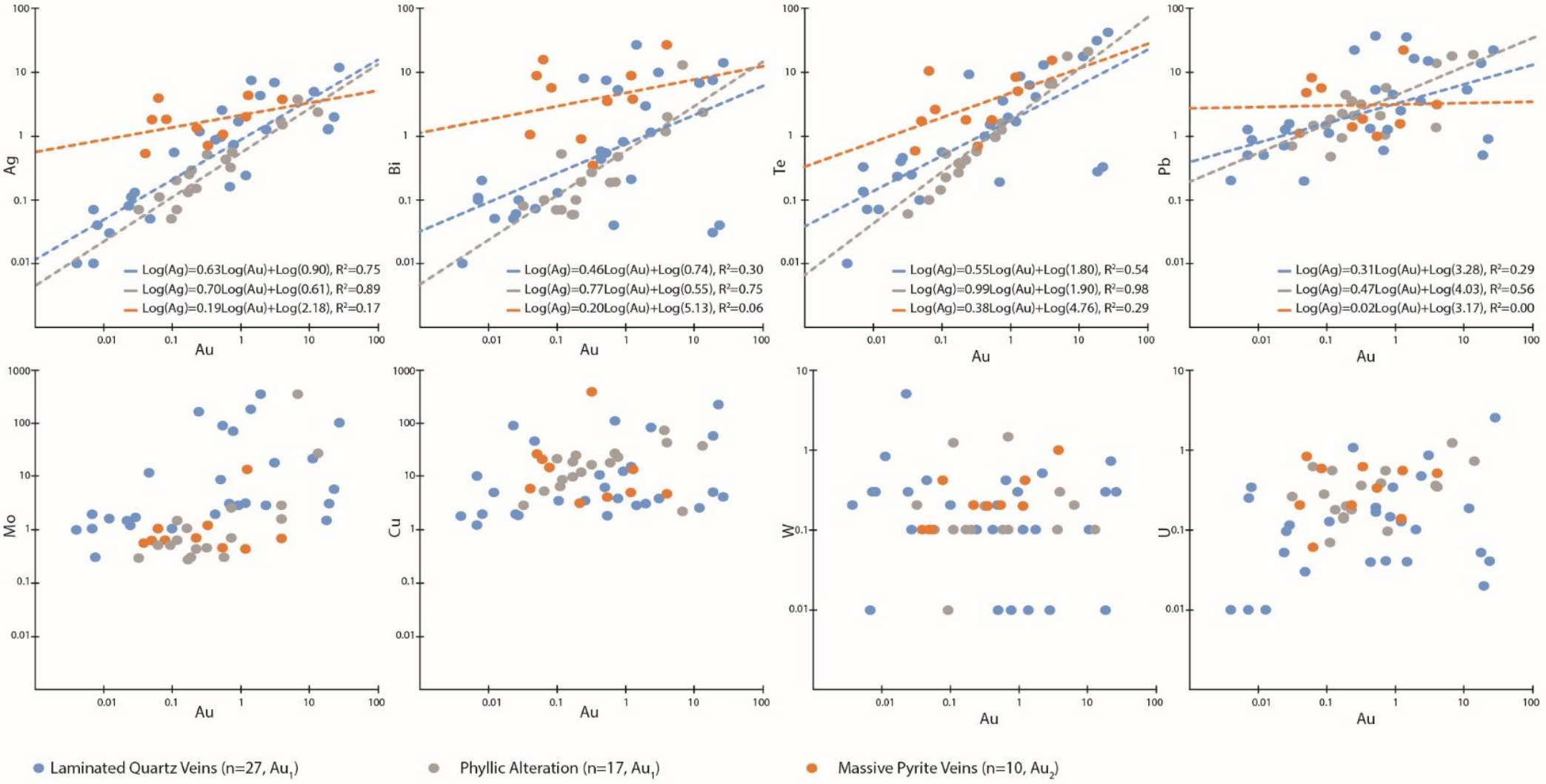
Ag
Au
Log(Ag)=0.63Log(Au)+Log(0.90), R²=0.75
Log(Ag)=0.70Log(Au)+Log(0.61), R²=0.89
Log(Ag)=0.19Log(Au)+Log(2.18), R²=0.17
Bi
Au
Log(Ag)=0.46Log(Au)+Log(0.74), R²=0.30
Log(Ag)=0.77Log(Au)+Log(0.55), R²=0.75
Log(Ag)=0.20Log(Au)+Log(5.13), R²=0.06
Te
Au
Log(Ag)=0.55Log(Au)+Log(1.80), R²=0.54
Log(Ag)=0.99Log(Au)+Log(1.90), R²=0.98
Log(Ag)=0.38Log(Au)+Log(4.76), R²=0.29
Pb
Au
Log(Ag)=0.31Log(Au)+Log(3.28), R²=0.29
Log(Ag)=0.47Log(Au)+Log(4.03), R²=0.56
Log(Ag)=0.02Log(Au)+Log(3.17), R²=0.00
Mo
Au
Cu
Au
W
Au
U
Au
Laminated Quartz Veins (n=27, Au1)
Phyllic Alteration (n=17, Au1)
Massive Pyrite Veins (n=10, Au2)

Figure 3.10 Results of LA-ICP-MS trace element mapping of Py_1. Note the presence of Au_1 alloys included within the pyrite displayed in the SEM-BSE image, an enlargement of the area indicated by the white box in the reflected light image. These inclusions are also shown in red on the grain map, which summarizes the important features of the mapped grain. The plots in the upper portion of the figure are trivariate element plots (the third element is denoted in brackets with concentration indicated by the size and color of the points); elemental distribution maps are shown on the lower portion of the figure.

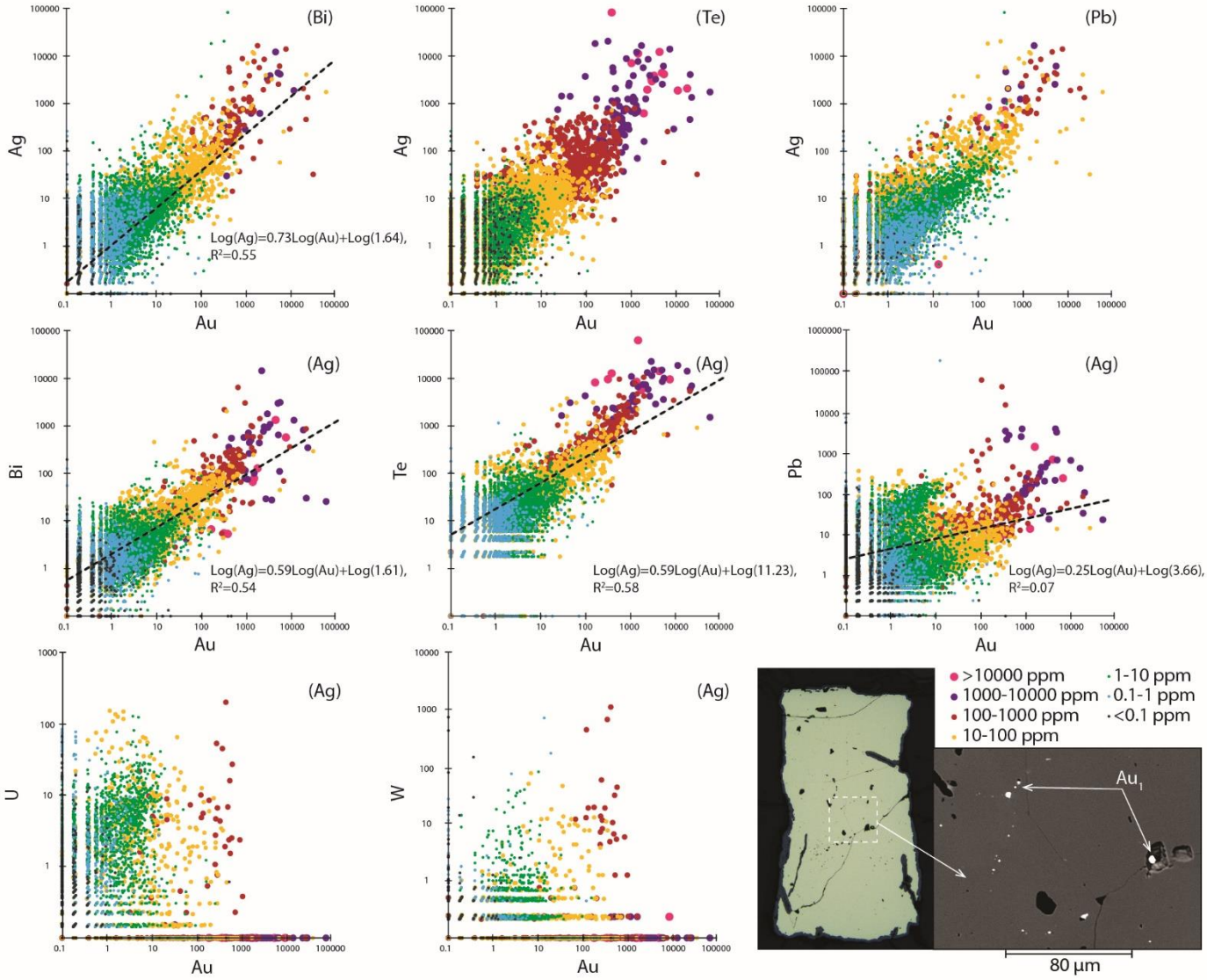
(Bi)
Ag
Au
Log(Ag)=0.73Log(Au)+Log(1.64),
R²=0.55
(Te)
(Pb)
(Ag)
Bi
Log(Ag)=0.59Log(Au)+Log(1.61),
R²=0.54
Te
Log(Ag)=0.59Log(Au)+Log(11.23),
R²=0.58
Pb
Log(Ag)=0.25Log(Au)+Log(3.66),
R²=0.07
U
W
>10000 ppm
1000-10000 ppm
100-1000 ppm
10-100 ppm
1-10 ppm
0.1-1 ppm
<0.1 ppm
Au1
80 µm

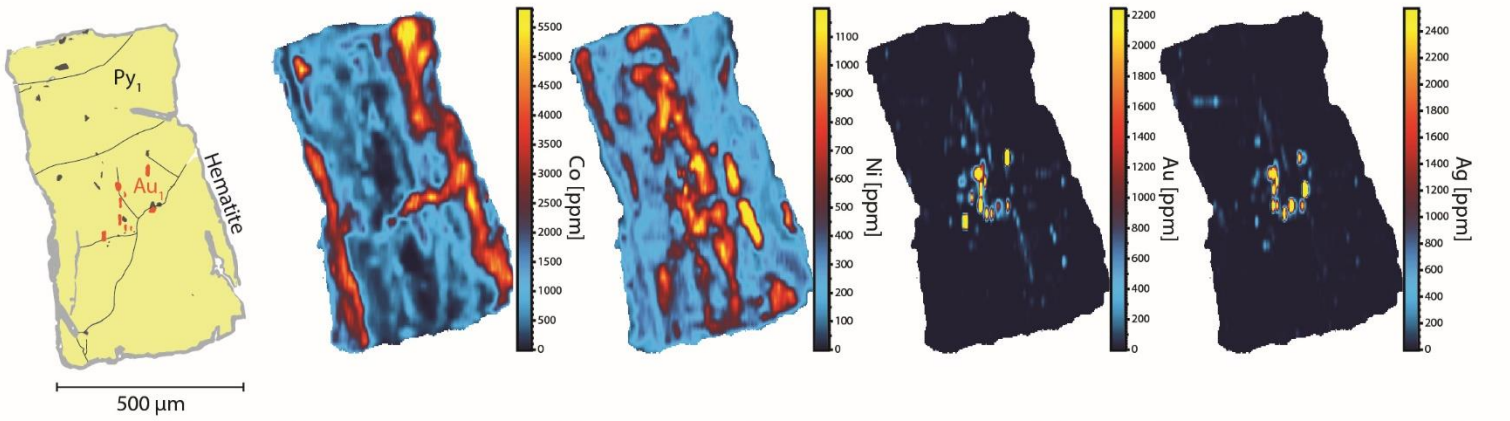
Py1
Au1
Hematite
500 µm
Co [ppm]
Ni [ppm]
Au [ppm]
Ag [ppm]

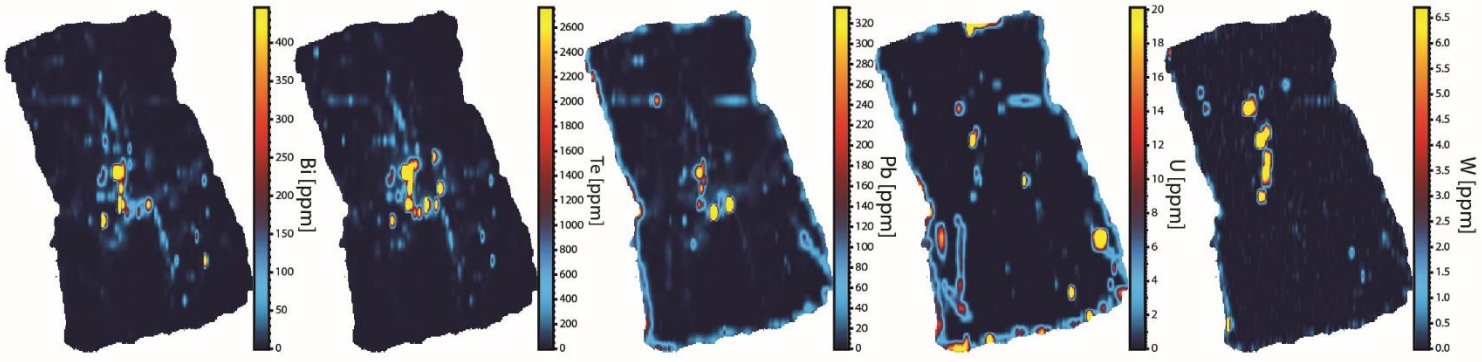
Bi [ppm]
Te [ppm]
Pb [ppm]
U [ppm]
W [ppm]

Figure 3.11 Results of LA-ICP-MS trace element mapping of Py_2. The plots in the upper portion of the figure are trivariate element plots (the third element is denoted in brackets with concentration indicated by the size and color of the points). Also note a reflected light image of the grain. A grain map along with elemental distribution maps are shown on the lower portion.

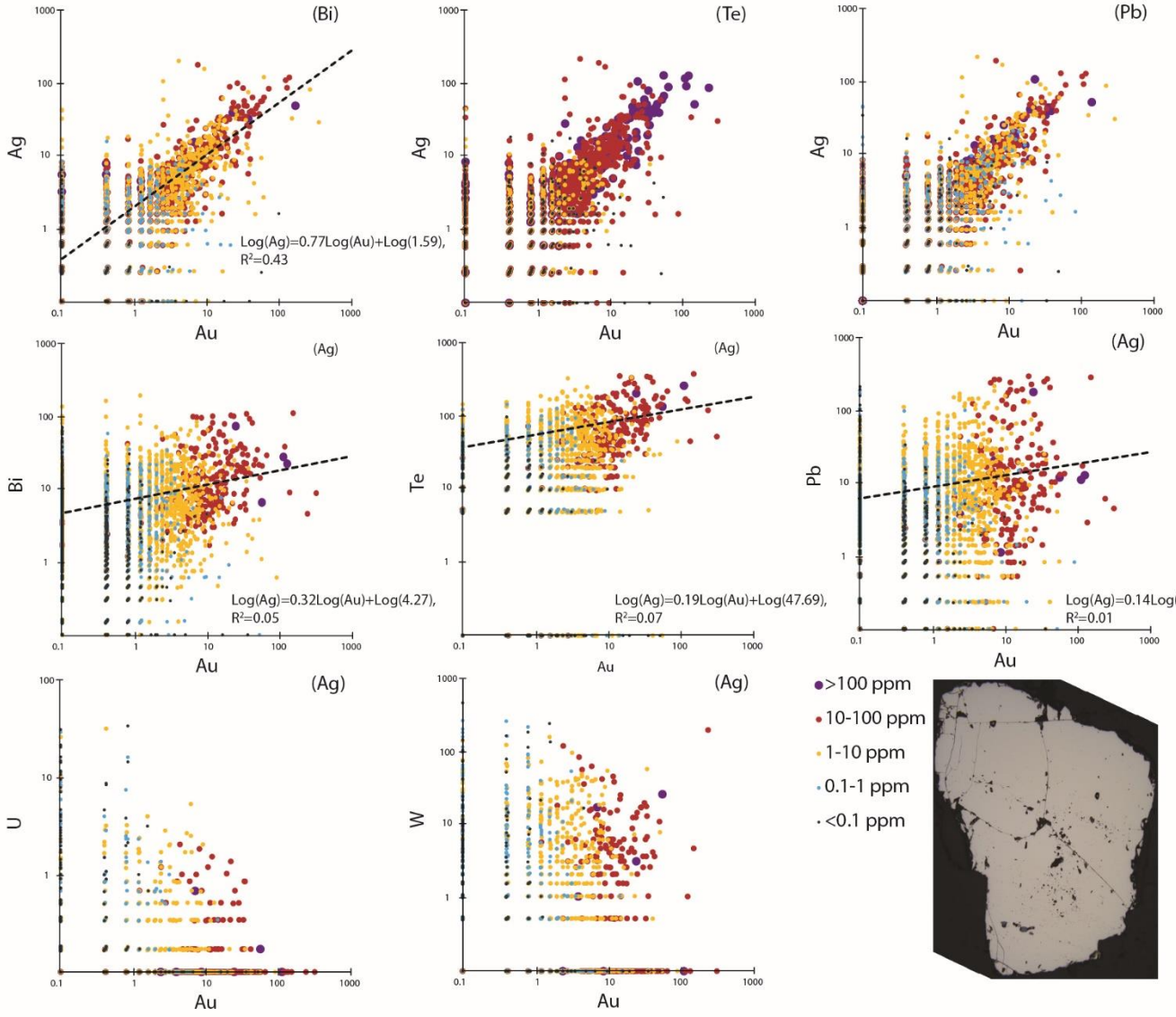
(Bi)
Ag
Au
Log(Ag)=0.77Log(Au)+Log(1.59),
R²=0.43
(Te)
Ag
Au
(Pb)
Ag
Au
(Ag)
Bi
Au
Log(Ag)=0.32Log(Au)+Log(4.27),
R²=0.05
(Ag)
Te
Au
Log(Ag)=0.19Log(Au)+Log(47.69),
R²=0.07
(Ag)
Pb
Au
Log(Ag)=0.14Log(Au)+Log(9.35),
R²=0.01
(Ag)
U
Au
(Ag)
W
Au
>100 ppm
10-100 ppm
1-10 ppm
0.1-1 ppm
<0.1 ppm

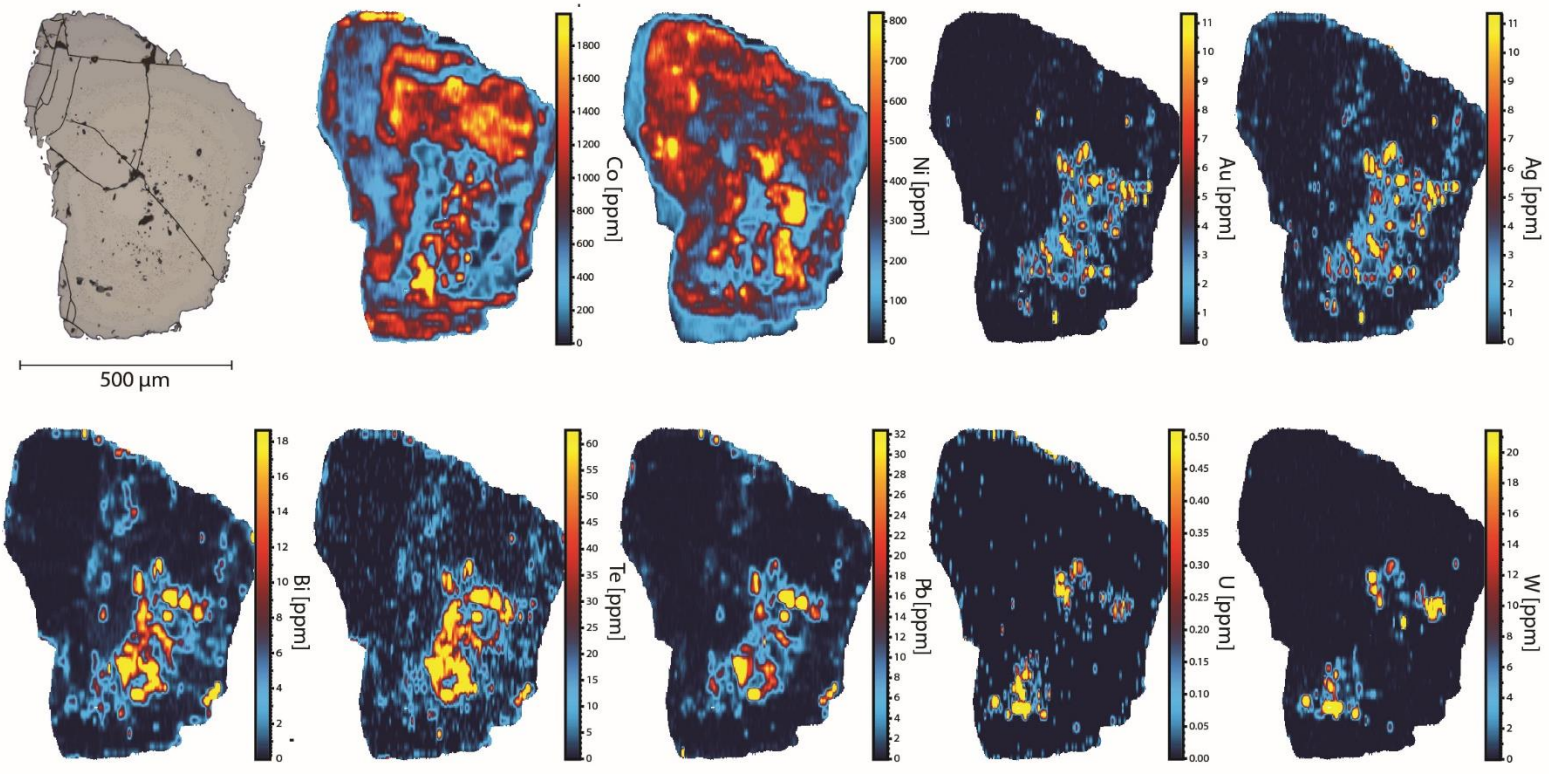
500 µm
Co [ppm]
Ni [ppm]
Au [ppm]
Ag [ppm]
Bi [ppm]
Te [ppm]
Pb [ppm]
U [ppm]
W [ppm]

Figure 3.12 Comparative diagrams displaying different populations of mineralized samples representative of the Au_1 and Au_2 events. (A) Pearson product-moment correlation coefficients defined from log_{10} whole rock (solid lines) and LA-ICP-MS (dashed lines) trace element data; $\sum\Delta C$ values are displayed on a histogram, and emphasize the general maintenance of the magnitude of correlations between different sample populations of the same gold event. (B) $X_{Au=1}$, $X_{Au=100}$, and ΔX_{Au} calculated from regression lines displayed in Figures 3.9 to 3.11. The colored lines correspond to $X_{Au=1}$ and $X_{Au=100}$ values, whereas the dashed black lines correspond to ΔX_{Au} values.

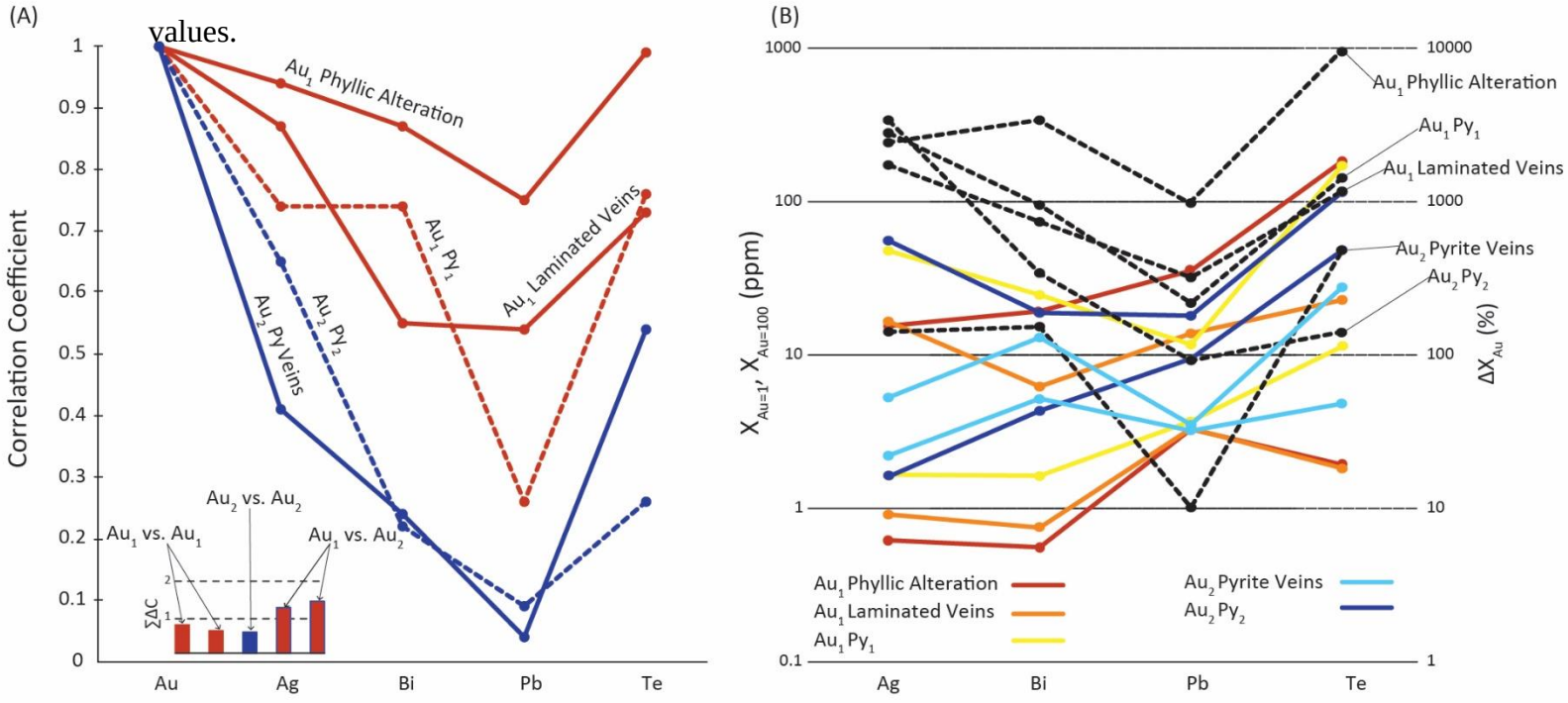

Figure 3.13 Summary of different fluid inclusion types and features. (A) Type 1 fluid inclusions (H_2O-CO_2, ~30 vol. % CO_2) within Qtz_1. Note the image was collected at 10℃ to show the carbonic phase (dark) unmixed to its liquid and vapor components. (B) Examples of CO_2-rich (type 2) and H_2O-rich (type 3) H_2O-CO_2inclusions and pure CO_2 (type 4) inclusions. The arrows denote a secondary FIA where type 2 and type 3 inclusions co-exist. (C) Pure H_2O liquid-vapour inclusions (type 5) within a primary FIA in Qtz_2 from the breccia vein at Nudulama East; note the negative-crystal shapes of these inclusions. (D) An FIA of type 5 inclusions from the breccia vein at Nudulama East. The image was taken at -30℃, subsequent to the melting of hydrohalite, to show that the only solid phase left is ice, and that these inclusions must, therefore, have an X_{NaCl} of about 0.4 (see Fig. 3.15C). (E) A back scattered electron image of a group of fluid inclusion evaporate mounds generated from type 5 inclusions in Qtz_2. (F) A close up of one of the fluid inclusion evaporate mounds shown in E. Note that the amorphous shape (i.e., versus cubic) of the mounds is typical of mounds that are Ca rich (see Kontak, 2004). (G) Sketch of secondary FIAs in Qtz_1 from sample BD-30 (cf., Fig. 3.13A, B). Note the co-existence of types 2 and 3 inclusions within the same FIA and nearby type 1 inclusions within a different FIA. The sketch was completed at 10℃ and the temperature values shown correspond to Th_{CO2} values. Note the variability of Th_{CO2} in type 1 inclusions, whereas the proportion of H_2O and CO_2 in these inclusions remains relatively consistent (see text for discussion).

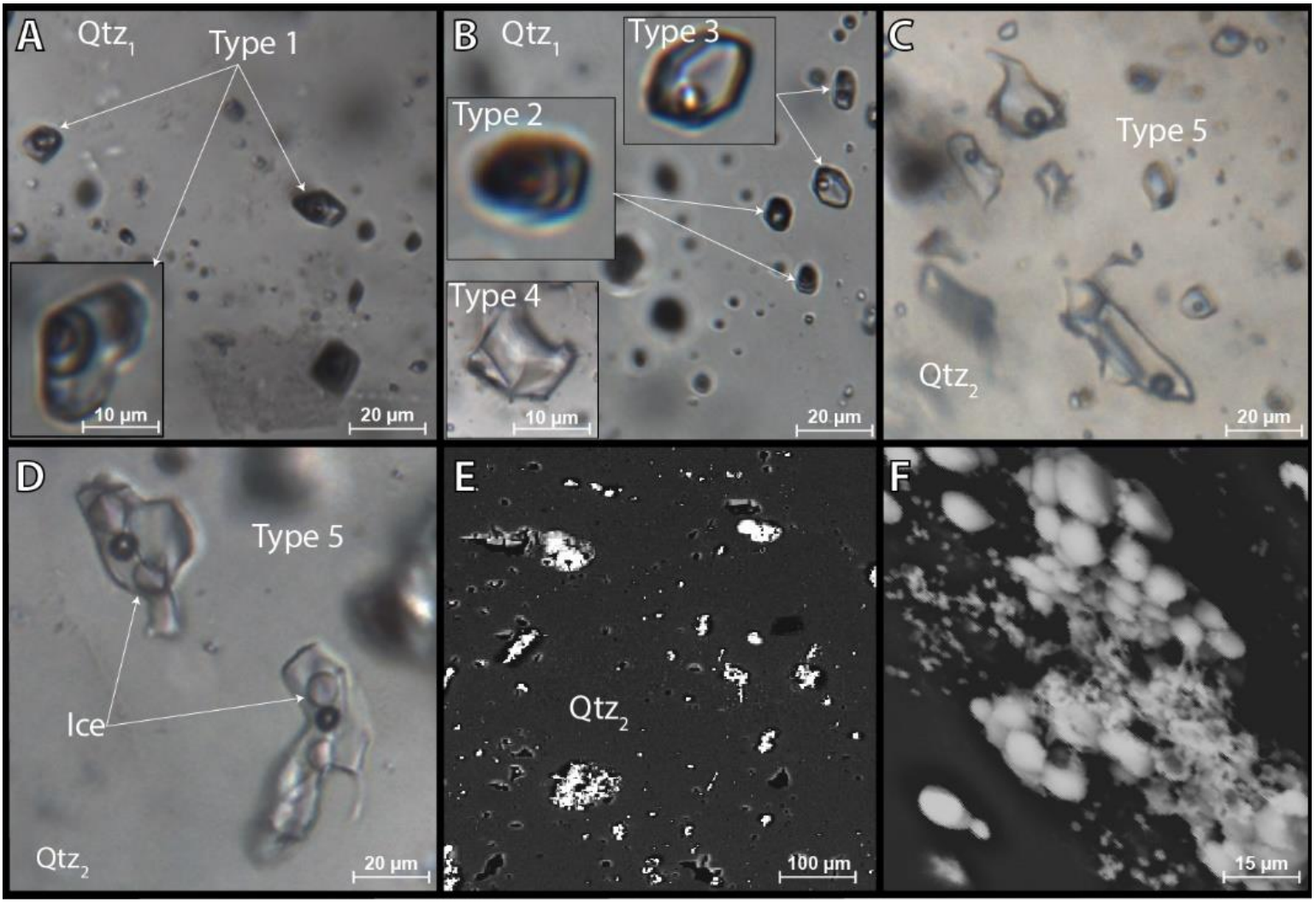
A
Qtz1
Type 1
10 µm
20 µm
B
Qtz1
Type 3
Type 2
Type 4
10 µm
20 µm
C
Type 5
Qtz2
20 µm
D
Type 5
Ice
Qtz2
20 µm
E
Qtz2
100 µm
F
15 µm

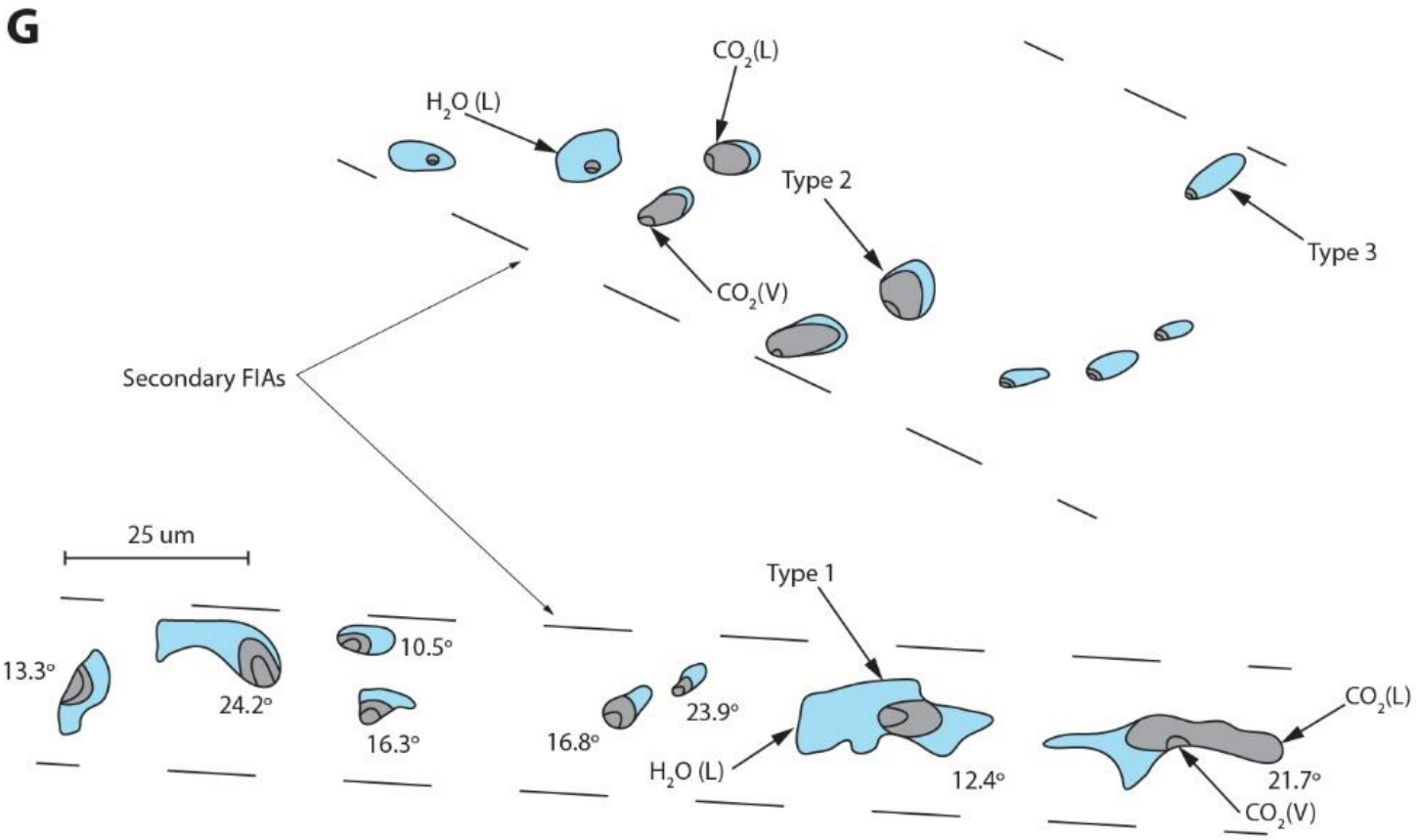
G
CO2(L)
H2O (L)
Type 2
Type 3
CO2(V)
Secondary FIAs
25 um
Type 1
13.3°
24.2°
10.5°
16.3°
16.8°
23.9°
H2O (L)
12.4°
CO2(L)
21.7°
CO2(V)

Figure 3.14 (A) A P-T diagram displaying the isochores for fluid inclusion types 1, 2, and 4 within sample BD-30. Petrographic observations display evidence for unmixing of type 1 inclusions to form CO_2 and H_2O rich endmembers (i.e., types 2, 3, and 4 inclusions), thus the solvus (dark black line) for the H_2O-CO_2-NaCl system (6 wt. % NaCl, 10 mol % CO_2; Schmidt and Bodnar, 2000) is used as a constraint in P-T space. The shaded yellow area displays the inferred range of P-T conditions for laminated quartz vein formation. (B) A P-T diagram displaying iso-T_h lines for 100°C and 150°C for type 5 inclusions along with the L-V curve for the NaCl-H_2O system with 20 wt.% NaCl (after Bodnar and Vityk, 1994). The Th data are for sample NUE-11 and are used to constrain the formation of the breccia vein at Nudulama East, assuming a minimum T of formation of 300°C, as displayed in yellow.

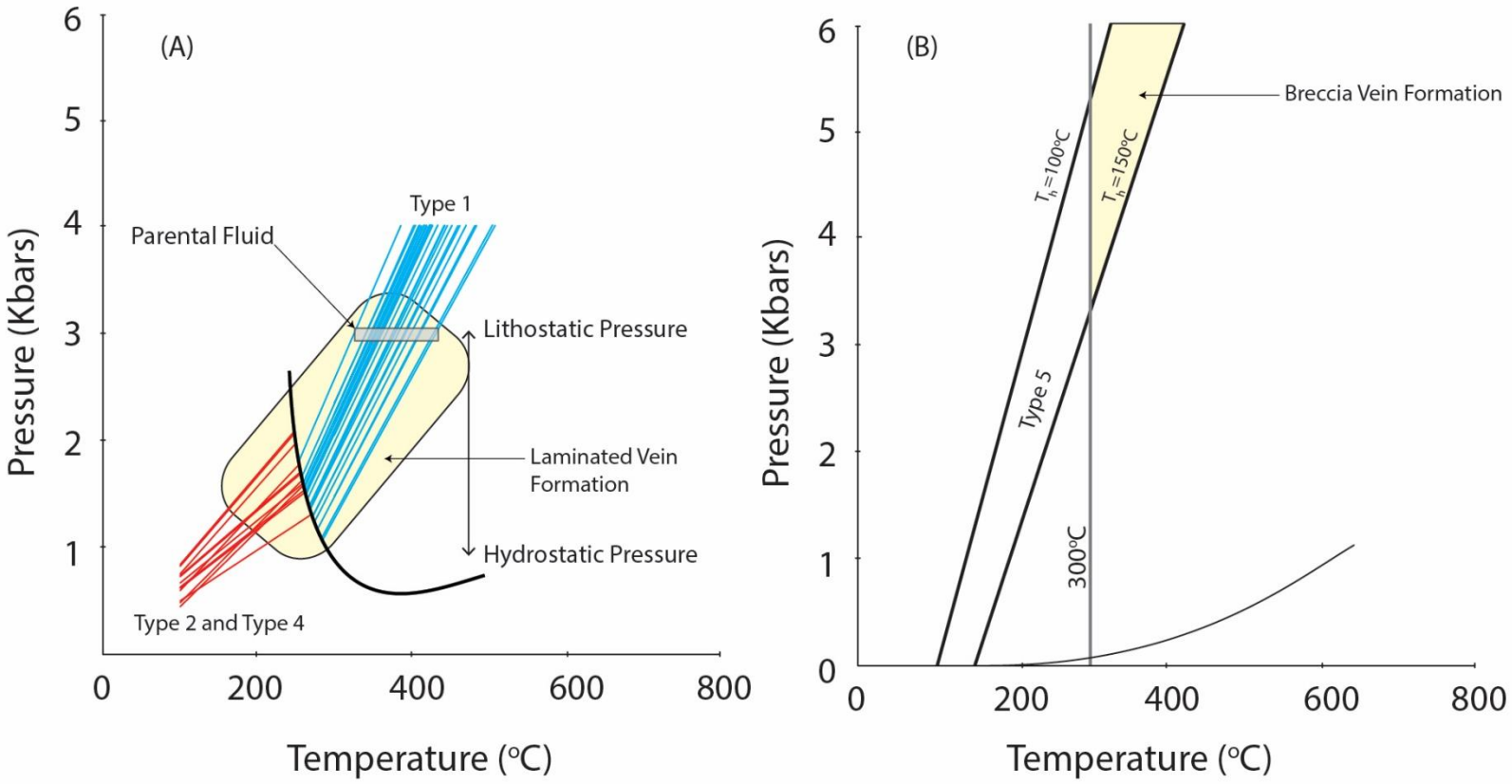

Figure 3.15 Plots summarizing microthermometric data for type 5 fluid inclusions in sample NUE-11. (A) Results for homogenization temperatures (Th). (B) Temperatures of melting for hydrohalite (bold and lower values) and ice (higher values). (C) The H_2O-NaCl-$CaCl_2$ ternary (after Oakes *et al*., 1990; Steele-MacInnis *et al*., 2012) showing the last melting of hydrohalite and ice which are used to estimate the bulk compositions of fluid inclusions. Note that the points represent average data for FIAs; (D) A Na-Ca-K ternary summarizing the results of SEM-EDS analysis of fluid inclusions decrepitate mounds (see Fig. 3.13E, F) for type 5 fluid inclusions in sample NUE-11.

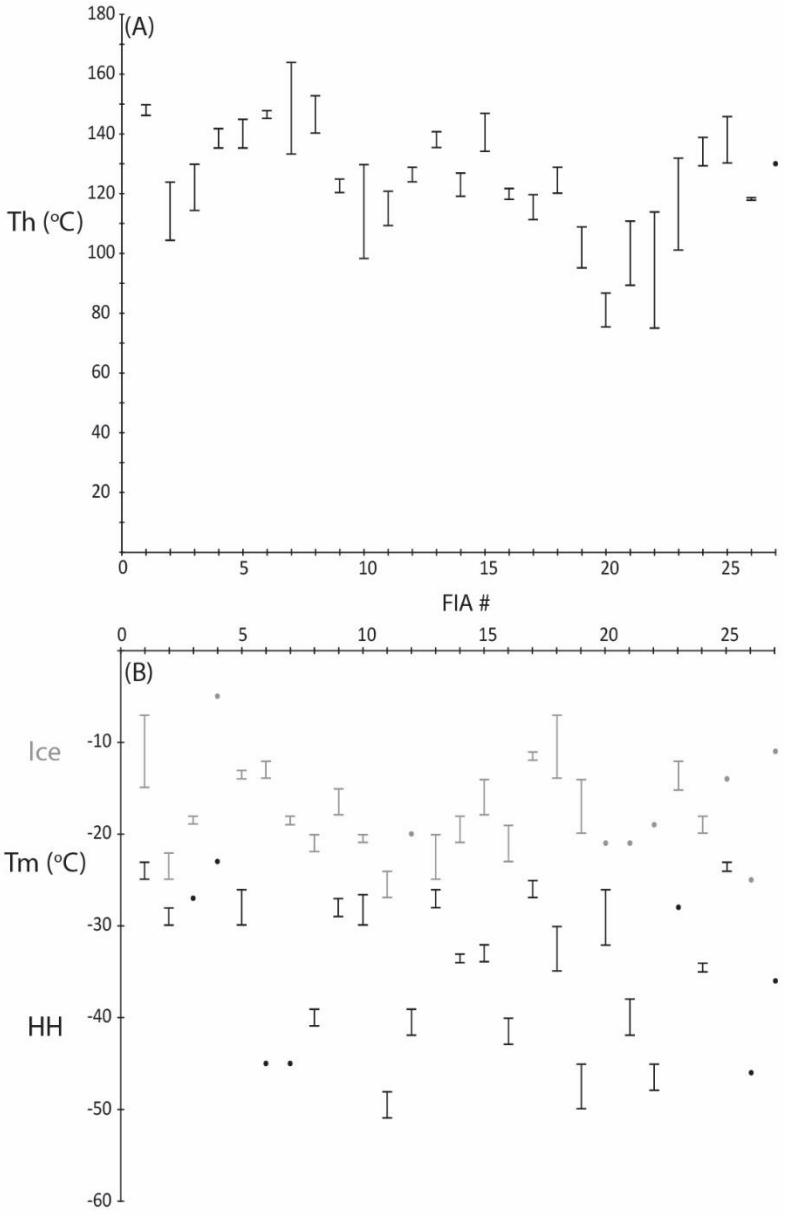

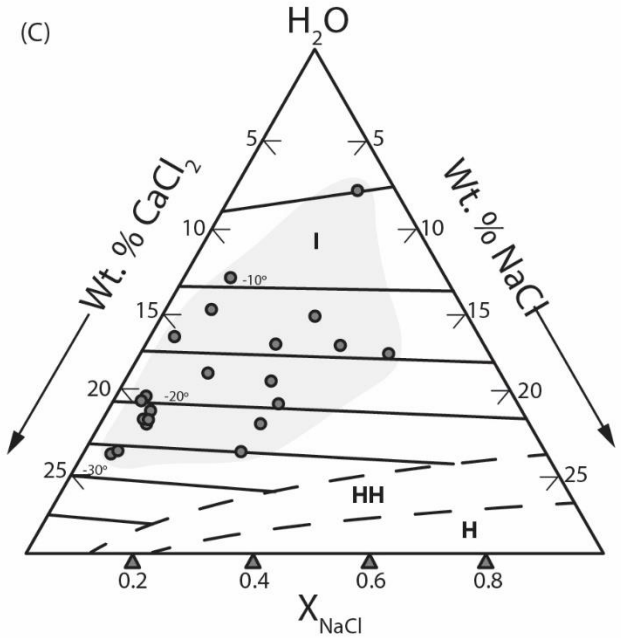

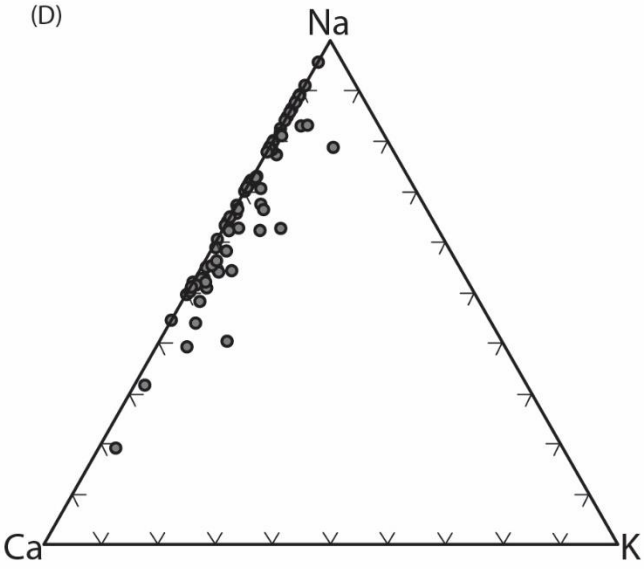

Figure 3.16 Histograms displaying the **r**esults of SIMS $\delta^{18}O$ analysis for quartz from the different generations of veins (A-D). The number of analyses for each vein type is provided. (E) A photomicrograph (PPL) of a euhedral Qtz_2 crystal cut perpendicular to its c-axis showing primary growth zones as defined by type 5 fluid inclusions. The area outlined in the black box indicates the location of the cathodoluminesence image shown in F. (F) Cathodoluminesence image of the Qtz_2 crystal shown in E. The white spots and corresponding values correspond to the location of SIMS spot analysis points and $\delta^{18}O$ values, respectively.

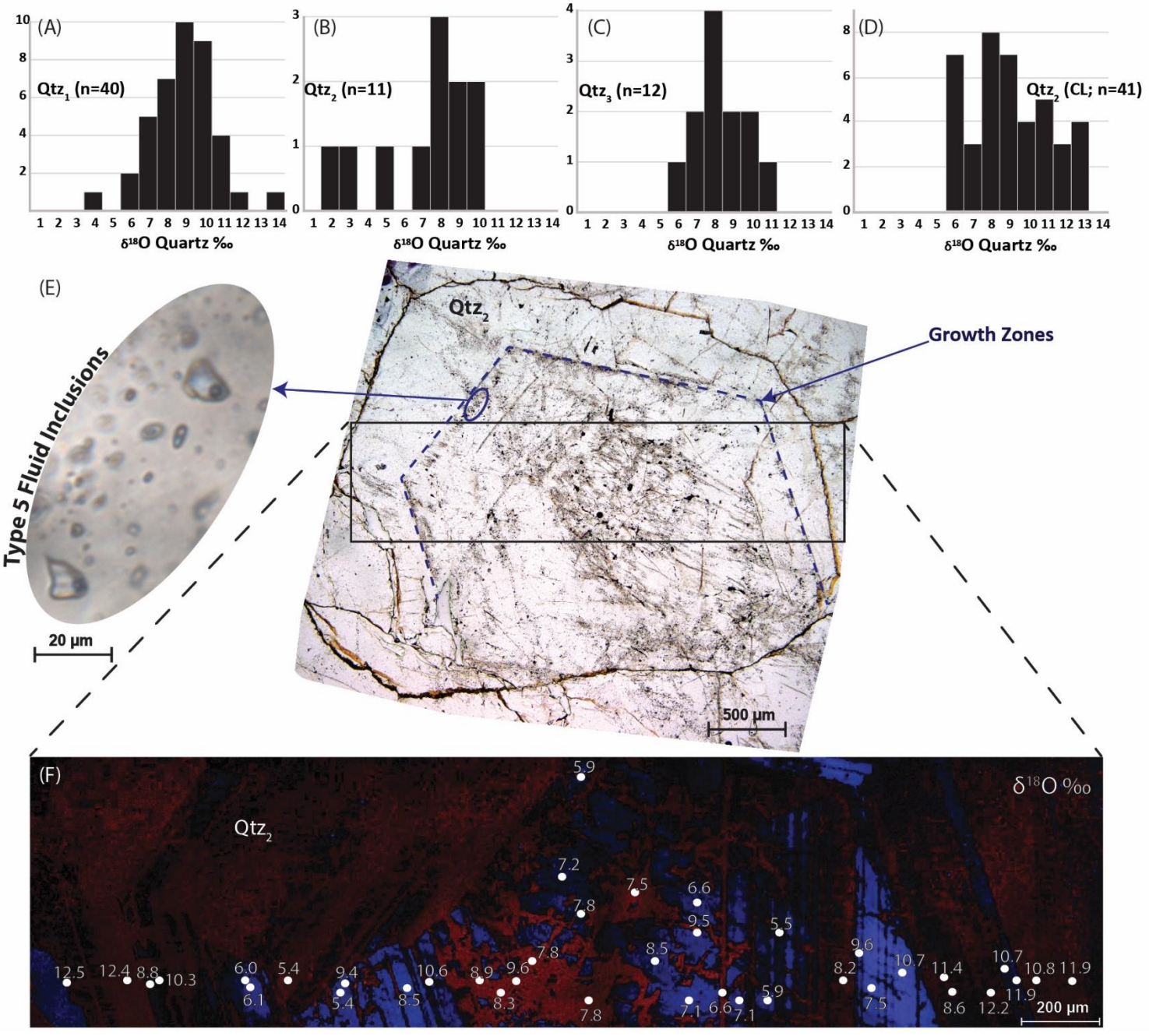

Figure 3.17 A P-T evolution model for the Missanabie-Renabie gold district with an emphasis placed on the hydrothermal and metamorphic events: (1) saussuritization; (2) laminated veins and phyllic alteration (the Au_1 event); (3) the prograde metamorphic assemblage; (4) hematite-associated veining and alteration (the Retrograde event). Shown for reference are the wet tonalite solidus (Chen and Grapes, 2007) and fields for greenschist and amphibolite facies metamorphism (Bucher and Grapes, 2011).

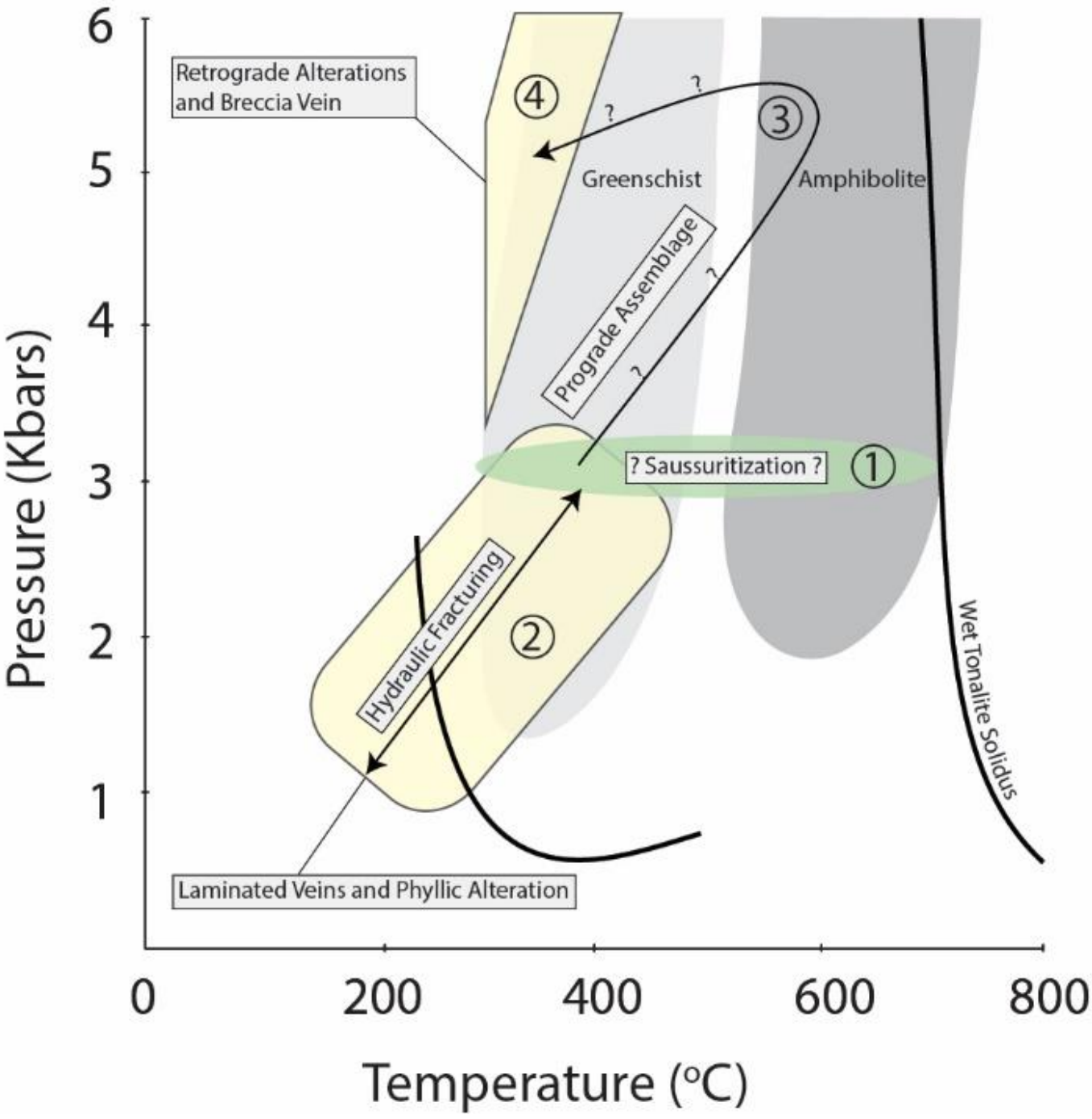

Figure 3.18 A schematic summary diagram, which is largely based on the Nudulama East outcrop, displaying the key hydrothermal, mineralogical, and structural features present at the mineralized zones. Note that the vein orientations are idealized based on preferred trends. The elemental gains and losses for different alteration zones are restricted to the most significant (i.e., ≥30 ‰) changes recorded for the major elements. The diagram emphasizes the composite nature of the ore zones, in the sense that they have formed as the result of a series of temporally distinct yet spatially overlapping hydrothermal events.

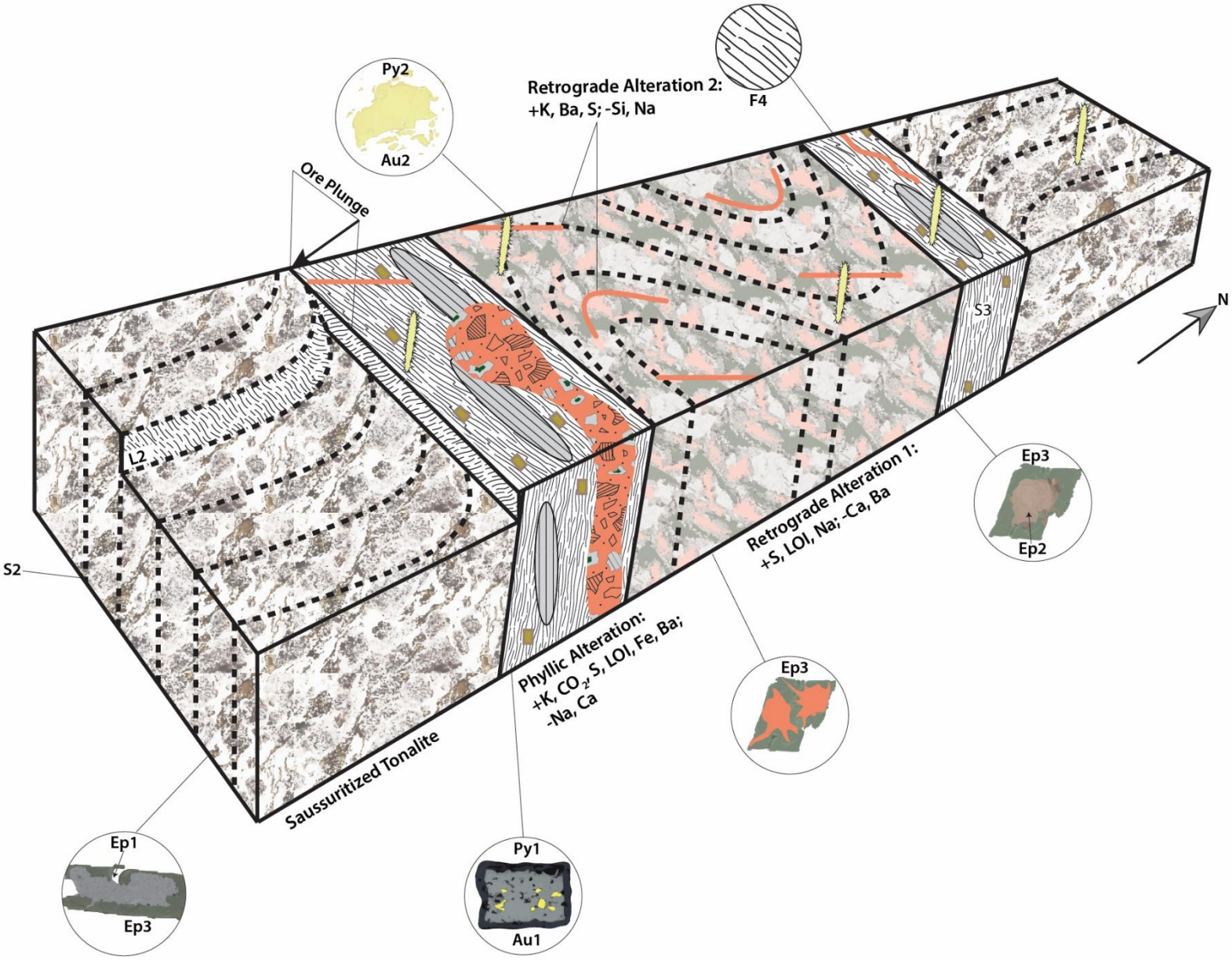

Figure 3.19 (A) Plot of $\delta^{18}O$ values for vein quartz (Y-axis) versus temperature (X-axis) with isopleths of corresponding $\delta^{18}O_{H2O}$ values calculated using the quartz-H_2O fractionation equation of Matsuhisha*et al*. (1979). Results from the SIMS $\delta^{18}O$ analysis of quartz grains from different vein types are shown as black dots. The field for $\delta^{18}O_{H2O}$ for Archean lode Au veins is from McCuaig and Kerrich, (1998), whereas the field for meteoric water is from Taylor (1974). For comparison are also shown the ranges for $\delta^{18}O_{quartz}$ from the Red Lake and Wawa areas (1; Kerrich, 1989) and from the Val-d'Or area (2; Beaudoin and Pirte, 2005). (B) Evaluation of a fluid-mixing model to explain the range in $\delta^{18}O_{H2O}$ values inferred from the Qtz_2 data over a temperature range of 200° to 500℃. The grey dashed lines are tie lines between endmember fluids ($\delta^{18}O_{H2O}$=10‰ and -15‰) with the numbers corresponding to the proportion of the fluid with $\delta^{18}O_{H2O}$=10‰ in the mixed system. (C) Evaluation of a Rayleigh fractionation model to explain the range in $\delta^{18}O$ Qtz_2 values (shown as the black bar).The curves for $\delta^{18}O_{quartz}$ and $\delta^{18}O_{H2O}$ at temperatures of 200°, 300° and 400°C were derived using the distillation equation in Faure (2005) using an initial $\delta^{18}O_{H2O}$= 10‰ (Kontak *et al*., 2016; Neydley*et al*., 2016). The f-value (x axis) corresponds to the fraction of unreacted fluid remaining.

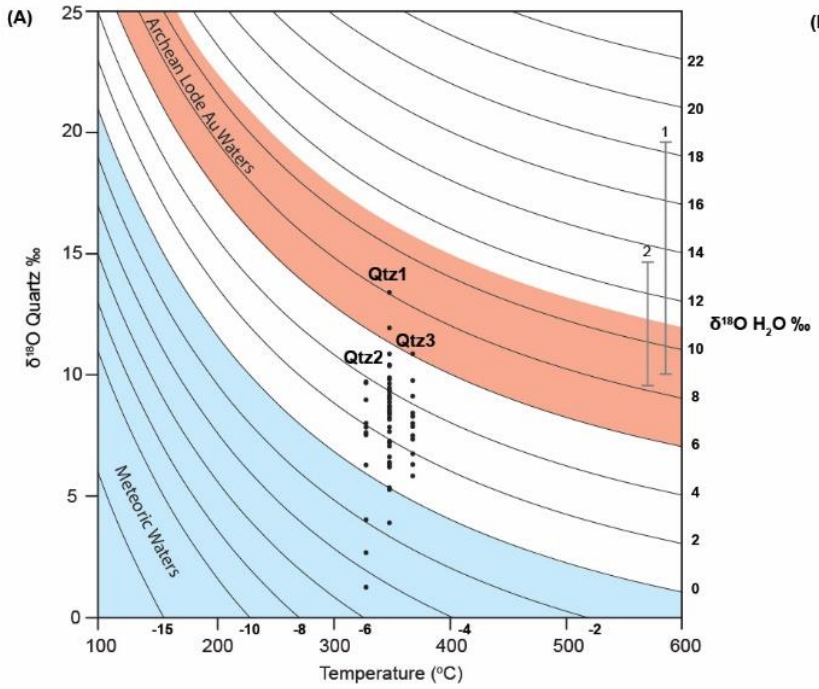
(A)
Archean Lode Au Waters
Meteoric Waters
Qtz1
Qtz2
Qtz3
δ18O Quartz ‰
δ18O H2O ‰
Temperature (ºC)

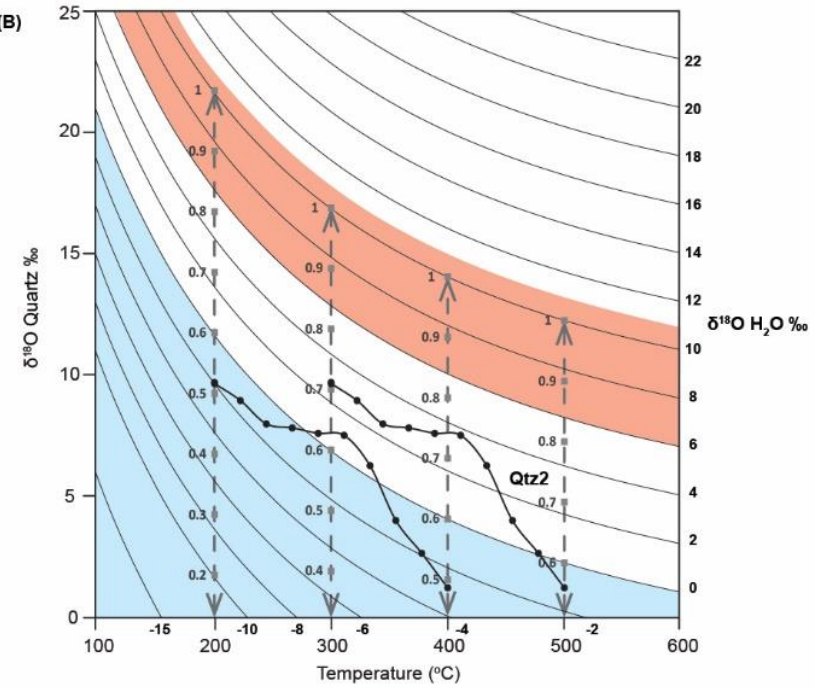
(B)
Qtz2
δ18O Quartz ‰
δ18O H2O ‰
Temperature (ºC)

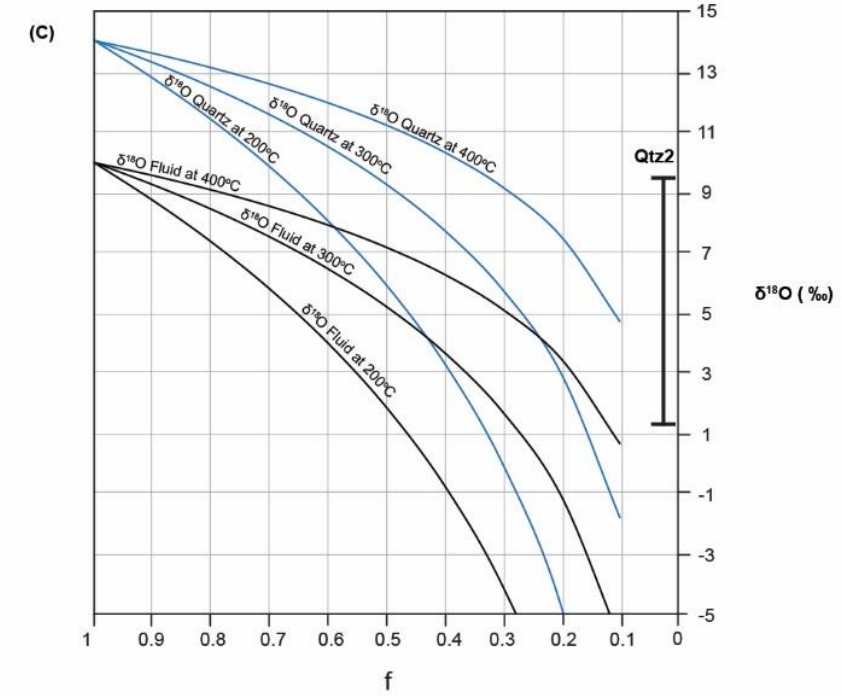
(C)
δ18O Quartz at 200ºC
δ18O Quartz at 300ºC
δ18O Quartz at 400ºC
δ18O Fluid at 400ºC
δ18O Fluid at 300ºC
δ18O Fluid at 200ºC
Qtz2
δ18O (‰)
f

Appendices

Appendix 3.1 Metal concentrations (ppm) from mineralized samples plotted in Figure 3.9. Lower limits of detection are reported in brackets.

Sample ID	Population	Outcrop	Au	Ag	As	Bi	Cu	Mo	Pb	Te	U	W	Zn
			(0.002)	(0.01)	(0.8)	(0.01)	(0.7)	(0.03)	(0.2)	(0.01)	(0.01)	(0.02)	(3)
C-8	Laminated Quartz Veins	C-zone	27.05	11.83	1.3	14.23	4.1	97.68	22.5	42.45	2.53	0.3	7.49
C-11			11.604	4.95	1.1	6.7	2.7	21.58	5.3	17.73	0.18	0.1	3.88
C-6			2.328	1.26	<0.8	1.1	83.6	2.88	3.6	4.15	0.46	0.5	60.66
BD-12		Baltic D	3.066	6.88	<0.8	9.57	4	18.1	14.9	13	0.86	<0.02	16.3
BD-17			1.41	7.47	<0.8	27.83	3.1	180.39	36.2	8.8	0.04	<0.02	<3
BD-13			0.526	2.54	<0.8	7.42	1.8	92.29	37.6	1.58	0.17	<0.02	3.7
BD-16			0.247	1.17	<0.8	7.92	3.6	164.58	22.4	9.59	1.05	0.1	7.55
BD-15			0.007	0.07	0.9	0.1	9.8	1.08	0.5	0.14	0.24	0.3	19.32
P-9.5		Nudulama	1.902	4.3	<0.8	2.92	3	>350	16.4	6.24	0.1	0.1	<3
P-10.5			0.509	0.96	1.1	0.55	6.4	8.12	5.1	1.56	0.18	0.2	17.83
P-10			0.012	0.03	<0.8	0.05	5	1.61	0.5	0.07	0.01	0.8	<3
Nu-12-04 #13		Nudulama (Drill Core)	18.564	1.26	<0.8	7.29	5.4	1.49	13.6	31.65	0.05	<0.02	<3
Nu-12-05 #18			1.174	0.24	1.1	0.21	15.6	3.05	2.4	1.7	0.13	0.1	16.15
Nu-12-05 #28			0.915	1.68	0.8	0.8	12.6	2.93	4.5	1.95	0.34	0.3	66.69
Nu-12-05 #30			0.777	0.73	1	5.08	3.8	66.23	1.3	3.52	0.14	<0.02	4.96
Nu-12-05 #29			0.422	0.87	0.9	0.43	11.1	2.02	1.3	1.02	0.04	0.1	6.61
NUE-27		Nudulama East	0.105	0.55	1.1	0.13	3.3	1.02	1.1	0.57	0.13	0.2	25.12
NUE-14			0.025	0.11	0.8	0.06	2	1.23	1.3	0.42	0.1	0.3	45.76
NUE-17			0.008	0.02	<0.8	0.07	2.1	0.46	0.6	0.04	0.12	0.1	36.19
NUE-24			0.007	0.07	<0.8	0.07	152.4	0.4	0.8	0.23	0.15	0.2	277.21
NUE-25			0.004	0.01	1	0.01	1.8	0.97	0.2	0.01	0.01	0.2	5.8
NUE-29b			0.028	0.13	<0.8	0.1	1.7	1.75	1.6	0.46	0.12	0.1	41.33
PL-9b		Pileggi No.1	22.832	1.98	1.5	0.04	232.7	5.73	0.9	0.33	0.04	0.7	44
PL-9a			18.858	1.3	1.1	0.03	55.3	3.05	0.5	0.28	0.02	0.3	27.13
PL-13			0.684	0.16	<0.8	0.04	109.6	3.15	0.6	0.19	0.04	0.4	118.95
PL-5			0.047	0.05	1.1	0.07	43.7	12.61	0.2	0.1	0.03	0.4	20.83
PL-6			0.023	0.08	<0.8	0.05	94.2	1.47	0.7	0.23	0.05	4.9	133.16
C-19	Phyllic Alteration (Quartz-Sericite-Pyrite Schist)	C-zone	6.697	3.76	1.6	12.56	2.2	>350	19.3	17.77	1.24	0.2	74.55
C-13			4.003	1.5	1	2.04	44.5	1.74	14.4	6.99	0.34	0.3	67.77
P-18		Nudulama	0.739	0.56	1.6	0.48	22.1	2.54	5.7	1.66	0.1	1.4	33.71
P-8			0.222	0.15	<0.8	0.19	12.2	0.44	3.8	0.42	0.18	0.1	54.58

P-9			0.189	0.29	<0.8	0.1	23.7	0.31	4.4	0.34	0.2	0.1	50.33
P-11			0.174	0.25	<0.8	0.06	10.1	0.28	2.3	0.37	0.14	0.1	47.39
P-4			0.032	0.07	<0.8	0.08	2.7	0.3	0.7	0.06	0.26	0.2	48.04
Nu-12-05 #18		Nudulama (Drill Core)	13.249	2.37	0.8	2.4	37.7	25.64	19.2	21.45	0.73	0.1	55.98
Nu-12-04 #13			3.782	1.71	<0.8	1.23	72.2	2.98	1.4	6.42	0.35	0.1	57.63
Nu-12-04 #13			0.704	0.32	1	0.19	26.9	0.75	1.1	1.23	0.55	0.1	52.67
Nu-12-05 #27			0.6	0.43	<0.8	0.19	18.6	0.32	2.2	0.93	0.38	0.1	49.7
Nu-12-05 #28			0.32	0.51	<0.8	0.27	16.7	0.48	3.3	0.56	0.36	0.2	99.83
Nu-12-04 #14			0.169	0.13	1	0.06	20.1	1.08	1	0.27	0.15	0.1	58.67
Nu-12-05 #18			0.115	0.07	0.9	0.07	8.6	0.65	1.9	0.22	0.56	0.1	47.64
Nu-12-05 #19			0.096	0.05	1	0.07	20.8	0.51	1.5	0.14	0.28	<0.02	66.33
Nu-12-05 #25			0.064	0.11	<0.8	0.1	5.4	0.51	1.5	0.1	0.62	0.1	85.97
NUE-13		Nudulama East	0.113	0.2	0.8	0.54	6.6	1.46	0.5	0.51	0.07	1.2	21.31
P-13	Massive Pyrite Veins	Nudulama	0.329	0.71	0.8	0.35	410.4	1.25	1.9	0.7	0.61	0.2	189.73
NUE-10		Nudulama East	3.993	3.75	2.6	26.53	4.9	0.68	3.1	15.93	0.51	1	16.68
NUE-1			1.271	4.34	2	3.75	14.1	14.02	23.6	5.11	0.56	0.4	59.62
NUE-31			1.182	2	1.4	9.05	5.2	0.45	1.6	8.35	0.14	0.2	11.71
NUE-6			0.544	1.06	1.4	3.47	4.4	0.49	1	1.79	0.33	0.2	42.8
NUE-26			0.225	1.33	1.3	0.94	3.2	0.7	1.4	1.75	0.2	0.2	28.04
NUE-22			0.081	1.82	<0.8	5.81	15.2	0.62	5.6	2.61	0.6	0.4	29.69
NUE-21			0.062	3.91	1.6	15.65	19.7	1.07	8.1	10.7	0.06	0.1	5.03
NUE-20			0.05	1.8	4.5	9.14	26.8	0.64	4.8	1.72	0.81	0.1	4.93
NUE-25			0.04	0.53	1.4	1.04	6.4	0.58	1.1	0.58	0.2	0.1	11.16

Appendix 3.2 Results of quartz vein SIMS O-isotope analysis.

Spot Analysis	Sample Type	Vein Type	Outcrop	Quartz Generation	$\delta^{18}O$ VSMOW (‰)
C-1 #1	Puck-Mounted Grain	Laminated Quartz	C-zone	Qtz_1	8.2
C-1 #2					8.5
C-11 #1					6.2
C-11 #2					11.9
C-11 #3					6.6
C-11 #4					8.7
C-2 #1					7.8
C-2 #2					6.3
C-8 #1					8.4
C-8 #2					9.2
C-8 #3					10.4
C-9 #1					10.4
C-9 #2					10.9
C-9 #3					7.7
C-9 #4					8.6
P-10 #1			Nudulama		5.3
P-10 #2					7.1
P-10 #3					8.7
P-10 #4					6.4
P-12 #1					7.2
P-12 #2					7.3
P-17 #1					8.4
P-17 #2					8.2
P-19 #1					9.3
P-19 #2					9.5
P-9.5 #1					9.6
P-9.5 #2					5.3
P-9.5 #3					8.5
Nu-12-05 #1			Nudulama (Drill Core)		9.1
Nu-12-05 #2					10.4
Nu-12-05 #3					3.9
Nu-12-05 #4					13.4
NUE-27 #1			Nudulama East		9.4
NUE-27 #2					9.9
NUE-27 #3					7.2
NUE-27 #4					9.8
NUE-27 #6					8.6
PL-9 #1			Pileggi No.1		9.0
PL-9 #2					8.9
PL-9 #3					6.2
PL-9 #4					7.2
NUE-11 #1		Breccia Vein	Nudulama East	Qtz_2	7.5
NUE-11 #2					9.7
NUE-11 #3					6.3

Spot Analysis	Sample Type	Vein Type	Outcrop	Quartz Generation	$\delta^{18}O$ VSMOW (‰)
NUE-11 #4		Breccia Vein	Nudulama East	Qtz_2	7.8
NUE-30 #1					9.0
NUE-30 #2					4.0
NUE-30 #3a					2.7
NUE-30 #3b					1.2
NUE-9 #1					8.0
NUE-9 #2					7.6
NUE-9 #3					9.7
PL-12 #1		Quartz Tension Gash	Pileggi No.1	Qtz_3	7.9
PL-12 #2					10.9
PL-12 #3					5.8
PL-12 #4					6.3
PL-7a #1					9.8
PL-7a #2					9.1
PL-7a #3					8.4
PL-7a #4					7.5
PL-9 #1					9.0
PL-9 #2					8.9
PL-9 #3					6.2
PL-9 #4					7.2
PL-9b #1					8.0
PL-9b #2					7.3
PL-9b #3					6.7
PL-9b #4					8.3
NUE-30 #1	Thin Section (Cathodoluminescence Image)	Breccia Vein	Nudulama East	Qtz_2	11.9
NUE-30 #2					11.4
NUE-30 #3					9.6
NUE-30 #4					5.5
NUE-30 #5					9.5
NUE-30 #6					7.8
NUE-30 #7					9.6
NUE-30 #8					10.6
NUE-30 #9					9.4
NUE-30 #10					6.1
NUE-30 #11					8.8
NUE-30 #12					12.5
NUE-30 #13					12.6
NUE-30 #14					5.9

Spot Analysis	Sample Type	Vein Type	Outcrop	Quartz Generation	$\delta^{18}O$ VSMOW (‰)
NUE-30 #15	Thin Section (Cathodoluminescence Image)	Breccia Vein	Nudulama East	Qtz_2	6.0
NUE-30 #16					12.4
NUE-30 #17					10.3
NUE-30 #18					6.0
NUE-30 #19					5.4
NUE-30 #20					5.4
NUE-30 #21					8.5
NUE-30 #22					8.9
NUE-30 #23					8.3
NUE-30 #24					7.8
NUE-30 #25					7.2
NUE-30 #26					7.8
NUE-30 #27					7.5
NUE-30 #28					8.5
NUE-30 #29					7.1
NUE-30 #30					6.6
NUE-30 #31					6.6
NUE-30 #32					7.1
NUE-30 #33					5.9
NUE-30 #34					8.2
NUE-30 #35					7.5
NUE-30 #36					10.7
NUE-30 #37					8.6
NUE-30 #38					12.2
NUE-30 #39					10.7
NUE-30 #40					10.8
NUE-30 #41					11.9